The University of Manchester

Oilfield Corrosion: Sweet Corrosion Scales

A thesis submitted to the University of Manchester for the degree of

Doctor of Philosophy (Ph.D.)

in the faculty of Science and Engineering

January 2020

Mohammed Al Kindi

School of Natural Sciences

Department of Materials

Table of Contents

List of Figures

List of Tables

Abstract

"Oilfield Corrosion: Sweet Corrosion Scales "

Mohammed Al Kindi, University of Manchester, 2020

Internal corrosion of oilfield pipelines, fabricated from carbon steel, due to dissolved CO_2 remains one of the major problems encountered in the oil and gas industry. Under specific conditions, CO_2 corrosion, more commonly known as '*sweet corrosion*', can result in the growth of corrosion scale on the inner pipeline walls. Such scale can lead to a considerable reduction in the corrosion rates, if it is densely packed and well adhered to the surface. The work in this thesis aims to improve understanding of the development of CO_2 corrosion products and how different factors can influence the formation and evolution of the formed scale.

Motivated by the recent identification of an *unexpected 'cylindrical'* habit for the primary sweet corrosion scale component, siderite ($FeCO_3$), effort has focused on examining habit variation as a function of environment. Initially, scales formed on both corroding Fe substrates, and non corroding PTFE substrates, after immersion in CO_2-saturated salt solution were explored. The siderite crystal habit was found to change as a function of $Fe^{2+}_{(aq)}$, varying from rhombohedral to cylindrical as the the amount of $Fe^{2+}_{(aq)}$ is increased in solution. These results are consistent with theoretical modelling of the $FeCO_3$ crystal habit by collaborators from Imperial College, and may be the basis of alternative approaches to corrosion control (e.g. habit engineering). Besides, the addition of Ca^{2+} resulted in formation of $Fe_xCa_yCO_3$ solid solution, while addition of the Mg^{2+} resulted in a formation of rhombohedral siderite with the appearance of un-identified elongated rods.

The siderite crystal habit on Fe substrates was further explored as a function of increasing CO_2 partial pressure and temperature by developing and implementing an autoclave facility for high pressures and high temperatures (HPHT) testing. An increase in CO_2 partial pressure from 0.5 to 4 bar was found to change the siderite crystal habit from '*cylindrical*' to rhombohedral. This observation is also found to be consistent with the theoretical modelling of siderite crystal habit, and demonstrates that crystal habits are likely to vary as fluids progress through an oilfield facility.

Finally, an improved design of a custom built cell for *in situ* synchrotron grazing incidence X-ray diffraction was employed to gain insight into sweet corrosion scale evolution as a function of time and temperature. Electrochemical data and *in situ* GIXRD diffractograms reveal that siderite is mainly responsible for the reduction in corrosion rate by forming a protective scale on Fe substrate immersed in CO_2-saturated water (buffered to pH = 6.8, T = 80°C, P_{CO_2} = 0.5 bar). Furthermore, a temperature excursion results in scale dissolution as the temperature decreases to $\sim$ 25°C, and scale regrowth with the increase in temperature back to 80°C, suggesting that local variations in temperature may be detrimental to scale properties.

Declaration

No portion of the work referred to in this thesis has been submitted in support of an application for another degree or qualification of this or any other university or institute of learning.

Copyright Declaration

i The author of this thesis (including any appendices and/or schedules to this thesis) owns certain copyright or related rights in it (the "Copyright") and s/he has given The University of Manchester certain rights to use such Copyright, including for administrative purposes.

ii Copies of this thesis, either in full or in extracts and whether in hard or electronic copy, may be made only in accordance with the Copyright, Designs and Patents Act 1988 (as amended) and regulations issued under it or, where appropriate, in accordance with licensing agreements which the University has from time to time. This page must form part of any such copies made.

iii The ownership of certain Copyright, patents, designs, trade marks and other intellectual property (the "Intellectual Property") and any reproductions of copyright works in the thesis, for example graphs and tables ("Reproductions"), which may be described in this thesis, may not be owned by the author and may be owned by third parties. Such Intellectual Property and Reproductions cannot and must not be made available for use without the prior written permission of the owner(s) of the relevant Intellectual Property and/or Reproductions.

iv Further information on the conditions under which disclosure, publication and commercialisation of this thesis, the Copyright and any Intellectual Property and/or Reproductions described in it may take place is available in the University IP Policy (see http://documents.manchester.ac.uk/DocuInfo.aspx?DocID=487), in any relevant Thesis restriction declarations deposited in the University Library, The University Library's regulations (see http://www.manchester.ac.uk/library/aboutus/regulations), and in The University's policy on Presentation of Theses.

Acknowledgement

Firstly, I would like to express my deepest gratitude and appreciation to my supervisor, Dr. Robert Lindsay. He was always there to provide invaluable guidance, direction, constant motivation and tremendous support. The passion that he had for this field pushed me to persevere past many obstacles.

This work would not have been possible without the financial support of Petroleum Development Oman and BP for my tuition and project funding respectively. I am grateful and fortunate to be involved in an exciting project in a class-leading institute.

I am indebted to Gaurav Joshi and Karyn Cooper for their advice and help especially at the beginning of my PhD. They provided me a platform from which I was able to further develop the research in this exciting field.

I would like to thank the experimental officers who trained and allowed me to access to their facilities; Mr Mike Faulkner, Dr. Chris Wilkins, Dr. Teruo Hashimoto and Dr. Ali Gholinia for for SEM/FIB-SEM; Mr Gary Harrison and Dr. John Warren for XRD; Mr. Andrij Zadoroshnyj for Raman μ-spectroscopy; and Dr. Rafael Leiva-garcia for Confocal microscopy. At the ESRF, I thank Dr. Oier Bikondoa for his assistance during our visits. Access to these pieces of high end laboratory equipment has been both a joy and honour for me.

I would like to also thank my special friends at the university who I worked and spent a great time with: Yasser Alaboura, Abdulati Rafefi, David Martelo, Rafa, Jake Andrews, Raunaq Singh, Rob Moorcroft, Phil Aldhous, Dominic Craske, David Ruiz, Maria and Gissele. It has been great to spend my time with a group dedicated to pushing boundaries and making new discoveries.

I would like to extend my love and gratitude to my parents, family and friends, who throughout this journey have been nothing but a beacon of light. Their

kind words and never ending encouragement pushed me to strive towards success. Without the warm presence and welcoming arms of my friends in Manchester, especially Haroon and Bobby, my experience would not be what it is right now. To my beloved wife, who has been a pillar of support throughout this entire time and encouraged me to go beyond and past what I never thought possible.

Publications

From the work presented in this thesis, the following have been published:

E. A. Ahmad, H.-Y. Chang, M. Al-Kindi, G. R. Joshi, K. Cooper, R. Lindsay, and N. M. Harrison, "Corrosion protection through naturally occurring films: New insights from iron carbonate," ACS applied materials & interfaces, vol. 11, no. 36, pp. 33435–33441, 2019.

Chapter 1.

Introduction

Corrosion remains a widespread concern and accounts for a large percentage of failures experienced in the oil and gas industry [1]. One of the main corrosion issues is the internal corrosion of oilfield equipment due to the produced CO_2 gas, which becomes corrosive only when dissolved in the aqueous phase flowing with the hydrocarbons [2, 3]. Moreover, carbon steel is still the preferred material, selected because of its effective cost and good mechanical properties [4]. However, it has poor corrosion resistance, especially in aggressive oil and gas conditions.

Various factors influence the oilfield CO_2, or *sweet*, corrosion process. Under specific conditions, it is possible to form a corrosion scale on the steel surface that can lead to a significant reduction in corrosion rate [5–7]. Furthermore, the breakdown of this layer can lead to localised corrosion [8, 9]. Despite the extensive research into CO_2 corrosion, it is still not well understood. This is partially because of the complexity of CO_2 corrosion and scale formation as it is greatly influenced by the change in testing conditions and environmental parameters.

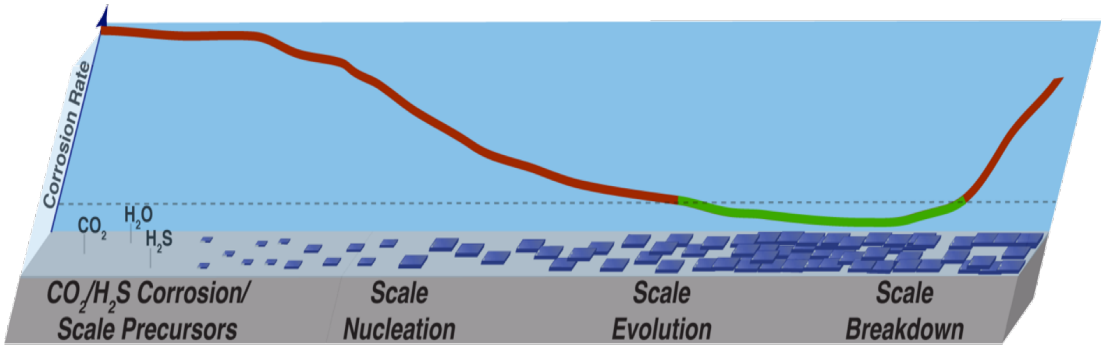

Figure 1.1: Schematic diagram illustrating the lifetime of CO_2/H_2S corrosion scales. The diagram is courtesy of Dr Robert Lindsay (Department of Materials, The University of Manchester)

Figure 1.1 shows an illustration of the lifetime of sweet corrosion scales where it starts with scale precursors and ends by scale breakdown. Formation of highly protective scale resulting in the reduction to low corrosion rates, as illustrated by a green zone in Figure 1.1, can provide an attractive engineering

solution to protect the steel surface. However, it is essential to understand if it is possible to rely on corrosion scales to maintain operating in the green zone without any local breakdown.

In light of the above, this project aims to fundamentally understand sweet scale evolution and the influence of several parameters on the properties of the formed scale. This project is systematically building upon a previous work done within the research group by keeping the environmental conditions and substrate microstructure as simple as possible in well-controlled laboratory experiments.

In this project, the scale formation has been investigated on high purity Fe samples, minimising microstructural influence. A number of techniques were used for *ex situ* characterisation of the formed scale post-immersion, including grazing incidence X-ray diffraction (GIXRD), scanning electron microscopy (SEM), electron backscattered diffraction (EBSD), and 3D confocal laser microscopy. In addition, focused ion beam (FIB) SEM was used to obtain cross-sections of the scale-substrate interface. The degree of protection provided by the scale was assessed using electrochemical techniques to estimate substrate corrosion rates. Also, the use of synchrotron radiation GIXRD enabled *in situ* characterisation of the scale.

This thesis is divided into seven chapters, including this introductory chapter. Chapter 2 provides a general overview of corrosion in the oil and gas industry, and introduces the sweet corrosion process and mechanisms. Subsequently, a review of relevant literature is presented, focusing on sweet corrosion scale and the influence of various parameters on its formation. Chapter 3 outlines the various experimental techniques used in this study. Chapters 4-6 present the results of the research programme. Chapter 4 focuses on iron carbonate ($FeCO_3$), a common component in the sweet corrosion scale, crystal habit formed on corroding and non-corroding surfaces. Furthermore, the influence of various factors on the iron carbonate, or siderite, crystal habit is also

explored. Chapter 5 extends the investigation of siderite crystal habit formed on Fe substrate, by focusing on the influence of changing the temperature and CO_2 partial pressure, implementing an autoclave facility. Chapter 6 explores temporal and temperature-related evolution of sweet corrosion scale on Fe substrate in an *in situ* synchrotron radiation GIXRD experiment. Finally, Chapter 8 provides a summary of the research work and the potential for future work.

Chapter 2.

Literature Review

2.1 Electrochemical aqueous corrosion

Metallic corrosion is the deterioration of metals as a result of a chemical reaction between the metals and its environment [10]. Unlike other materials such as ceramics, almost all metals are chemically unstable [11]. The corrosion process returns the metal to its more stable combined state, e.g. an oxide, which was the state prior to extraction from a mineral source. Most of metallic corrosion processes involves charge transfer in an aqueous environment [12]. It involves an oxidation reaction where a metal loses one or more electrons and a reduction reaction where an the equivalent number if electrons are gained [13]. For example, corrosion of a metal in acidic conditions proceeds according to the overall reaction:

$$\mathrm{M} + \mathrm{n}\mathrm{H}^{+} \rightleftharpoons \mathrm{M}^{n+} + \frac{\mathrm{n}}{2}\mathrm{H}_2 \tag{2.1}$$

where M is the metal, and M^{n+} is the metal cation. This overall reaction can be also represented by two half reactions:

$$\mathrm{M} \rightleftharpoons \mathrm{M}^{n+} + \mathrm{n}e^{-} \tag{2.2}$$

$$\mathrm{H}^{+} + \mathrm{n}e^{-} \rightleftharpoons \frac{\mathrm{n}}{2}\mathrm{H}_2 \tag{2.3}$$

From the two reactions above, metal oxidation occurs through the anodic half reaction and the reduction occurs through the cathodic half reaction of the hydrogen cation in this case. These two half reactions occur at two different reaction sites; an anode and a cathode (at the surface-electrolyte interface). A conductive path is required for the electrons to transfer between an anode and a cathode. An electrolyte is also required to provide an electrolytic conductive path for the ions between the two reactions. This can be illustrated by a simple schematic diagram of a metal corroding in an acidic environment as shown

in Figure 2.1. At higher pH, other possible cathodic reactions are oxygen reduction or water reduction (in the absence of oxygen). These cathodic reaction are represented by the two half reactions below:

$$O_2 + 2\,H_2O + 4\,e^- \rightleftharpoons 4\,OH^- \tag{2.4}$$

$$2\,H_2O + 2\,e^- \rightleftharpoons H_2 + 2\,OH^- \tag{2.5}$$

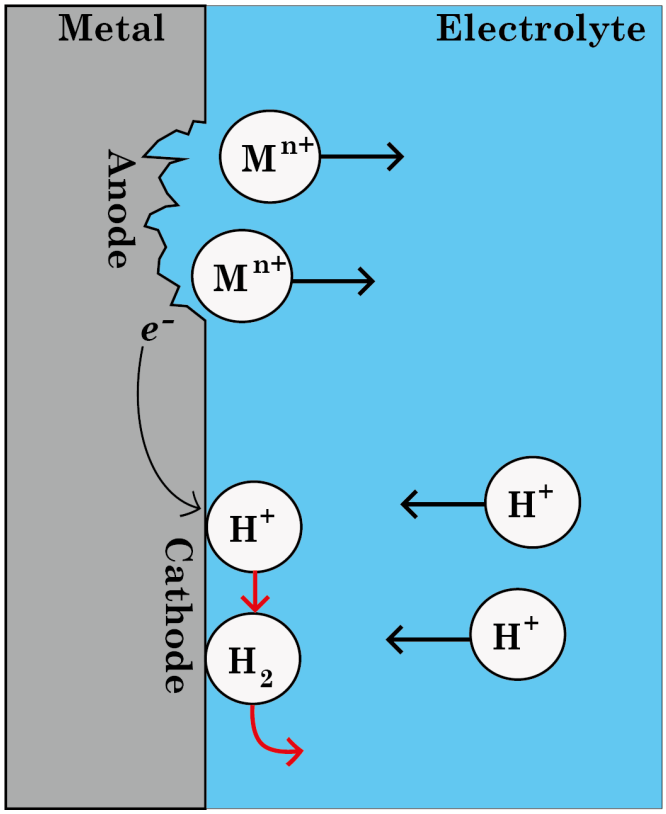

Figure 2.1: Schematic illustration of an electrochemical cell at the metal-solution interface.

2.2 Corrosion in the oil and gas industry

Worldwide demand for energy has risen in the past few decades and will continue to increase in the coming years. Nearly 60% of global energy is derived from crude oil and natural gas [14]. Figure 2.2, shows an illustration

summarising the journey of crude oil/natural gas from the production wells to the final end product of fuel. In addition to oil and gas, wells also produce water, other organic compounds, and acid gases. Corrosion presents economic, safety and environmental related issues in this process network. A wide range of corrosion problems are encountered as a consequence of materials exposure to a range of environments (e.g. production/injection) and operating conditions (e.g. temperature, pressure, flow) [15].

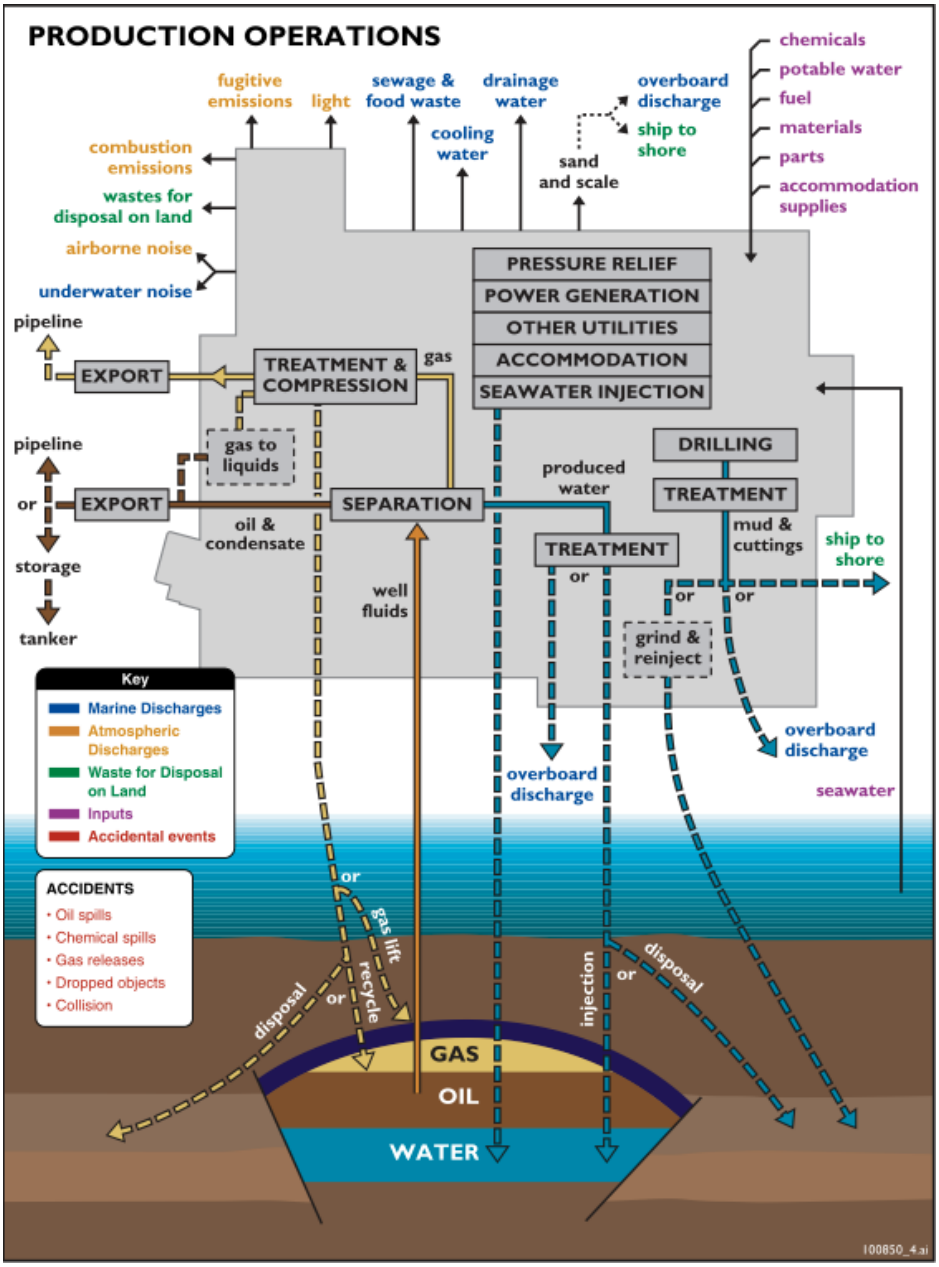

Figure 2.2: Schematic illustration of oil/gas production with sources of potential issues from the production operations. Reproduced from [16].

Corrosion issues are estimated to cost approximately 1.37 billion USD annually in the oil and gas production industry [1]. Internal corrosion accounts for 56% of corrosion-related failures suffered [17, 18]. Figure 2.3 shows main types of internal corrosion issues of carbon steel surfaces exposed to the oilfield brines. Nearly half of these problems occur in CO_2-dominant and H_2S-dominant environments [2]. 'Sweet' is commonly used to refer to CO_2-containing environments, and 'sour' to refer to H_2S-containing environments and these terms will be used throughout this thesis. Despite extensive research of sweet (see, for example, Ref. [4, 19–29]) and sour systems (see e.g. Ref.[30–33]) in the past few decades, there is still no full understanding of corrosion mechanisms and influence of many factors on corrosion.

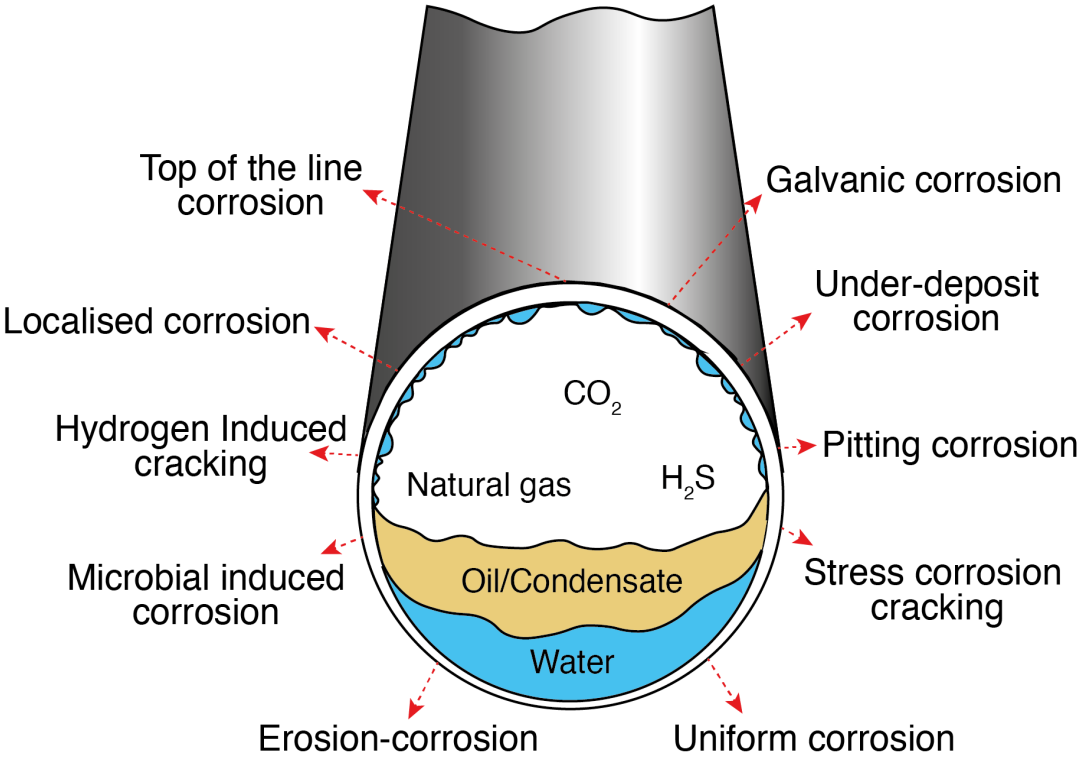

Figure 2.3: Main types of corrosion during transport of produced fluids.

2.3 Sweet corrosion

2.3.1 Overview of CO_2-water system

CO_2 as a dry gas is not corrosive under oilfield environments. However, it becomes corrosive when dissolved in water. Therefore, solution chemistry of CO_2-water system must be described to help understand sweet corrosion. The CO_2-water equilibrium has been studied extensively [34–39]. CO_2 gas dissolves in water forming carbonic acid H_2CO_3, which further dissociates to form bicarbonate (HCO_3^-) and carbonate(CO_3^{2-}). Chemical reactions are listed in Table 2.1 with the corresponding equation for their equilibrium constants.

Table 2.1: Chemical reactions and equilibrium constant expressions of CO_2/water chemistry [40].

Chemical reaction	Equilibrium constant expressions
$\mathrm{CO_{2(g)} \rightleftharpoons CO_{2(aq)}}$ (2.6)	$\mathrm{K_{CO_2} = \frac{[CO_{2(aq)}]}{pCO_{2(g)}}}$ (2.7)
$\mathrm{CO_{2(g)} + H_2O_{(l)} \rightleftharpoons H_2CO_{3(aq)}}$ (2.8)	$\mathrm{K_{hyd} = \frac{[H_2CO_3]}{[CO_{2(aq)}]}}$ (2.9)
$\mathrm{H_2CO_{3(aq)} \rightleftharpoons HCO_3^-{}_{(aq)} + H^+_{(aq)}}$ (2.10)	$\mathrm{K_{ca} = \frac{[H_2CO_3^-][H^+]}{[H_2CO_3]}}$ (2.11)
$\mathrm{HCO_3^-{}_{(aq)} \rightleftharpoons CO_3^{2-}{}_{(aq)} + H^+_{(aq)}}$ (2.12)	$\mathrm{K_{bi} = \frac{[CO_3^{2-}][H^+]}{[HCO_3^-]}}$ (2.13)
$\mathrm{H_2O_{(l)} \rightleftharpoons OH^-_{(aq)} + H^+_{(aq)}}$ (2.14)	$\mathrm{K_w = [OH^-][H^+]}$ (2.15)

The CO_2 dissolution reaction (Eq. 2.6) can be expressed in the case of ideal gas

and ideal solution behaviour by Henry's law (Eq. 2.7) [41]. CO_2 gas solubility varies as a function of different parameters such as pressure, temperature, and ionic strength [37, 42–46]. For the hydration reaction of CO_2 (Eq. 2.8), some studies report a lack of temperature dependence of the equilibrium constant (Eq. 2.9) [35, 39, 47–49]. On the other hand, other studies developed a temperature-pressure dependence relationship to describe equilibrium constants of carbonic acid H_2CO_3 and carbonate HCO_3^- dissociation reactions [38, 46]. Note that non-ideal gas/solution behaviour and presence of foreign ions can alter equilibria in CO_2-water system [38, 42, 50].

In order to determine the pH of a CO_2-saturated solution, an extra equation is required to solve the system, which describes the electroneutrality of the solution [51]:

$$[H^+] = [HCO_3^-] + 2[CO_3^{2-}] \tag{2.16}$$

The electroneutrality equation can be extended to include produced $Fe^{2+}_{(aq)}$ due to the corrosion process. In addition, the hydrolysis of $Fe^{2+}_{(aq)}$ reaction is to be also considered [51, 52]:

$$Fe^{2+}_{(aq)} + H_2O <=> FeOH^+_{(aq)} + H^+_{(aq)} \tag{2.17}$$

2.3.2 Sweet corrosion mechanism

The sweet corrosion mechanism has been extensively studied over the last 50 years [53]. Despite this effort, this topic is still debated, especially concerning the cathodic reaction mechanism in CO_2 environments, which has received more attention. The challenge in studying the CO_2 corrosion mechanism arises from system complexity by the added chemical species as a consequence of CO_2 hydration and subsequent dissociation reactions. The main cathodic

reactions proposed by several authors are listed below:

$$2\,H^{+}_{(aq)} + 2\,e^{-} \rightleftharpoons H_{2(g)} \tag{2.18}$$

$$2\,H_2CO_{3(aq)} + 2\,e^{-} \rightleftharpoons H_{2(g)} + 2\,{HCO_3}^{-}{}_{(aq)} \tag{2.19}$$

$$2\,{HCO_3}^{-}{}_{(aq)} + 2\,e^{-} \rightleftharpoons H_{2(g)} + 2\,{CO_3}^{2-}{}_{(aq)} \tag{2.20}$$

$$2\,H_2O_{(l)} + 2\,e^{-} \rightleftharpoons H_{2(g)} + 2\,OH^{-}_{(aq)} \tag{2.21}$$

Reaction (2.18) is hydrogen ion reduction reaction, which is a common cathodic reaction in acidic/deareated environments [54–58]. In CO_2 environments, some studies suggest that the carbonic acid direct reduction reaction (equation 2.19) occurs as a cathodic reaction [19, 59–62] while others conclude that carbonic acid only acts as a buffer to produce H^+ required for hydrogen ion reduction reaction (equation 2.18) [21, 63, 64]. Carbonate ion reduction is another proposed cathodic reaction (equation 2.20) [62, 65, 66]. However, it is unlikely to be the case at the pH range faced in oilfield conditions and should only be considered at more alkaline pH. The water reduction reaction (equation 2.21) has also minimal contribution as it is kinetically slower and does not explain the high cathodic currents experienced in sweet oilfield environments [40]. It is important to note that a combination of these suggested cathodic reactions possibly occur at the steel surface [67,68].

As regards the anodic reaction, the overall electrochemical reaction of iron can be expressed as:

$$Fe_{(s)} \rightleftharpoons Fe^{2+}_{(aq)} + 2\,e^{-} \tag{2.22}$$

It is still debated whether there is an influence of CO_2 on iron dissolution mechanism. This led to different proposed reaction pathways [23, 69–71]. As mentioned earlier, CO_2 system complexity presents a challenge to provide

experimental evidence for the proposed mechanisms.

2.3.3 Sweet corrosion products

Siderite

Siderite ($FeCO_3$) is a sparingly soluble salt that is isostructural with calcite ($CaCO_3$) and magnesite ($MgCO_3$) [72]. Siderite crystallizes in the hexagonal system as shown in Figure 2.4 The density of siderite ($FeCO_3$) is approximately 3.96 g/cm^3 [73].

The space group of siderite is $R\bar{3}C$ and the unit cell consists of two Fe atoms. Within the unit cell, the C atoms are surrounded by three O atoms forming ${CO_3}^{2-}$ planar that is perpendicular to the c axis. Six O atoms (${CO_3}^{2-}$ group) surrounds each Fe atom, forming a FeO_6 octahedron.

Siderite is considered the main corrosion product observed under CO_2 environments [4, 68]. At certain conditions, formation of protective siderite scale can result in a significant decrease in corrosion rates. Siderite forms from ferrous ions (Fe^{2+}) originated by the corrosion process and carbonate ions (${CO_3}^{2-}$) present due to CO_2 dissolution in water according to the precipitation reaction:

$$\mathrm{Fe^{2+}_{(aq)} + {CO_3}^{2-}{}_{(aq)} \rightleftharpoons FeCO_{3(s)}} \tag{2.23}$$

Precipitation of $FeCO_3$ occurs when the concentrations of $Fe^{2+}_{(aq)}$ and ${CO_3}^{2-}{}_{(aq)}$ exceeds the solubility limit K_{sp} of $FeCO_3$ formation [75]. The driving force for $FeCO_3$ precipitation is supersaturation (S), which can described by equation (2.24) [47,76]:

$$S = \frac{a_{\mathrm{Fe^{2+}}}.a_{\mathrm{{CO_3}^{2-}}}}{K_{sp}} \tag{2.24}$$

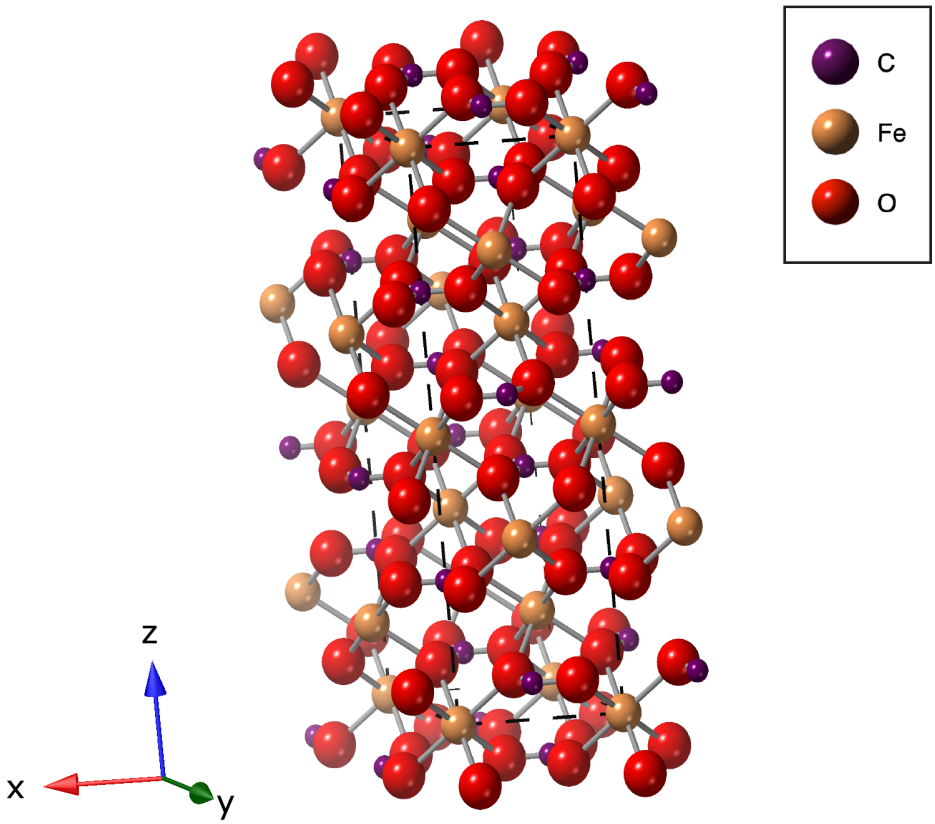

Figure 2.4: Siderite crystal structure generated by CrystalMaker software [74].

where $a_{Fe^{2+}}$ is the ferrous ion activity, $a_{CO_3^{2-}}$ is the carbonate ion activity and K_{sp} is the solubility product constant of $FeCO_3$. Siderite K_{sp} is dependant on aqueous solution temperature and ionic strength [77–81].

Precipitation theoretically initiates when supersaturation value is above > 1. However, critical values of supersaturation much higher than unity are typically required to favour precipitation of $FeCO_3$ [82, 83]. The two main processes involved in precipitation are nucleation and crystal growth [76]. The process starts with nucleation which results in a formation of $FeCO_3$ nuclei followed by crystal growth of the stable nuclei. Heterogeneous nucleation, which occurs on imperfection sites on the corroded steel surface, is more common than homogeneous nucleation, as it requires less energy of formation [83]. Nucleation and crystal growth rates are both dependant on the degree of supersaturation. It is believed that crystal growth rate increases linearly with

supersaturation, while there is an exponential relation between nucleation rate and supersaturation [73]. As a consequence, crystal growth process dominates at lower supersaturation levels, whereas nucleation is more dominant at higher levels of supersaturation [67,75].

Siderite is often described as displaying a rhombohedral crystal habit (3D shape), as shown in Figure 2.5 (a) [84–86]. However, in a recent work by Joshi et al [5], siderite crystal habit was found to be a mircofaceted cylinder with trigonal/pyramidal caps (Figure 2.5 b). This crystal habit is common for siderite formed on corroded iron/steel, although not previously reported. Siderite crystal habits are discussed in further detail in *Chapters 4 and 5*.

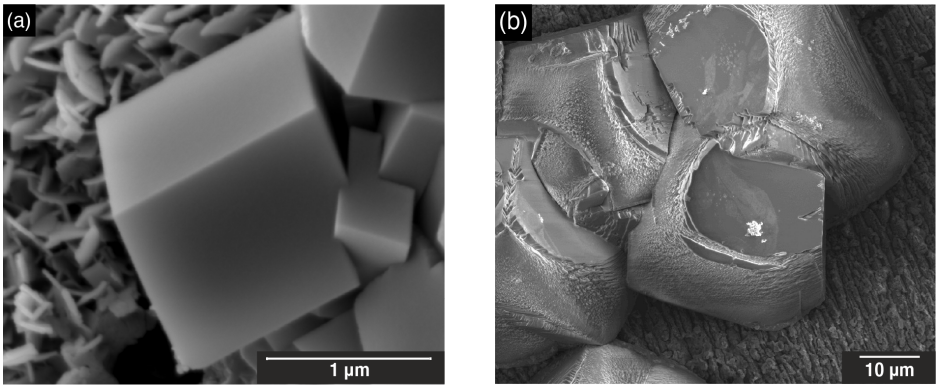

Figure 2.5: Different siderite crystal habits formed at on (a) PTFE substrate immersed for 24 hours in CO_2-saturated 0.01 M $FeCl_2$ solution (T = 80°C, pH = 6.8, P_{CO_2} = 0.54 bar) (b) Fe substrate immersed for 24 hours in CO_2-saturated 0.1 M NaCl solution (T = 150°C, pH = 4.55, P_{CO_2} = 0.54 bar).

Chukanovite

Chukanovite ($Fe_2(OH)_2CO_3$) is an iron hydroxide carbonate that is structurally similar to pokrovskite, malachite and rosasite-group. It was observed for the first time in 1976, as one of the corrosion products on a steel surface in a heat exchanger and was described as '*malachite-like basic iron carbonate*' [87]. Chukanovite crystallizes in the monoclinic crystal system and belongs to $P2_1/a$ space group. Figure 2.6 shows the crystal structure of chukanovite generated by Crystal Maker software [74], and using data from [88].

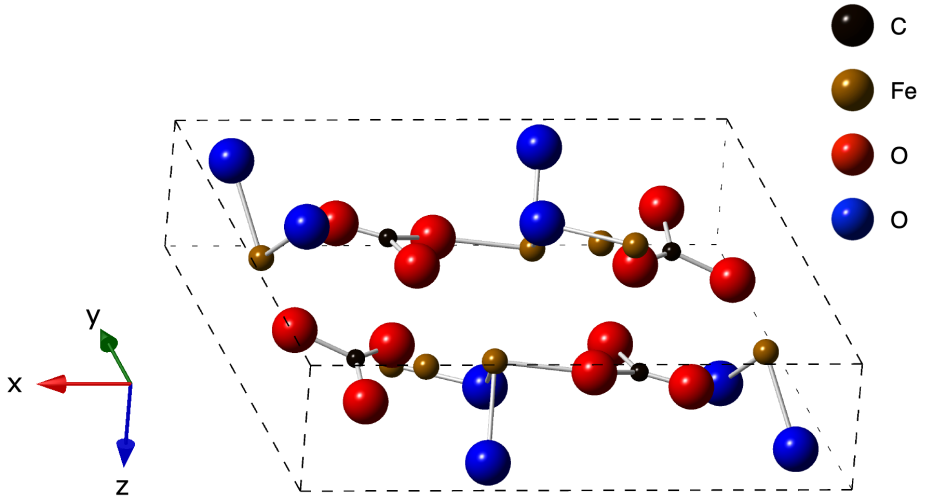

Figure 2.6: Chukanovite crystal structure generated by CrystalMaker software [74].

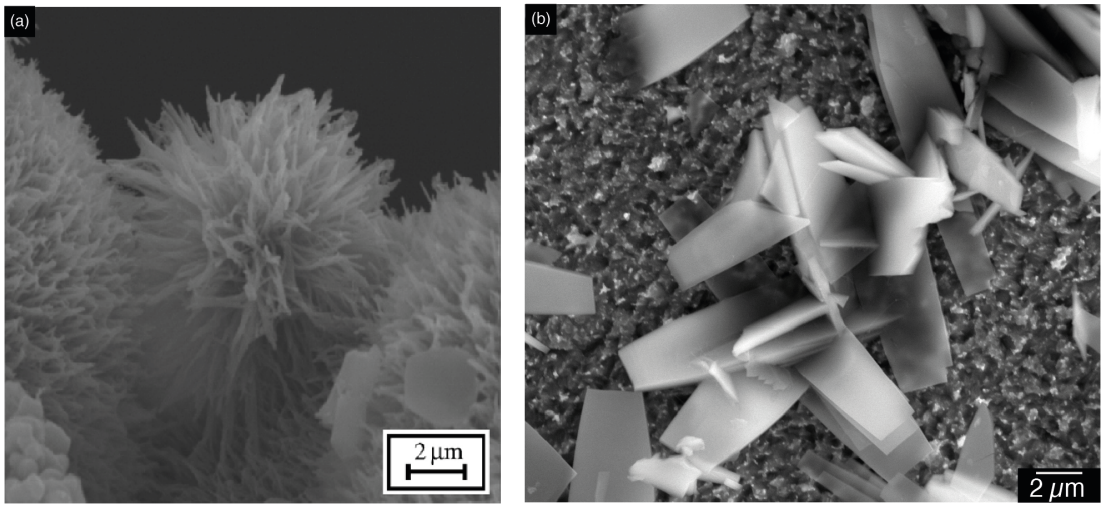

Figure 2.7: Chukanovite crystal morphology examples: (a) acicular/fibrous [87], and (b) platy structure.

Chukanovite has been observed on archaeological samples [89, 90], as a corrosion product on steel in nuclear-waste repository conditions [91–93], and on iron/steel surfaces in oil and gas CO_2-saturated conditions [5, 94]. Chukanovite morphology is described as acicular/fibrous or platy structure as shown in Figure 2.7. As regards formation in oil and gas conditions, chukanovite is not commonly observed in the formed corrosion scale. This is possibly due to chukanovite being unstable with respect to siderite, and

can rapidly oxidise in the presence of oxygen [87, 95]. Some studies have observed chukanovite formation as a result of sample anodic polarisation [96, 97]. However, other studies have formed chukanovite forming naturally at the corrosion potential [5, 94]. It is still unclear whether the formation of chukanovite can offer any degree of protection to steel against corrosion.

2.3.4 Factors influencing sweet corrosion scales formation

Sweet corrosion scale formation is influenced by a wide number of environmental, operational, metallurgical (corroding material) factors. This section focuses on discussing the influence of temperature, CO_2 partial pressure, pH, solution chemistry and steel microstructure, as shown in Figure 2.8.

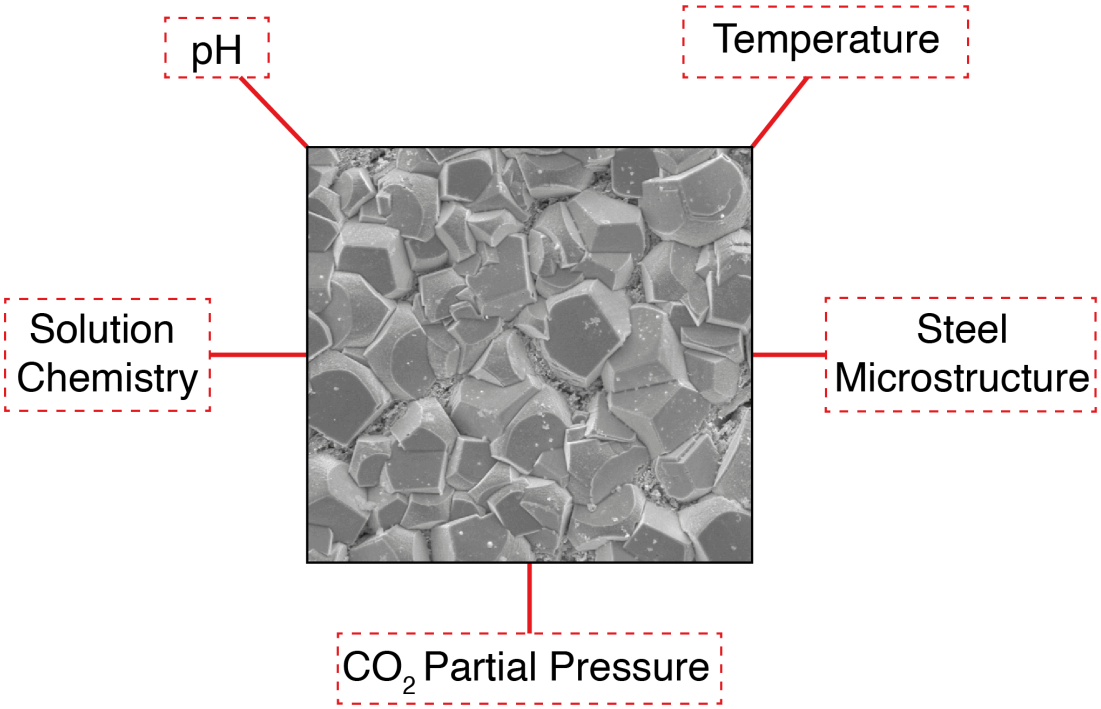

Figure 2.8: Main parameters influencing sweet corrosion scale formation discussed in this section.

Temperature

Generally, an increase in temperature enhances corrosion kinetics leading to higher corrosion rates [51]. However, the increasing temperature also decreases siderite solubility leading to its formation on the steel surface [81]. At elevated temperatures (> 60°C), a dense and tightly packed layer forms resulting in a decrease in corrosion rate [5, 27, 51, 75, 98, 98–104]. Studies show either no detectable corrosion products or porous, loosely packed films form at lower temperatures (< 40°C) [27].

Siderite has been reported in many studies to be the most dominant component in the scale layer formed at a temperature range 60°C - 150°C [82, 104–107]. The solubility product of siderite decreases as a function of temperature and this is shown in Figure 2.9, promoting precipitation and scale formation resulting in the decrease in corrosion rate.

In addition to siderite, other carbonate compounds have been detected at temperatures lower than 40°C, namely; chukanovite ($Fe_2(OH)_2CO_3$), iron oxy-carbonate ($Fe_2O_2CO_3$), and carbonated green rust ($Fe_6(OH)_{12}CO_3$)[108, 109]. Chukanovite is also observed in a few studies to form alongside siderite in the scale layer at a higher temperatures [5, 110–113]. Although carbonated green rust has been observed in deoxygenated CO_2-environment at near-neutral and alkaline pH, a more recent *in situ* GIXRD work by Ingham et al. showed that carbonated rust forms as a result of oxygen ingress to the system [114].

Magnetite has been also observed as one of the corrosion products formed in sweet environments. Some studies showed that magnetite forms in a mixed layer of siderite/magnetite at temperatures above 100°C and becomes the most dominant phase at 250°C [51, 84, 115–117].

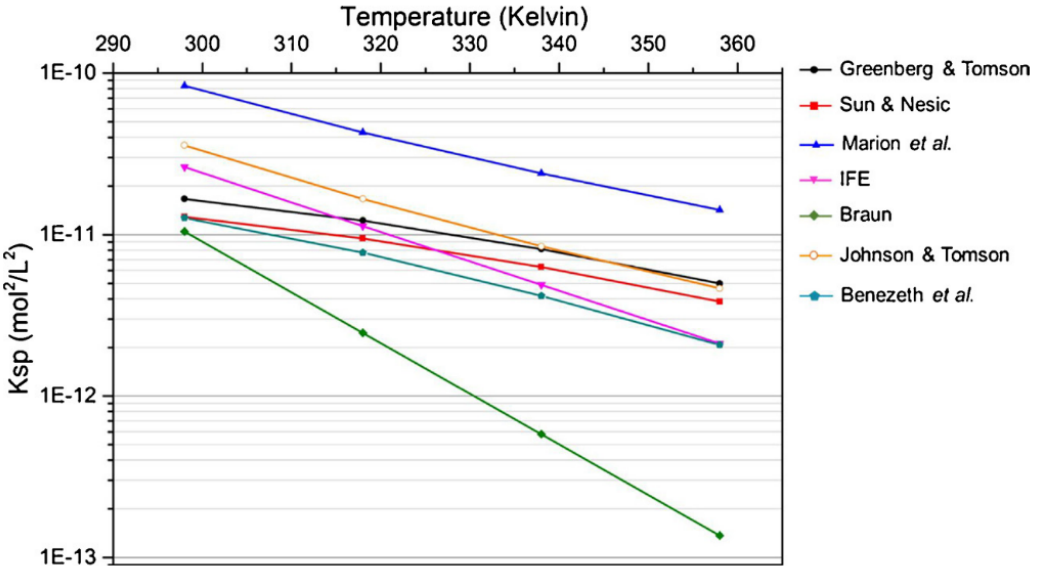

Figure 2.9: Plots of $FeCO_3$ solubility product constant as a function of temperature. Plot is reproduced from [68].

Solution pH

Solution pH can directly influence corrosion rates through the change in hydrogen ions (H^+) concentration, which is the primary cathodic reagent in hydrogen evolution reaction. Furthermore, a change in pH can also influence siderite ($FeCO_3$) solubility, as carbonate species concentrations changes with pH. As the pH increases, higher concentrations of carbonate ions exist in solution, thus less $Fe^{2+}_{(aq)}$ is required to reach supersaturation. Figure 2.10 shows the influence of pH on the required concentration of Fe^{2+} to reach supersaturation. As a consequence, higher pH solutions lead to lower corrosion rates by suppressing cathodic reactions and also by promoting film formation.

Studies typically suggest a more protective, compact, and dense layer of $FeCO_3$ is formed at higher pHs across a range of temperatures [24, 86, 118–121]. At CO_2 partial pressure of 0.5 bar and temperature ~ 60°C, studies showed that protective scales only form when pH > 6 within 20 days of immersion [86,105]. This critical pH that is required to form a protective layer decreases with the increase in temperature and CO_2 partial pressure [119,122].

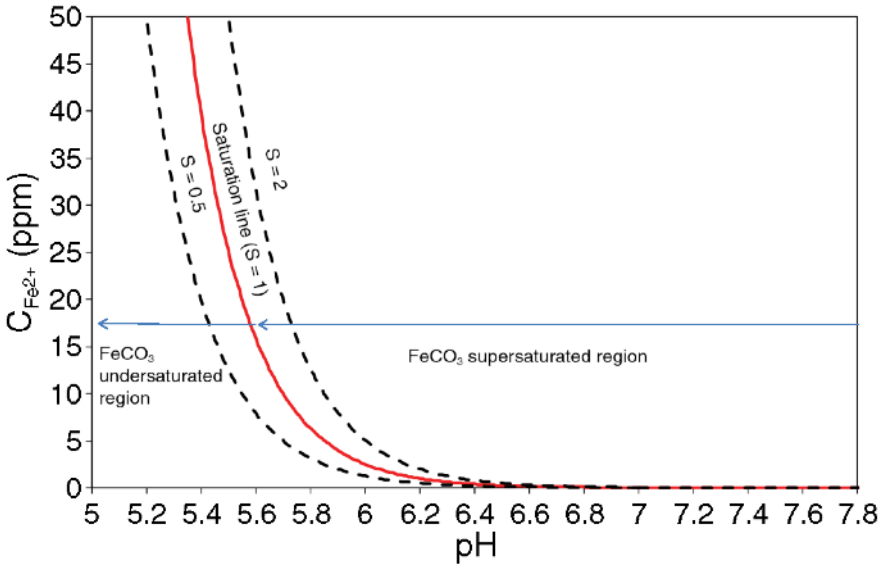

Figure 2.10: Required amount of Fe^{2+} to reach saturation limits as a function of pH (at T= 80°C, P_{CO_2}= 0.53 bar, 1 wt% NaCl). Reproduced from [121].

CO_2 partial pressure

Under film-free corroding conditions, an increase in CO_2 partial pressure leads to a greater corrosion rate [123]. This is mainly due to the increase in dissolved $CO_{2(aq)}$ and $H_2CO_{3(aq)}$ concentration that result in a decrease in pH. Several studies have confirmed this increase in corrosion rate and showed that no scale is detected on steel surfaces with increasing CO_2 partial pressure up to 80 bar at lower than the critical temperature to form scales (< 50°C) [124, 125]. However, many studies have shown that an increase in CO_2 partial pressure promotes film formation even at lower pH, which becomes protective only when formed at temperatures (> 60°C) [24, 29, 98, 125, 126]. The reason behind this observation is that the increase in CO_2 partial pressure increases concentration of carbonate ions and thus decreases decreases the amount of Fe^{2+} required to exceed the solubility limit of $FeCO_3$. However, Dugstad suggested that the influence of increasing CO_2 partial pressure on the solubility product of $FeCO_3$ is more complex and depends on solution pH as shown in Figure 2.11. From this study, the influence of CO_2 partial pressure on the required amount of Fe^{2+} to form $FeCO_3$ was investigated at a constant pH. $NaHCO_3$ was added to compensate for the decrease in pH due to the increase in CO_2 partial pressure. From this work, the amount Fe^{2+} required at higher pH (>5.5) decreases with the increase in CO_2 partial pressure. Nevertheless, the amount required of Fe^{2+} to exceed the solubility limits increases at low constant pH (∼4) with an increase in CO_2 (see Figure 2.11) [67]. This behaviour can be related to the changes in the solubility limits of $FeCO_3$ by the increase in ionic strength, due to the addition of $NaHCO_3$.

Few studies reported that although thicker, dense layers form, the increase in CO_2 partial pressure increased the likelihood of localised corrosion attacks after analysing the surface after scale [24, 94, 103].

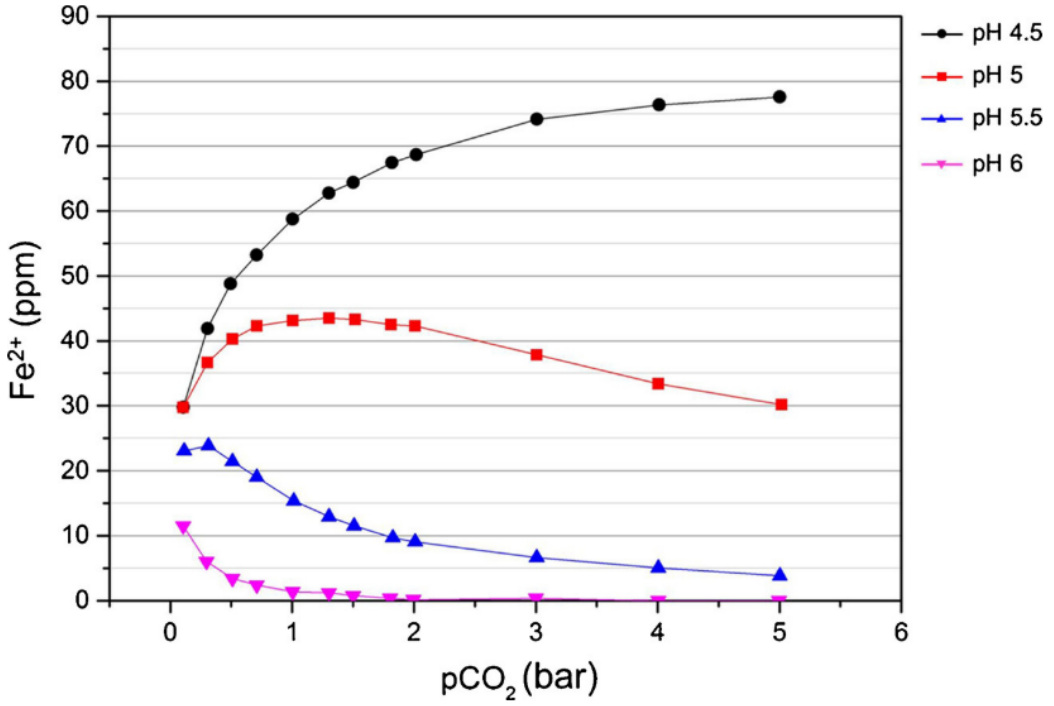

Figure 2.11: Required amount of Fe^{2+} to reach saturation limits as a function of CO_2 partial pressure at pH = 4.5, 5, 5.5, 6. Reproduced from [68].

Solution chemistry

Formation water, which is usually produced from oil and gas wells, contains a range of ions and other species, increasing the complexity of the system. This includes dissolved $Ca^{2+}_{(aq)}$, $Mg^{2+}_{(aq)}$, $Na^{+}_{(aq)}$, $Cl^{-}_{(aq)}$, and organic compounds. A number of studies focused on determining the influence of each factor on the corrosion behaviour and scale formation under sweet environments.

The presence of $Ca^{2+}_{(aq)}$ and $Mg^{2+}_{(aq)}$ can result in the formation of mineral scales: calcium carbonate ($CaCO_3$), or magnesium carbonate ($MgCO_3$) scales under CO_2-saturated environments. The solubility product of $CaCO_3$ and $MgCO_3$ decreases with the increase in temperature, which is similar to the behaviour of $FeCO_3$ [127,128]. In comparison, $FeCO_3$ has the lowest K_{sp} compared to $CaCO_3$ and $MgCO_3$, as shown in Figure 2.12.

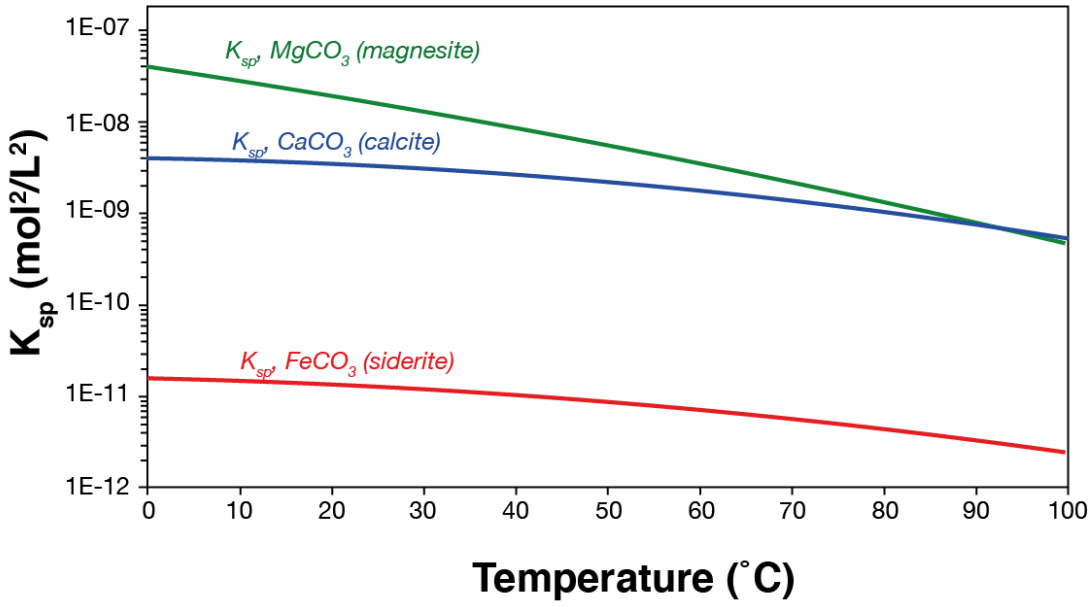

Figure 2.12: Comparison between solubility product of $FeCO_3$, $CaCO_3$, and $MgCO_3$ as a function of temperature. Plot is reproduced from [129].

As mentioned earlier in section 2.3.3, siderite ($FeCO_3$) is isostructural with calcite ($CaCO_3$) and magnesite ($MgCO_3$) as they share the same hexagonal structure. This means that Fe^{2+} can be replaced with Mg^{2+} and Ca^{2+} in the crystal structure forming a solid solution [$(Fe, Mg, Ca)CO_3$], which can alter the protective properties of the formed scale.

The impact of $Ca^{2+}_{(aq)}$ and/or $Mg^{2+}_{(aq)}$ on the sweet corrosion mechanism and formed scale properties has received little attention. Furthermore, the studies investigating this topic so far have provided conflicting results. A number of studies have found a negative impact on corrosion by the addition of $Ca^{2+}_{(aq)}$, where corrosion rates increase [130, 131]. On the other hand, some researchers concluded that the addition of $Ca^{2+}_{(aq)}$ promotes formation of a more protective layer of $FeCO_3$ or $Fe_xCa_yCO_3$ [132, 133]. In Esmaeely et al.'s work, where the influence of a range of added concentrations of $Ca^{2+}_{(aq)}$ on scale formation was investigated, it was observed that more protective $FeCO_3$ can form by the addition of small amounts of $Ca^{2+}_{(aq)}$ [134]. However, a non-protective $CaCO_3$ scale formed at higher concentrations $Ca^{2+}_{(aq)}$, and $FeCO_3$ no longer exist. Several authors reported an increase in localised corrosion by the addition of

$Ca^{2+}_{(aq)}$ [132, 135]. However, it is still not quite clear on the mechanism behind the contribution of $Ca^{2+}_{(aq)}$ ions to localised corrosion.

As regards to the presence of $Mg^{2+}_{(aq)}$, a few studies suggested that addition of $Mg^{2+}_{(aq)}$ ions can enhance the protectiveness of the formed $FeCO_3$ scale [97,136]. Ingham et al. suggested that addition of $MgCl_2$ promotes scale precipitation at lower super-saturation and reduction in nucleation induction time [97]. Formation of $Fe_xMg_yCO_3$ solid solution is less frequently observed compared to $Fe_xCa_yCO_3$, possibly due to the higher solubility product of $MgCO_3$ leading also to an increase in the solubility of the solid solution [129].

Regarding the influence of increasing acetic acid (an organic acid) on the corrosion behaviour, it will increase the corrosion rates mainly by decreasing the solution pH and enhancing the cathodic reaction kinetics [137, 138]. In terms of $FeCO_3$ formation, it was suggested that more $Fe^{2+}_{(aq)}$ will be required to precipitate $FeCO_3$, thus an increase in the solubility [67,137]. However, this influence is insignificant at higher pH values (pH> 6) [139].

Steel microstructure

Various studies to investigate the effect of steel microstructure on sweet corrosion rates and the formation of corrosion products focus on how iron carbide (Fe_3C) in carbon steel can influence these processes. Iron carbide, commonly known as cementite, is electrically conductive, thus cathodic reactions can possibly occur on its surface [140].

The role of cementite to modify the degree of protection of the scale is still debated, with contradicting observations. The effect of cementite has been studied mainly by comparing corrosion behaviour of normalised steels with ferritic-pearlitic microstructure, and quenched and tempered steel with martensitic microstructure [111, 141]. It has been suggested that the presence of larger cementite particles in the normalised steel in the pearlite phase can result in a higher corrosion rate than in quenched and tempered steel, where

carbides are smaller and more distributed in solid solution [111]. However, other studies suggest that the presence of cementite, especially in normalised steel, can enhance the protectiveness of the formed corrosion scale [28, 142].

A number of studies suggest that presence of cementite in the corrosion scale can act as an 'anchoring effect', enhancing the protectiveness of the scale [28, 143–145]. J. Crolet et al. suggested that a more protective morphology can exist when a mixed siderite/cementite layer is formed on the surface [143]. Farelas et al. suggested that the same morphology, where a mixture of cementite and siderite scale formed on the steel surface, resulted in a protective scale forming on two different heat treated carbon steel samples with a better protection in the pearlite microstructure steel [142]. However, Dugstad et al. concluded in their study that more coverage and better adherence of the formed scale in a quenched-tempered steel (with no free carbides) under flowing conditions, which contradicts the suggestion of the 'anchoring effect' of cementite [146]. This has been also shown in a more recent work, where a more protective scales formed on low carbon steel compared to a heat treated ferritic-pearlitic high carbon steel [147]. In a recent study by Escrivà-Cerdán et al, where they assessed a corrosion resistance of a Cr-Mo low-alloy steels at different tempering states and showed that tempering at higher temperatures can lead to a decrease in uniform CO_2 corrosion rates [148].

In conclusion, it is not quite clear whether the steel microstructure has a direct effect on the formation and protectiveness of the formed scale, or whether it is possibly contributing to the initial corrosion rates and supersaturation near the steel surface leading to the change in the properties of the scale formed.

2.4 Conclusion

The literature review above presented an overview of CO_2 corrosion and focused mainly on the sweet corrosion scales. The review demonstrated how

sweet corrosion scales can provide protection to the steel surface under specific conditions. Despite the extensive research, there is still no complete understanding on how to control different variables to form a highly protective scale. In fact, a number of studies investigating influence of different factors reported contradicting results. The complexity of CO_2 systems present a challenge, that any subtle changes in the various parameters can significantly change the scale formation process. A fundamental approach, where the impact of different variables are investigated in a systematic fashion starting with a simple system, can aid in providing a better understanding on the sweet corrosion formation.

Since sweet scale formation is sensitive to the environmental conditions including oxygen concentration, it is important to carefully design the experimental setup and procedure to minimise exposure to air or oxygen during and after samples immersion. Establishing good practices can aid in improving the quality of the obtained results reducing any experimental artefacts. Ideally, employing different techniques to perform *in situ* experiments can provide useful insight on the kinetics of sweet scale formation and can avoid any risk of scale modification post-immersion.

The work presented in this thesis will systematically build upon previous work conducted in the research group [5, 149, 150]. This includes improving and development of experimental setup and procedure for an *in situ* synchrotron GIXRD work and HPHT autoclave testing. In addition, it will provide a first attempt to link between theoretical modelling and experimental results of the siderite crystal habit, the building block of protective sweet corrosion scale.

Chapter 3.

Experimental Techniques

3.1 Introduction

In this project, various experimental techniques have been used to investigate scale growth on different surfaces immersed in CO_2-saturated solutions. Figure 3.1 presents the experimental techniques used. This chapter discusses a basic theoretical background and some practical considerations of the various techniques used.

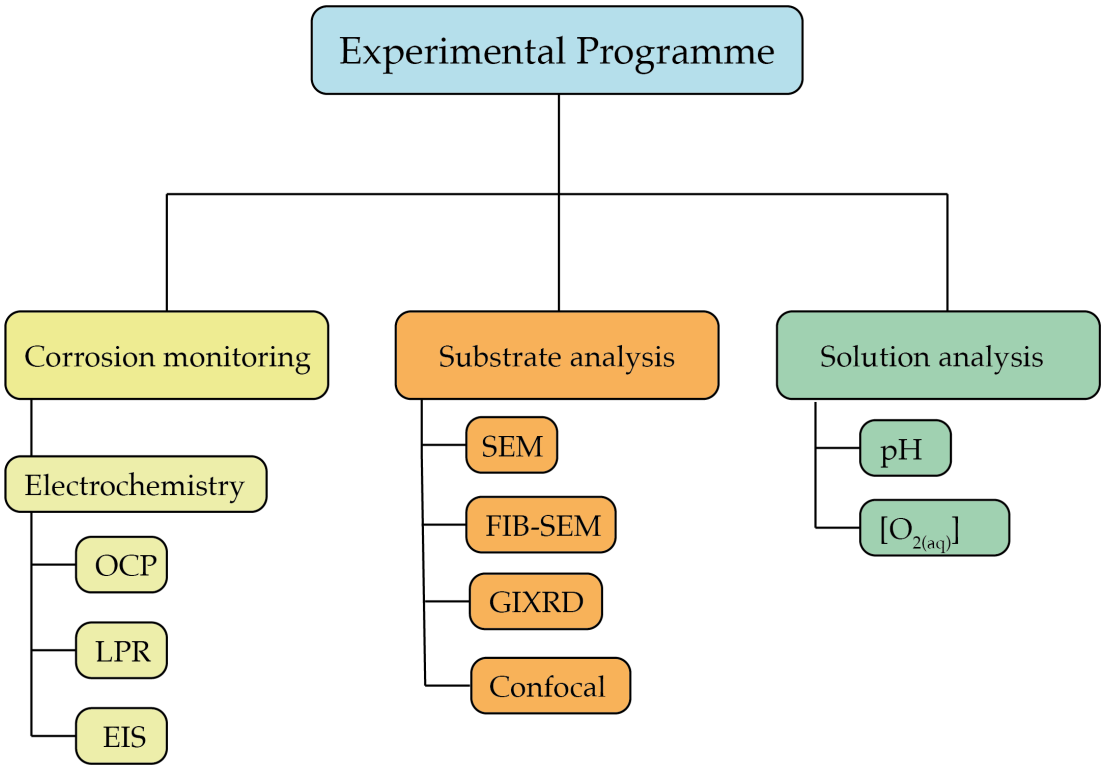

OCP: Open circuit potential
LPR: Linear polarisation resistance
EIS: Electrochemical impedance spectroscopy
SEM: Scanning electron microscopy
FIB: Focused ion beam
GIXRD: Grazing incidence x-ray diffraction
Confocal: 3D laser scanning confocal microscopy
$[O_{2(aq)}]$: Dissolved oxygen measurement

Figure 3.1: Experimental techniques used in this project.

3.2 Electrochemistry

Electrochemical techniques are suitable to evaluate the corrosion behaviour of the samples and have been used in many CO_2 corrosion studies (e.g. [151–153]). In this project, electrochemical techniques are employed to determine the corrosion rate of immersed Fe samples in CO_2-saturated solution at different conditions. The use of electrochemical techniques in conjunction with surface characterisation can provide useful insight to assess the degree of protection offered by the formed sweet corrosion scale on the investigated surface at different conditions (Chapter 5 and 6). This section discusses the electrochemical system setup, details of direct current (DC) and alternating current (AC) techniques used for this work.

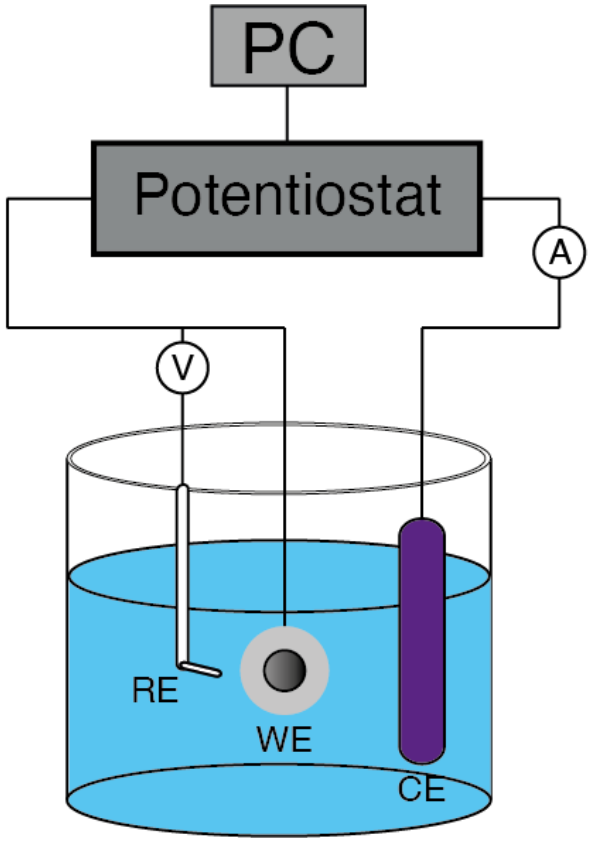

Figure 3.2: Schematic diagram showing the 3-electrode setup configuration for electrochemical measurements.

Basic three-electrode setup configuration was used as illustrated in Figure 3.2. The working electrode (WE) is the sample under investigation, and high purity iron (Fe) electrodes were used for all the electrochemical measurements carried out in this project. The reference electrode (RE) serves as a reference point to measure the WE potential. This means that RE should hold a stable potential in the solution during the immersion experiments. Platinum (Pt) wire pseudo-reference electrode was selected here due to the low solution conductivity, elevated operating temperatures and to avoid solution contamination. The last element in the three-electrode setup is the counter electrode (CE) which is an inert electrode that completes the path of the current in this setup. Pt wire/flag was used here as a counter electrode. The three electrodes were connected to Gamry Interface 1000 potentiostat.

3.2.1 Open circuit potential (OCP)

Open circuit potential is the interfacial electrochemical potential of the working electrode with respect to a reference electrode. Mixed or corrosion potential (E_{corr}) are other common terms used to describe the OCP. At this potential, the rates of the anodic dissolution (i_a) and the cathodic reduction (i_c) are equal to the rate of corrosion (i_{corr}).

$$i_a = i_c = i_{corr} \tag{3.1}$$

Therefore, the sample is freely corroding in the solution without applying any external voltage from the potentiostat. The reference electrode (RE) should be at thermodynamic equilibrium with a stable electrochemical potential throughout the whole duration of an experiment. Thus, any changes in OCP throughout the conducted experiment will be mainly due to changes occurring only on the surface of interest: (WE). Stability of OCP is important to ensure reliability of the measurements before varying the potential in LPR and EIS

measurements (details of these techniques will be discussed below).

3.2.2 Potentiodynamic Polarisation (PDP)

Potentiodynamic polarisation is a DC technique used to study the electrochemical kinetics of the anodic and cathodic reactions occurring on a corroding metal surface. In this technique, an external voltage is applied on the surface away from OCP, and the current response is measured. The measured current (i) will equal to the amount of increase in cathodic/anodic rates as the external voltage is applied.

$$i = |i_a - i_c| \tag{3.2}$$

As mentioned in the previous section, the cathodic and anodic rates are equal at OCP, and the measured current is equal to zero (see Figure 3.3). The current response by applying a negative over-potentials (away from OCP to the negative side) is representative of the cathodic half-reaction in the system. On the other hand, polarisation to a positive over-potentials is representative of the anodic half-reaction. Ideally, data fitting of the PDP data produces a linear relationship between anodic or cathodic over-potentials ($\eta_{a/c}$) and log i (equation 3.3). These two lines can be extrapolated to obtain the corrosion potential, and current at their intersection.

$$\eta_{(a/c)} = \beta_{(a/c)} log \frac{i_{(a/c)}}{i_{corr}}, \tag{3.3}$$

where $\beta_{a/c}$ is the anodic or cathodic Tafel constant, and i_{corr} is the corrosion current density measured at E_{corr}. Systems displaying such linear relationship are commonly known as exhibiting 'Tafel' or 'activation controlled' behaviour. However, usually polarisation curves deviate from this ideal Tafel behaviour

and the straight lines cannot be obtained. This might be due to several reasons such as, concentration polarisation, or ohmic resistance. PDP is a destructive technique to the tested sample and not suitable for studies requiring continuous monitoring of corrosion rates. Alternative non-destructive techniques can be used to estimate the corrosion rate of a corroding sample: linear polarisation resistance (LPR) and electrochemical impedance spectroscopy (EIS) [154, 155].

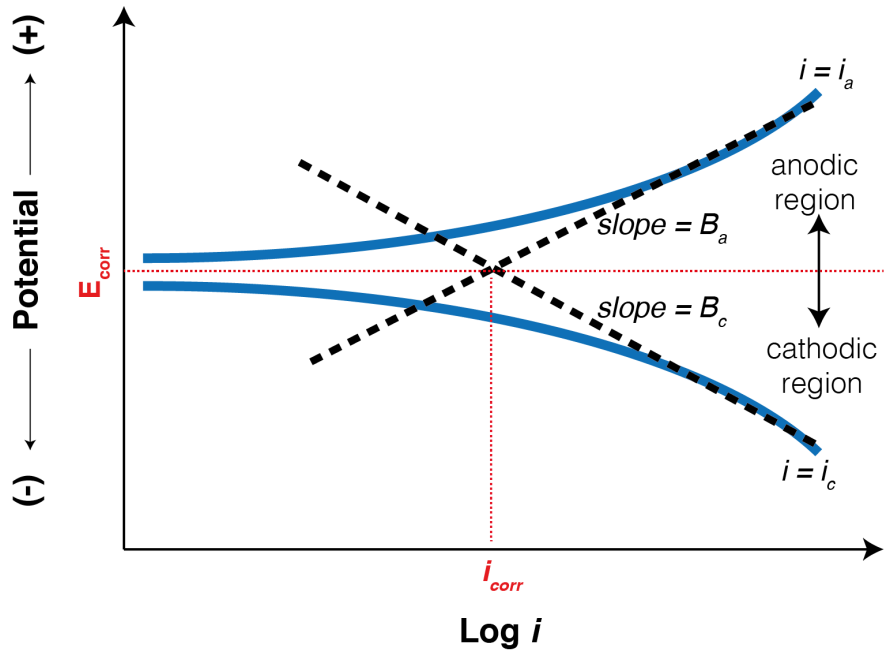

Figure 3.3: Schematic of a PDP plot of an activation controlled behaviour showing Tafel extrapolation, corrosion potential (E_{corr}) and corrosion current density (i_{corr}).

3.2.3 Linear Polarisation Resistance (LPR)

Linear polarisation resistance is a DC electrochemical technique used to estimate an average corrosion rate or charge transfer rate at the electrode surface-environment interface. It is considered as a non-destructive technique by applying small over-potentials, up to a few millivolts, from a steady-state electrode corrosion potential [156]. At a small over-potentials ($\pm$), the (E-i) relationship is linear in the polarisation curve. The slope of the graph (see

Figure 3.4) gives the polarisation resistance (R_p) according to equation (3.4), which can then be used to estimate corrosion rates as explained in section 3.2.5. It is important to note that a linear relationship is not always produced, depending on the nature of the corroding system and when the Tafel behaviour no longer applies [157].

$$R_p(slope) = \frac{\Delta E}{\Delta i} \tag{3.4}$$

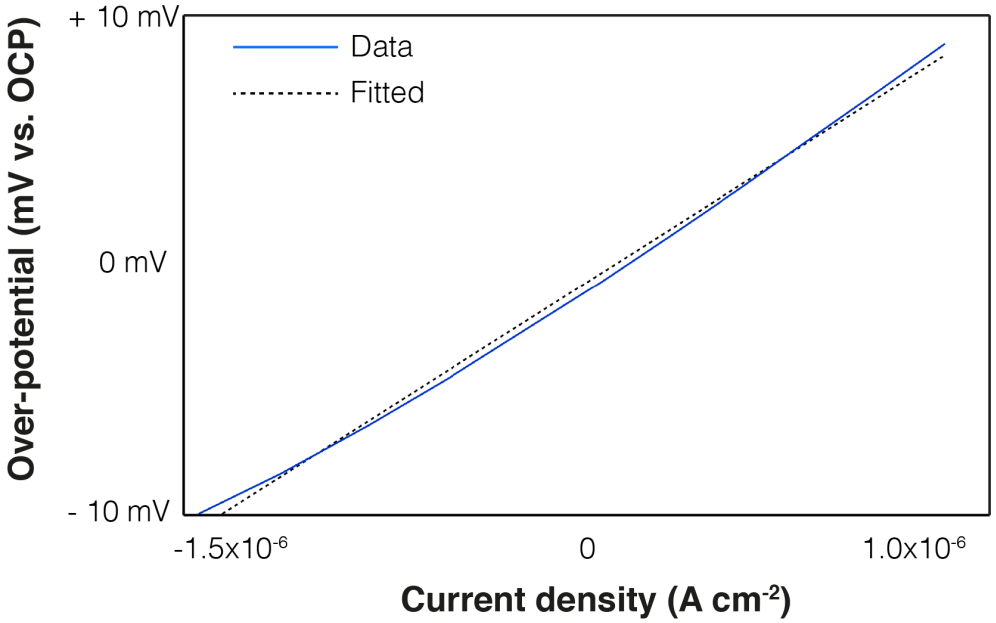

Figure 3.4: LPR plot showing a linear relationship between the potential and current response at small applied over-potential (± 10 mV).

3.2.4 Electrochemical Impedance Spectroscopy (EIS)

Electrochemical impedance spectroscopy is a non-destructive AC electrochemical technique used to determine the corrosion rate of an electrode. It determines the corrosion response of an electrode at small amplitude over-potentials (±10 mV) at various frequencies. Impedance (Z), which is equivalent to the resistance in DC measurements, can be determined from a time-dependent response current I(t) of an sinusoidally oscillating

applied potential E(t) according to the equation:

$$Z(\omega) = \frac{E(t)}{I(t)} = \frac{E_o sin\omega t}{I_o sin(\omega(t+\phi)} = Z'(\omega) + jZ''(\omega), \tag{3.5}$$

where ω is the angular frequency, ϕ is the phase shift between the potential and the current response, $Z'(\omega)$ is the real impedance component, and $Z''(\omega)$ is the imaginary impedance component.

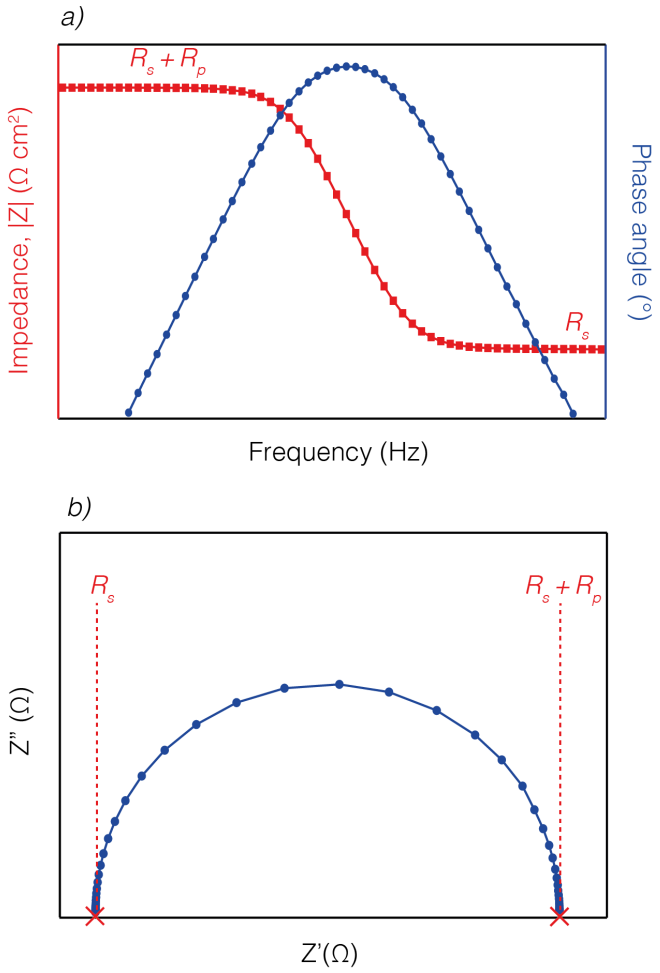

Figure 3.5: EIS data representation by (a) Bode plot and (b) Nyquist plot. Solution resistance (R_s) and polarisation resistance (R_p) can be obtained from low and high-frequency range data.

The measured impedance data can be presented by either Nyquist or Bode plots. In the Bode plots, the data are expressed as log of the impedance

magnitude |Z| and the phase shift (ϕ) versus the frequency (Hz), as shown in Figure 3.5 a). In the Nyquist plot, the data are expressed in terms of the imaginary versus the real components of impedance (Z″ and Z′), as shown in Figure 3.5 b).

EIS plots shown in Figure 3.5 is a basic example of an actively corroding system where it can be represented by Randles electrochemical equivalent circuit illustrated in Figure 3.6. From this circuit, R_s is the solution resistance (Ω cm^2), R_{ct} is the charge transfer resistance (Ω cm^2), and C_{dl} is the double-layer capacitance. R_s and R_{ct} values can be determined from EIS plots at the high and low range of frequencies as annotated in Figure 3.5. These values are then used to estimate the corrosion rate of the sample (details in section 3.2.5). In addition to corrosion rate estimations, EIS data can provide useful insight to understand the corrosion behaviour/scale formation when linked with the physical characterisation data. Furthermore, EIS data for more complex corrosion systems (e.g. formation of scale, coating) produce different plots than can be only fitted with more complicated equivalent circuits. Data fittings and equivalent circuits of a scaled Fe sample immersed in CO_2 are discussed further in the *in situ* synchrotron GIXRD work in Chapter 6.

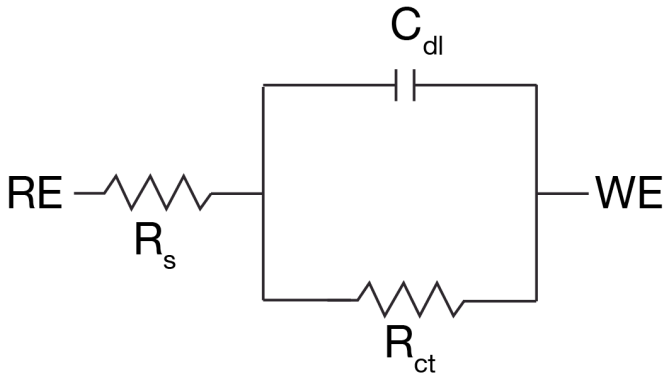

Figure 3.6: Randles electrochemical equivalent circuit.

3.2.5 Corrosion rate estimation (CR)

The values obtained from LPR and EIS measurements can be used to provide a corrosion rate estimates in (mm/yr). After obtaining the R_p values from LPR and EIS techniques, i_{corr} can be calculated using equation (3.6), which can then be used to estimate the CR according to equation (3.7):

$$i_{corr} = \frac{\beta_a \beta_c}{2.303 R_p(\beta_a + \beta_c)} = \frac{\beta}{R_p} \tag{3.6}$$

$$CR = \frac{i_{corr} MW}{\rho n F} .31,536,000, \tag{3.7}$$

where MW is the molecular weight of the WE, ρ is the density of the WE, n is the number of electrons lost in the anodic reaction, and F is Faraday's constant (9.6485 x 10^4 $Cmol^{-1}$). Tafel constants (β_a and β_c) can be obtained from PDP plots which can be used to estimate Stern-Geary coefficient (β). The reported β values are reported between β = 26 mV (for activation controlled systems) and β = 52 mV (for diffusion-controlled systems) [158].

3.3 Electron microscopy techniques

3.3.1 Scanning electron microscopy (SEM)

Scanning Electron Microscope (SEM) can be used to produce high-resolution images of a specimen surface. These images are produced when a focused electron beam scans the surface of the specimen. The main two advantages of a scanning electron microscope over an optical microscope are: (i) higher resolution, and (ii) larger depth of field (focus). The shorter wavelength beam of electrons enables much higher magnification than in optical microscopes. In

addition, the larger depth of focus in a scanning electron microscope is due to a smaller aperture angle from the objective compared to the optical microscope.

An SEM instrument consists of an electron column, a sample holder, and detectors, as shown in Figure 3.7. An electron beam is produced by an electron gun before passing through magnetic lenses (condenser and objective lenses), where the electron beam can be finely focused. When an electron strikes a specimen, various possible types of electrons and electromagnetic waves can be emitted from the specimen, and can be collected by detectors installed in the SEM (Figure 3.8).

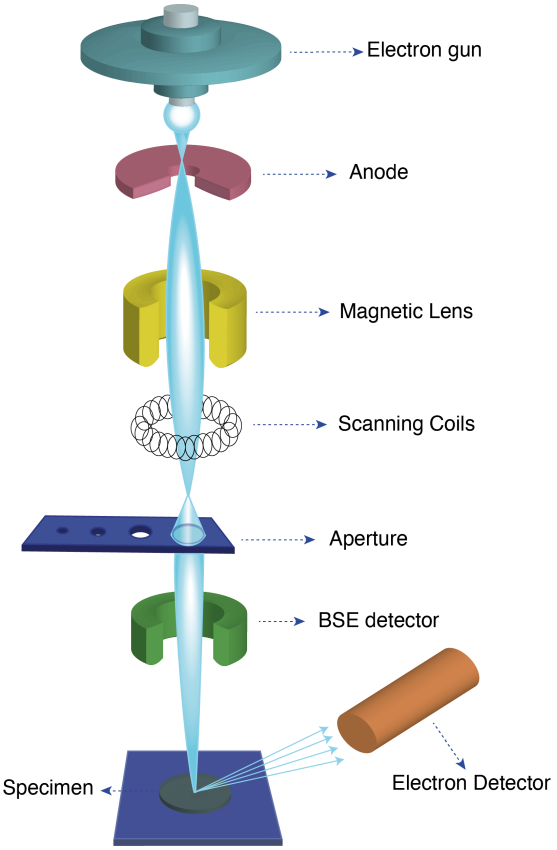

Figure 3.7: Schematic representation of the main components of an SEM. Interpreted and modified from [159].

Secondary electrons (SE) are produced due to an inelastic interaction between the primary electron beam (incident beam) and the atoms in the specimen, resulting in an expulsion of an electron from the atoms. SE are surface sensitive

due to the ∼ low kinetic energy of SE (< 50 eV), and can provide topographic information of the observed surface [160]. The topographic information in the final SE image depends on the number of SE emitted and the number of SE reaching the detector. Therefore, edges appear brighter as more SE are emitted compared to a flat surface, as illustrated in Figure 3.9. In addition and depending on the position of the detector, specimen topography can prevent electrons from reaching the detector, thus resulting in darker shadowed regions in the produced image.

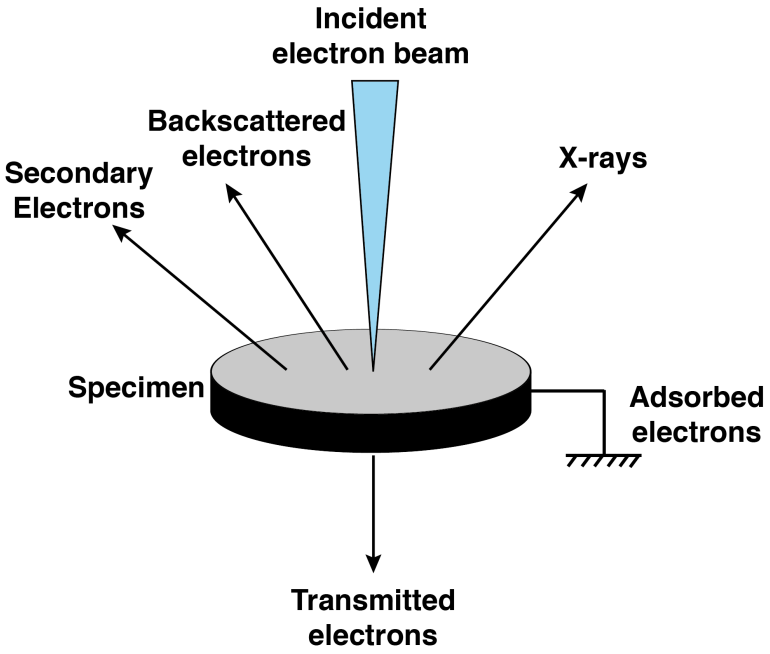

Figure 3.8: Schematic representation showing electrons and electromagnetic waves emitted from a surface bombarded with an incident electron beam.

In addition to SE, detection of backscattered electrons can produce an image in the SEM. Backscattered electrons (BSE) are reflected incident electrons from the sample surface. BSE are more sensitive to the atomic composition, as they scatter from a larger depth than the secondary electrons [161]. Elements with higher atomic numbers will result in more BSE signal compared to lower atomic number elements due to a greater interaction between electron and atoms. This reflects in the contrast of the produced BSE image, where brighter areas correspond to higher atomic mass regions. SE imaging mode was used

more frequently throughout this work as the lateral resolution of SE mode ($\sim$ 10 nm) is better than of BSE mode ($\sim$ 1 μm). An example is shown in Figure 3.10, displaying the difference between BSE and SE imaging modes in the SEM.

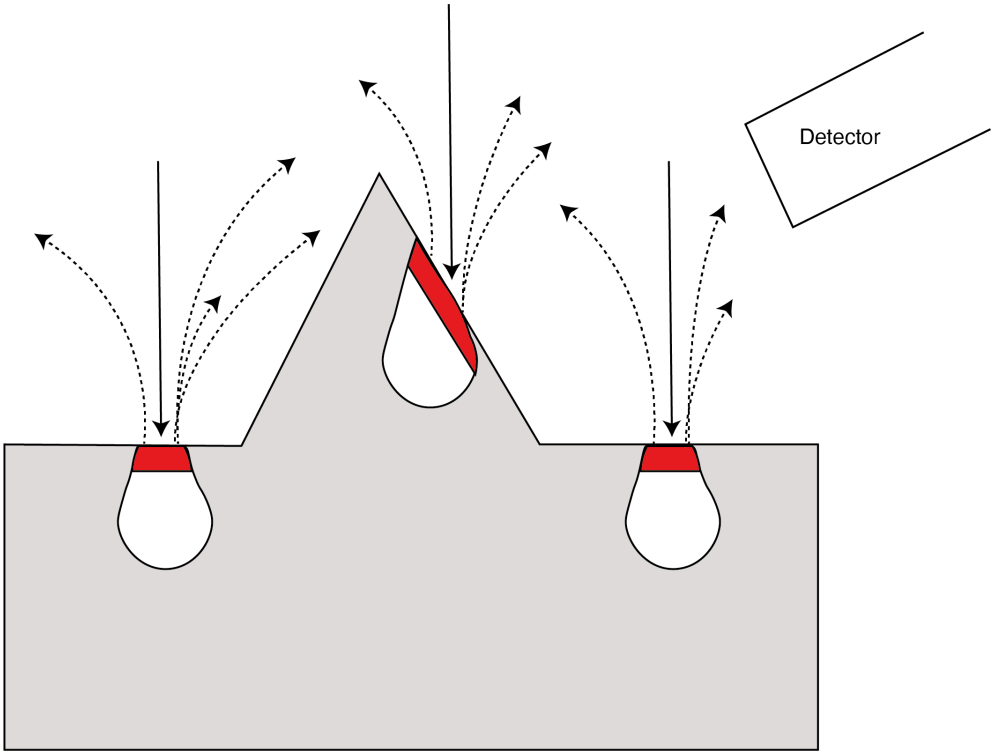

Figure 3.9: Schematic illustration showing the effect of surface topography on secondary electron detection. Secondary electrons are produced only from the red highlighted region. Interpreted and modified from [160, 162].

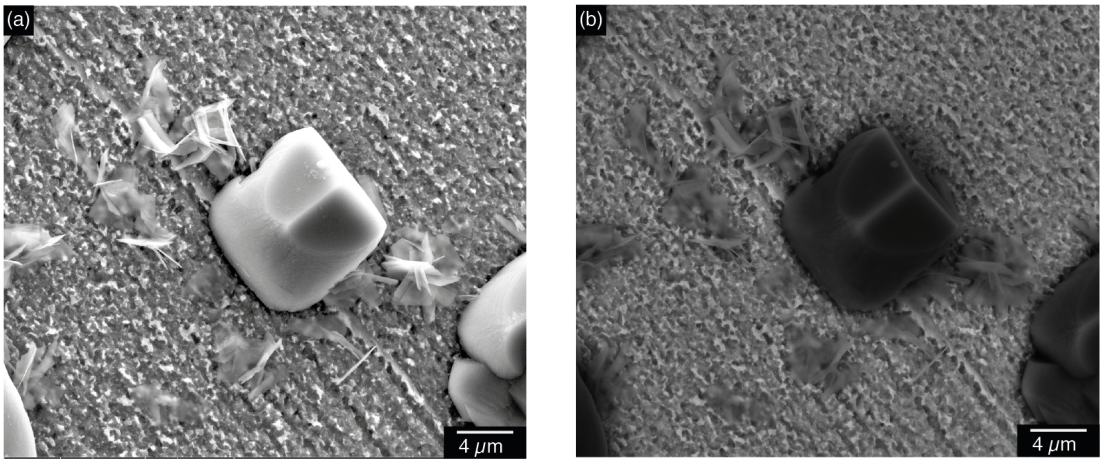

Figure 3.10: Comparison between images taken in (a) SE mode and (b) BSE mode using FEI Quanta 650 FEG-SEM of a corrosion scale formed on Fe substrate after immersion in CO_2-saturated solutions.

3.3.2 Energy Dispersive Spectroscopy (EDS)

SEM capability can be extended to provide spatially resolved elemental information, which can be obtained using an energy dispersive X-ray spectrometer detector (EDS) that detects emitted X-rays from the sample. For more accurate elemental identification, EDS measurements are typically obtained using high energy beams (15 - 20 keV), to avoid peak overlaps at the lower energy range of the spectrum [163]. However, the beam interaction volume is larger at higher accelerating voltages. Therefore, it is necessary to consider the beam interaction volume when performing analysis of particularly small features on the substrate, especially compounds from the feature of interest that has common elements with the substrate. For this work, EDS technique was only used to perform a qualitative analysis of certain features on the surface.

3.3.3 Electron Backscatter Diffraction (EBSD)

Electron backscatter diffraction (EBSD) is a suitable technique for the measurement of a local crystallographic orientation with high spatial and angular resolution. EBSD provides statistically relevant information about local texture or micro-texture in a sample, which includes grain size, grain orientation and local misorientation between grains. EBSD also has the capability of identifying different phases based on knowledge from crystallographic data emerging from diffraction processes rather than being determined by the composition of a phase and then inferring the identity of the phase (i.e. EDS). EBSD is used in this project in conjunction with confocal microscopy to identify the crystallographic orientation of siderite facets (Chapter 4).

The crystallographic information provided by the EBSD is held within the Kikuchi diffraction patterns that are generated by a series of elastic and

inelastic scattering events of the primary electron beam with the specimen just beneath the surface [164]. The scattered electrons in bulk will interact with the atomic lattice planes, and some electrons will eventually arrive at Bragg's angle at a set of lattice planes. These electrons will undergo elastic scattering and produce an electron beam that escapes the sample surface. The occurrence of this backscattering phenomenon at the various sets of lattice planes forms the Kikuchi diffraction pattern. The Kikuchi diffraction pattern is generated from one illumination point of the primary electron beam on the specimen surface, thus by rastering across the sample surface microtexture and phase maps can be obtained. The EBSD configuration in an SEM chamber involves tilting the sample to 70 ° with respect to the pole piece to maximise the backscatter coefficient to enhance the intensity of the Kikuchi patterns (Figure 3.11) [165]. A position-sensitive detector with a phosphor screen is positioned near the tilted specimen to capture the Kikuchi diffraction patterns. The captured Kikuchi patterns on the phosphor screen are then transferred to a charge-coupled device situated behind the phosphor screen to register the pattern digitally for further processing of the data.

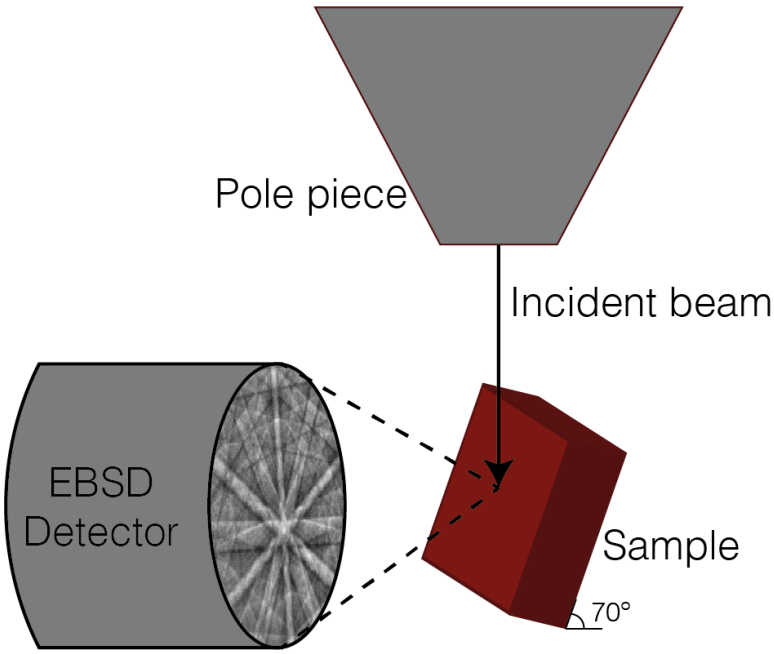

Figure 3.11: Schematic illustration of the EBSD configuration in the SEM.

3.3.4 SEM- Focused Ion Beam (SEM-FIB)

Obtaining cross-sections of the scales formed on the surfaces can provide useful information about the scale structure at the interface, scale thickness and porosity. Focused-ion beam (FIB) milling can be used for cutting cross-sections at specific sites across the sample. This technique offers several advantages over mechanical cutting techniques, including site-specific and accurate sub-μm cross-sections, while the rest of the sample is not disrupted. Also, conventional methods include mechanical cutting, mounting, grinding and polishing the sample can damage the formed scale, especially carbonate scales of interest that are sensitive and can easily oxidise upon exposure to water/air [114].

Fundamentally, the cutting/milling process using FIB occurs as a beam of high-energy ionized atoms (Ga^+ in this work) strikes the sample, expelling surface atoms at a specific area of the sample. As a result of ions bombarding the surface, secondary electrons are produced, which allows imaging of the sample [166]. FIB and SEM can both be incorporated in a dual-beam system. Dual platform instruments are usually equipped with a FIB column mounted at an angle with respect to vertically mounted SEM column as shown in Figure 3.12. The use of SEM can be implemented for imaging without sputtering the sample surface, and allows also for continuous observation of the milling process [167]. The SEM-FIB instrument is usually equipped with gas injection systems (GIS) that are used in conjunction with the ion beam to deposit metals (e.g. platinum) on specific sites on the sample.

The milling procedure includes positioning the sample, using a motorised stage within the vacuum chamber of the instrument, at a eucentric height where the focus point of the electron beam and the ion beam is coincident. The stage is tilted normal to the ion-beam at an angle of 52°, as shown in Figure 3.12. A 0.5 - 1 μm thick layer of platinum is deposited on the area of interest to protect the scale/substrate. This is followed by the milling process

at higher ion beam currents (15-65 nA) in the area below the Pt-deposited region. Milling at higher currents produce a rough cut, and a series of cuts are required at lower ion beam currents (50-300 pA), to produce the final refined cross-section. These process steps are illustrated in Figure 3.13.

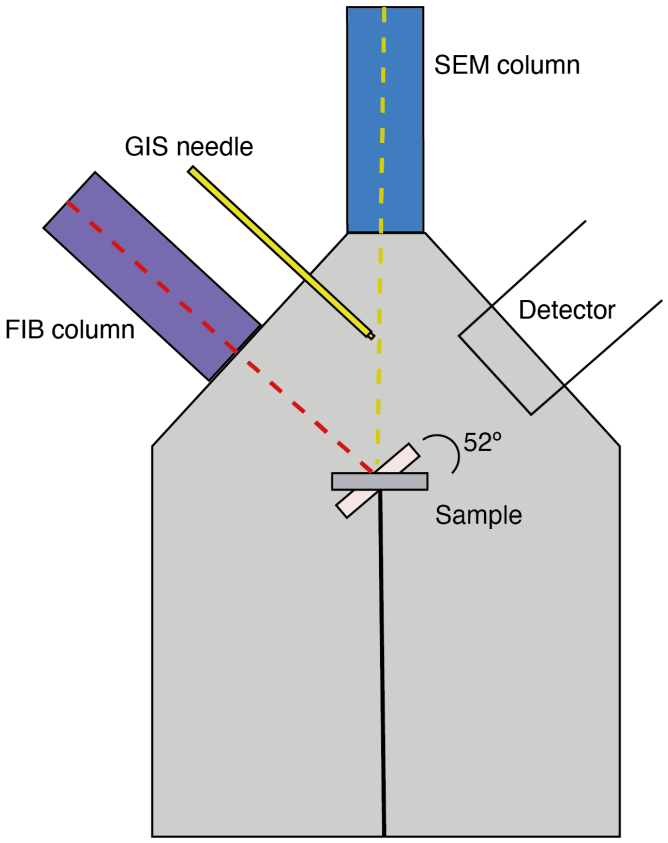

Figure 3.12: Schematic diagram of SEM-FIB setup. See text for details of the setup components.

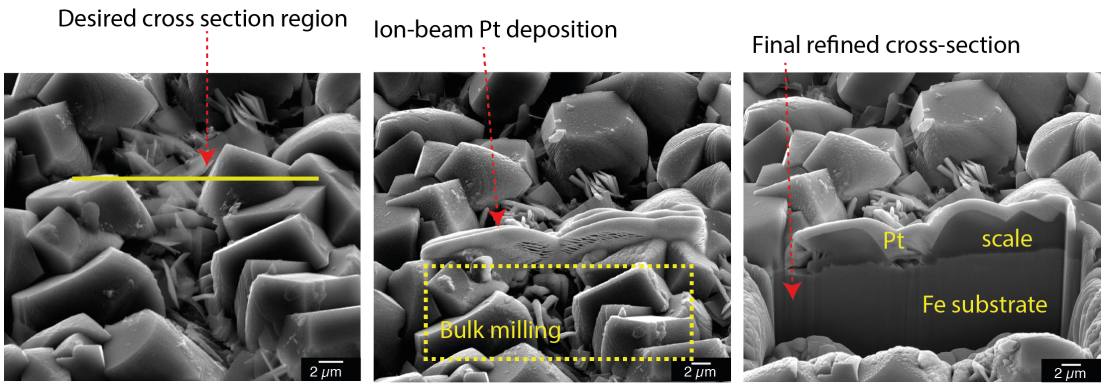

Figure 3.13: SEM images explaining FIB cross-sectioning procedure starting from (left) selection of desired cross-section region to (middle) Pt deposition and bulk milling of the area in front and (right) final refined cross-section.

3.3.5 SEM/FIB-SEM: Sample preparation and instrumentation

In order to prepare for SEM imaging, the samples were secured on 15 mm diameter aluminium stubs using superglue adhesive. Silver paint was used to ensure a conductive electrical path for electrons between the sample and the mounting stub. Poorly-conductive samples (especially PTFE samples used in Chapter 4) were coated with a thin layer of 2-5 nm of gold/palladium in a 40:60 ratio using a precision coating physical vapour deposition system. The instruments used in this project are listed below:

SEM/EDS: FEI Quanta 650 FEG-SEM

FIB-SEM: FEI Quanta 3D FEG SEM

EBSD: Oxford Instruments EBSD detector inserted in TESCAN Mira3 FEG-SEM.

3.4 X-ray diffraction (XRD)

X-ray diffraction (XRD) is one of the most powerful techniques widely used in materials science. It is used extensively to characterise crystalline materials and for crystal structure determination. The X-rays are $\sim$ 5000 times shorter than the visible light, and similar to the interatomic spacing within crystal structures (0.5 - 2.5 Å) [168, 169]. Therefore, scattering of X-rays occurs due to the interaction between the electromagnetic waves from X-rays and the electrons in the atoms. X-ray diffraction is the elastic scattering of X-rays by periodically ordered atoms in a crystalline solid. The X-ray "diffraction" phenomenon was first discovered in 1912 by Max von Laue. After this discovery, W.H Bragg and W.L Bragg used this phenomenon for crystal analysis with the development of Bragg's law. Lattice parameters can be obtained using Bragg's law, which applies in a condition of constructive

interference of diffracted beams. Bragg's law is described below, and Figure 3.14 shows a schematic illustration of the law:

$$n\lambda = 2dsin\theta, \tag{3.8}$$

where n is the order of diffraction, λ is the wavelength of the incident x-ray, d is the spacing between atom planes in a crystal, and θ is the angle at which constructively interfering X-rays leave the crystal.

X-ray powder diffraction can be used to identify phases present in a specimen. This can be done by comparing the recorded diffraction pattern of the phases and known standard diffraction patterns of various compounds available in the *Powder Diffraction File* (PDF) database [170].

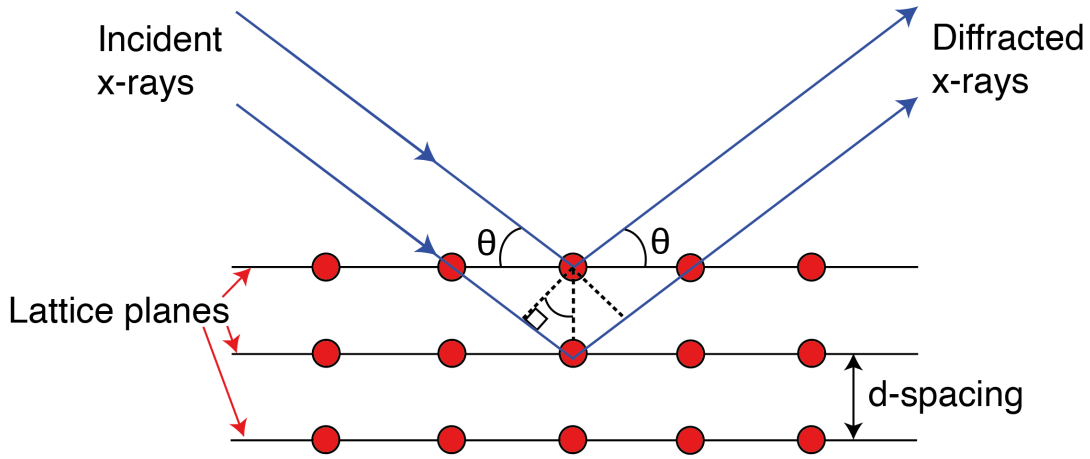

Figure 3.14: Schematic illustration of Bragg's law

XRD technique is employed in this work to examine formed corrosion scales on the corroded Fe substrates. As the x-ray beam can penetrate the bulk material deeply, a special configuration is necessary to control penetration depth and maximise the diffraction signals from the top layers with respect to the bulk of a specimen [171]. This enhanced surface sensitivity can be obtained using grazing incidence x-ray diffraction (GIXRD) configuration, where the incident beam is fixed at a small angle with respect to the sample surface.

3.4.1 Laboratory source GIXRD

Laboratory source GIXRD has been employed to carry out most of the surface characterisation in this project. For this purpose, a Philips X'Pert Philips X'Pert Modular Powder Diffractometer (MPD) is used for these measurements. In this instrument, X-rays are produced in an *x-ray tube*, where an electron beam (cathode) is accelerated at a voltage of 40 kV and a current of 10 mA to hit a copper target (anode). The energy emitted from the copper target is in the form of characteristic CuKα radiation with a wavelength of λ = 1.54 Å. A nickel filter is used to suppress CuKβ radiation. For the measurements undertaken in the GIXRD mode for this project, the incidence angle is fixed at either α = 3° or 6° with respect to the sample, which is placed on a stage within the instrument (see Figure 3.15). Diffracted beams are detected using a point detector which moves in the specified range from 2θ = 15°- 85° at 0.05° intervals with scan step time of t = 8 s. A graphite monochromator and long Soller slits are used to minimise x-ray fluorescence from Fe samples. Phase identification and diffraction pattern analysis were carried out using the International Centre for Diffraction Data (ICDD) database [172], and Highscore Plus software [173].

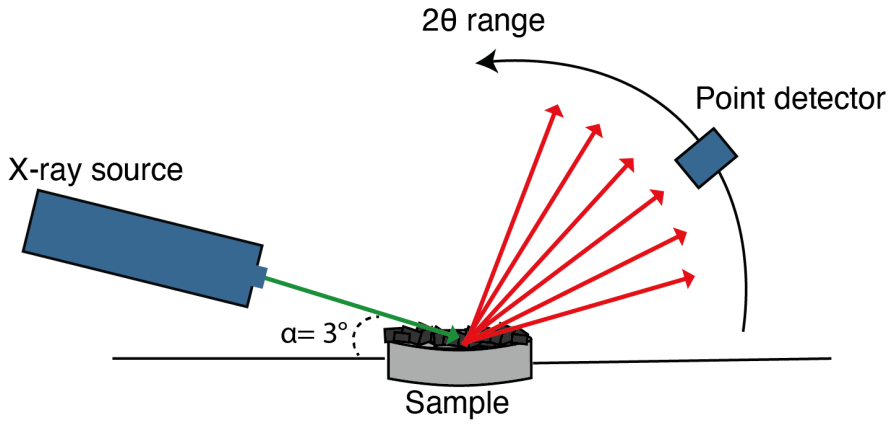

Figure 3.15: Schematic illustration laboratory source GIXRD configuration.

3.4.2 Synchrotron radiation source GIXRD

Performing *in situ* GIXRD measurements can provide valuable insight on sweet corrosion scale formation. Limited space, lower energy X-rays and inappropriate detectors present an obstacle to feasibly perform *in situ* experiments using our laboratory source GIXRD. On the other hand, the higher energy beams and higher brilliance of a synchrotron radiation source are some of the advantages over a laboratory source, allowing for such *in situ* experiments. Synchrotron radiation (SR) is emitted by accelerating electrons to high velocities in a circular orbit [174]. Currently, there are more than 70 such facilities in the world producing synchrotron radiation that are employed in experiments with a wide range of applications. For the *in situ* work detailed in Chapter 6, the experiment was conducted at the European Synchrotron Radiation Facility (ESRF) in Grenoble, France. Figure 3.16 shows a schematic layout of the ESRF facility.

A synchrotron facility consists of an electron accelerator, a storage ring and beamlines. At the ESRF, the electrons are produced by an electron gun, then gradually accelerated in *'bunches'* to velocities close to the speed of light. The electrons are accelerated up to 200 MeV in a linear accelerator (Linac), and then injected into a booster synchrotron, which is a ring with a circumference of 300 meters. The electrons circulate around the booster synchrotron gaining additional energy, that reaches 6 GeV. Then the electrons are transferred to the storage ring (844 meters circumference), which stores the 6 GeV electron beam. The electrons produce electromagnetic radiation (synchrotron radiation) as they pass through bending magnets and insertion devices (ID) in the beamline. As a result of this radiation, the electrons lose energy and it is restored using radio frequency cavities, maintaining the energy level close to 6 GeV in the storage ring. The ESRF has 43 different beamlines and the experiment conducted in this project was carried out at the BM28 (XMaS) beamline.

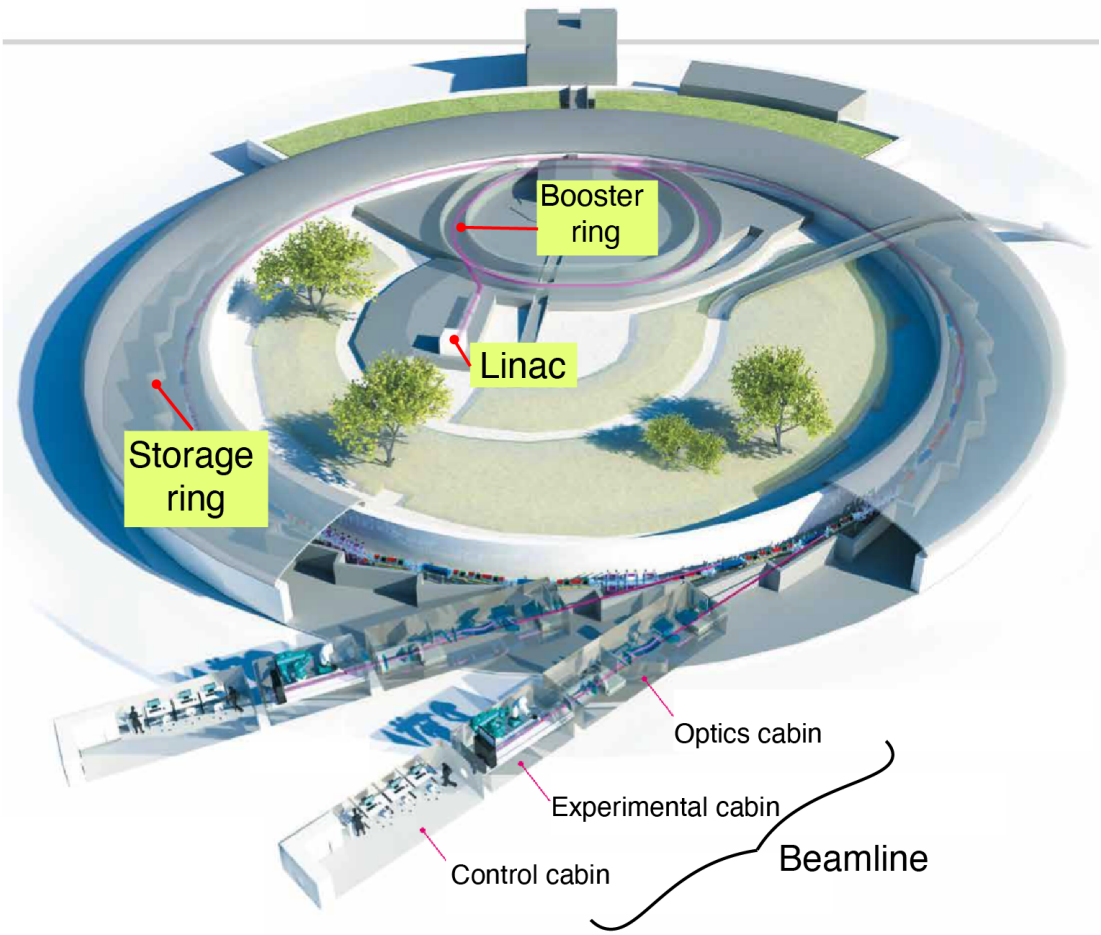

Figure 3.16: Schematic of ESRF facility. Modified from [175].

BM28 (XMaS) beamline

This beamline is designed to perform various scattering experiments on an 11-axis Huber diffractometer over an energy range of 2.4 keV to 15 keV. The optics configuration of this beamline, as shown in Figure 3.17, consists mainly of a double-crystal monochromator and a toroidal mirror. The monochromator comprises of two Si{110} crystals used to select a specific wavelength of X-rays from the broad white beam. The toroidal mirror focuses the monochromatic beam to a small spot that exits through a station shutter to the sample surface mounted on the diffractometer in the experimental hutch. The toroidal mirror surface is coated with a thin layer of rhodium enhancing the X-ray reflectivity up to 15 keV. Experimental details regarding the *in situ* setup geometry

on the Huber diffractometer, *in situ* synchrotron cell design, and operating procedures are discussed further in Chapter 6.

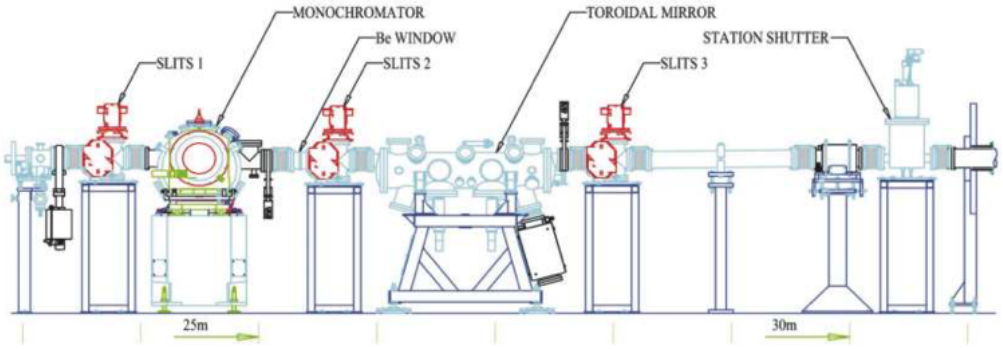

Figure 3.17: Schematic of optics in BM28 at ESRF facility. Reproduced from [176].

3.5 3D confocal laser scanning microscopy

Confocal microscopy is a powerful tool to obtain topographical information from a sample surface. In addition, confocal microscopy can produce higher-resolution, and sharper images of the sample compared to a conventional light microscope. Depth information obtained from a series of images at different heights using the confocal microscope can be used to reconstruct 3D images of the surface. In this project, a Keyence VK-X200K 3D confocal laser scanning microscope is used in this project to obtain height information and produce 3D reconstructed images of siderite crystals formed on Fe surfaces after immersion in CO_2 saturated solution (Chapter 4).

In the confocal microscope optics, the use of a pinhole positioned in front of the detector (photoreceptor) ensures that only the reflected light from the focal point of the sample passes through to the detector [177]. This eliminates out-of-focus scattered lights from the sample that usually responsible for blurred images in conventional light microscopes (Figure 3.18). In the confocal microscope used here, the sample can be placed on a motorised stage. After

selecting the area of interest, the sample surface is moved in μm steps through the focal point producing a stack of images. These series of images can be assembled using Multi-File Analysis software to produce a 3D reconstructed image from which information about surface profile/height can be acquired [178].

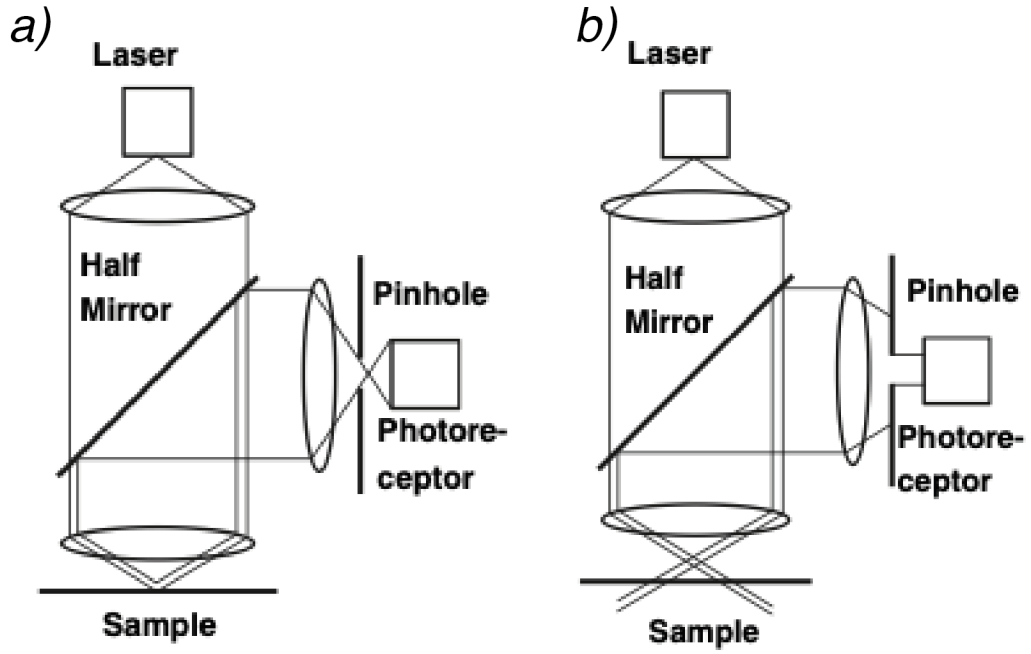

Figure 3.18: Schematic illustration of confocal microscope and the use of pinhole to (a) allow reflected light from the focal plane to pass to the detector and (b) eliminate out-of-focus reflected light. Reproduced from [179].

3.6 Solution analysis

3.6.1 pH measurements

A glass body pH electrode with refillable double junction (Hanna Instruments Model: HI-1043B) connected to a pH meter (Hanna Instruments Model No. 2210) was used to carry out pH measurements. The instrument was calibrated prior to immersion by a 2 point calibration procedure using pH = 4.01 and 7.01 buffers. Solution pH measurements were undertaken during pH adjustment

of CO_2-saturated solutions, prior to immersion of the WE and at the end of an immersion. The pH electrode was stored in saturated KCl storage solution and was washed thoroughly before taking any measurements. As the pH reading is influenced by temperature, all measurements were undertaken at the experimental condition (usually 80°C). The temperature compensation feature was also used by recoding the temperature reading in the instrument to measure the pH accurately.

3.6.2 Dissolved oxygen concentration measurements

Dissolved oxygen can influence the CO_2 corrosion process and alter the formation of corrosion products [85, 114]. Therefore, dissolved oxygen concentration measurements were required to ensure low oxygen levels. These measurements were undertaken using an electrochemical oxygen sensor (Orbisphere A1100) for experiments performed using a pressure vessel to prepare the CO_2-saturated solutions (Chapter 5 and Chapter 6). In addition, a luminescence-based oxygen dipping probe (PreSens, DP-PSt8) was used for oxygen measurements for the glass-cell/glovebox experimental setup (Chapter 4).

The electrochemical oxygen sensor measures the current response as a result of the electrochemical reaction of oxygen from the solution flowing through the sensor. This measured current response is proportional to the amount of oxygen in the solution, which is displayed on a meter (Orbisphere 410). During the measurements, the solution is required to flow continuously to avoid erroneous recordings. Regarding the procedure followed for oxygen measurements, the solution was delivered to the sensor from the pressure vessel using a peristaltic pump (Masterflex, Cole Parmer). Low-oxygen permeable viton tubing was used to transfer the solution through the oxygen measurement loop, as shown in Figure 3.19. It was found that 16-24 hours of CO_2 sparging is required to reduce dissolved oxygen concentrations to <10

pbb.

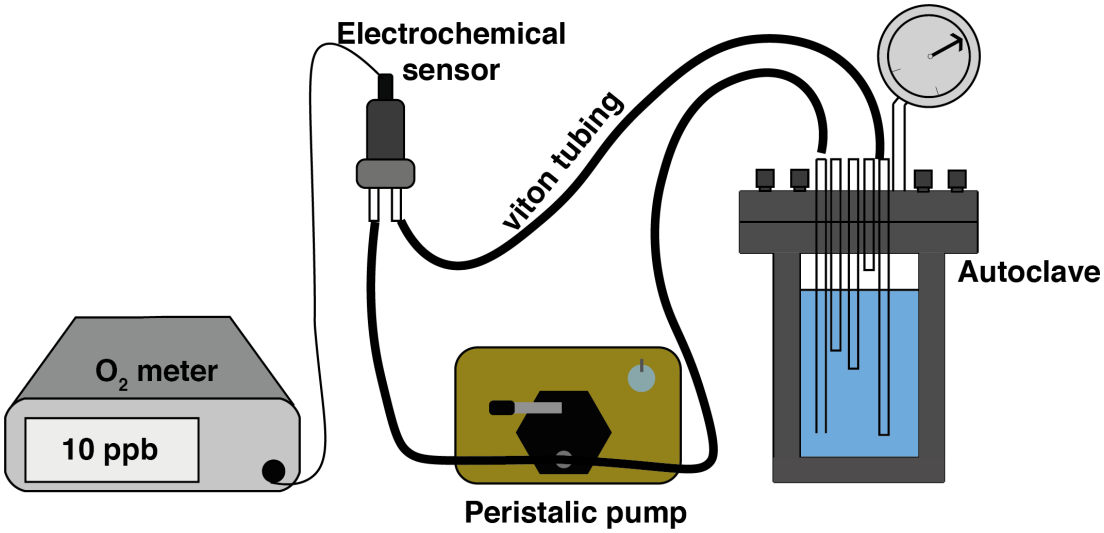

Figure 3.19: Schematic diagram of the flow loop for oxygen measurements using an electrochemical sensor.

For the luminescence-based oxygen sensor, the instrument transduces changes in luminescence characteristics of organic/inorganic dyes, as a result of interaction with oxygen, to an electrical parameter that provides a reading of oxygen content in the system in parts per billion (ppb) [180]. Measurements were taken by dipping the probe through one of the glass-cell ports prior and after WE immersion (setup described in Chapter 4). The O_2 probe is connected to a portable oxygen meter (Presens, Microx 4 trace). Luminescence-based oxygen sensors are sensitive to measurements at high temperatures and can result in larger drifts. Therefore, the measurements were undertaken at room temperature, and the oxygen levels were ensured to be < 10 ppb. After that, the solution was heated to the desired experimental temperature condition.

Chapter 4.

Exploring Siderite Crystal Habit: Impact of Environmental Conditions

4.1 Introduction

Internal corrosion of pipelines due to dissolved CO_2 produced from wells presents both safety and economic problems for the oil and gas industry [17, 181]. Corrosion product scales formed on the steel surface can provide a mean of protection by acting as a barrier reducing the steel corrosion rate significantly [182]. On the other hand, local breakdown of corrosion scales can lead to problematic localised corrosion issues [183–187]. Many factors can influence the formation and protectiveness of such corrosion scales, including temperature, pH, pressure, flow and solution chemistry. Understanding the impact of those factors on corrosion scale, particularly iron carbonate ($FeCO_3$), has been of an interest in various studies, e.g. [4, 68]. Despite the effort, scale formation is still not understood enough to enable prediction of its formation/protectiveness behaviour and to incorporate it effectively in sweet corrosion prediction models or mitigation strategies.

Iron carbonate, commonly known as siderite, is identified as the main corrosion product formed in sweet environments. It has been widely reported that siderite ($FeCO_3$) forms rhombohedral shaped crystals (e.g. Figure 4.1 (a) and Ref. [24, 85, 107]). However, another siderite crystal habit is seen when reviewing various studies, where siderite is formed on corroded surfaces under CO_2- saturated environments in a range of operating conditions. Figure 4.1 (b-d) shows selected SEM images from different studies showing siderite forming a different habit. Only recently Joshi et. al described this siderite habit, which formed on corroded Fe sample in CO_2-saturated solution at T = 80°C and pH =6.8, as micro-facetted cylinder with trigonal/pyramidal caps. In fact, although it has not been described, this habit is quite common for siderite forming under corroding sweet environments [24, 86, 94, 105, 125, 188–193].

Given the above, one topic of interest is to focus on siderite crystal habit and investigate changes as a function of different conditions. Therefore, this

chapter focuses on the influence of different factors on the siderite crystal habit. This includes a comparison of siderite habits formed on corroding and non-corroding surfaces immersed in CO_2-saturated solution at T = 80°C and pH = 6.8. The influence of other factors, namely: $Fe^{2+}_{(aq)}$ concentration, NaCl concentration, added $Ca^{2+}_{(aq)}$ and $Mg^{2+}_{(aq)}$ will also be investigated. In addition, observed results will be compared with theoretical ab initio modelling of siderite crystal habit: a work that been conducted with collaborators at Imperial College, London. Furthermore, crystallographic orientation of siderite facets will be obtained by employing EBSD and confocal microscopy techniques. SEM and GIXRD techniques will also be employed to characterise the formed scale under investigated conditions.

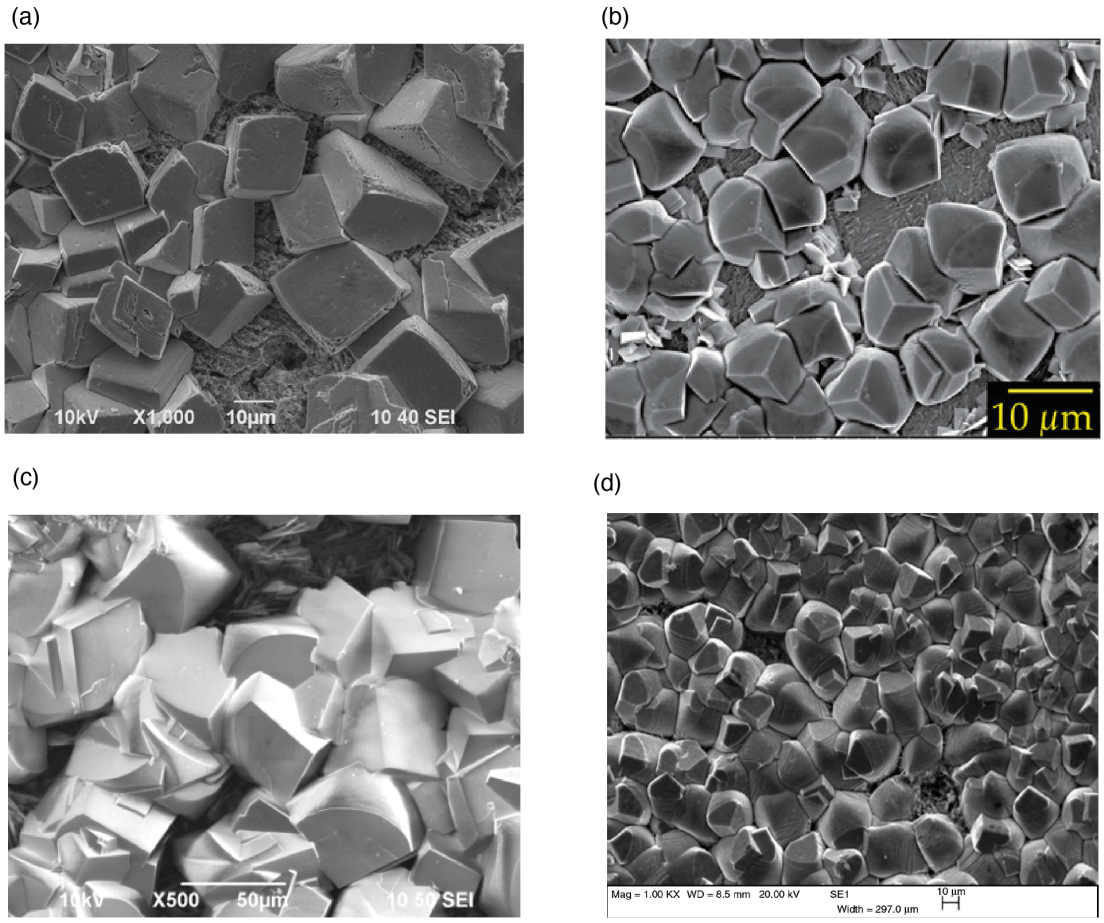

Figure 4.1: Examples of siderite (a) rhombohedral crystal habit and (b-d) micro-facetted cylinder with trigonal/pyramidal caps crystal habit, formed in CO_2-saturated solutions at a range of temperatures, pressure, and pH. SEM images are reproduced from: (a) Ref. [86] (b) Ref. [94] (c) Ref. [5] (d) Ref. [24].

4.2 Experimental Details

4.2.1 Materials

High purity Fe discs (depth $\sim$ 4 mm) were cut from a 10 cm rod (10 mm diameter, 99.99+% , sourced from Goodfellow). Minor elements present in the Fe sample are shown in Table 4.1. Figure 4.2 shows an EBSD orientation map of the Fe substrate displaying the microstructure, which consists of irregular grains of ferrite. The samples were polished to 4000 grit using silicon carbide paper (series of 240, 600, 1200, 2400, 4000). In order to suspend the Fe sample in solution, the back face of the sample was secured to a capillary glass tube. Lacomit stopping-off lacquer (supplied by MacDermid plc) was used to paint the sides of Fe sample to ensure only one surface exposure to the solution.

Table 4.1: Other elements present in high purity Fe sample. Values are in ppm.

Al	**Cr**	**B**	**Co**	**Cu**	**Ga**	**Ge**	**Mn**
1.6	6.6	0.77	12	2.1	0.7	6.2	4.1
Mo	**Ni**	**P**	**Ta**	**Sn**	**Ti**	**W**	**Zn**
0.36	2.8	7.2	1	0.15	1.4	0.15	0.3

Polytetrafluoroethylene (PTFE) samples were used in some immersion experiments to observe growth of siderite on a non-corroding surface. PTFE is chemically stable and can also resist high temperatures [194]. The PTFE samples used were cut (20 x 15 x 3 mm) from a PTFE sheet (supplied by Direct Plastics). Prior to immersion, the samples were washed thoroughly with deionised water and ethanol, then dried. The samples were suspended in solution by a PTFE thread tape passed through a drilled hole ($\sim$2 mm diameter) on top side of the PTFE sample.

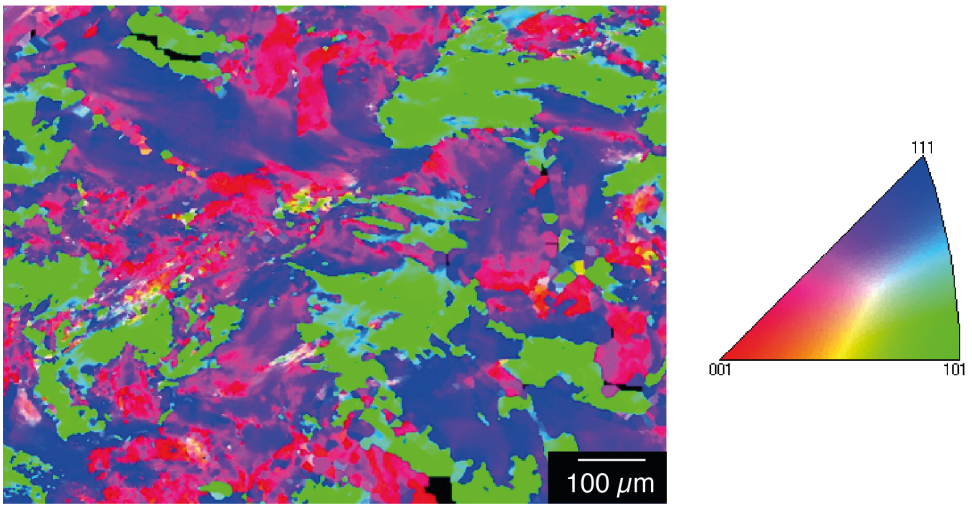

Figure 4.2: EBSD map showing the microstructure of Fe substrate used for the immersion experiments performed in this chapter. The plot is reproduced with the permission of Raunaq Singh [195].

4.2.2 Immersion Experiments

All immersion experiments were performed in a 1-L jacketed glass cell (Pine Instruments) located in a N_2-filled glovebox (see Figure 4.3). Prior to immersion, 0.9 L of CO_2 saturated base aqueous solution was prepared by bubbling high purity CO_2 gas (99.95%, supplied by BOC) for 18-24 hours. Table 4.2 summarises the salt solutions used for immersion experiments performed in this chapter.

To prepare the salt solution, the required amount of $FeCl_2$ /$CaCl_2$ /$MgCl_2$ was added to produce 0.1 L of the solution. This solution was bubbled with N_2 gas in a Dreschel bottle for 18-24 hours. Dissolved oxygen concentrations were checked to be less than 10 ppb using optical oxygen sensor (PreSens, DP-PSt8), before adding the 0.1 L $FeCl_2$ /$CaCl_2$ /$MgCl_2$ solution to the base CO_2-saturated 0.9 L solution. In all experiments, the pH was adjusted to 6.8 ± 0.05 using $NaHCO_3$ and temperature was maintained at 80 ± 1°C by circulating hot water from a temperature regulated water bath. Figure 4.4 shows a summary plot of the conditions discussed in this chapter.

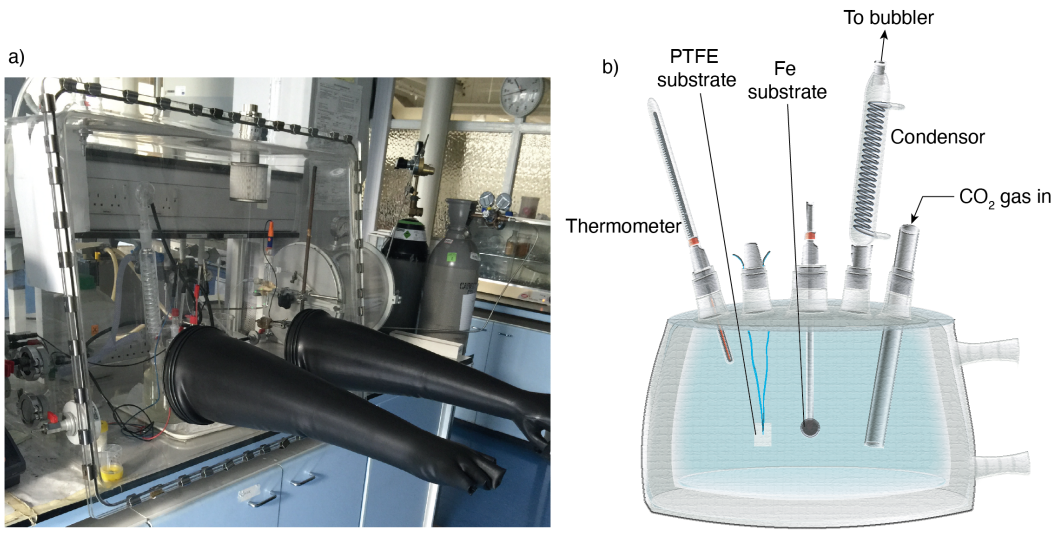

Figure 4.3: (a) Photo of a N_2-filled glovebox. (b) Schematic diagram of a jacketed glass cell used for immersion experiments of a Fe and PTFE substrates.

Table 4.2: Experimental conditions and salt component of CO_2-saturated solutions for experiments performed in this chapter.

Solution	Temperature	pH	Number of experiments
0.01 M $FeCl_2$	80°C	6.8	4
0.1 M $FeCl_2$			2
0.01 M $FeCl_2$ + 0.18 M NaCl			2
0.01 M $FeCl_2$ + 0.001 M $CaCl_2$			2
0.01 M $FeCl_2$ + 0.001 M $MgCl_2$			2

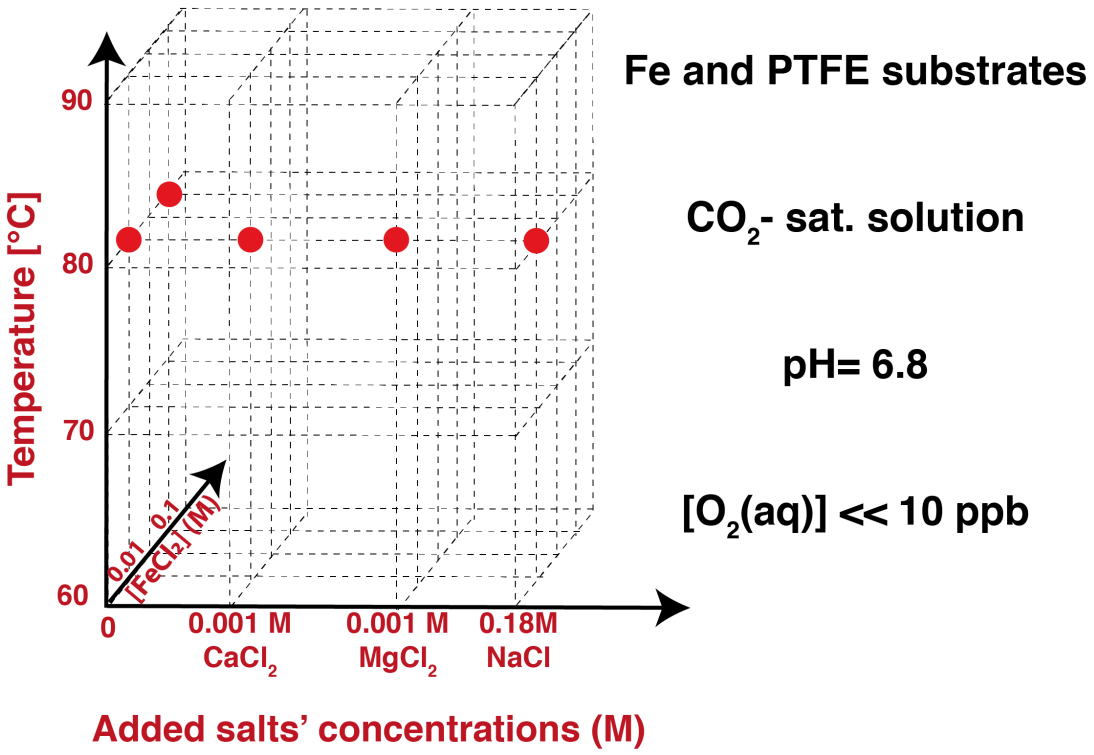

Figure 4.4: 3-D parameter space plot illustrating experimental conditions used in this chapter

4.2.3 Post immersion characterisation

Scales formed on the samples were characterised post-immersion using GIXRD, SEM, EDS and laser confocal microscopy. GIXRD measurements were undertaken at an incidence angle of α_i = 3° from 2θ = 15°- 85°, using Philips X'Pert MPD diffractometer. SEM and EDS were performed using a FEI Quanta 650 SEM. Laser confocal microscopy was used to obtain topographical information of the formed scales, using a Keyence X200K 3D Laser Microscope. EBSD measurements were undertaken with Oxford Instruments EBSD detector inserted in a TESCAN Mira3 FEG-SEM.

4.3 Results and discussion

The results presented in this chapter are discussed in three main sections. The first section shows the variation of siderite habit on corroding and non-corroding surfaces. Then the presumed crystal habit is further confirmed by explicitly determining the crystallographic orientation of one of the facets. Finally, the influence of other factors on siderite crystal habit is discussed, i.e. concentration variation of $Fe^{2+}_{(aq)}$, NaCl, addition of $Ca^{2+}_{(aq)}$ and $Mg^{2+}_{(aq)}$.

4.3.1 Exploring siderite crystal habit formation on corroding and non-corroding substrates

Siderite crystal habits were explored here on corroding Fe and non-corroding PTFE samples immersed in CO_2-saturated 0.01 M $FeCl_2$ solution. This amount of $FeCl_2$ added is sufficient to reach supersaturation $FeCO_3$ (SS $\approx$ 200) and ensure its formation on non-corroding PTFE substrate. Figure 4.5 shows GIXRD patterns of Fe and PTFE samples prior to immersion. Peaks can be attributed to either α-Fe and PTFE.

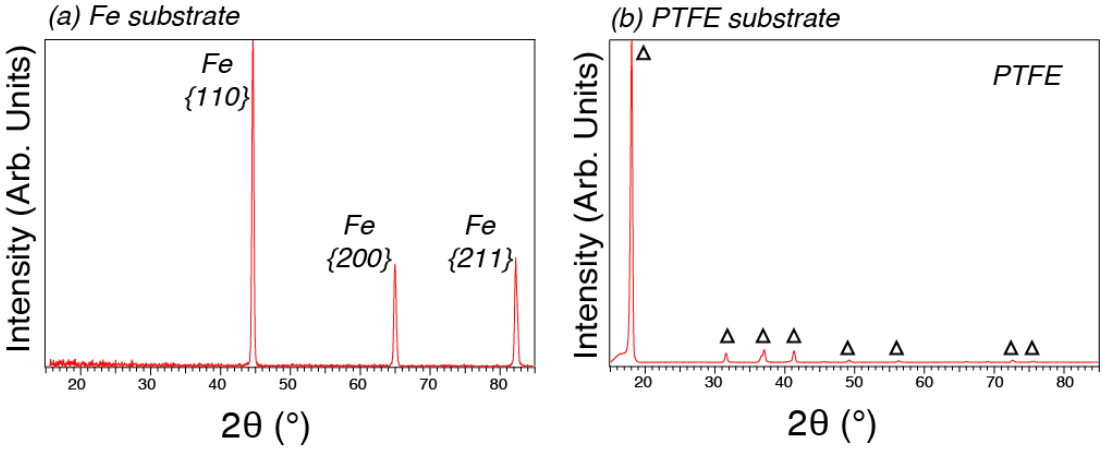

Figure 4.5: GIXRD diffractograms (acquired at α = 3°, CuKα source λ = 0.154 nm) of polished (a) Fe substrate and (b) PTFE substrate prior-immersion.

Figure 4.6 shows post-immersion GIXRD diffractograms of Fe and PTFE samples in CO_2-saturated 0.01 M $FeCl_2$ at 80°C and pH = 6.8 for 24 hours. Both diffraction patterns indicate formation of siderite scale.

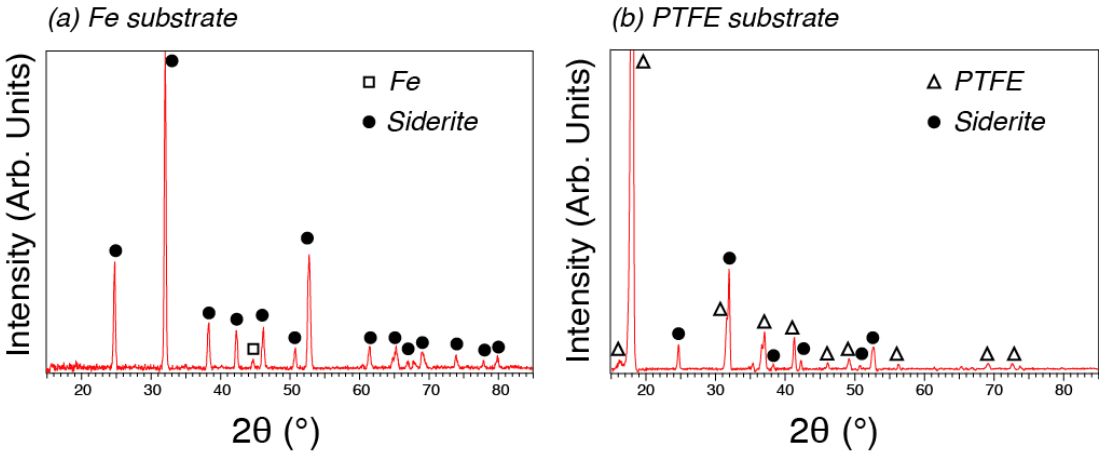

Figure 4.6: GIXRD diffractograms (acquired at α = 3°, CuKα source λ = 0.154 nm) of (a) Fe substrate and (b) PTFE substrate immersed in CO_2-saturated 0.01 M $FeCl_2$ solution (T = 80°C, P_{CO_2}= 0.54 bar, pH = 6.8) in a jacketed glass cell setup for a total of 24 hours.

Comparing the corresponding crystal habits, as shown in the SEM images in Figure 4.7 (a), it can be seen that the dominant siderite crystal habit on non-corroding PTFE substrate is rhombohedral. In contrast, a different siderite habit is observed on the corroding Fe substrate, as shown in Figure 4.7 (b), which can described as microfaceted cylinder with trigonal pyramidal caps, as per Joshi et al. [5]. For simplicity, this siderite crystal habit observed on Fe substrate will henceforth be referred to as the '*cylindrical*' habit.

The only source of $Fe^{2+}_{(aq)}$ to form siderite on the non-corroding PTFE substrate is from the added $FeCl_2$. On the other hand, the corroding metal provides an additional $Fe^{2+}_{(aq)}$ source near the surface of Fe substrate, as illustrated in the schematic diagram in Figure 4.7 (a) and (b). This suggests that the local concentration of $Fe^{2+}_{(aq)}$ can result in a change of siderite crystal habit. At low $Fe^{2+}_{(aq)}$, rhombohedral siderite crystals form and as the $Fe^{2+}_{(aq)}$ increases, cylindrical shaped crystals form.

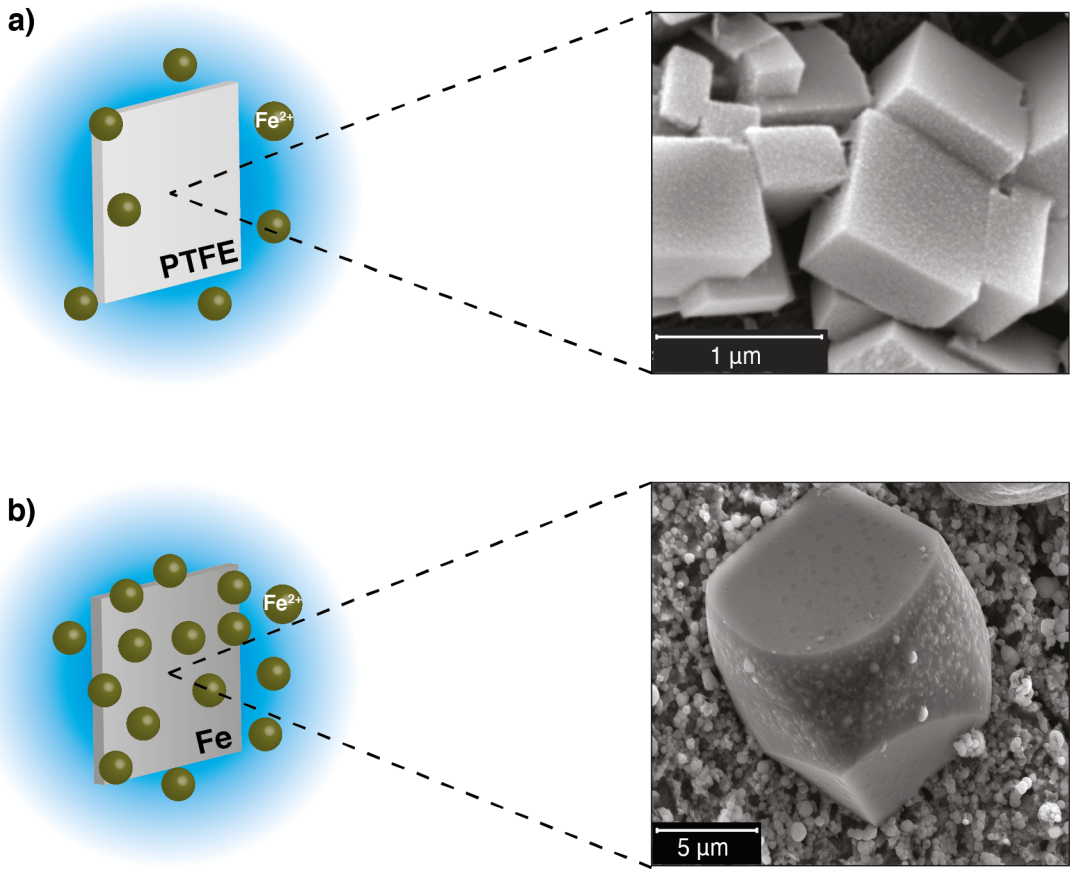

Figure 4.7: SEM images of siderite ($FeCO_3$) crystallites formed on (a) Fe substrate and (b) PTFE substrate after a total of 24 hours of immersion in CO_2-saturated 0.01 M $FeCl_2$ solution (T = 80°C, P_{CO_2} = 0.54 bar, pH = 6.8) in jacketed glass cell setup. Schematic illustrations shown to left of SEM images show the difference in $[Fe^{2+}_{(aq)}]$ near the surface of (a) PTFE and (b) Fe substrate [196].

The obtained result can be compared to a theoretical model predicting the siderite crystal habit published recently in collaboration with Nicholas Harrison research group at Imperial College London [196]. From this work, a correlation between relative chemical potential of iron ($\Delta\mu$Fe) and surface energies of selected facets is obtained by employing density functional theory (DFT) calculations. Then the ab initio crystal habit was predicted using Wulff construction as shown in Figure 4.8. Stoichiometric (S) and non-stoichiometric (NS) surfaces were selected and from the Figure 4.8 it is clear that S surfaces display constant surface energy, whereas NS surfaces display a change in the surface energy as a function of $\Delta\mu$Fe. Furthermore, ab initio modelling of

siderite revealed that by increasing the Fe chemical potential (analogous to increasing [$Fe^{2+}_{(aq)}$]), the siderite crystal habit changes. In Fe poor conditions, the habit forms a rhombohedral shape with {104} surfaces (see Figure 4.8 a and b). Under Fe rich conditions, NS{110} now becomes more thermodynamically stable and forms hexagonal shaped facets capped by trigonal S{104} facets (see Figure 4.8 c and d). Clearly, siderite crystal habits obtained from this model, specifically at $\Delta\mu$Fe= -5.95 eV (rhombohedral) and $\Delta\mu$Fe= -4.95 eV (cylindrical), are very similar to experimental observations seen in Figure 4.7.

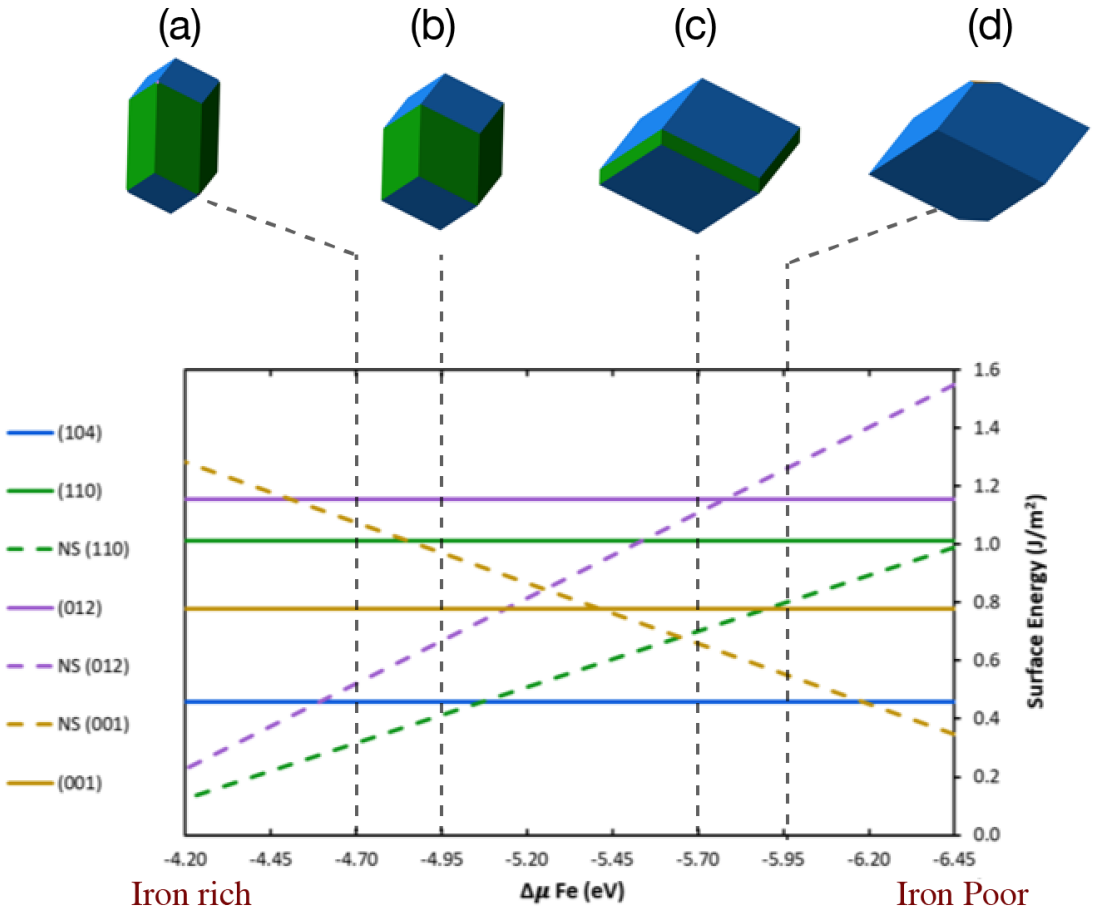

Figure 4.8: Computed surface free energies of formation of siderite ($FeCO_3$) surfaces plot as function of $\Delta\mu$Fe. Predicted siderite crystal habits are shown at the top at (a, b) $\Delta\mu$Fe= -4.95 eV and -4.7 eV (cylindrical) and (c, d) $\Delta\mu$Fe= -5.7 eV and -5.95 eV (rhombohedral). The plot is reproduced with the permission of Dr. Ehsan Ahmed [196].

Based on the modelling results, the crystallographic orientation of facets can be suggested as illustrated in Figure 4.9. Rhombohedral crystals facets are likely

to be suggested to be of {104} crystallographic orientation, as shown in Figure 4.9 (a). The same {104} orientation is also suggested for the trigonal/pyramidal caps of the cylinderical shaped siderite crystals (Figure 4.9 (b)). However, only NS{110} is considered in the model, which resulted in a hexagonal shaped facets instead of microfacetted cylinders observed experimentally. It is suggested that these mirco-facets are likely to be of multiple {*hk*0} planes [5].

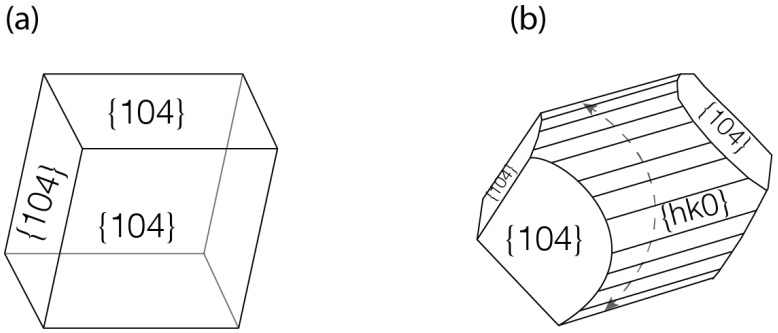

Figure 4.9: Schematic representation of the suggested habits of siderite at (a) lower [$Fe^{2+}_{(aq)}$] and (b) higher [$Fe^{2+}_{(aq)}$] conditions. Facets are labelled with suggested crystallographic orientation.

In order to confirm the assignments of the facets experimentally, the following section discusses employing EBSD and confocal microscopy techniques to identify the crystallographic orientation of siderite crystal facets.

4.3.2 Identification of crystallographic orientation of siderite facets

As shown in the previous section 4.3.1, there is an apparent agreement between the theoretical model of the siderite habit and what has been observed experimentally.

EBSD technique has been employed to confirm the crystallographic orientation of flat surfaces/facets [165]. This approach requires the use of additional techniques, such as photogrammetry or confocal microscopy to obtain facet geometry with respect to the specimen [197, 198]. The use of EBSD

coupled with photogrammetry techniques has been used previously to investigate the crystallography of fracture surfaces [199–202]. EBSD diffraction information is used here in conjunction with confocal microscopy to confirm the crystallographic indices of the flat surfaces of the trigonal/pyramidal caps of siderite formed on high purity Fe substrate in CO_2-saturated 0.1 M NaCl solution at 80°C, P_{CO_2}= 0.54 bar and pH = 6.8. This technique is suitable for planar, and relatively large grains/surfaces [165]. Therefore, it is more challenging to employ such technique to identify crystallographic orientation of the micro-faceted cylinders of the siderite crystals, and it has not been investigated as part of this work.

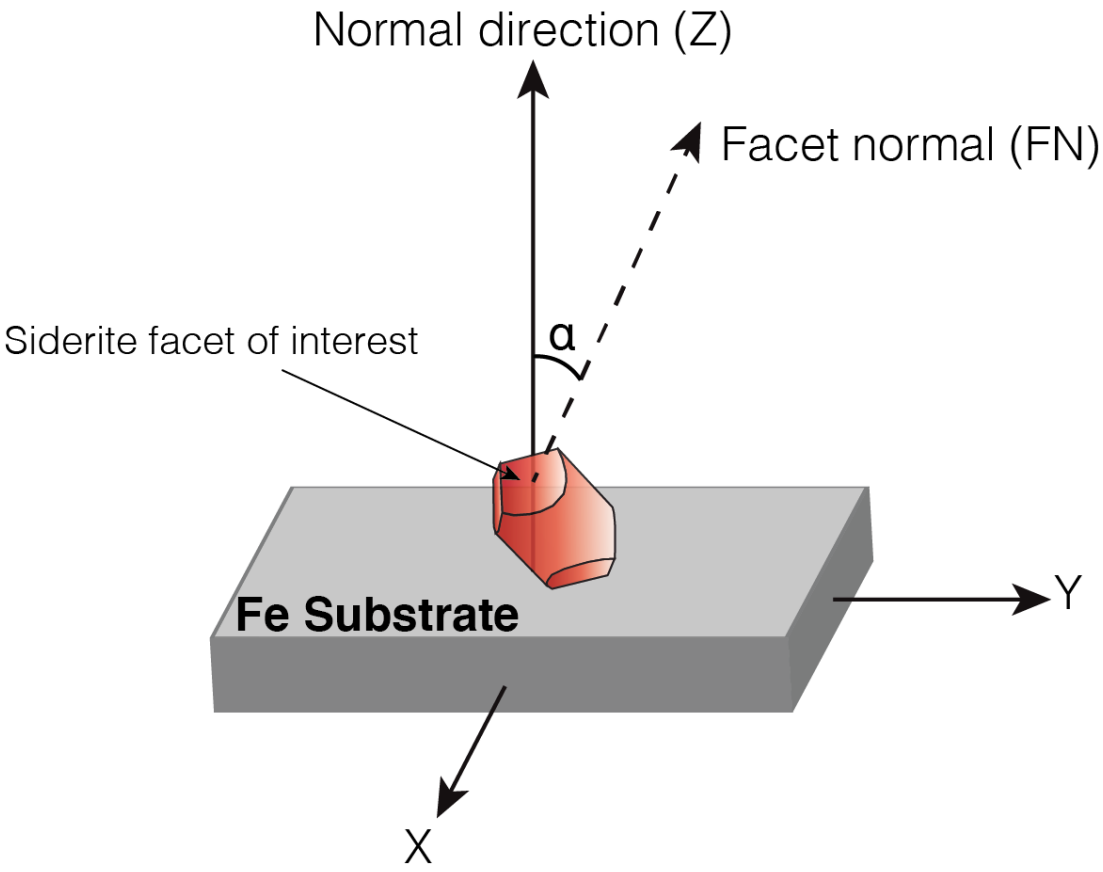

Figure 4.10: Illustration of siderite crystal on Fe substrate, which represents the specimen reference geometry system. Illustration shows the deviation of the siderite facet of interest crystallographic orientation from specimen normal direction (Z) by an angle α.

The main challenge here is that the facets are inclined with respect to the specimen coordinate system as shown in Figure 4.10. The specimen coordinate system is defined by the sample setup for EBSD measurements in the SEM, where Z is the normal direction of the Fe surface and parallel to the normal direction from the EBSD detector. In order to obtain the crystallographic orientation of siderite facets that are not flat with respect to the specimen geometry, two measurements are required:

1- The crystallographic orientation of the grains across the facet of interest. This can be accomplished from direct EBSD measurements.

2- The inclination of the facet with respect to the specimen reference geometry coordinate system. This can be accomplished using 3D-reconstruction from measurements obtained from confocal laser microscopy.

The information obtained from the two techniques can be correlated to identify the crystallographic orientation of a particular facet. The results from each step are discussed below.

1- Crystallography results from EBSD

Figure 4.11 shows an SEM image of siderite crystals formed on a high purity Fe substrate immersed for 24 hours in 0.1 M NaCl CO_2-saturated solution at 80 °C, P_{CO_2} = 0.54 bar and pH = 6.8. EBSD was acquired from 10 facets as highlighted in the SEM image in Figure 4.11. Note that due to the topography of the crystals, not all of the siderite crystals produce a clear diffraction patterns that could be indexed. In fact, most of the clear patterns produced were from facets of trigonal/pyramidal caps that appear to deviate by relatively small angles from the specimen coordinate system. At least 22 data points and up to 44 data points were acquired from each facet selected for the analysis.

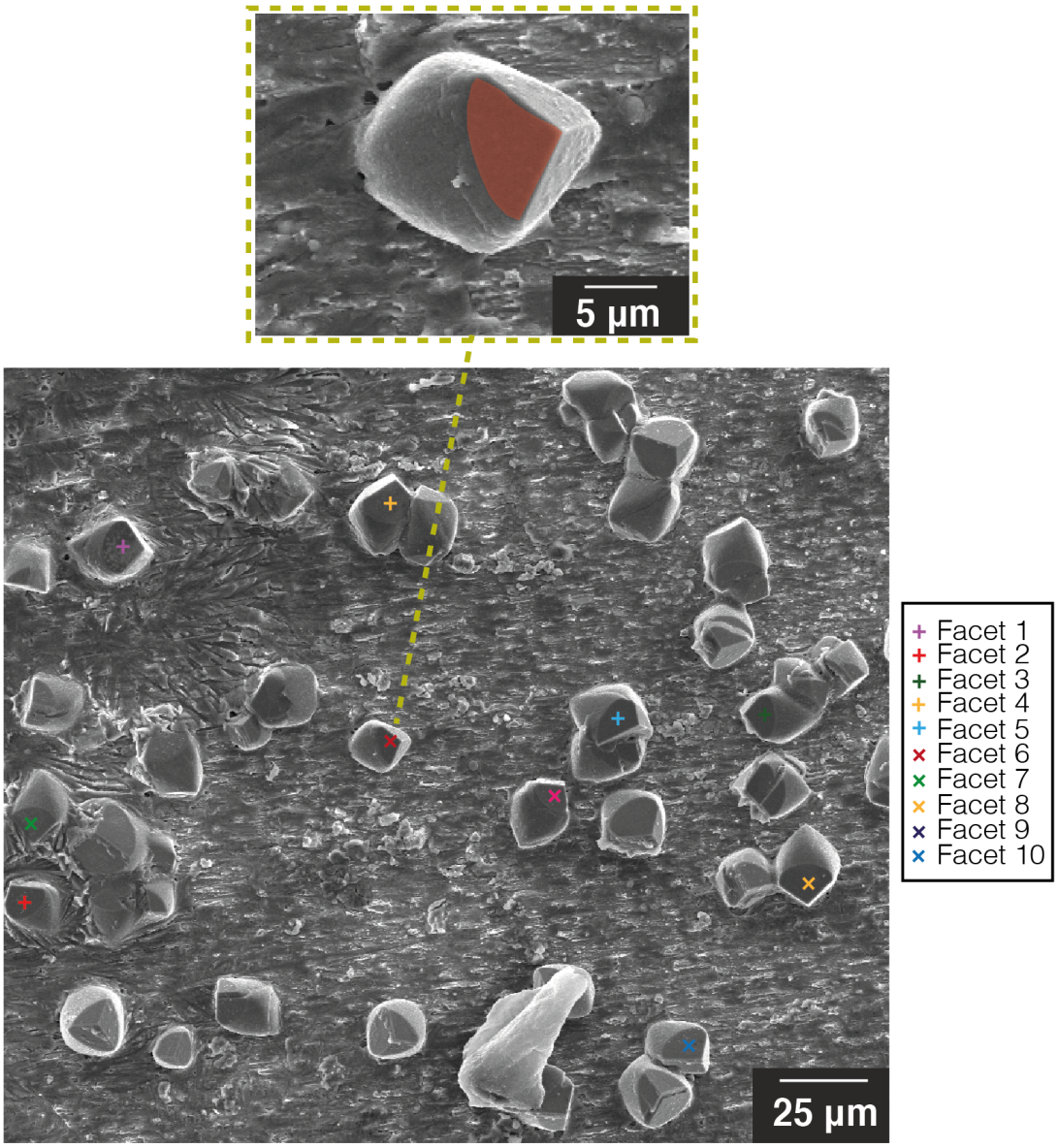

Figure 4.11: SEM image of siderite ($FeCO_3$) crystallites formed on Fe substrate after a total of 24 hours of immersion in CO_2-saturated 0.1 M NaCl solution (T = 80°C, P_{CO_2} = 0.54 bar, pH = 6.8) in a jacketed glass cell setup. Highlighted facets 1-10 were selected for EBSD measurements to determine the crystallographic orientation.

Figure 4.12 shows a {104} pole figure with plotted stereographic projection of poles from the 10 facets marked in the SEM image. It can be seen that a pole from all of the facets, marked in the dotted red box, is always close to the centre of the diagram (Z direction). This recorded crystallographic orientation is unlikely to be representing facet planes as it is certainly deviates from

the EBSD geometry set-up. The facet normal direction deviates from the the normal direction of the EBSD detector (along Z axis) by an angle α. The angle (α_{EBSD}) between the 10 poles marked in red box and the Z axis ranges between 6-24°. The angles were determined from the pole figure using Oxford CHANNEL5 software.

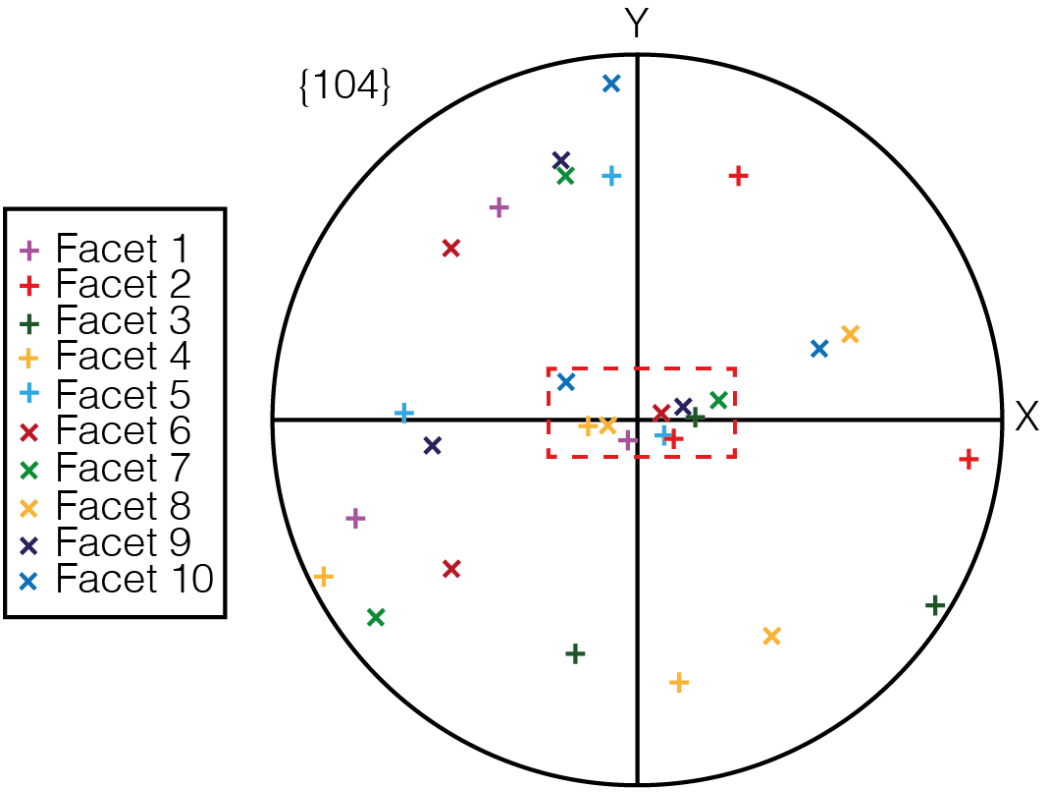

Figure 4.12: {104} pole figure of 10 siderite facets (see SEM image in Figure 4.11). Stereographic projection of one pole from each facet is highlighted within the red box showing a small deviation from the pole figure centre (Z direction).

2- Facet inclination from 3-D reconstruction images

Now moving to the next step where the 3-D reconstructed images of the siderite crystals from confocal microscopy are used to determine inclination of the facets with respect to specimen reference axes. Figure 4.13 presents an example of a 3-D reconstructed image of siderite crystals. The inclination of the facet can be determined by obtaining the direction of the facet normal. This can be done by obtaining the coordinates of three points on the facet of

interest; A (x_1, y_1, z_1), B (x_2, y_2, z_2) and C (x_3, y_3, z_3).

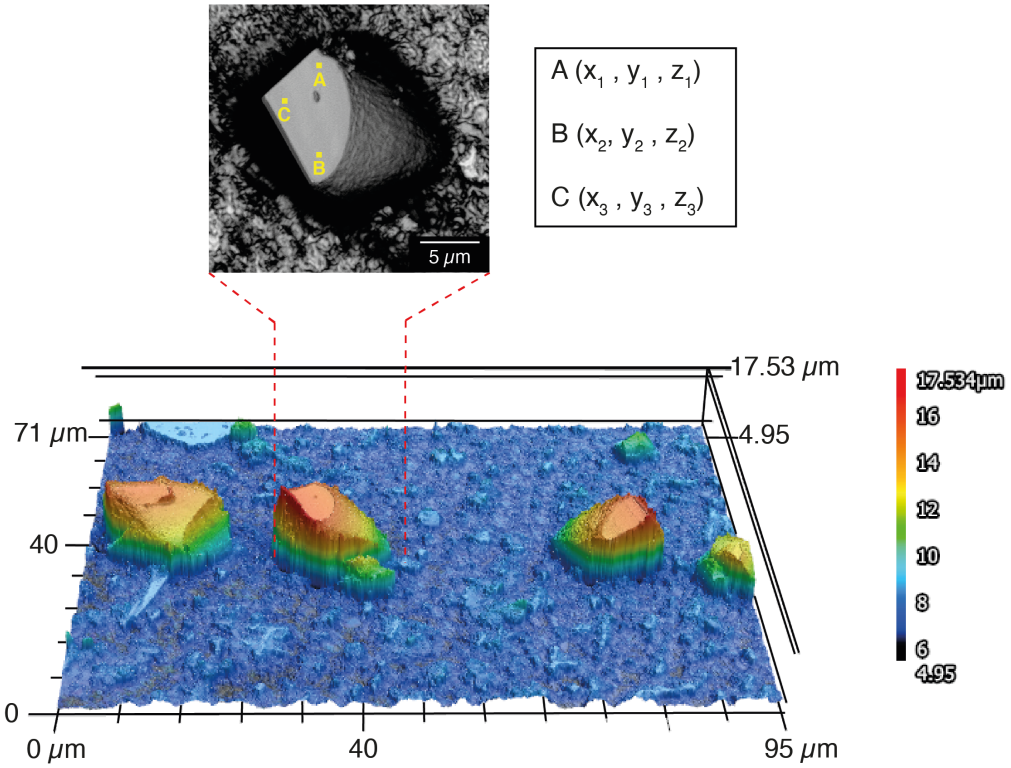

Figure 4.13: Example of a 3-D reconstruction of siderite crystals formed on Fe substrate using confocal microscopy. Planar view 2-D laser image of one siderite crystal is shown at the top with the selected coordinate points A, B, C on the surface needed to obtain the direction of facet normal.

The points selected on each facet are spread as far as possible to ensure reliability of information obtained about the facet inclination. From these three points, the angular direction of the plane normal ($\vec{n}$) is then computed by the cross product of vectors from the facet plane BA and CA where:

$$\overrightarrow{BA} = (x_2 - x_1)\mathbf{i} + (y_2 - y_1)\mathbf{j} + (z_2 - z_1)\mathbf{k} \tag{4.1}$$

$$\overrightarrow{CA} = (x_3 - x_1)\mathbf{i} + (y_3 - y_1)\mathbf{j} + (z_3 - z_1)\mathbf{k} \tag{4.2}$$

The angle between the plane normal ($\vec{n}$) and the specimen reference Z axis is

then obtained from direction cosine as follows:

$$\alpha_c = cos^{-1}(\frac{\overrightarrow{n}.\mathbf{k}}{|\overrightarrow{n}|}) \tag{4.3}$$

Table 4.5 lists the obtained angles α_{confocal} for facets 1-10 shown in Figure 4.11 and compared with the calculated α_{EBSD} angles from the {104} pole figure. It can be seen that the angles are in general agreement with an uncertainty of less than 1°. Correlating the results from these measurements confirms that the trigonal caps facets' crystallographic orientation is {104}.

Table 4.3: Obtained deviation angle of the 10 selected siderite facets from the normal direction in specimen geometry by EBSD and confocal microscopy.

Facet number	Angle measured by confocal (α_c) [°]	Angle determined from pole figure (α_{EBSD}) [°]	Absolute angle difference [°]
1	7.0	7.1	0.1
2	12.3	12.5	0.2
3	16.8	17.7	0.9
4	14.4	14.7	0.3
5	9.8	9.7	0.1
6	7.1	6.4	0.7
7	24.7	25.6	0.9
8	9.1	8.6	0.5
9	14.2	14.1	0.1
10	23.8	23.9	0.1

From the above results, only one facet out of the three facets in the trigonal/pyramidal caps from each crystal has been analysed to determine the crystallographic orientation, which has been found to be {104}. To determine if the three facets represent the same crystallographic orientation, the angles between each facet from confocal 3-D reconstructed images is determined using MultiAnalyzer software [178], as illustrated in Figure 4.14. The selected crystals were oriented so that the three facets are visible in the 2D image.

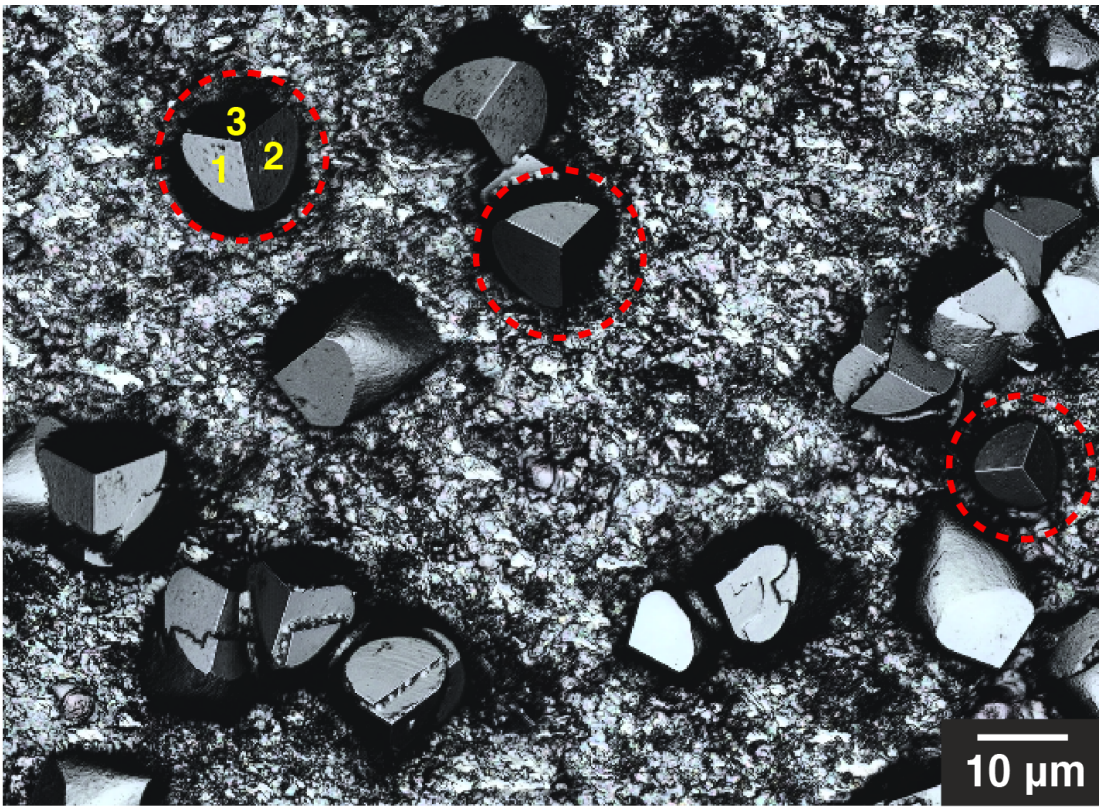

Figure 4.14: Laser/optical image of siderite siderite ($FeCO_3$) crystallites formed on Fe substrate after a total of 24 hours of immersion in CO_2-saturated 0.1 M NaCl solution (T = 80°C, P_{CO_2} = 0.54 bar, pH = 6.8) in a jacketed glass cell setup. Dotted red marker highlights facets oriented with all 3 trigonal/pyramidal caps visible.

The average angle between the three facets of the trigonal/pyramidal caps from 5 different siderite crystals was calculated and it was found to be 105.5°±5.2°.

The angle difference between two planes of {104} family, for example the angle between (104) and $(1\bar{1}\bar{4})$, can be calculated using CrystalMaker software [74] (see Figure 4.15). The calculated angle was found to be 106.93°, which is in close agreement with the values obtained experimentally using 3-D reconstructed siderite crystal image. This further confirms that all three facets of the trigonal/pyramidal caps are identical and of {104} family crystallographic orientation planes.

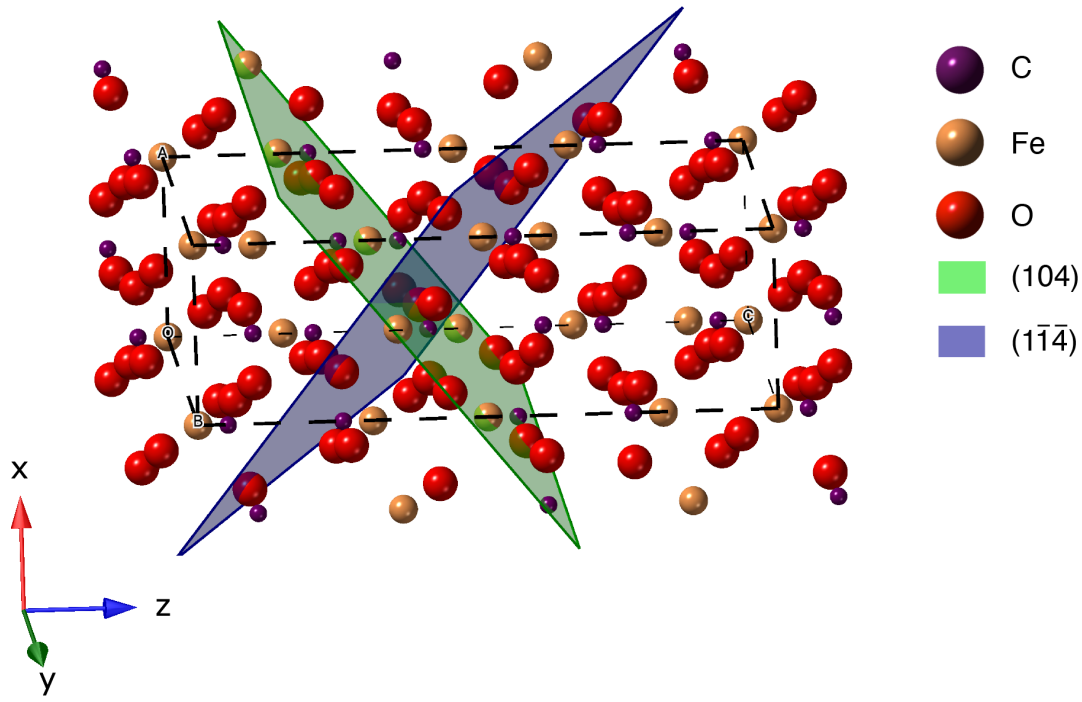

Figure 4.15: Crystal structure of siderite ($FeCO_3$) generated by Crystal Maker software [74]. Examples of (104) and (1$\bar{1}\bar{4}$) planes are shown from {104} family planes.

4.3.3 Influence of [Fe^{2+}] on siderite habit

The results obtained from both ab initio modelling and experiments presented in section 4.3.1 suggest that $Fe^{2+}_{(aq)}$ concentration has an influence on siderite crystal habit. In order to investigate if the increase in the amount of $Fe^{2+}_{(aq)}$ in the bulk solution can replicate this change, the amount of $FeCl_2$ in solution is increased from 0.01 M to 0.1 M. The influence of this change is then observed on non-corroding PTFE and corroding Fe samples.

Figure 4.16 shows SEM images of typical siderite crystals formed on a PTFE substrate immersed for 24 hours in CO_2-saturated 0.01 and 0.1 M $FeCl_2$ solutions at 80°C, P_{CO_2}= 0.54 bar and pH = 6.8. It can be seen that there is a change in siderite crystal habit from rhombohedral to cylindrical shape. Such an observation further confirms the ab initio modelling results, which suggest that an increase in $Fe^{2+}_{(aq)}$ stabilises NS{110} (or {*hk*0} facets) and resulting in this

habit change.

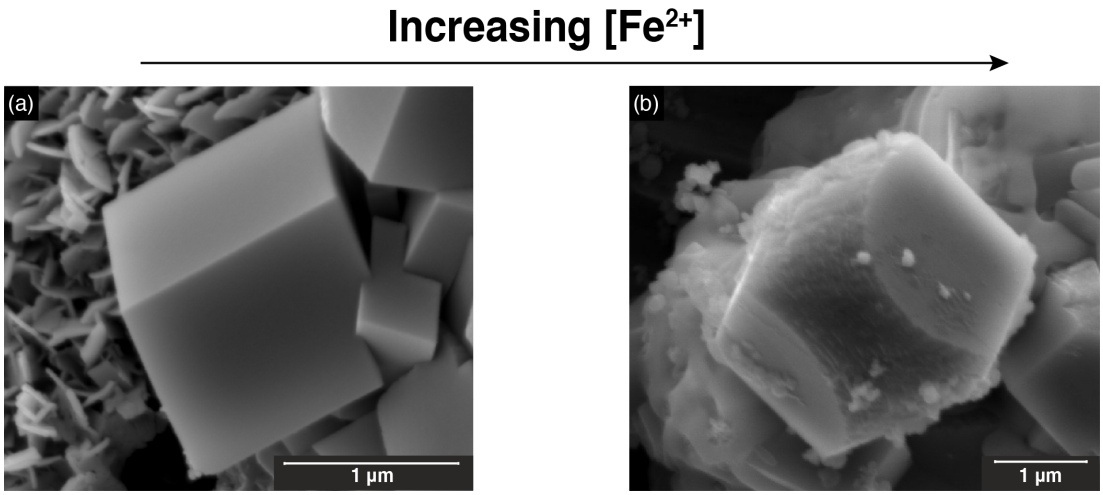

Figure 4.16: SEM images of siderite ($FeCO_3$) crystallites formed on PTFE substrate after 24 hours of immersion in CO_2-saturated (a) 0.01 M $FeCl_2$ solution and (b) 0.1 M $FeCl_2$ solution, (T = 80°C, P_{CO_2} = 0.54 bar, pH = 6.8) in a jacketed glass cell setup.

Looking more closely at multiple SEM images from substrates immersed in both conditions, it appears that both shapes form under each condition (Figure 4.17). However, the majority of crystals formed in 0.01 M $FeCl_2$ solutions form rhombohedral shape while less rhombohedral crystals form at 0.1 M $FeCl_2$.

Table 4.4 presents average percentage of the amount siderite crystals formed and their habit at under both conditions. This is done by analysing multiple SEM images of PTFE samples post-immersion from total of 6 repeated experiments (4 at 0.01 M $FeCl_2$ and 2 at 0.1 M $FeCl_2$). From the table, it can be seen that 85% of the formed siderite crystals in 0.01 M $FeCl_2$ solutions are rhombohedral while majority of the crystals formed at 0.1 M $FeCl_2$ are of cylindrical shape with a fraction of 60%.

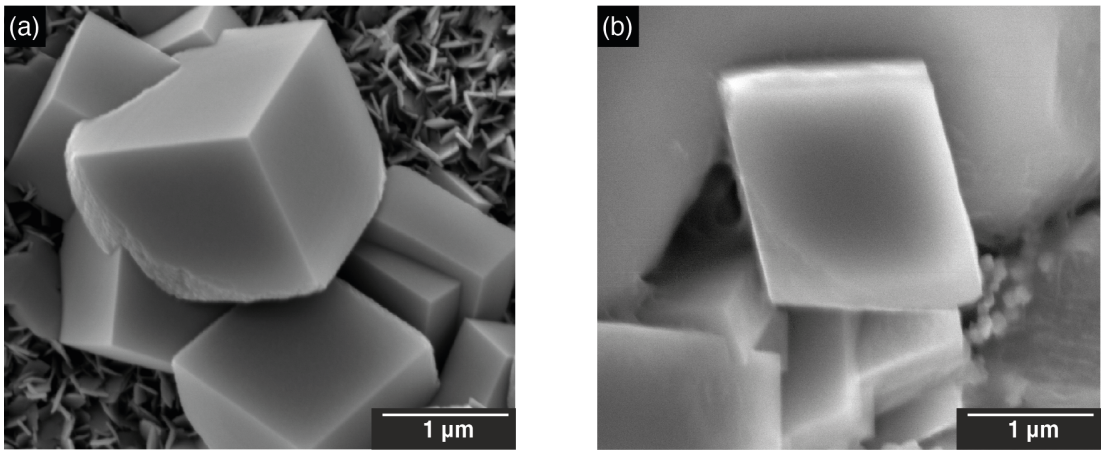

Figure 4.17: SEM images of showing the formation of (a) cylindrical siderite ($FeCO_3$) crystal on PTFE substrate after 24 h immersion in CO_2-saturated 0.01 M $FeCl_2$ and (b) rhombohedral crystals in CO_2-saturated 0.01 M $FeCl_2$.

Table 4.4: Calculated percentage of each habit of siderite crystallites formed on PTFE after immersion for 24 hours in CO_2-saturated (a) 0.01 M $FeCl_2$ solution and (b) 0.1 M $FeCl_2$ solution, (T = 80°C, P_{CO_2}= 0.54 bar, pH = 6.8).

Solution	Number of analysed crystals	Rhombohedral crystals	Micro-faceted cylinders with trigonal caps crystals
0.01 M $FeCl_2$	3664	∼85%	∼15%
0.1 M $FeCl_2$	661	∼40%	∼60%

Moving now to the Fe substrate, Figure 4.18 shows SEM images of siderite crystals formed on high purity Fe substrate immersed in CO_2-saturated 0.01 and 0.1 M $FeCl_2$ solution at 80°C, P_{CO_2}= 0.54 bar and pH = 6.8. The crystal habit of siderite remained as '*cylindrical*' when the [$Fe^{2+}_{(aq)}$] increased from 0.01 to 0.1 M in the solution. However, the increase in [$Fe^{2+}_{(aq)}$] resulted in elongation of the micro-faceted cylinder of the crystallite. For example, the ratio between micro-faceted cylinder/total crystal length increased from $\sim$ 0.34 at 0.01 M $FeCl_2$ to $\sim$ 0.58 at 0.1 M $FeCl_2$ in the SEM image presented in Figure 4.18, which confirms the elongation of the micro-faceted cylinders relative to the change in crystal size. This suggests that an increase in [$Fe^{2+}_{(aq)}$] concentration further stabilises {hk0} facets resulting in its elongation/growth. Such an observation is consistent with the ab initio modelling results and referring back to Figure

4.8 (a and b), the increase in $\Delta\mu$Fe= -4.95 eV to -4.7 eV resulted in an elongation of NS{110} facet. Elongation of the micro-faceted cylinder in siderite has been also observed previously due to the addition of malic acid, but to an even larger extent than observed here [149].

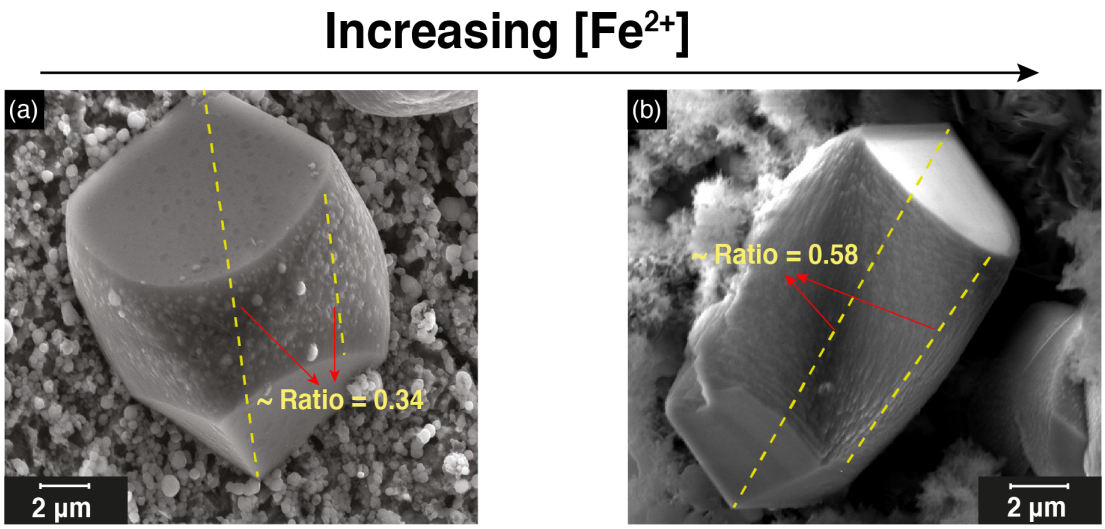

Figure 4.18: SEM images of siderite ($FeCO_3$) crystallites formed on Fe substrate after 24 hours of immersion in CO_2-saturated (a) 0.01 M $FeCl_2$ solution and (b) 0.1 M $FeCl_2$ solution (T = 80°C, P_{CO_2} = 0.54 bar, pH = 6.8) in jacketed glass cell setup.

To summarise and combining the results observed from the two substrates, it is clear that the increase in the concentration of $Fe^{2+}_{(aq)}$ alters the siderite crystal habit. Initial increase in $Fe^{2+}_{(aq)}$ (from Fe poor to medium conditions), as shown in Figure 4.19, results in a change from rhombohedral shape to micro-facetted cylinder with trigonal-pyramidal caps. A further increase in the amount of $Fe^{2+}_{(aq)}$ results in an elongation of the micro-faceted cylinder of the crystallite. Similarly and as predicted by ab initio modelling, the increase to Fe-rich conditions thermodynamically stabilise the formation of {110} surfaces leading to its appearance and then further elongation as shown in Figure 4.8.

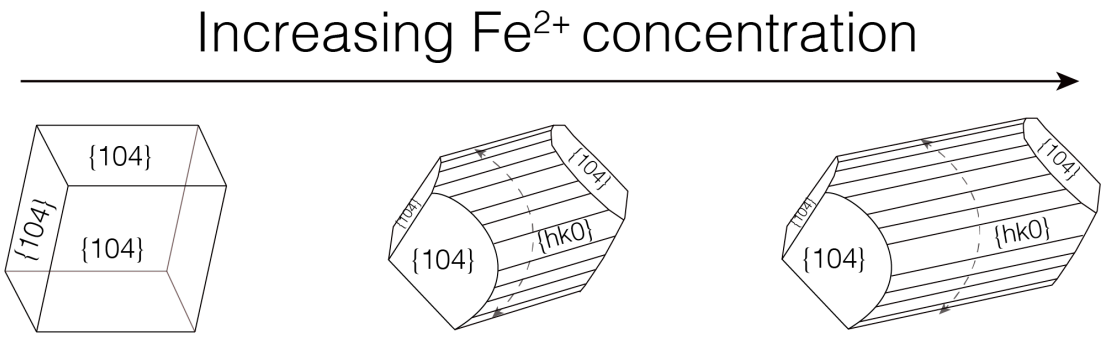

Figure 4.19: Schematic representation of siderite habits change as a function of increasing [$Fe^{2+}_{(aq)}$].

4.3.4 Influence of NaCl on siderite crystal habit

In the experiments investigating the influence of increasing the amount of $Fe^{2+}_{(aq)}$ in solution, the concentration of $FeCl_2$ is varied from 0.01 M to 0.1 M. The amount of Cl^- is also increasing by 0.18 M. Therefore, this was a motivation to decouple these two factors and investigate if NaCl can influence siderite crystal habit in addition to Fe^{2+}. This was performed by immersion of a PTFE substrate in CO_2-saturated 0.01 M $FeCl_2$ + 0.18 M NaCl solution at 80°C, P_{CO_2}= 0.54 bar and pH = 6.8. Figure 4.20 shows SEM images of siderite formed on a PTFE substrate with and without the addition of 0.18 M NaCl. It can be seen that by the addition of NaCl, more siderite crystals formed a cylindrical habit. However, there is still considerable number of rhombohedral shaped crystals formed.

Table 4.5 presents a quantitative analysis on the percentage of crystals formed in each habit. Although there is a change in the crystal habit by the addition of NaCl, the majority of formed crystals exhibit a rhombohedral habit with a percentage of 58%. Therefore, this indicates that the change in NaCl concentration can enhance the ability of changing habits. It is not quite clear whether only $Cl^-_{(aq)}$ resulted in such a change, as $Na^+_{(aq)}$ is also added and can possibly influence such a change in crystal habit. This can be further investigated by the addition of Na^+ salts, e.g. sodium sulphate (Na_2SO_4).

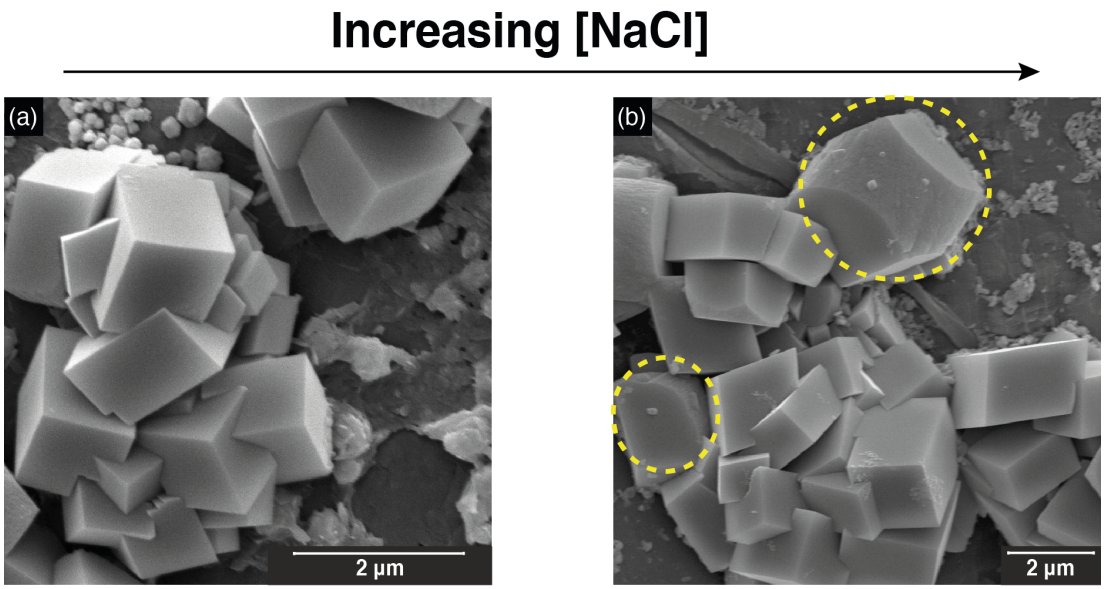

Figure 4.20: SEM images of siderite ($FeCO_3$) crystallites formed on PTFE substrate after 24 hours of immersion in CO_2-saturated (a) 0.01 M $FeCl_2$ solution and (b) 0.01 M $FeCl_2$ + 0.18 NaCl solution, (T = 80°C, P_{CO_2} =0.54 bar, pH = 6.8) in a jacketed glass cell setup.

Table 4.5: Calculated percentage of each habit of siderite crystals formed on PTFE after immersion for 24 hours in CO_2-saturated (a) 0.01 M $FeCl_2$ solution and (b) 0.01 M $FeCl_2$ + 0.18 M NaCl solution, (T = 80°C, P_{CO_2}= 0.54 bar, pH = 6.8).

Solution	Number of analysed crystals	Rhombohedral crystals	Micro-faceted cylinders with trigonal caps crystals
Without NaCl	3664	85%	15%
With 0.18 M NaCl	450	58%	42%

4.3.5 Influence of Ca^{2+} on siderite crystal habit

This section discusses the influence of the addition of $Ca^{2+}_{(aq)}$, which is a typical compound present within solutions in oilfield conditions. First, focusing on the influence of $Ca^{2+}_{(aq)}$ on scale formation on corroding surfaces, Figure 4.21 (a) shows post immersion GIXRD diffraction pattern of corroded Fe substrate in CO_2-saturated 0.001 M $CaCl_2$ + 0.01 M $FeCl_2$ solution. The observed peaks appeared to be shifted away from pure siderite/calcite when compared with the reference patterns as shown in Figure 4.21 (a).

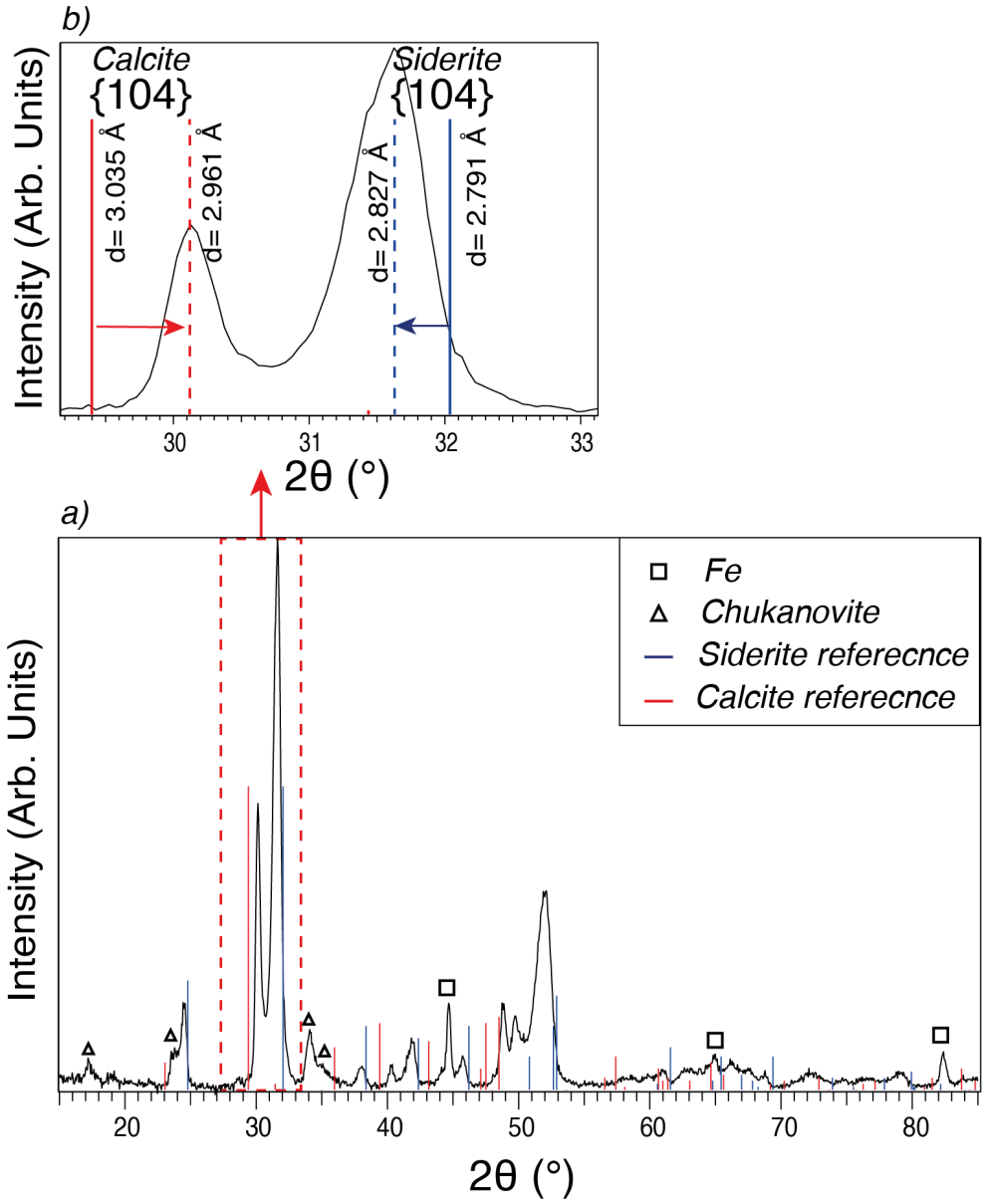

Figure 4.21: (a) GIXRD diffractogram (acquired at α = 3°, CuKα source λ = 0.154 nm) and of Fe substrate immersed for 24 hours in CO_2-saturated 0.01 M $FeCl_2$ + 0.001 M $CaCl_2$ solution (T = 80°C, P_{CO_2} = 0.54 bar, pH = 6.8) in jacketed glass cell setup. (b) Peak shifts from pure siderite and pure calcite shown in the region of 2θ = 29°- 35°

To illustrate this further, Figure 4.21 (b) shows the diffraction pattern in the range of 2θ = 29° to 32.5°, focusing on the shifts of the observed peaks from the most intense {104} peak of pure siderite and calcite. At this range, two observed peaks are shown at 2θ = 30.15° and 31.62°($\pm$ 0.05°). The first peak is slightly shifted to a higher 2θ value from calcite {104} peak (2θ = 29.35°),

changing the d-spacing from d= 3.035 Å to d= 2.961 Å (± 0.019 Å). The second peak is shifted from siderite {104} peak (2θ = 32.03°), changing the d-spacing from d= 2.791 Å to d= 2.827 Å (± 0.019 Å). These peak shifts are consistent when comparing other observed peaks in Figure 4.21 (a) with the reference siderite/calcite peaks across the full measured range of 2θ = 15°- 85°. Peak shifts of pure siderite peaks to a larger d-spacing value (or lower 2θ) indicates substitution of Fe^{2+} (ionic radius = 0.75 Å) with the larger Ca^{2+} (ionic radius = 1.14 Å) in lattice positions [203]. On the other hand, peak shifts of pure calcite peaks to a smaller d-spacing value (or higher 2θ) indicates substitution of Ca^{2+} with the smaller Fe^{2+} in lattice positions. Peak shifts suggest formation of a mixed iron/calcium solid solution phase: $Fe_xCa_yCO_3$, where x + y = 1. The formed solid solution phase exist in two different ratios/molar fractions of Fe^{2+} and Ca^{2+}, one with x closer to unity where few Fe^{2+} substituted by Ca^{2+} in the lattice structure, while in the other y is closer to unity where few Ca^{2+} substituted by Fe^{2+} in the lattice structure.

Molar fractions of Fe^{2+} and Ca^{2+} in $Fe_xCa_yCO_3$ solid solution can be determined using the XRD data. This can be done firstly by calculating unit cell parameters a and c, knowing that $Fe_xCa_yCO_3$ is of hexagonal crystal structure. For a hexagonal crystal structure (Figure 4.22), unit cell parameters a and c can be calculated by the following equations:

$$sin^2\theta = A(h^2 + hk + k^2) + Cl^2 \tag{4.4}$$

$$A = \frac{\lambda^2}{3a^2} \tag{4.5}$$

$$C = \frac{\lambda^2}{4c^2}, \tag{4.6}$$

where h, k, and l represent the Miller indices of a plane, λ is wavelength of the incident x-ray, a and c are the unit cell parameters. Here the angle θ can be obtained from the GIXRD plot and *hkl* plane can be obtained from corresponding planes of siderite/calcite reference data. Once unit cell

parameters of each phase is determined, molar fraction (y) of calcium in $Fe_xCa_yCO_3$ can be calculated using equation (4.7) assuming linear behaviour of Ca^{2+} incorporation in the crystal structure [135].

$$y = 0.5922c - 9.1045 \tag{4.7}$$

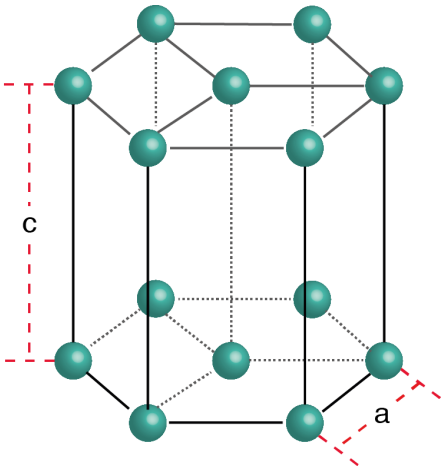

Figure 4.22: Hexagonal crystal structure with unit cell parameters a and c.

Table 4.6 shows the molar fractions of $Fe_xCa_yCO_3$ present on the Fe surface. From the table, it can be seen that the first phase formed has only 0.1 molar fraction of calcium. This is possibly as result of Ca^{2+} incorporation in formed siderite usually due to the corrosion process resulting in high Fe^{2+} near the corroding surface. On the other hand, the second phase with higher calcium molar fraction of 0.72 is likely to deposit on the Fe surface after precipitation from the bulk solution.

Table 4.6: Calculated unit cell parameters and composition of the $Fe_xCa_yCO_3$ solid solution phase formed on Fe substrate after 24 hours of immersion in CO_2-saturated 0.01 M $FeCl_2$ + 0.001 M $CaCl_2$ solution, (T = 80°C, P_{CO_2} = 0.54 bar, pH = 6.8).

No.	Calculated unit cell parameter		$Fe_xCa_yCO_3$	
	a	c	x	y
1	4.76 ± 0.03	15.63 ± 0.09	0.90 ± 0.05	0.10 ± 0.05
2	4.89 ± 0.01	16.59 ± 0.01	0.28 ± 0.01	0.72 ± 0.01

Moving to the influence on crystal habit, SEM images in Figure 4.23 shows also formation of much rough cylindrical shaped crystals. Interestingly, although $Fe_xCa_yCO_3$ phase formed at two different molar fractions, all crystals have similar shape.

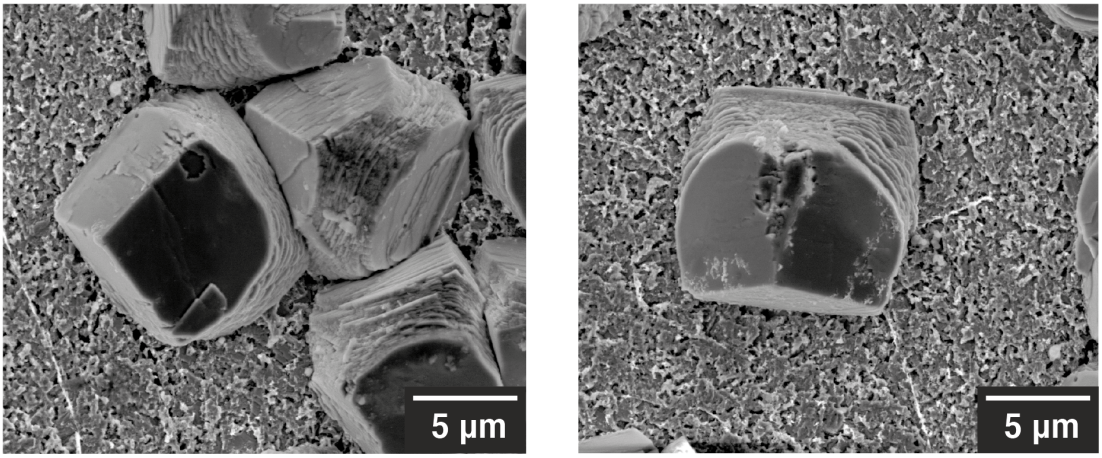

Figure 4.23: SEM images of siderite ($FeCO_3$) crystallites formed on Fe substrate after 24 hours of immersion in CO_2-saturated 0.01 M $FeCl_2$ + 0.001 M $CaCl_2$ solution, (T = 80°C, P_{CO_2} = 0.54 bar, pH = 6.8) in jacketed glass cell setup.

Regarding the non-corroding substrate, Figure 4.24 (a) shows post immersion GIXRD diffraction pattern of non-corroding PTFE substrate in CO_2-saturated 0.001 M $CaCl_2$ + 0.01 M $FeCl_2$ solution. Similar to the scale formation on Fe substrate, the GIXRD pattern indicate formation of a mixed iron/calcium carbonate solid solution phase $Fe_xCa_yCO_3$. The formed phase has two different ratios/molar fractions of Fe^{2+} and Ca^{2+}. This is evident by the presence of two shifted peaks at 30.04° and 31.29° across 2θ range from 29° to 32.5° as shown in Figure 4.24 (b). Table 4.7 shows the molar fractions of $Fe_xCa_yCO_3$ present on the PTFE surface. The first solid solution phase formed on the PTFE consist of less Fe atoms compared to the phase formed on Fe surface. This is expected as more Fe ions are provided by the corroded Fe substrate.

Table 4.7: Calculated unit cell parameters and composition of the $Fe_xCa_yCO_3$ solid solution phase formed on PTFE substrate after 24 hours of immersion in CO_2-saturated 0.01 M $FeCl_2$ + 0.001 M $CaCl_2$ solution, (T = 80°C, P_{CO_2} = 0.54 bar, pH = 6.8).

No.	Calculated unit cell parameter		$Fe_xCa_yCO_3$	
	a	c	x	y
1	4.77 ± 0.02	15.78 ± 0.05	0.75 ± 0.03	0.24 ± 0.03
2	4.93 ± 0.01	16.59 ± 0.01	0.28 ± 0.01	0.72 ± 0.01

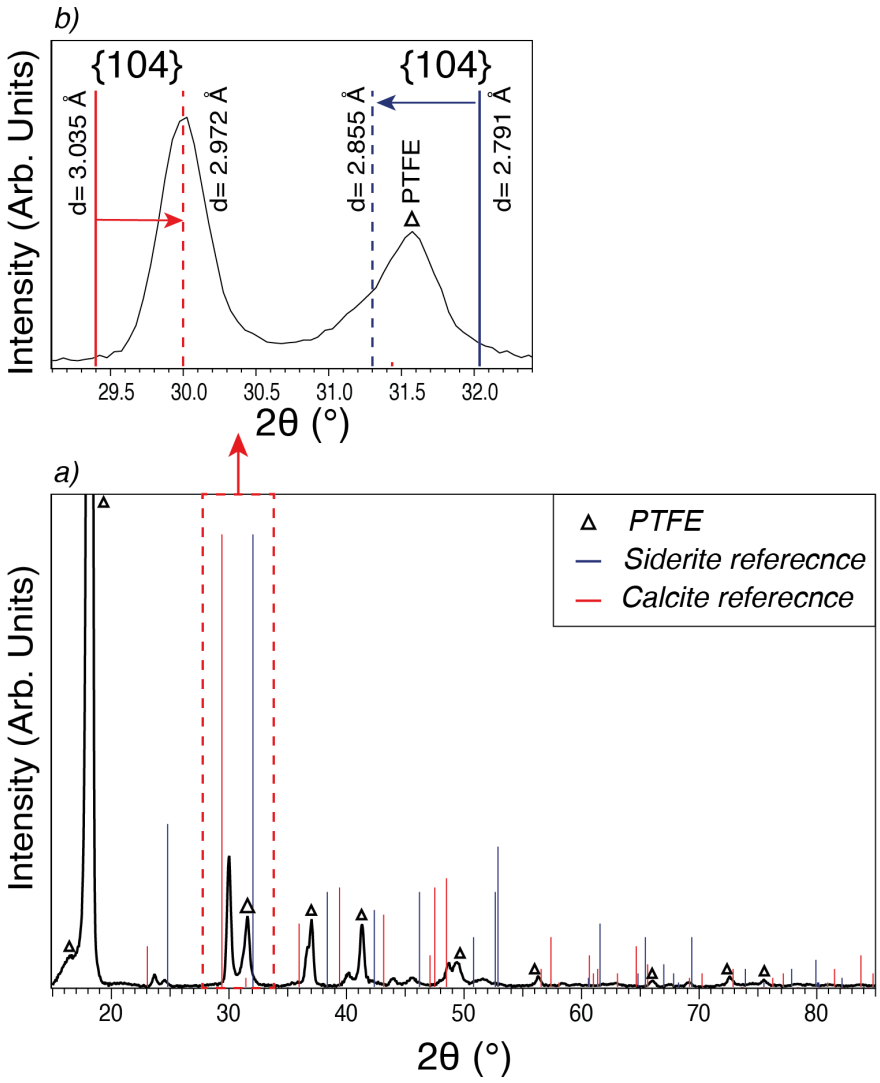

Figure 4.24: (a) GIXRD diffractogram (acquired at α=3 °, CuKα source λ = 0.154 nm) and of PTFE substrate immersed for 24 hours in CO_2-saturated 0.01 M $FeCl_2$ + 0.001 M $CaCl_2$ solution (T = 80°C, P_{CO_2} = 0.54 bar, pH = 6.8) in jacketed glass cell setup. (b) Peak shifts from pure siderite and pure calcite shown in the region of 2θ = 29°- 35°.

As regards to the crystal habit, SEM images in Figure 4.25 shows formation of cylindrical-like crystals. Here, a change in crystal habit is seen compared to athe formation of rhombohedral crystal habit on PTFE substrate without the addition of 0.001 M $CaCl_2$, as shown previously in Figure 4.7 (a). Furthermore, the micro-facets between the two trigonal/pyramidal caps grow here to clear steps as shown in Figure 4.25 (b). These steps are is not usually observed in pure siderite crystals formed either in corroded iron surface on non-corroding PTFE at various conditions.

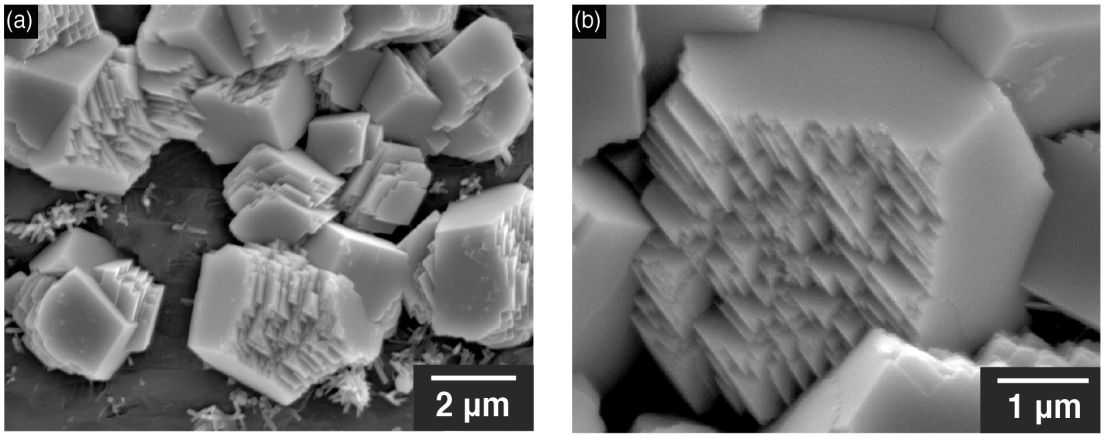

Figure 4.25: SEM images of siderite ($FeCO_3$) crystallites formed on PTFE substrate after 24 hours of immersion in CO_2-saturated 0.01 M $FeCl_2$ + 0.001 M $CaCl_2$ solution, (T = 80°C, P_{CO_2} =0.54 bar, pH = 6.8) in jacketed glass cell setup.

4.3.6 Influence of Mg^{2+} on siderite crystal habit

The influence of $Mg^{2+}_{(aq)}$ on siderite crystal habit by adding 0.001 M of $MgCl_2$ and 0.01 M $FeCl_2$ in CO_2-saturated solution and observing the habits on non-corroding PTFE substrate and corroding Fe substrate.

Figure 4.26 shows post immersion GIXRD diffraction pattern of PTFE substrate in CO_2-saturated 0.001 M $MgCl_2$ + 0.01 M $FeCl_2$ solution. The diffraction pattern indicate formation of a mixed layer of siderite and chukanovite on PTFE substrate.

Siderite crystals formed, as shown in Figure 4.27, have a rhombohedral shape. This suggest that the presence of $Mg^{2+}_{(aq)}$ at such concentrations does not alter the crystal habit of siderite. However, looking at the magnified SEM image in Figure 4.27 c), relatively small elongated rods shaped crystals have formed on the surface.

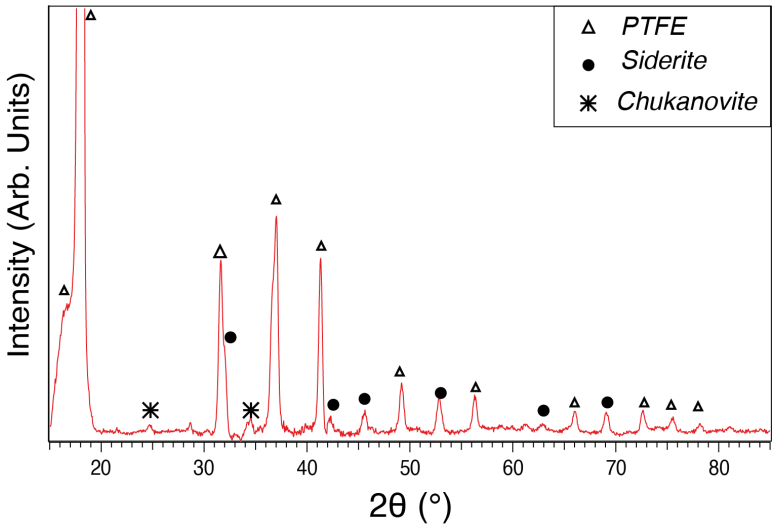

Figure 4.26: GIXRD diffractogram (acquired at α=3 °, CuKα source λ=0.154 nm) and of PTFE substrate immersed for 24 hours in CO_2-saturated 0.01 M $FeCl_2$ + 0.001 M $MgCl_2$ solution (T = 80°C, P_{CO_2} = 0.54 bar, pH = 6.8) in jacketed glass cell setup.

In order to investigate the elongated rods, an EDS line-scans were performed across the rods and adjacent siderite crystals. It can be seen from the line scan in Figure 4.28, that there is no apparent change in Fe or oxygen amount across the selected region. In addition, the Mg amount remained almost zero and relatively constant across the scanned line. This suggest that these elongated rods are possibly siderite crystals. Since these rods have not been observed previously without the addition of $Mg^{2+}_{(aq)}$, it is possible that $Mg^{2+}_{(aq)}$ alters the growth of these crystals resulting in formation of such elongated rods.

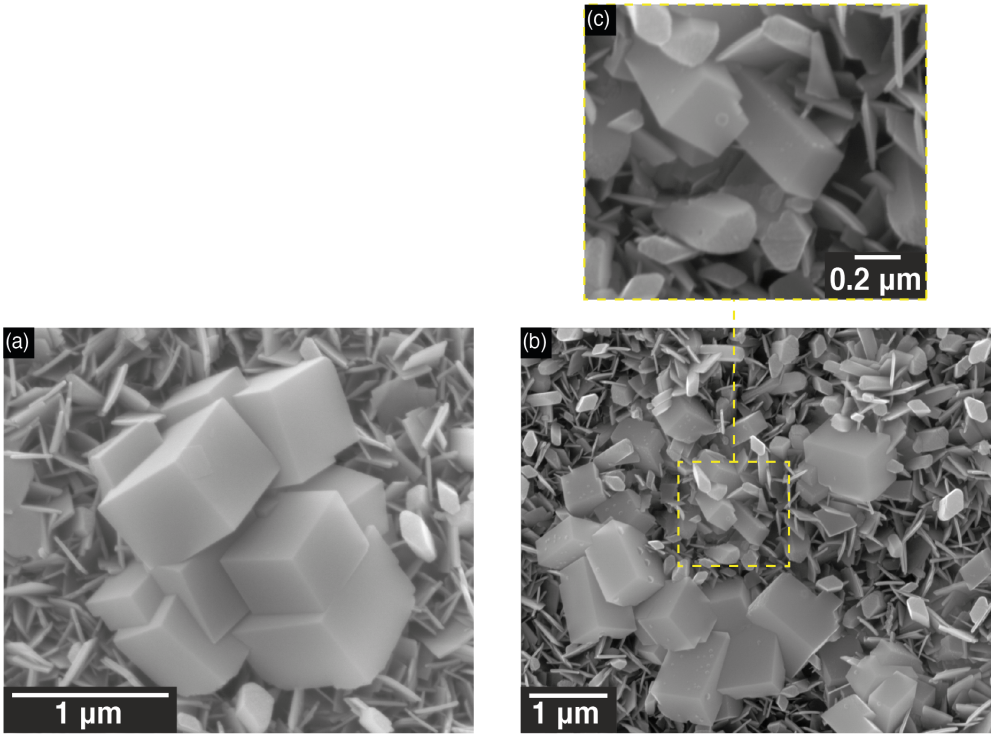

Figure 4.27: SEM images of siderite ($FeCO_3$) crystallites formed on PTFE substrate after 24 hours of immersion in CO_2-saturated 0.01 M $FeCl_2$ + 0.001 M $MgCl_2$ solution, (T = 80°C, P_{CO_2}=0.54 bar, pH= 6.8) in jacketed glass cell setup.

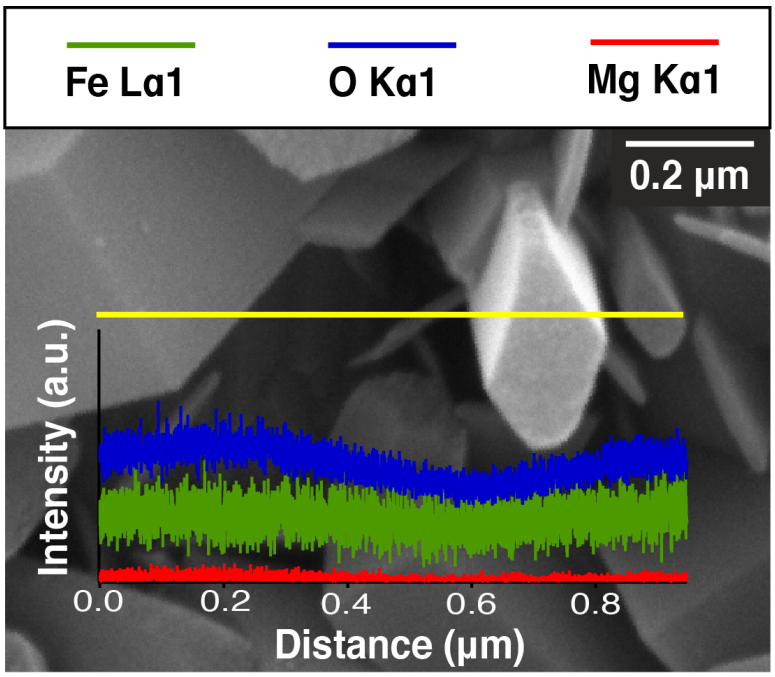

Figure 4.28: SEM image and overlaid EDS linescan across elongated rod crystals.

As regards to the influence of Mg^{2+} on siderite crystal habit formed on corroding Fe substrate, Figure 4.29 shows GIXRD diffraction pattern Fe substrate in CO_2-saturated 0.001 M $MgCl_2$ + 0.01 M $FeCl_2$ solution. The diffraction pattern also indicate formation of a mixed layer of siderite and chukanovite on corroding Fe substrate.

Focusing on crystal habit, as shown in Figure 4.30, cylindrical shaped siderite formed on Fe substrate, which is similar to the habit observed without the addition of $Mg^{2+}_{(aq)}$ ions. This indicates that adding 0.001 M of $Mg^{2+}_{(aq)}$ does not alter the phase formed and crystal habit compared to adding the same concentration of $Ca^{2+}_{(aq)}$. This is possibly due to higher solubility of magnesium carbonate ($MgCO_3$) compared to calcium carbonate ($CaCO_3$) [129].

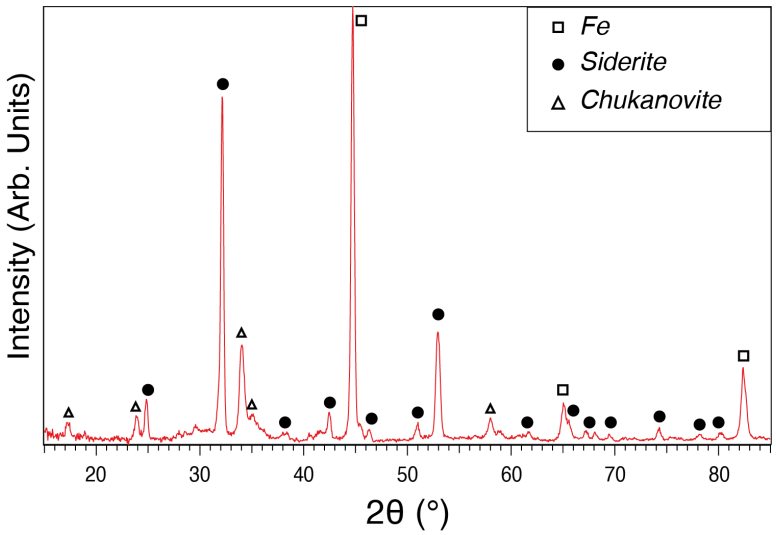

Figure 4.29: GIXRD diffractogram (acquired at α=3 °, CuKα source λ=0.154 nm) and of PTFE substrate immersed for 24 hours in CO_2-saturated 0.01 M $FeCl_2$ + 0.001 M $MgCl_2$ solution (T = 80°C, P_{CO_2}=0.54 bar, pH= 6.8) in jacketed glass cell setup.

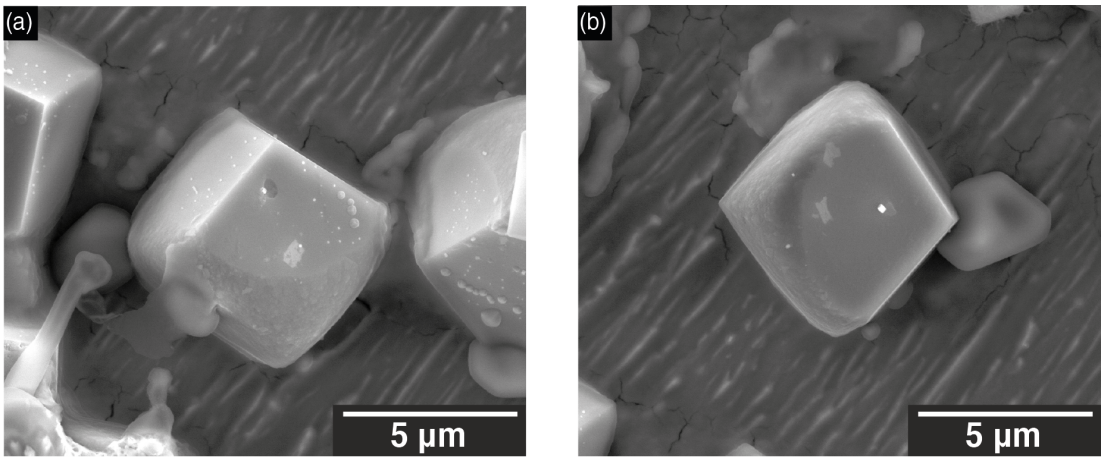

Figure 4.30: SEM images of siderite ($FeCO_3$) crystallites formed on Fe substrate after 24 hours of immersion in CO_2-saturated 0.01 M $FeCl_2$ + 0.001 M $MgCl_2$ solution, (T = 80°C, P_{CO_2}=0.54 bar, pH= 6.8) in jacketed glass cell setup.

4.3.7 Summary

The influence of number of factors on siderite crystal habit has been studied in this chapter. The factors investigated include: Fe^{2+} concentration, NaCl concentration, addition of Ca^{2+} and Mg^{2+}. It was found that these factors can possibly alter siderite crystal habit. Figure 4.31 presents a summarised illustration of the influence of each factor, which are:

- **Increase in Fe^{2+} concentration:** it was found that increasing [Fe^{2+}] results in a change from rhombohedral to cylindrical shape that further elongates with the increase in [Fe^{2+}]. This is due to stabilising {*hk*0} surfaces at higher [Fe^{2+}]
- **Increase in NaCl concentration:** the increase in [NaCl] have a similar influence to the increase in [Fe^{2+}] where rhombohedral habit changed to cylindrical habit. However, such an influence does not seem to be as strong as the increase in [Fe^{2+}]. Further work is required to understand the influence of Na^+ and Cl^- ions separately on the siderite crystal habit, as both of these ions can have a contribution in the change of the crystal habit.
- **Addition of Ca^{2+}:** this resulted in formation of $Fe_xCa_yCO_3$ solid solution phase.
- **Addition of Mg^{2+}:** addition of the same concentration of Mg^{2+} as Ca^{2+} has not resulted in a similar shape. In fact, siderite crystal habit remained the same before and after the addition of Mg^{2+}.

The observed results has been compared with ab initio modelling of siderite crystal habit. Similar result is observed in the model and experimental results as the increase in Fe^{2+} concentration changes the habit from rhombohedral to cylindrical habit. Controlling the siderite crystal habit can be key to improve

forming more protective scale with less susceptibility to dissolution and breakdown. Being able to link theoretical models to experimental observation is crucial to help achieving the goal of forming protective scales.

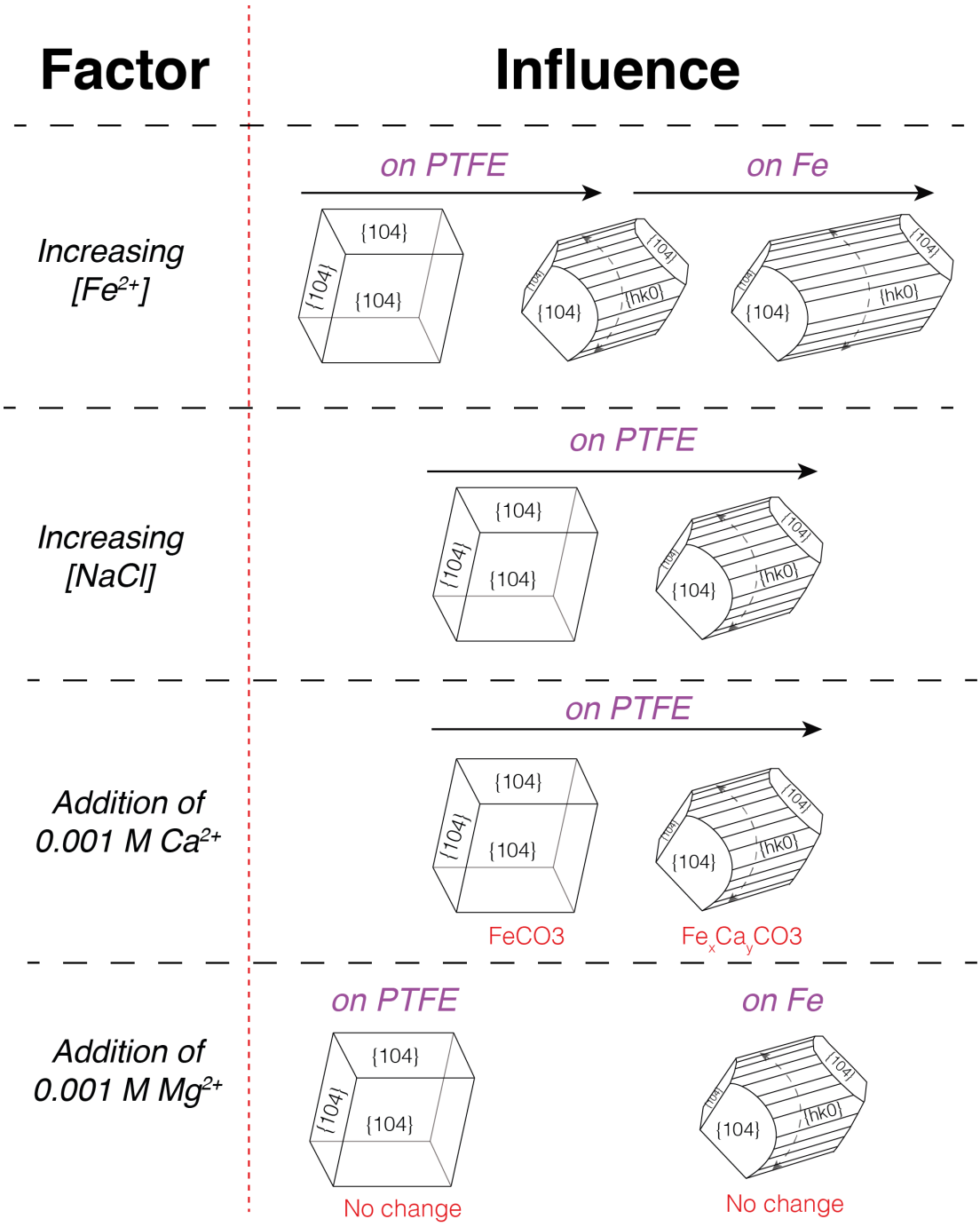

Figure 4.31: Summary of the influence of factors investigated in this chapter on siderite ($FeCO_3$) crystal habit.

Chapter 5.

Impact of Temperature and Pressure on Sweet Scale Habit: Implementation and Exploitation of Autoclave Facility

5.1 Introduction

Iron carbonate ($FeCO_3$) is identified as the main corrosion product formed under sweet environment and can offer significant protection against corrosion. It was reported by a number of authors that higher temperature, pH and CO_2 partial pressure can result in a formation of compact, dense and protective layer of siderite [86, 105, 204, 205]. Others reported a porous or non-protective layer of siderite at lower temperatures (<50°C) and pH [67, 86]. Although a more protective film forms at higher temperature and pressure, some studies suggested that it can lead to an increase in localised corrosion issues [103, 183]. Despite the number of studies focusing on sweet scale formation, scale formation mechanisms and the degree of protection at higher pressures and higher temperatures (HPHT) has received less attention.

In addition, chukanovite $Fe(OH)_2CO_3$ has been observed in a few studies alongside siderite [5,97,206,207]. Magnetite has been also reported to be one of the scale components, specially at higher temperatures (>120°C) [24, 115, 188]. The presence of magnetite can be due to oxygen ingress to the experimental setup at temperatures < 150°C [114,208]. However, at temperatures above >200 °C, it is believed that magnetite is the dominant scale component replacing siderite [94].

Ab Initio modelling to predict siderite crystal habit, as mentioned previously in Chapter 4, showed an influence of increasing iron chemical potential ($\Delta\mu Fe$) (analogous to increasing $[Fe^{2+}_{(aq)}]$) on changing the crystal habit. It is also possible to express this change as a function of CO_2 chemical potential ($\Delta\mu CO_2$), as shown in Figure 5.1. Therefore, according to the model, it is possible that the change in CO_2 concentration can result in a change of siderite crystal habit.

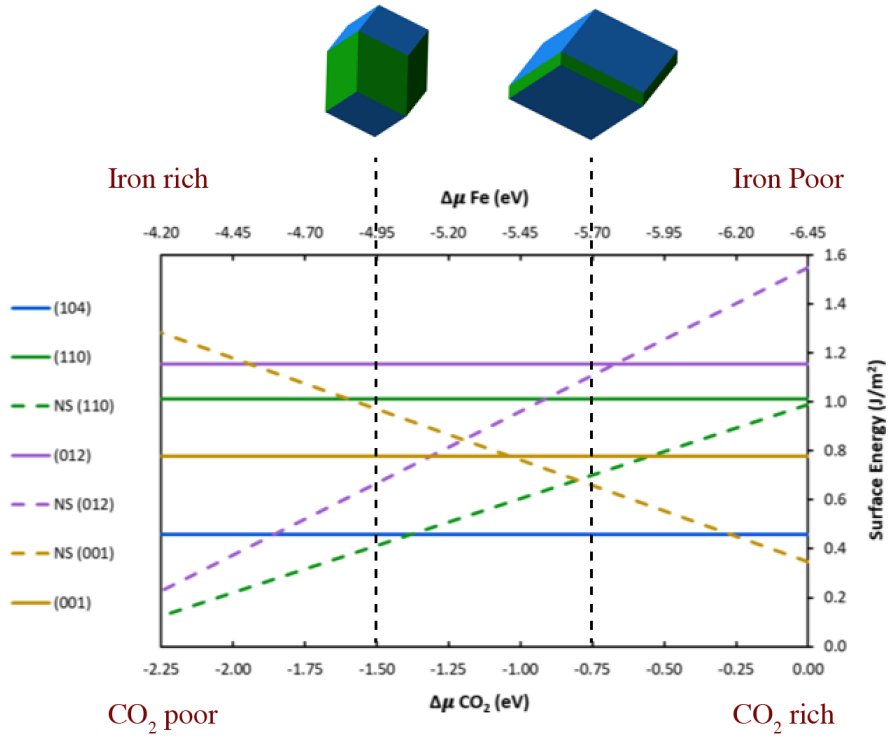

Figure 5.1: Computed surface free energies of formation of siderite ($FeCO_3$) surfaces plot as function of $\Delta\mu$Fe and $\Delta\mu CO_2$. Predicted siderite crystal habits are shown at the top of the plot, at $\Delta\mu$Fe= -5.70 eV, $\Delta\mu CO_2$= -0.75 eV (rhombohedral) and $\Delta\mu$Fe= -4.95 eV, $\Delta\mu CO_2$= -1.50 eV (cylindrical) [196].

Given the above, this chapter focuses on the impact of changing the temperature and pressure on scale formation and siderite crystal habit under a controlled sweet environment. Specifically, the targeted ranges of temperature and CO_2 partial pressure change are between T= 80°C - 150°C , and P_{CO_2} = 0.5 - 4 bar, respectively. Conditions within this temperature and pressure range can be encountered in the oil and gas industry [209]. An autoclave facility is implemented to perform the experiments and the setup/procedure is optimised to obtain more reliable results. The scale formed after 24 hours of immersion is characterised by different techniques: scanning electron microscopy (SEM), focused ion beam (SEM-FIB), and grazing incidence x-ray diffraction (GIXRD). The corrosion behaviour is monitored here by electrochemical measurements using linear polarisation resistance (LPR) as well as post-immersion weight loss measurements (WL) after removal of the

scale. By employing these techniques, corrosion scale components, crystal habit and their protectiveness is determined. Figure 5.2 summarises the operating conditions of experiments performed in this chapter.

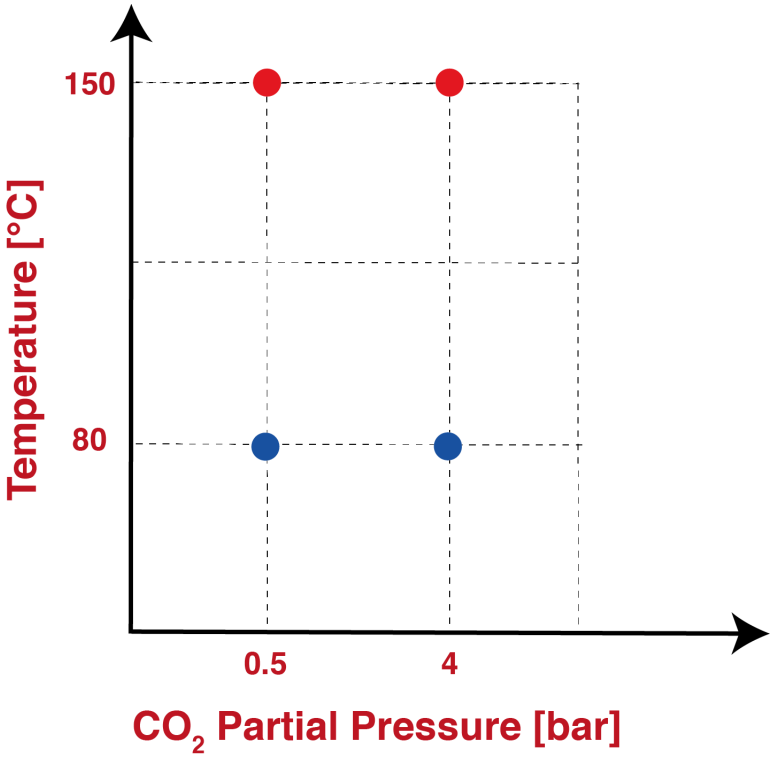

Figure 5.2: 2-D parameter plot illustrating experimental conditions explained in this chapter.

5.2 Experimental Details

5.2.1 Material and sample preparation

High purity Fe discs (depth $\sim$ 4 mm) were cut and polished as described in Chapter 4.2.1. The back face of the sample was spot welded to a Ni-Cr wire to allow electrical connection for electrochemical measurements. The sides and the back face of the Fe sample were coated with 45 stopping-off lacquer (supplied by MacDermid plc) to ensure only one surface is exposed to the solution. For samples used for weight loss corrosion rate analysis, the samples were attached to a PTFE tube that was secured in the testing autoclave.

5.2.2 Experimental setup and operating conditions

Two Hastelloy pressure vessels (Parr Instrument Model No. 4760) were used for this work, each with a capacity of 0.6 L. The first was used to prepare the solution to the required conditions and the second one to run the immersion of the Fe substrate following solution transfer.

Detailed procedure for running the autoclave experiments considering practical challenges normally faced when using pressure vessels and operating at HPHT conditions is discussed in Section 5.3. The Fe substrate was immersed in CO_2-saturated 0.1 M NaCl solutions at four different operating conditions at a temperature range of: T= 80°C - 150°C and CO_2 partial pressures range of: P_{CO_2}= 0.5 bar - 4 bar. Table 5.1 outlines the experimental operating conditions under which immersion was performed in this chapter. From henceforth, the four conditions will be written as T(80)/P_{CO_2}(0.5), T(80)/P_{CO_2}(4), T(150)/P_{CO_2}(0.5), and T(150)/P_{CO_2}(4), as shown in Table 5.1.

Table 5.1: List of operating temperature, CO_2 partial pressure, and total pressure for each immersion experiment performed in this chapter of Fe substrate in 0.1 M CO_2-saturated solutions.

No.	Temperature (°C)	CO_2 Partial Pressure (bar)	Total Pressure (bar)	Shorthand
1	80	0.5	1	$T(80)/P_{CO_2}(0.5)$
2	80	4	4.5	$T(80)/P_{CO_2}(4)$
3	150	0.5	5.2	$T(150)/P_{CO_2}(0.5)$
4	150	4	8.7	$T(150)/P_{CO_2}(4)$

5.2.3 Corrosion rate measurements

Corrosion rates were estimated by electrochemical linear polarisation resistance (LPR) and weight loss measurements (WL). The electrochemical measurements were carried out using Gamry instruments (Interface 1000) potentiostat. The sample was polarised to $\pm$ 10 mV from open circuit potential (OCP) at a scan rate of 0.5 mV/s. The solution OCP was measured in between those LPR measurements. For corrosion rate measurements by WL, the samples were weighed after scale removal using Clark's solution for a total of 1 min.

5.2.4 Surface characterisation

The surfaces of the immersed samples were characterised post immersion using GIXRD, SEM and FIB-SEM. GIXRD measurements were undertaken at an incidence angle α_i = 3 and 6° over a range of 2θ = 15° - 85° using Philips X'Pert MPD diffractometer. SEM images were taken using FEI Quanta 650 FEG-SEM and FIB-SEM imaging was carried out using FEI Quanta 3D FEG-SEM.

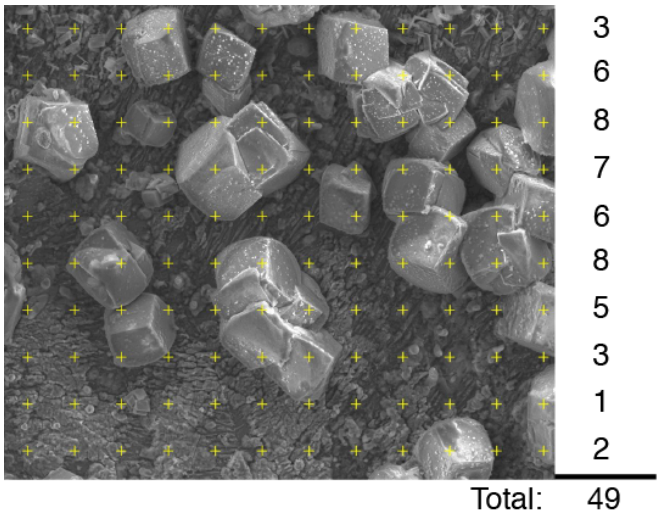

Figure 5.3: An example of point count analysis performed on an SEM image of Fe substrate partially covered with corrosion scale post-immersion in 0.1 M NaCl CO_2-saturated solution at T = 80°C and P_{CO_2} = 4 bar for a total of 24 hours.

In order to determine scale coverage on the surface of immersed Fe samples, point count analysis was used [210]. The analysis was undertaken by placing a grid on SEM images as illustrated by crosses in Figure 5.3. The scale coverage was then estimated by counting the number of crosses that lie on a scale and dividing it by the the total number of grid crosses. The analysis was done using 20 SEM images at a fixed magnification (1000x) from random locations on each surface. The grid placed on the surface has a total of 120 intercept points (crosses). A higher number of crosses will increase the accuracy of the scale coverage analysis. However, decreasing the grid size to produce, for example, 240 intercept points will only result in an error within $\sim$ 3%. All of this analysis was performed using Fiji Image J software [211]. In addition to surface coverage estimation, siderite average crystallite size was estimated from 5 crystals in each SEM image, and a total of 100 crystals from each surface.

5.3 Implementation of Autoclave Facility: optimising the experimental setup and procedure

There are several challenges one faces experimentally when studying CO_2 corrosion and scale formation, especially at higher temperatures and pressure conditions. The potential concerns of experiments performed in sweet environments at HPHT conditions include:

- **Oxygen content**: low levels of oxygen are required before immersion to avoid any oxygen contribution in the corrosion process or scale formation.
- **CO_2-water equilibrium at t = 0 h**: it is difficult to reach the equilibrium at the beginning of immersion, as it common to heat and pressurise the vessel to the desired experimental condition after solution transfer to test vessels.
- **Post-immersion sample handling**: exposure of samples to air post-immersion can modify the formed scale, especially knowing that carbonate scales are prone to oxidation [88, 114].

Experimental practices by others performing experiments in HPHT conditions includes: exposure of CO_2 saturated solutions to air prior to immersion, insufficient purging period to lower oxygen content, and non-cautious handling of the sample post-immersion (e.g.[82, 107]). Therefore, the experimental set-up and procedure was designed considering these factors and minimising their influence on the obtained results. These considerations are discussed below by explaining the developed experimental procedure before, during and after immersion (Section 5.3.1). Furthermore, grounding-

related issues were also considered for electrochemical measurements (Section 5.3.2).

5.3.1 Experimental procedure

This section discusses the operating procedure of autoclave experiments, taking into account minimising oxygen content in the system, CO_2-system reaching near equilibrium conditions prior immersion and preserving the scale post-immersion. Figure 5.4 shows a schematic diagram of the overall setup of the two vessels used for solution preparation and immersion experiments.

Firstly, 0.5 L of 0.1 M NaCl solution was poured into the prep-vessel shown in Figure 5.4 before it is sealed. The solution was then bubbled by high purity CO_2 gas (99.95%) for $\sim$ 16-24 hours. Oxygen concentration measurements [$O_{2(dissolved)}$] were measured regularly using an electrochemical oxygen sensor (O_2 sensor, Orbisphere A1100). Solution can only be transferred after reaching the desired $O_{2(dissolved)}$ concentration of < 10 ppb. During the period of solution bubbling in the prep-vessel, CO_2 gas is flowed through the test-vessel to remove any O_2 from the system. In addition, all the lines were also filled with CO_2 to ensure removal of oxygen from the whole system network.

The samples were immersed at two different CO_2 partial pressures of P_{CO_2} = 0.54 and 4 bar. Also, at a different temperatures of T=80 and 150 °C. Figure 5.5 shows a flow diagram describing the operating procedure for each experiment.

In all experiments, the CO_2-saturated solution in the prep-vessel is heated prior to solution transfer to 80°C using a hot plate. For experiments running at 80°C, the solution temperature was maintained after solution transfer to the test-vessel using Parr instruments temperature controller (4838 Reactor Controller) and electric heater. On the other hand, the CO_2-saturated solution is heated from 80°C to 150°C after transfer to the test-vessel for immersion experiments at higher temperatures.

In order to minimise the required time for the solution to reach equilibrium once it is transferred to the test-vessel at the beginning of immersion (t = 0h) for experiments running at P_{CO_2} = 4 bar, the prep-vessel was pressurised by CO_2 gas to approximately 8 bar before 2 hours of solution transfer. The extra pressure is required as it will be distributed between the two vessels when opening the connecting valve. Once the solution was transferred to the test-vessel, the valve is closed and the total pressure is checked. Extra CO_2 gas can be supplied directly to the test-vessel to pressurise the system to the desired pressure, if required. Finally, all valves on the test-vessel were closed and immersion starts.

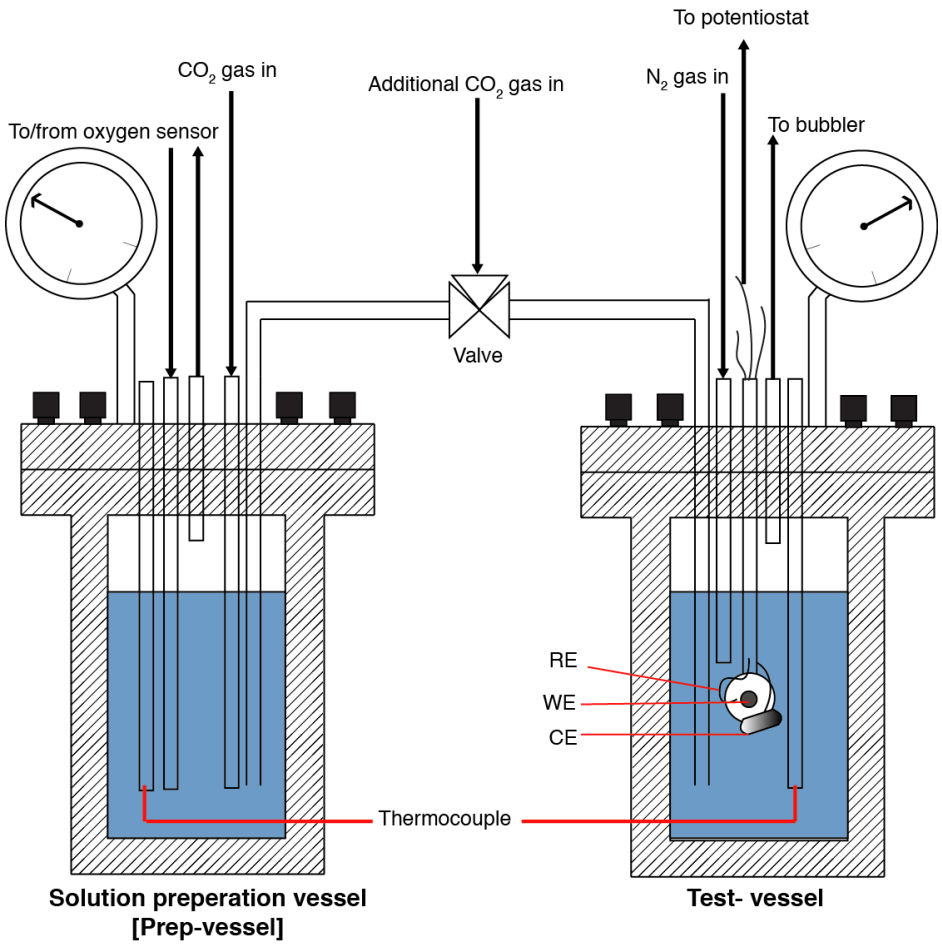

Figure 5.4: Schematic representation of HPHT autoclave experimental set-up.

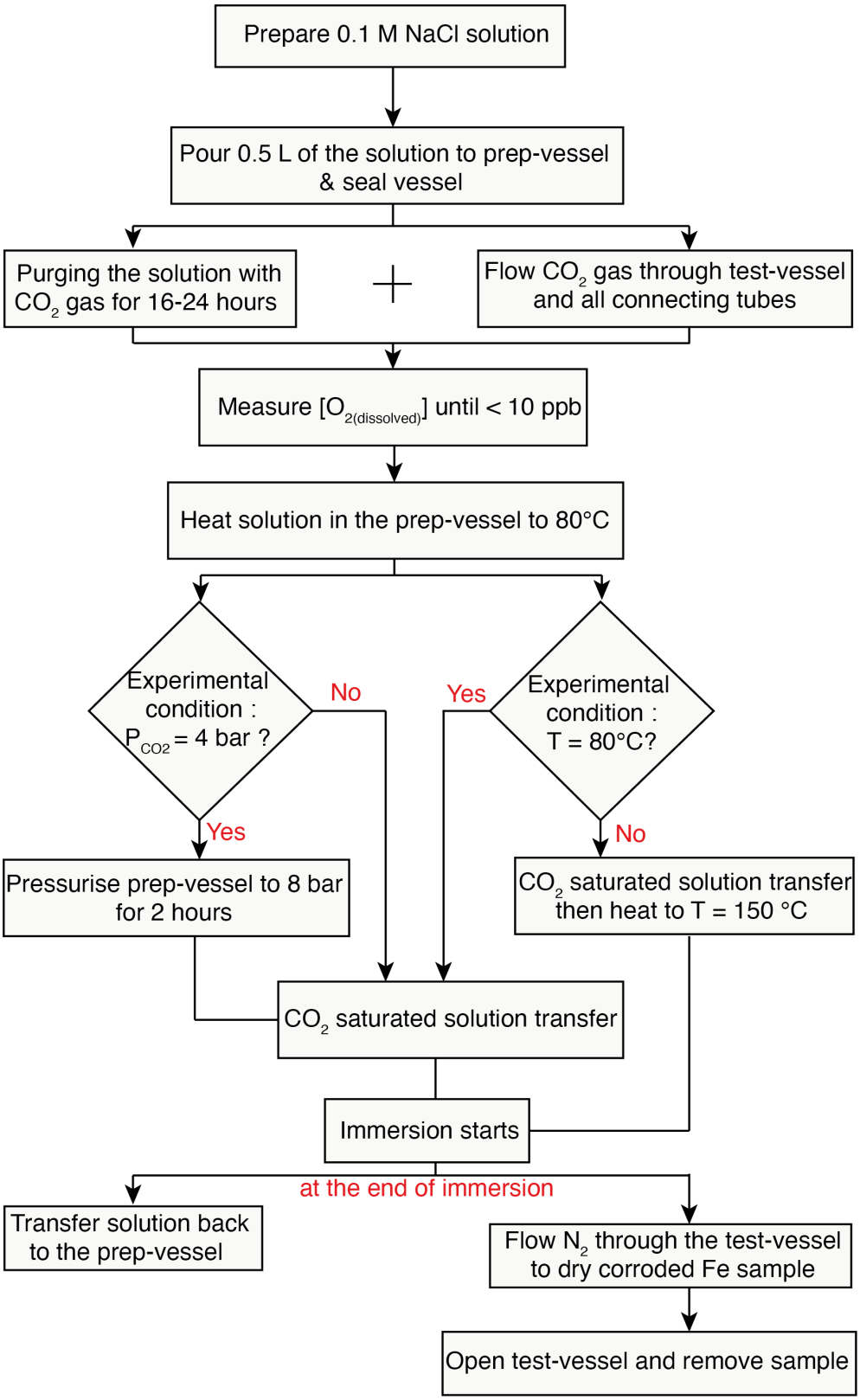

Figure 5.5: Flow diagram of the experimental procedure followed in HPHT experiments carried out in this chapter.

After starting the immersion, the prep-vessel, which is now isolated from the test-vessel after closing the connecting valve, was depressurised and CO_2 gas was flowed through the vessel to ensure low oxygen in the vessel as it was used to transfer the solution back at the end of the experiment. By the end of the immersion period of 24 hours, the solution was transferred back from the test-vessel to the prep-Vessel using the pressure difference between the two vessels. Then N_2 was flowed through the test-vessel for 5-15 minutes to dry the sample. After that, the test-vessel is opened to remove the sample and it is further flushed with N_2 to ensure drying it.

Since the pressure difference between the two vessels in experiments running at $T(80)/P_{CO_2}(0.5)$ was not sufficient to transfer the solution from the test-vessel to the prep-vessel, N_2 is also used for the purpose of solution transfer in this case. The same procedure as described above was followed to remove the sample.

5.3.2 Other issues: ground loops and pH measurements

Additional care must be taken when performing electrochemical measurements in grounded cells such as autoclaves [212]. In order to properly obtain electrochemical measurements from grounded cells, measuring equipments must be operating in 'floating mode' [213]. Problems associated with the use of grounded cells can be due to presence of two ground points [214]. Ground loops can exist in this case leading to noise and current fluctuations in the electrochemical measurements. Such interference with higher currents can lead to erroneous results by polarising the working electrode (Fe sample). Therefore, it is extremely important that the equipment operates in floating mode where it is allowed to float with respect to earth ground since the autoclave vessel surface can be at earth ground [215].

Some modern potentiostats allow floating mode operation where the circuits

in the equipment are designed to switch to an internal floating ground rather than earth ground. It is also possible to use galvanic isolation dongles that can isolate the potentiostat and the connected electrochemical system from the computer's ground and hence operates in floating mode [216]. Floating Gamry instruments (Interface 1000) potentiostat is used to perform all electrochemical measurements for this work. To ensure reliable measurements, preliminary experiments were conducted and compared with a typical non-grounded glass-cell setup and the results obtained from the two setups were consistent.

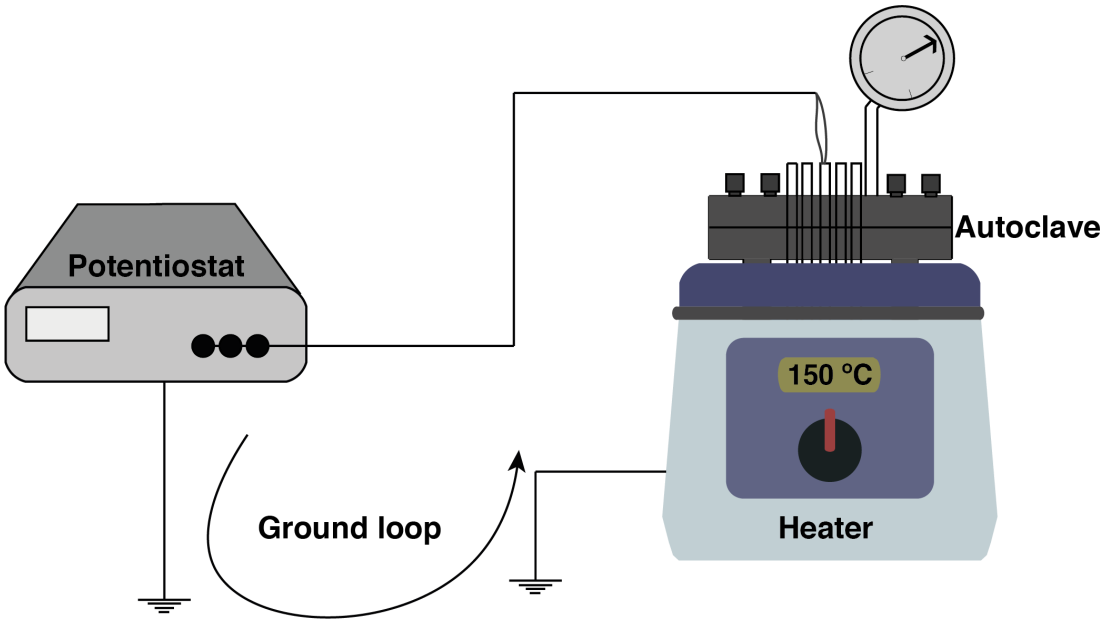

Figure 5.6: Schematic illustration of ground loop circuit in an autoclave setup connected to grounded instrument (potentiostat)

As regards to the pH measurements, it is technically difficult to employ pH probes for *in situ* monitoring at high temperatures (specially >100°C). In order to accurately measure the pH at HPHT conditions, it is required to use a chemically and thermally stable probe/sensor [217, 218]. In addition, lack standard buffer solution data at high temperatures magnifies the margin of errors at this range of operating conditions [219, 220]. Therefore, pH measurements were not performed in this work and the pH values were estimated using Promax and PHREEQC software as discussed in section 5.4.1.

5.4 Results and Discussion

5.4.1 Determination of solution pH

As mentioned in section 5.3.2, the pH values were not obtained experimentally. An estimation of the pH values using Promax and PHREEQC software are shown in Table 5.2, along with other solution species composition [221,222].

Table 5.2: Dissolved concentrations and pH estimation using Promax and PHREEQC software of 0.1 M NaCl CO_2-saturated solutions at different experimental conditions of temperature and pressure [221,222].

Solution 1	T= 80°C, P_{CO_2}= 0.5 bar, and P(total)= 1.0 bar	
Solution species (mol/L)	**Promax**	**PhreeqC**
$[CO_2]$	0.0059	0.0066
$[CO_3^{2-}]$	1.29e-10	2.09e-10
$[H^+]$	5.7e-5	6.9e-5
pH	4.24	4.16
Solution 2	T= 80°C, P_{CO_2}= 4 bar, and P(total)= 4.5 bar	
Solution species (mol/L)	**Promax**	**PhreeqC**
$[CO_2]$	0.0438	0.0482
$[CO_3^{2-}]$	1.28e-10	2.04e-10
$[H^+]$	1.5e-4	1.9e-4
pH	3.82	3.72
Solution 3	T= 150°C, P_{CO_2}= 0.5 bar, and P(total)= 5.2 bar	
Solution species (mol/L)	**Promax**	**PhreeqC**
$[CO_2]$	0.004	0.005
$[CO_3^{2-}]$	8.99e-11	3.02e-10
$[H^+]$	2.8e-5	2.6e-05
pH	4.55	4.59
Solution 4	T= 150°C, P_{CO_2}= 4 bar, and P(total)= 8.7 bar	
Solution species(mol/L)	**Promax**	**PhreeqC**
$[CO_2]$	0.0286	0.0322
$[CO_3^{2-}]$	8.98e-11	1.87e-10
$[H^+]$	7.42e-5	8.50e-05
pH	4.12	4.07

These estimates are used to determine initial pH values for the different experimental conditions of pressure and temperature. Generally, initial pH varies between 3.8 to 4.5 under all experimental conditions. From this table it can be seen that the pH increases with the increase in temperature, at a constant CO_2 partial pressure. The increase in temperature reduces solubility of CO_2 in the solution leading to such an increase in pH [223]. On the other hand, the pH decreases as the CO_2 partial pressure increases, and this is due to the increase in amount of dissolved CO_2 concentration in solution within this pressure range [41]. In terms of the results obtained from PHREEQC and ProMax, the calculated values are in general agreement with a difference of less than 3% in pH estimations.

5.4.2 Corrosion rate analysis

Figure 5.7 shows corrosion rate profiles of high purity Fe samples immersed in 0.1 M NaCl CO_2 saturated solutions at different temperatures (T= 80°C and 150°C) and CO_2 partial pressures (P_{CO_2} = 0.5 bar and 4 bar). CR rates presented here were calculated using LPR. At immersion time t = 0 h, where no scale formation is expected on Fe surface, the corrosion rate was highest for samples immersed at T(150)/P_{CO_2}(4) and lowest at T(80)/P_{CO_2}(0.5). This indicates that under non-scaling conditions, an increase in both temperature and CO_2 partial pressure results in a rise in corrosion rate [123].

Over the 24 hours of immersion, the CR of the Fe sample immersed in T(80)/P_{CO_2}(0.5) remained at $\sim$ 4 mm/yr throughout the immersion period. Under the other three conditions, calculated corrosion rates decreased over time suggesting a formation of a semi-protective corrosion scale resulted in this decrease in corrosion rate. After the 24^{th} hour of immersion, corrosion rate was the lowest for the sample immersed at T(150)/P_{CO_2}(4) and the highest at T(80)/P_{CO_2}(0.5). This suggests formation of a more protective films at both higher temperatures and CO_2 partial pressures after 24 hours of immersion.

In addition, the fact that corrosion rates remained high throughout the immersion period at T(80)/P_{CO_2}(0.5) suggest either no scale or non-protective scale formation.

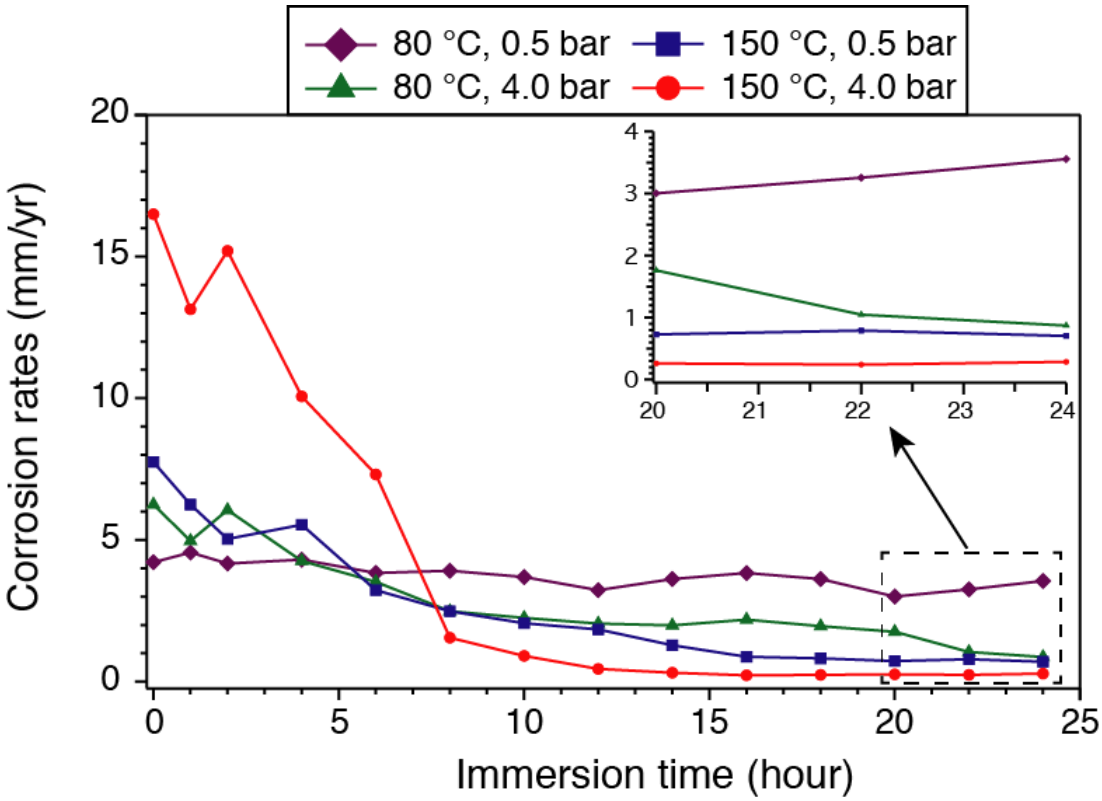

Figure 5.7: Average corrosion rates estimated by LPR, assuming Stern-Geary coefficient β= 52 mV, of Fe substrates immersed in 0.1 M NaCl CO_2 saturated solution (T = 80°C - 150°C, P_{CO_2} = 0.5 - 4 bar) in the autoclave as a function of immersion time of 24 hours.

Table 5.3 lists corrosion rates determined from weight loss measurements along with the average corrosion rate estimated from LPR over the 24 hour immersion. It is seen that average corrosion rate estimated from WL for samples immersed in solutions at T(80)/P_{CO_2}(0.5) were highest, and lowest for T(150)/P_{CO_2}(4). This is a similar trend to estimated final corrosion rates in Figure 5.7.

Comparing the corrosion rate estimates from WL and average LPR corrosion rates, the values are in general agreement apart from the sample immersed at T(150)/P_{CO_2}(4). The average corrosion rate from LPR data at this condition is

the highest (4.76 mm/yr) of the four due to its initially high corrosion rates as seen from Figure 5.7 where it started at $\sim$ 16 mm/yr before dropping drastically to $\sim$ 2 mm/yr within 7 hours of immersion. The significant difference between estimates from LPR and WL can be due to irreproducibility in the kinetics of corrosion rate reduction usually observed at short immersion times in CO_2 systems. Such irreproducibility has been also observed by Joshi et al. work, where they reported lack of quantitative reproducibility in both corrosion rates and scale formation kinetics within 72 hours of immersion in CO_2 saturated solutions at T= 80°C, P_{CO_2} = 0.5 bar and pH = 6.8 [5].

Table 5.3: Estimated average corrosion rate by WL and LPR of Fe substrates immersed for 24 hours in 0.1 M NaCl CO_2 saturated solution (T = 80°C - 150°C, P_{CO_2} = 0.5 - 4 bar) in the autoclave.

Experimental condition	CR (weight loss)	Average CR (LPR)
T= 80°C P_{CO_2}= 0.5 bar	3.92	3.77
T= 80°C P_{CO_2}= 4 bar	3.49	2.98
T= 150°C P_{CO_2}= 0.5 bar	3.14	2.82
T= 150°C P_{CO_2}= 4 bar	1.80	4.76

5.4.3 Surface analysis

Figure 5.8 shows GIXRD patterns and SEM images of the samples immersed in CO_2 saturated 0.1 M NaCl solutions at different pressures and temperatures. At T(80)/P_{CO_2}(0.5) (Figure 5.8 a), no scale has formed on the Fe surface as the GIXRD pattern shows only three peaks attributed to α-Fe at 2θ= 44°, 65° and 82°(ICDD-PDF 04-007-9753). This is also seen from the corresponding SEM image where it shows a scale-free Fe surface. This observation is consistent with nearly constant CR data presented previously in Section 5.4.2 and Figure 5.7.

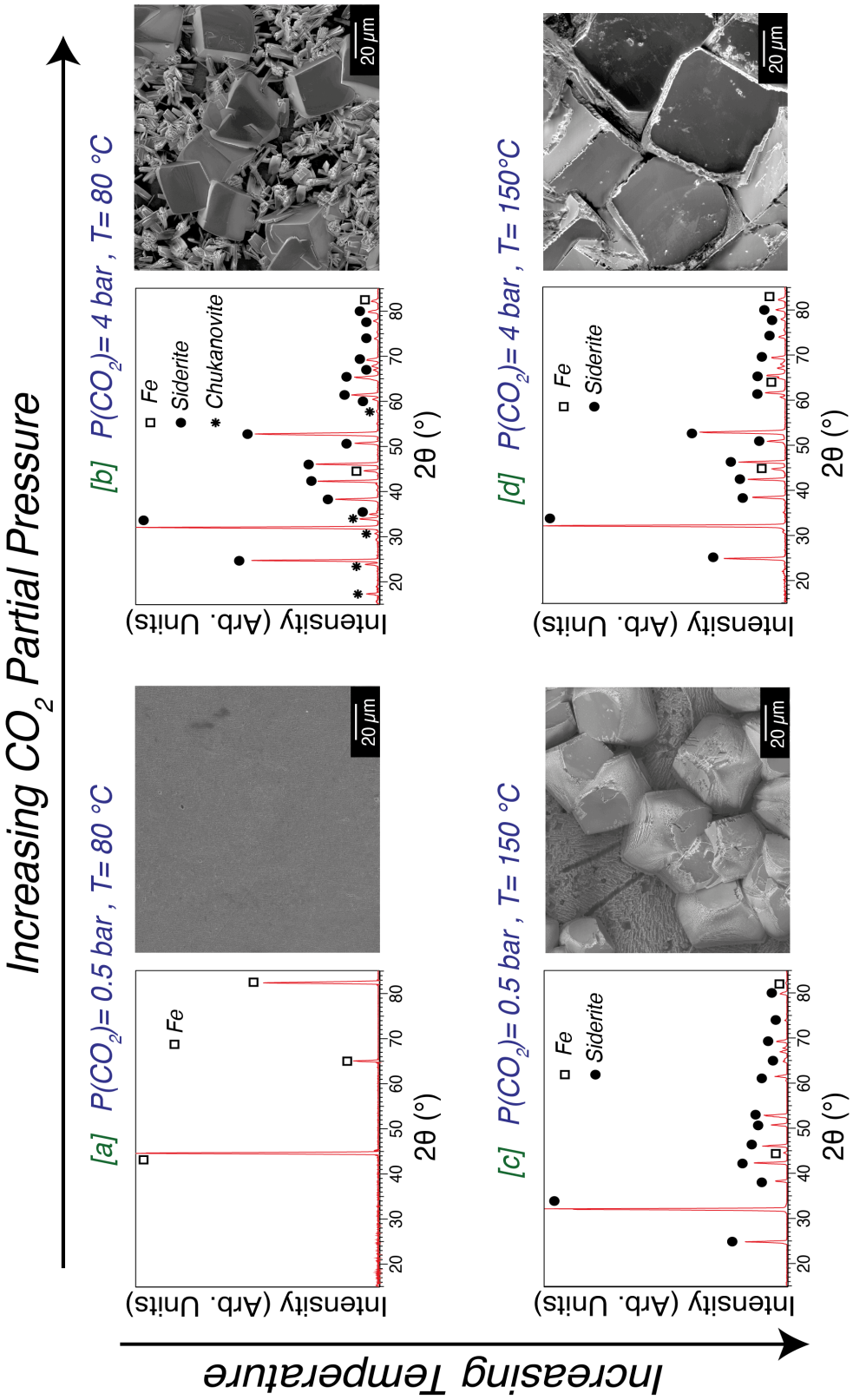

Figure 5.8: GIXRD diffractograms (acquired at α = 6°, CuKα source λ=0.154 nm) and corresponding SEM images of Fe substrates immersed in 0.1 M NaCl CO_2 saturated solution (T = 80°C - 150°C, P_{CO_2}= 0.5 - 4 bar) in the autoclave after 24 hours of immersion.

A corrosion scale has formed on the corroded Fe surface in the three other cases. At T(80)/P_{CO_2}(4)(Figure 5.8 b), the GIXRD diffraction pattern shows a mixed layer of siderite and chukanovite has formed on the Fe surface. This is also seen from the corresponding SEM image that shows platy chukanovite crystals and siderite crystals. At T(150)/P_{CO_2}(0.5)and T(150)/P_{CO_2}(4)(Figure 5.8 b and d), the diffraction pattern suggest formation of exclusively siderite scale on the corroded Fe surface. However, corresponding SEM images shows a different crystal habit of siderite formed under each condition. This is discussed in further details in the section below.

5.4.4 Influence of CO_2 partial pressure on siderite crystal habit

This section focuses on the changes in siderite crystal habit as a function of increasing CO_2 partial pressure, which in turn increases the amount of dissolved CO_2 in the solution. Figure 5.9 (a) shows siderite crystal habit to be as trigonal pyramidal caps with micro-faceted cylinders at T(150)/P_{CO_2}(0.5). A schematic representation of the habit formed in this condition is shown in Figure 5.9 (b) with facet orientation labelled according to the results presented previously in Chapter 4. From this schematic representation, {hk0} micro-faceted cylinders are capped by {104} pyramidal caps.

By increasing CO_2 partial pressure to 4 bar but at T= 80°C (Figure 5.9 c and d), {hk0} facets shrink reducing the size of the cylinder and the crystal habit becomes nearly rhombohedral. At T(150)/P_{CO_2}(4) crystal habit changes to a rhombohedral shape as shown in Figure 5.9 (e). However, {hk0} facets still exist but less developed to only appear at the edges of rhombohedral shaped crystals. A schematic representation of this crystal habit is shown in Figure 5.9 (f).

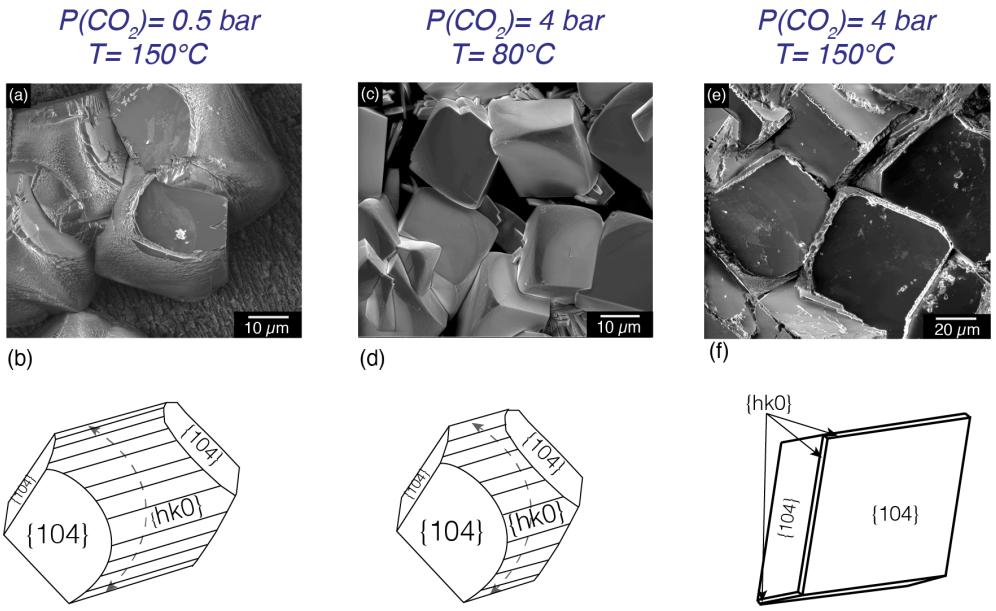

Figure 5.9: SEM images showing siderite crystal on Fe sample immersed in 0.1 M NaCl CO_2 saturated water at (a) T(150)/P_{CO_2}(0.5), (c) T(80)/P_{CO_2}(4), and (e) T(150)/P_{CO_2}(4). (b,d,f) Schematic illustration of siderite crystal habit with predicted crystallographic orientation of facets observed in (a,c,e) respectively

As mentioned earlier, siderite crystal habit can be theoretically modelled based on surface energies estimation as a function of CO_2 partial pressure (or $\Delta\mu CO_2$). Comparing the results, the predicted crystal habit change agree with what has been observed experimentally (refer to Figure 5.1). At high CO_2 concentrations, a rhombohedral crystal habit is predicted with S{104} facets separated by a narrow strip of NS{110} surfaces. At a lower CO_2 concentrations, the model predicts an elongation of NS{110} as it becomes more stable forming a hexagonal shaped facets capped by S{104} trigonal-pyramidal caps.

5.4.5 Impact of temperature and pressure on sweet scale coverage and average crystal size

The results will be discussed in two parts in order to simplify the discussion and focus on the influence of each individual factor. Part one will discuss the

impact of temperature on scale formation at constant CO_2 partial pressure. Part two will discuss the impact of CO_2 partial pressure on scale formation at a constant temperature.

Impact of temperature on sweet scale formation

To study the influence of increasing the temperature from 80 °C to 150 °C on scale formation, two sets of experiments can be compared from Figure 5.8. The first set is varying the temperature at constant P_{CO_2} = 0.5 bar and the second set is at constant P_{CO_2} = 4 bar.

At P_{CO_2} = 0.5 bar, increasing the temperature resulted in moving from non-scaled surface at 80°C to formation of siderite layer at 150°C. At 150°C, the increase in corrosion kinetics represented by high initial CR, resulting in higher amounts of Fe^{2+} released from the surface coupled with the decrease in solubility of siderite at higher temperatures, provided scaling conditions for siderite to precipitate and grow on the surface. The formation of such layer confirms the reason behind the decrease in CR at 150°C compared to 80°C where it remained higher as shown in CR data in Figure 5.7.

In the case of varying the temperature at a constant P_{CO_2} = 4 bar, in both conditions at 80°C and 150°C a layer of corrosion scale has formed. However, as shown in Figure 5.10, the area of the surface that is covered with scale is higher at higher temperature with 98% coverage at 150°C compared to 70% coverage at 80°C. This explains why the final corrosion rate value at 150°C is lower in this case. Although at both temperatures scale formation has occurred, the degree of protection and scale coverage is greater at the higher temperatures. Another observation is that chukanovite ($Fe_2(OH)_2CO_3$) no longer appeared in the scale with the increase in temperature to 150°C.

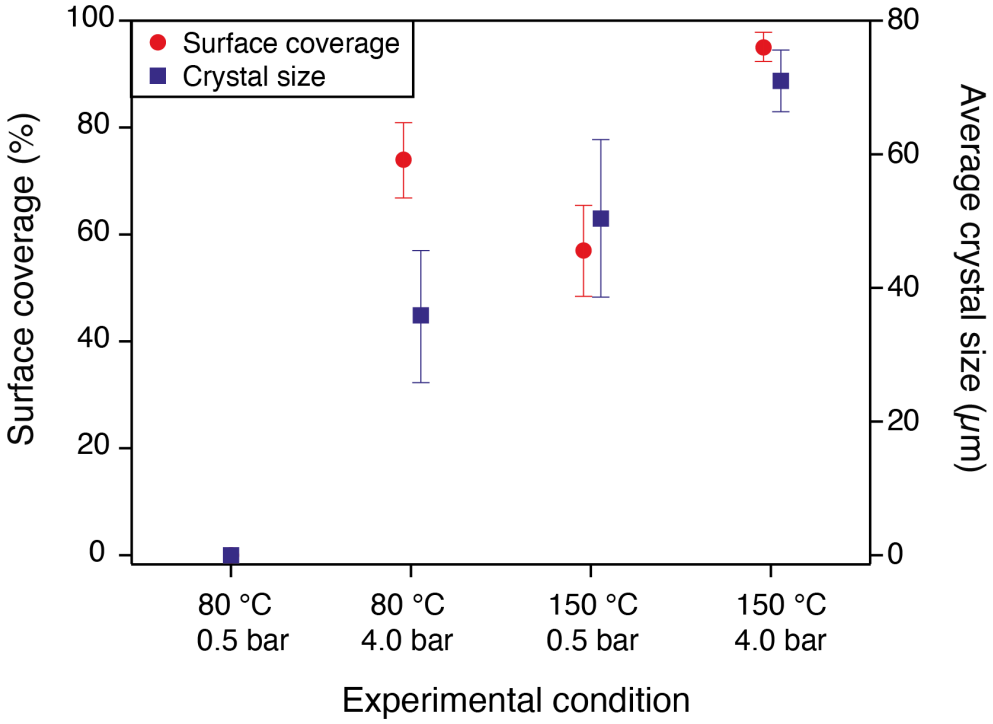

Figure 5.10: Surface coverage and average siderite crystal size estimated by point count analysis of Fe substrates immersed in 0.1 M NaCl CO_2 saturated solution (T = 80°C - 150°C, P_{CO_2}= 0.5 - 4 bar) in the autoclave for 24 hours of immersion. Data are off-setted to clarify the error bars.

Impact of CO_2 partial pressure on sweet scale formation

To study the influence of increasing CO_2 partial pressure on scale formation, two sets of experiments can be compared from Figure 5.8 (a-d). The first set is varying CO_2 partial pressure at a constant temperature T = 80°C and the second set is at T= 150°C. Firstly, at T = 80 °C the increase in CO_2 partial pressure from 0.5 bar where no scales have formed on the surface to 4 bar which resulted in formation of a mixed layer of siderite and chukanovite. In addition, this also resulted in an increase of Fe^{2+} supply from the corroded surface illustrated by higher corrosion rates. Also, the increase in $P(CO_2)$ results in the increase in $CO_{2(dissolved)}$ and $CO_3^{2-}{}_{(dissolved)}$ concentrations. This will lead to higher supersaturation required to thermodynamically promote precipitation $FeCO_3$ and hence scale formation occurs at higher CO_2 partial pressure of P_{CO_2} = 4 bar [68].

In the case of varying the partial pressure in the second set at 150°C, scale coverage increases from $\sim$ 60% at P_{CO_2}= 0.5 bar to 98% at P_{CO_2}= 4 bar. This further indicates that the increase in CO_2 partial pressure promotes scale formation. Note also that the increase in CO_2 partial pressure results also in an increase in average siderite crystal size from 50 μm to 71 μm. Crystal growth is known to be the dominant process at lower supersaturation while nucleation rate increases exponentially at higher supersaturations [67]. It is possible that due to the rapid drop in corrosion rates to lower values at higher P_{CO_2} = 4 bar, led to an increase in crystal growth to larger crystals at this condition compared to lower CO_2 partial pressure.

5.4.6 Chukanovite and its role in corrosion protection

Chukanovite was identified here on Fe surface immersed for 24 hours in 0.1 M NaCl CO_2-saturated solutions at T(80)/P_{CO_2}(4). However, chukanovite no longer appeared in the scale formed at a higher temperature of T= 150°C, where exclusively siderite scale has formed. A possible explanation behind its disappearance at higher temperatures is that changes in local chemistry near the surface due to the increase in temperature hindered formation of chukanovite at such conditions.

Chukanovite is thermodynamically metastable phase compared to siderite at certain conditions [95]. Chukanovite formation has been reported by Joshi et. al [5] on Fe substrate immersed in CO_2-saturated water at the same temperature T= 80°C but at a higher pH= 6.8 and lower P_{CO_2} = 0.5 bar. From their study, chukanovite was no longer observed after 288 hours of immersion and an exclusive layer of siderite is only observed beyond that. Such time-dependent transformation from chukanovite to siderite possibly occurs faster at higher temperatures. Therefore, it is also possible that chukanovite disappeared at earlier stages of immersion (<24 hours) at higher temperatures of T= 150°C.

Exploring GIXRD pattern of chukanovite and comparing it with reference data as shown in Figure 5.11 (a), the peak attributed to (021) plane at 2θ=33.9° appears to be the most intense peak in both the diffraction pattern and reference data. Nonetheless, peaks from (220) and (210) planes at 2θ=17° and 25° respectively, have higher relative intensities compared to the reference data.

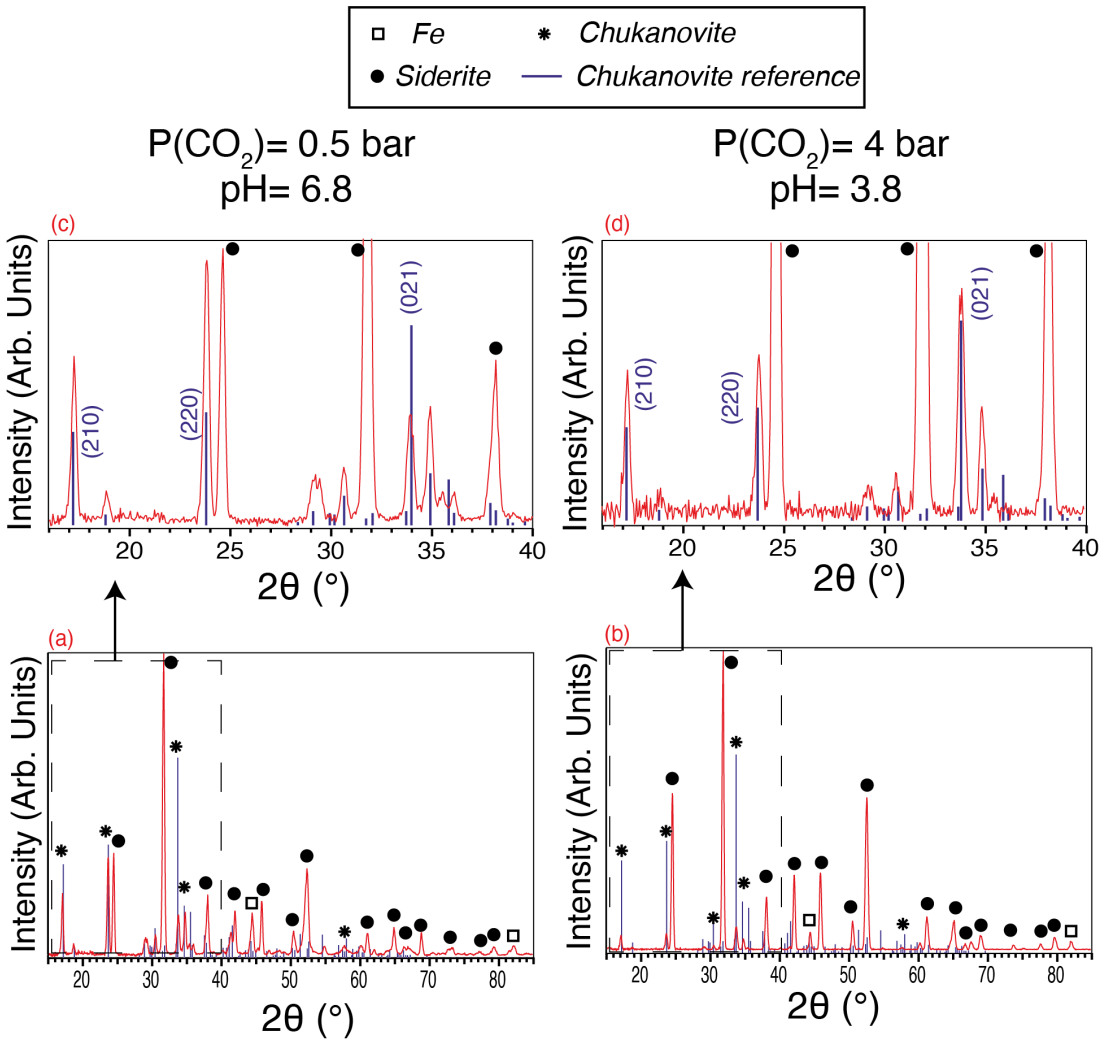

Figure 5.11: GIXRD diffractograms (acquired at α = 3°, CuKα source λ=0.154 nm) of Fe substrate immersed in CO_2 saturated water at T = 80°C, (a) P_{CO_2} = 0.5 bar, pH = 6.8 (reproduced from [149]) and (b) P_{CO_2} = 4 bar, pH = 3.8. Expanded GIXRD diffractograms in the range of 2θ= 15°- 40° are shown in (c,d) for both conditions

Comparing this result with the scale formed on high purity Fe substrate immersed in CO_2-saturated solution at T = 80°C, P_{CO_2} = 0.5 bar and pH = 6.8, where chukanovite is also formed in a mixed siderite/chukanovite layer after 24 hours of immersion [149]. The diffraction pattern, as shown in Figure 5.11 (b), shows a depressed peak, attributed to (021) plane, and the peak attributed to (220) plane is the most intense peak instead. These differences between experimental and reference data can be due to differential absorption of X-ray beam and a degree of preferred orientation [5].

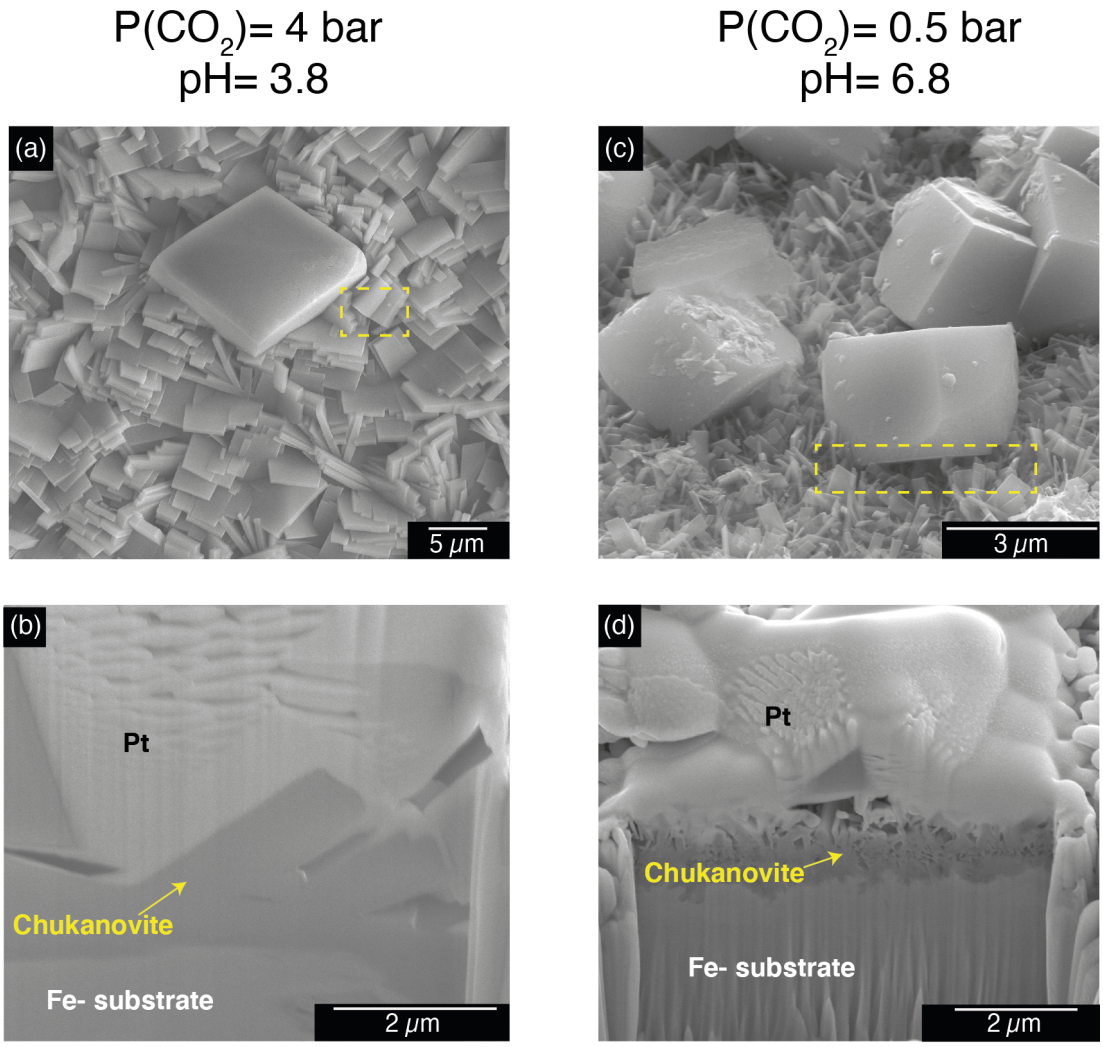

Figure 5.12: Plan view SEM and cross sectional FIB-SEM images of Fe substrate immersed for 24 hours in CO_2-saturated water at T = 80 °C, (a,b) P_{CO_2}= 4 bar, pH = 3.8 (c,d) P_{CO_2}= 0.5 bar, pH= 6.8.

Regarding the difference in chukanovite appearance and morphology between

the two conditions mentioned above, Figure 5.12 shows an SEM and FIB cross-section images of chukanovite platy crystals. It can be seen that chukanovite crystals appears to have larger and thicker plates at P_{CO_2} = 4 bar than the ones formed at P_{CO_2} = 0.5 bar. This is possibly can influence the difference in peak intensities observed between the two conditions.

As regards to corrosion protection, Joshi et al. discussed how chukanovite does not provide any significant protection to the substrates immersed in CO_2-saturated solutions at T= 80°C, P_{CO_2} = 0.5 bar and pH= 6.8 [5]. It appears to be a similar case at higher CO_2 partial pressure, although the chukanovite formed is different in terms of crystal size and thickness. This can be clearly concluded by looking at the amount of scale coverage at T(80)/P_{CO_2}(4) , where it has more coverage than scales formed at T(150)/P_{CO_2}(0.5) , as shown in Figure 5.10. However, a mixed layer of chukanovite/siderite does not provide any extra significant protection compared to only-siderite scale at lower coverage percentage.

5.4.7 Cross-sectional analysis of formed scale

Figure 5.13 shows SEM images of cross-sections across the Fe substrate immersed in solutions at the varied operating temperatures and pressures. At T(80)/P_{CO_2}(0.5) (Figure 5.13 a and b), the cross-section SEM image shows a rough surface uniformly corroded with no scale layer on the surface. Note that black crystal-like features appear on top of all cross-sections SEM images in Figure 5.13. All of these features are from Bakelite mounting resin and should be distinguished from corrosion layers on top of the Fe surface.

On the other extreme at higher pressure and temperature T(150)/P_{CO_2}(4) (Figure 5.13 g and i), the cross-section SEM image shows a compact layer of siderite fully covering the surface of Fe. In the cross-section images of the samples immersed at conditions between those two extremes (Figure 5.13 c-

f), the Fe substrate is partially covered with scale. It can be observed also that the thickness of the scale increases generally with the increase in temperature and P_{CO_2} partial pressure.

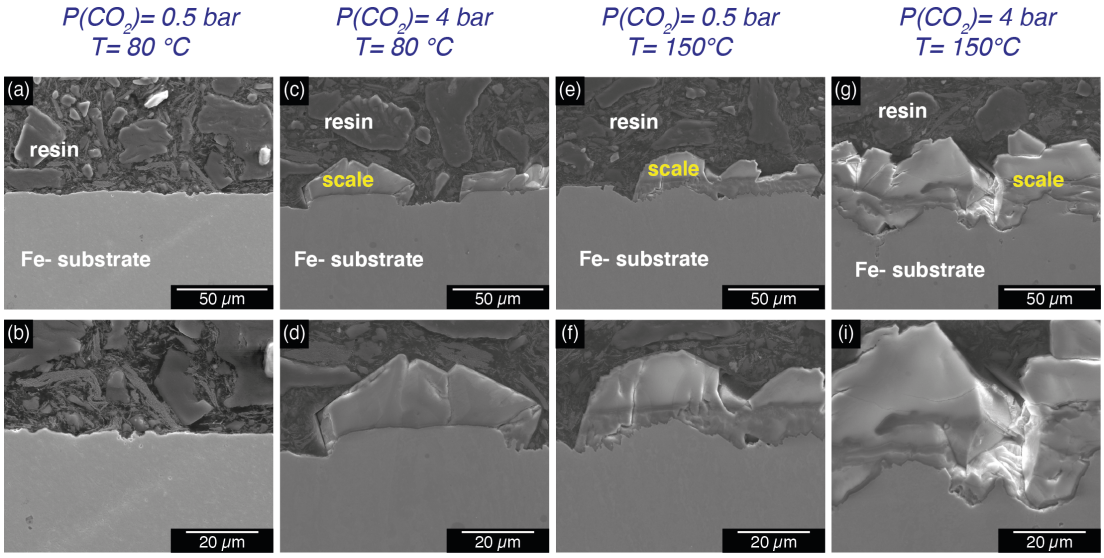

Figure 5.13: Cross sections SEM images of Fe substrates immersed for 24 hours in 0.1 M NaCl CO_2 saturated solution (T = 80°C - 150 °C, P_{CO_2}= 0.5 - 4 bar) in the autoclave.

As regards to the number layers formed observed from these cross-section, the difference in contrast within the scale seen in Figure 5.13 (e-i) suggests formation of a multi-layered scale. In comparison, Figure 5.14 shows SEM images of cross-sections performed on the same samples at T(80)/P_{CO_2}(4) and T(150)/P_{CO_2}(0.5) , but by FIB-SEM. Here only a single layer of scale is observed. FIB-SEM is a preferred technique to obtain cross-sections of the samples with less disruption to the scale. However, it was not practically feasible to use this technique to obtain cross-sections of such thick scales formed, specially at higher temperatures and pressures, at T(150)/P_{CO_2}(4). The alternative method of mounting the samples in resin followed by wet grinding/polishing can result in possible modifications to scale appearance, knowing that carbonate scales are prone to oxidation. Therefore, it might not be suitable to determine whether the scale formed a single or multi-layer from cross-sections obtained in Figure 5.13.

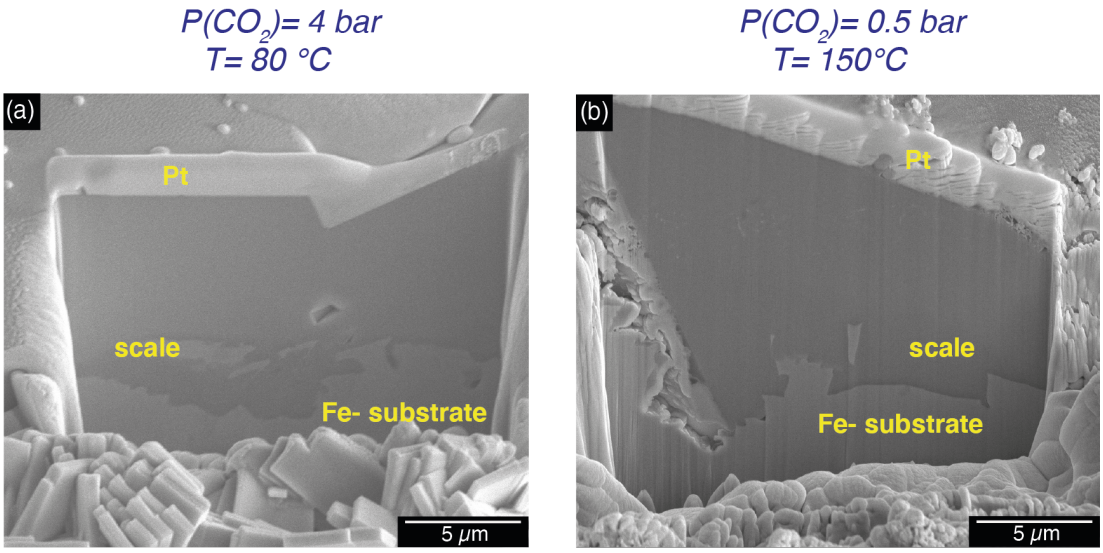

Figure 5.14: Cross sections SEM images of Fe substrates immersed for 24 hours in 0.1 M NaCl CO_2 saturated solution (T = 80°C - 150 °C, P_{CO_2}= 0.5 - 4 bar) in the autoclave.

Looking closely at the cross-sectional SEM images in Figure 5.13, it can be seen that the corroded surface is rougher with the increase of temperature and pressure. Figure 5.15 shows further examples cross-section SEM images from samples immersed in 0.1 M NaCl CO_2 solutions at T(80)/P_{CO_2}(4) (a-b) and T(150)/P_{CO_2}(4) (c-d). At T = 80°C, shallow and wide cavities as shown in Figure 5.15 (a-b) can be seen at areas uncovered by scale. At T = 150°C, as shown in Figure 5.15 (c-d), appears to have similar width but deeper reducing the width/depth aspect ratio to $\sim$ 2. However, cavities are covered with compact layer of scale.

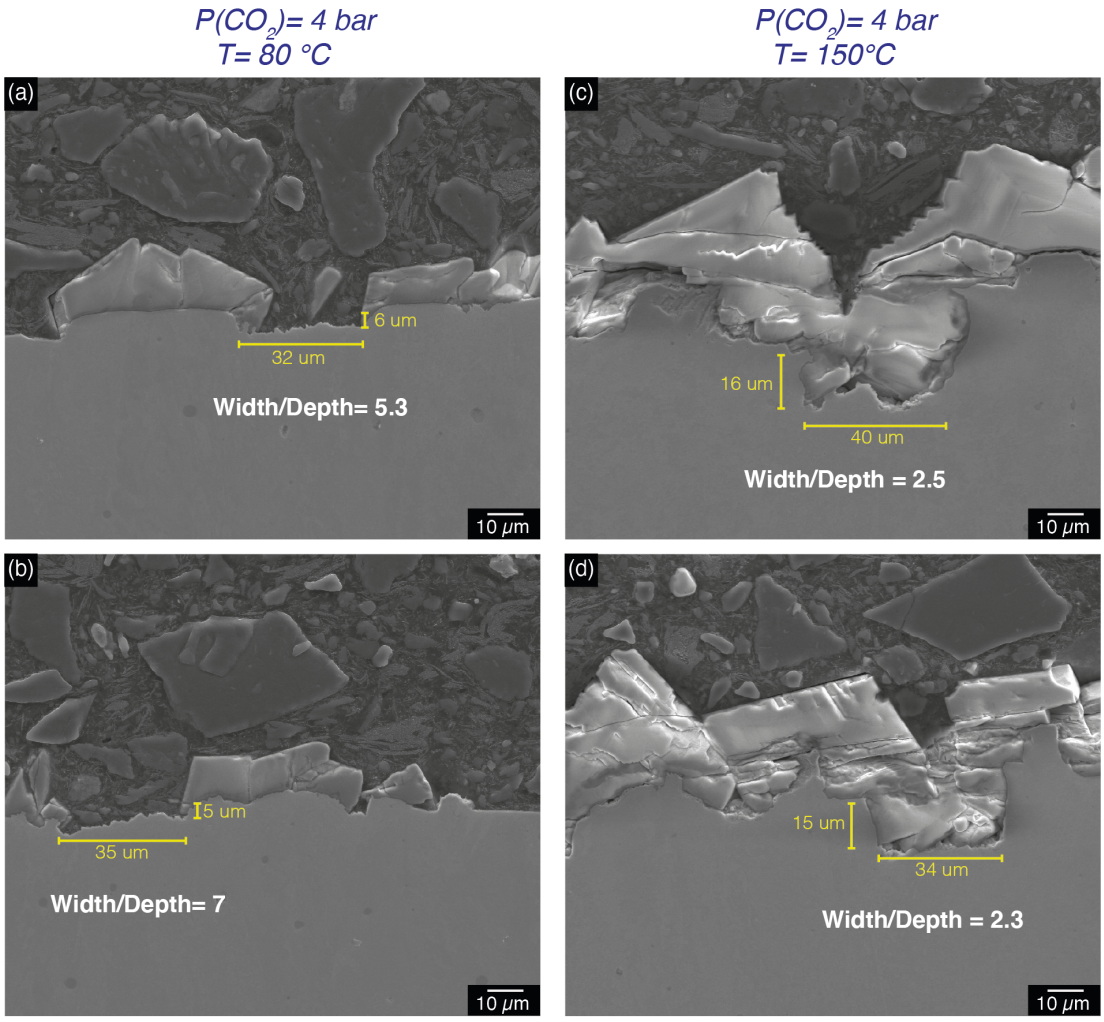

Figure 5.15: Cross sections SEM images of Fe substrates immersed for 24 hours in 0.1 M NaCl CO_2 saturated solution (T = 80°C - 150 °C, P_{CO_2}= 0.5 - 4 bar) in the autoclave showing local cavities on the surface as a result of high corrosion rates of initially uncovered areas with scale.

It is clear that as the temperature and CO_2 partial pressure increases, uncovered areas suffer higher corrosion rates driven by the increase in corrosion kinetics while adjacent covered areas are protected considerably against corrosion. Such differences in corrosion rates led to the appearance of cavities on the surface that are deeper at higher temperatures and CO_2 partial pressure. However, the results suggest that eventually a similar compact layer of scale formed on such locally depressed regions. Such observation is clear and consistent by surveying multiple regions across the cross-sections of the substrate at T(150)/P_{CO_2}(4) as shown in Figure 5.15 (c,d). The presence of such

a compact layer of scale might indicate that such regions behave differently to a stable pit where low pH is maintained via hydrolysis preventing formation of scale. Figure 5.16 presents a schematic illustration of a suggested mechanism of scale formation and corrosion behaviour over time in uncovered areas from the previous observation.

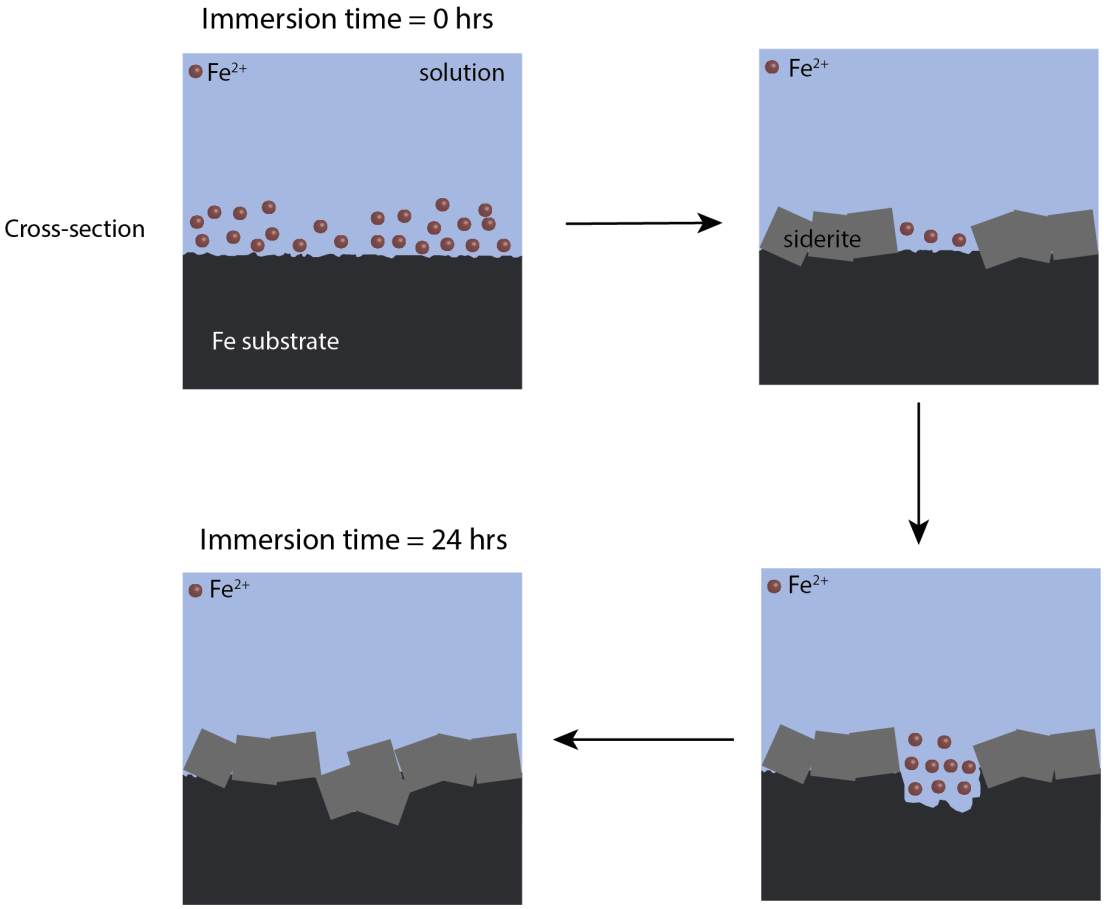

Figure 5.16: Schematic illustration of a suggested mechanism of corrosion leading to locally attacked areas on Fe substrate at higher temperatures and pressure.

5.4.8 Summary

The influence of temperature and CO_2 partial pressure (P_{CO_2}) in range of temperature T= 80°C - 150°C, and P_{CO_2} = 0.5 - 4 bar has been investigated in this chapter. Based on the observations above, operating temperature and CO_2 partial pressure can significantly influence the corrosion behaviour and scale formation under CO_2 saturated environment. Under no scaling conditions, the corrosion rates increased as a result of increasing both the temperature and CO_2 partial pressure. However, the increase in initial corrosion rates promoted formation of protective scales reducing corrosion rates significantly. The formed scale protectiveness and coverage was better after 24 hours of immersion at the scales formed at higher range of temperature and pressure investigated in this chapter: T= 150°C and P_{CO_2} = 4 bar.

In addition to the influence on corrosion rates, the increase in CO_2 partial pressure resulted in a change of siderite crystal habit from a micro faceted cylinder with trigonal/pyramidal caps to rhombohedral shape. Such observation is confirmed by theoretical calculation and ab initio modelling of siderite habits where it showed that the decrease of CO_2 content stabilises {110} facets resulting in the change of shape observed experimentally. It might be possible that this change in crystal habit can play a role in enhancing the protection. Crystals formed with higher surface energy surfaces can possibly increase the likelihood of its dissolution against changes in environmental conditions, which normally occurs under oilfield conditions. Further work is required to determine if there are any differences in dissolution rates of different siderite crystal habits as the conditions change such as temperature, pressure, ionic species.

As regards to chukanovite formation, it appears that the increase in temperature from 80°C to 150°C resulted in disappearance of this phase. Also, little protection is offered from chukanovite as concluded from the results of this work and from other study.

Finally, the increase in temperature and pressure resulted in the appearance of locally attacked areas. It is suggested that such cavities appear as a result of high corrosion rates of uncovered areas. Figure 5.17 shows a schematic illustration summarising the main observations found from this chapter.

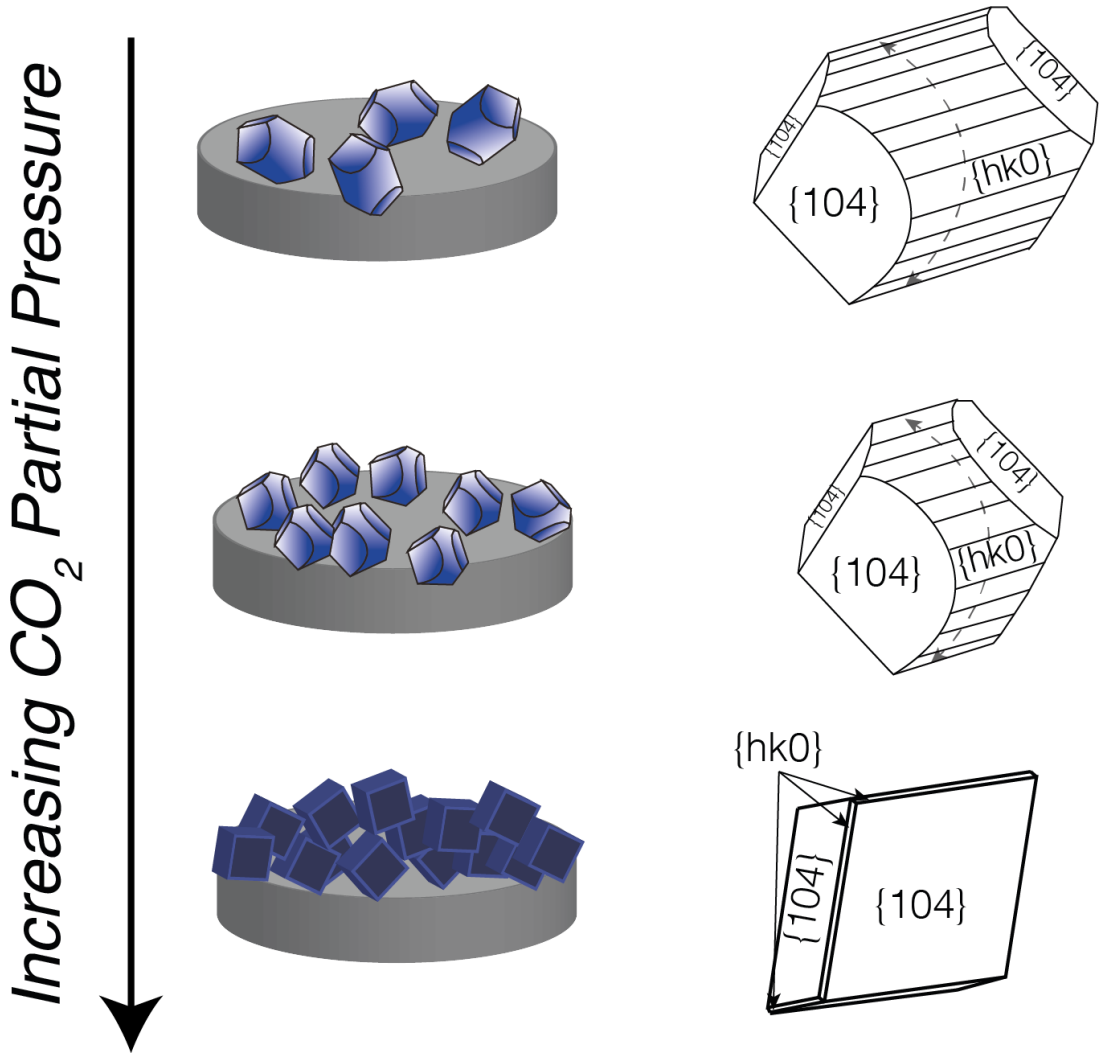

Figure 5.17: Schematic illustration summarising scale formation observations in this chapter.

Chapter 6.

Temporal and Temperature-Related Evolution of Sweet Oilfield Corrosion Scale: *In Situ* Grazing Incidence X-ray Diffraction

6.1 Introduction

Iron carbonate ($FeCO_3$) is the most common corrosion product formed in sweet environments. Besides, chukanovite ($Fe_2(OH)_2CO_3$) and magnetite (Fe_3O_4) have also been reported to form in CO_2 -containing environments [5, 115]. Many of the studies used *ex situ* scale characterisation techniques to identify/study the formed corrosion products. However, in *ex situ* measurements, carbonate products are prone to oxidation which can limit the reliability of such analysis. A recent *in situ* synchrotron GIXRD study by Ingham et al. showed that phases such as carbonate green rust ($Fe_6(OH)_{12}CO_3$), goethite (FeOOH) and magnetite (Fe_3O_4) appeared when trace of oxygen introduced to the system [114]. *In situ* techniques can also provide additional insights into the kinetics of formation of the scale.

A number of *in situ* synchrotron XRD studies have been conducted to study scale formation in CO_2-saturated environments utilising various electrochemical cells' designs. Ingham et al. and Ko et al. *in situ* studies focused on the scale formation under accelerated condition by anodically polarising the substrate [96, 97, 224–226]. From their work, chukanovite has been identified as one of the corrosion products in addition to siderite. In these studies, the authors investigated the impact of adding magnesium (Mg^{2+}), chromium (Cr^{3+}) and scale inhibitors on sweet scale formation [97, 225, 226]. From the results, it has been suggested that Mg^{2+} and Cr^{3+} promote protective scale formation while the use of scale inhibitors resulted in a corrosion rate increase by inhibiting the sweet scale formation. Burkle et al. studied in their *in situ* work, the scale formation under flowing conditions and short immersion periods ($\sim$ 4 hours) [204, 227]. From this work, only siderite has been detected as a corrosion product under the conditions of immersion in 3.5 wt% NaCl, T = 80°C, flow rate = 0.1 m/s and range of pH = 6.3 - 7. The authors suggested based on their observation that the increase in pH results in a decrease in induction time for $FeCO_3$ formation and an increase

in protectiveness by forming a more compact layer of the scale.

In this work, synchrotron GIXRD technique is employed to study scale evolution on a high purity iron substrate in CO_2-containing environment. An improved version of the synchrotron cell (SR-cell), which has been utilised in a previous *in situ* work by Joshi et al. [208], is used. The improvements in the design have been made to limit oxygen ingress issues encountered in the previous work. Also, the improvements considered enabling the use of the SR-cell to study scale evolution for extended immersion times, as the current *in situ* studies mentioned earlier have been conducted for only short immersion periods (maximum 4 hours). The corrosion rates determined by electrochemical impedance spectroscopy (EIS) and scale evolution is monitored over an immersion period of 28 hours. Initially, scale evolution at T = 80°C and pH = 6.8 have been investigated. The results are compared with preliminary laboratory glovebox experiments in this initial 12 hours of immersion. The effect temperature excursions, which is usually encountered in oilfield conditions, on the formed scale is also studied by introducing cooling and heating in the *in situ* synchrotron experiment while monitoring scale behaviour during this period. From corrosion rates and *in situ* GIXRD data, siderite formation/dissolution rates in addition to its protectiveness are determined.

6.2 Experimental details

Figure 6.1 summarises the experimental operating conditions in both laboratory and *in situ* synchrotron experiment.

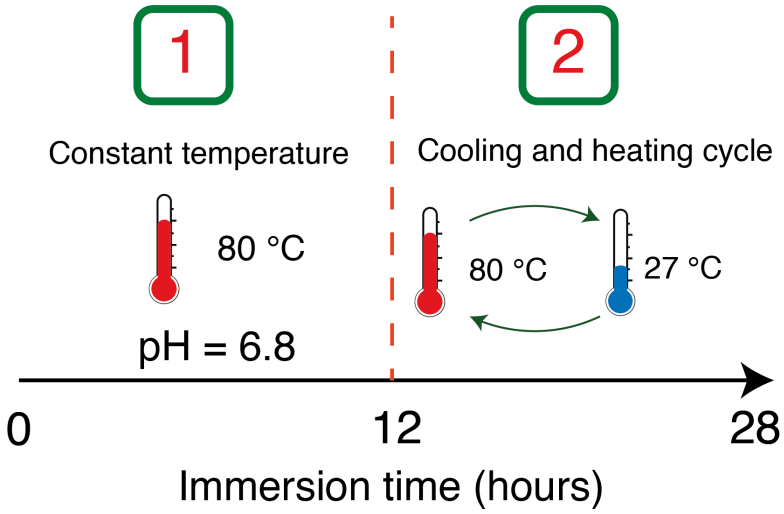

Figure 6.1: Schematic diagram illustrating experimental conditions in this chapter.

6.2.1 Materials and sample preparation

High purity Fe discs (depth $\sim$ 4 mm) were cut from a 10 cm rod (10 mm diameter, 99.99+% , sourced from Goodfellow). Minor elements present in Fe sample are shown in Table 6.1.

Table 6.1: Other elements present in high purity Fe sample. Values are in ppm.

Al	**Cr**	**B**	**Co**	**Cu**	**Ga**	**Ge**	**Mn**
1.6	6.6	0.77	12	2.1	0.7	6.2	4.1
Mo	**Ni**	**P**	**Ta**	**Sn**	**Ti**	**W**	**Zn**
0.36	2.8	7.2	1	0.15	1.4	0.15	0.3

The samples were polished to 4000 grit using silicon carbide paper (series of 240, 600, 1200, 2400, 4000). The bottom face of the sample was spot welded to a Ni-Cr wire to allow electrical connection for electrochemical measurements. The sample was then mounted on a polyvinylidene fluoride (PVDF) post and the sides were painted with lacomit paint to ensure exposure of only the top surface to the testing solution.

Prior to cutting the Fe discs, the high purity Fe rod was normalised by heat treatment in an argon furnace at 950°C for 30 minutes, followed by furnace cooling [228]. Figure 6.2 shows an SEM image revealing a microstructure of the heat treated high purity Fe sample showing ferrite grains with a well-defined grain boundaries.

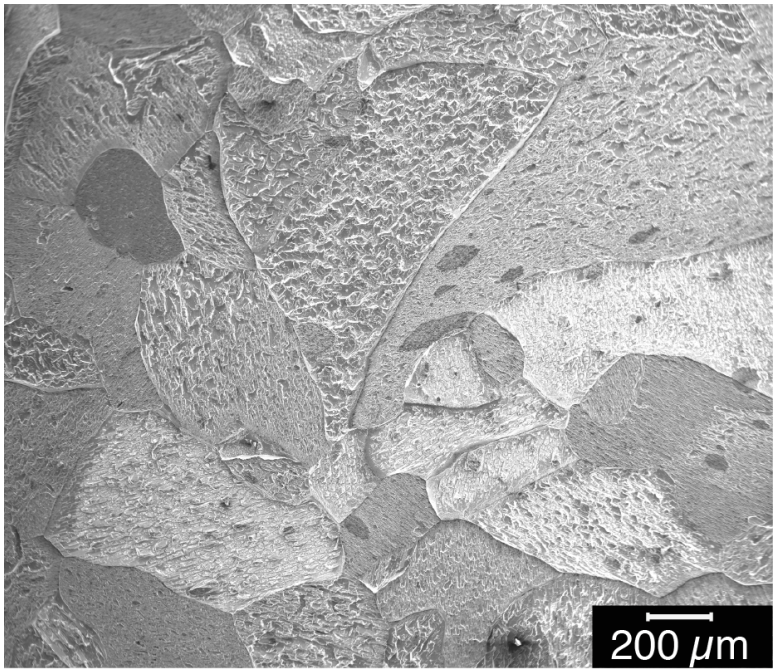

Figure 6.2: SEM image showing iron substrate microstructure following heat treatment

6.2.2 Synchrotron cell design

The synchrotron cell (SR-cell) design developed for this work is based on a previous design used in an *in situ* GIXRD work [208]. The cell design allows for both *in situ* GIXRD and electrochemical measurements. Also, the cell has heating capabilities to enable conducting the experiments at elevated temperatures (T_{max} = 80°C).

SR-cell design comprises of three main parts: aluminium mounting stand, SR-cell main body and inert atmosphere polyimide hood as shown in Figure 6.3. The aluminium mounting stand is used to attach the SR-cell to the diffractometer at the synchrotron facility. The SR-cell main body is manufactured from polyether ether ketone (PEEK), replacing polychlorotrifluoroethylene (PCTFE) from the previous design, as it is suggested to have lower oxygen sorption [229]. There are 11 threaded ports in the side of the body. For electrochemical measurements, a platinum (Pt) counter and reference electrodes are inserted through two ports. Solution temperature is controlled by pumping hot water from a water bath through 3-mm diameter coiled polytetrafluorethene (PTFE) tubing. These tubes are inserted through six of the threaded ports. The remaining three ports are used as solution inlet/outlet and for the insertion of a type-K thermocouple to measure the temperature of the solution in the SR-cell. The sample acts as a working electrode by connecting the back face of to a Ni-Cr wire. The sample PVDF post is secured in the middle of the cell and sealed by using 35 mm diameter O-ring. The height of the sample can be adjusted using a brass adjustment screw at the bottom of the cell.

The cell is sealed from the top by a polyimide kapton film (thickness=25.4 μm) and brass supported kapton (thickness=127 μm) hood. The hood is filled with CO_2 gas continuously flowing throughout the experiment. This to maintain low oxygen level above the solution and to avoid any possible permeation of O_2 through the kapton film sealing the solution in the SR-cell.

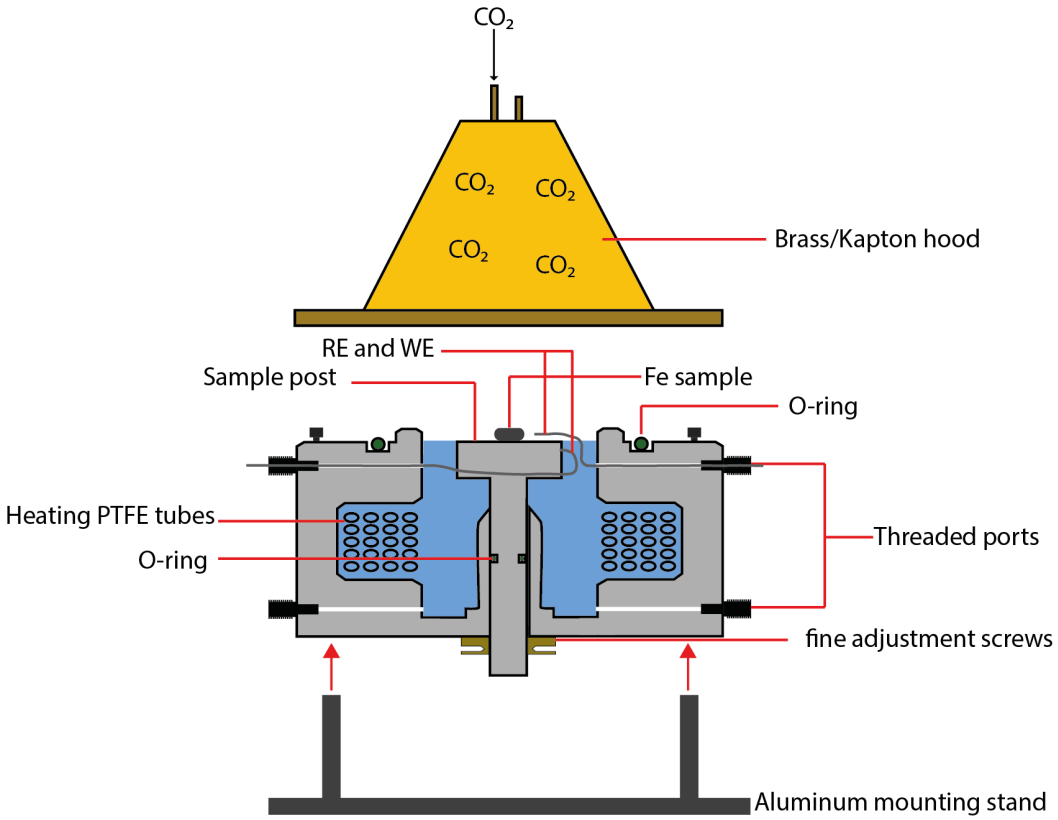

Figure 6.3: Schematic diagram illustrating synchrotron cell design.

6.2.3 Solution Preparation and Experimental Details

Figure 6.4 shows a schematic illustration of the synchrotron experimental setup. A CO_2-saturated deionised water solution was prepared in a 1-L glass duran bottle by purging the solution with high purity CO_2 gas (99.95%) for 2 hours. The solution was heated to 80°C and the pH was adjusted using sodium bicarbonate ($NaHCO_3$) to 6.8±0.05 once the temperature of the solution reached the desired test temperature. After pH adjustment, the solution was transferred and sealed into a 0.6-L Hastelloy pressure vessel (Parr Instrument Model No. 4760), where it was further purged with CO_2 gas for 28 hours to lower the dissolved oxygen concentration. [$O_{2(dissolved)}$] was measured regularly by an electrochemical oxygen sensor (O_2 sensor, Orbisphere A1100). All the lines were filled with CO_2 gas, including the SR-cell, to ensure low oxygen level throughout the whole system prior to solution transfer to the SR-

cell. After reaching $[O_{2(dissolved)}] < 20$ ppb, approximately 350 ml of the solution was transferred the SR-cell.

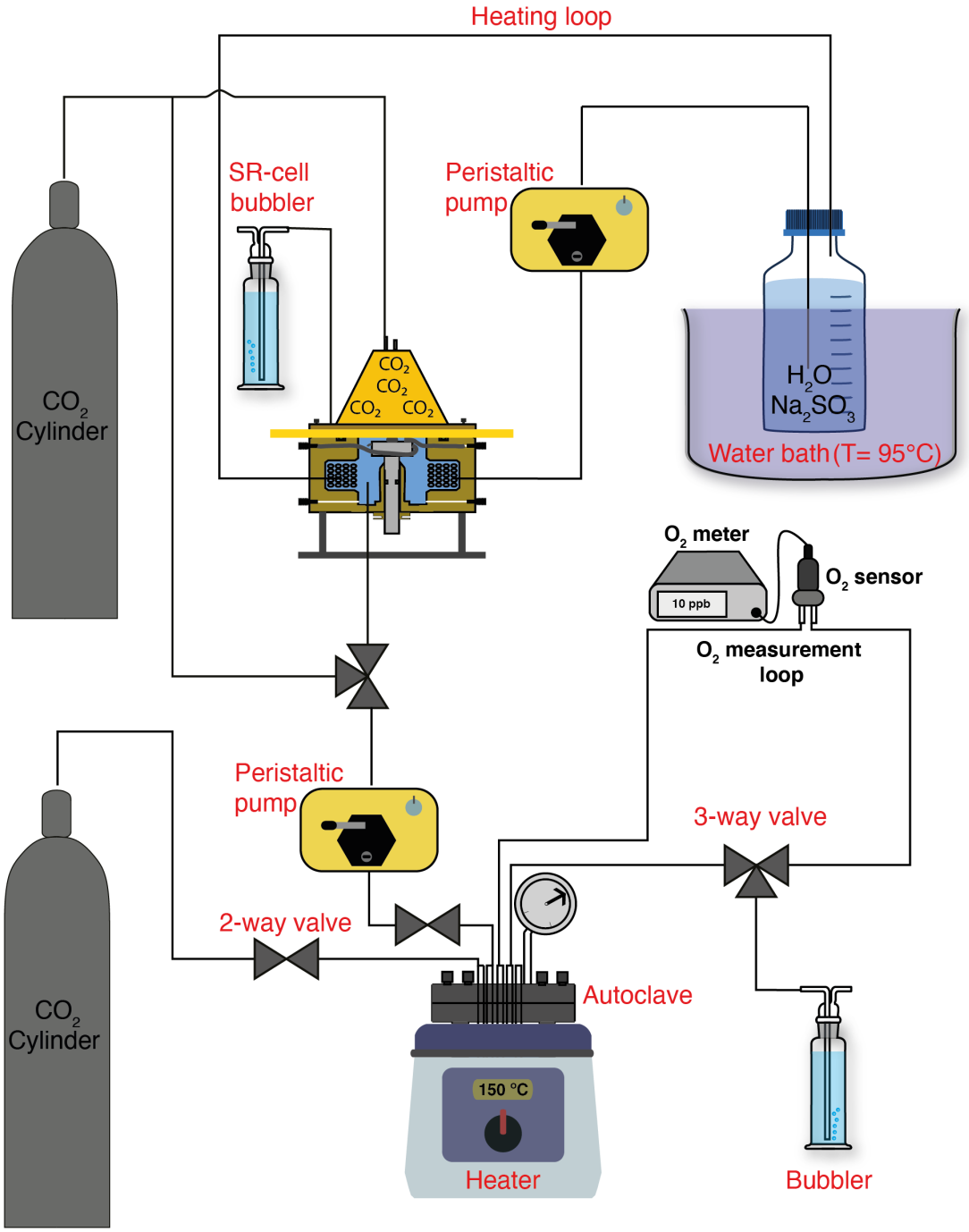

Figure 6.4: Schematic diagram of synchrotron experimental setup. Viton/stainless tubing were used to connect between components in the diagram.

The SR-cell was oriented vertically, as shown in Figure 6.5 to avoid trapped gas bubbles between the sample and kapton film, which might affect the corrosion scales/ electrochemical measurements. After transferring the solution to the cell and immersion of Fe substrate starts, the experiment ran for 28.5 hours. In the first 12 hours, the solution was maintained at 80°C. After the 12 hours of immersion, cooling then heating cycle is introduced by allowing the solution to cool down to 25°C after 14.5 hours of immersion. This was followed by reheating until temperature reaches 80°C at 17th hour of immersion and maintained at the same temperature until the end of the experiment.

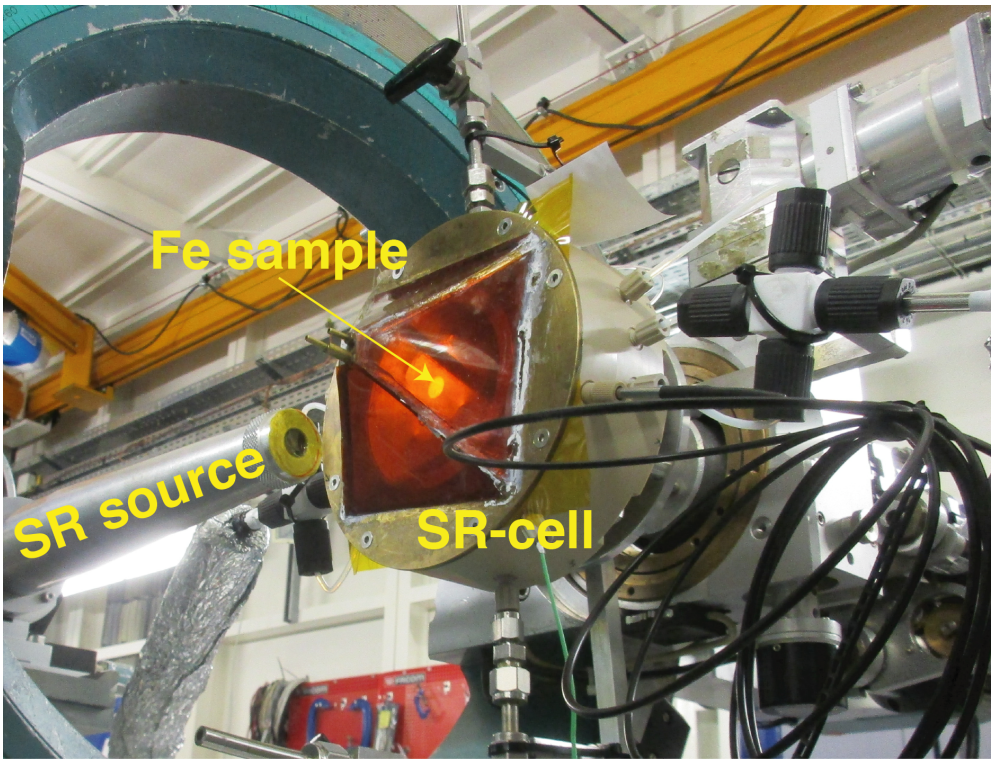

Figure 6.5: Experimental setup of SR-cell (oriented vertically) on BM28 beamline

In order to control the temperature of the solution inside the SR-cell, deionised water was heated to ~ 95°C in a 1-L duran bottle and pumped by a peristaltic pump to the heating coils inside the SR-cell. Approximately 10 g of sodium sulphite (Na_2SO_3), that acts as an oxygen scavenger, was added to the heating water in the bottle. During the period between the 12-14.5 hours of immersion,

the pump was stopped to allow for the test solution to cool down during the cooling cycle. After that, the pump was restarted again to re-heat the solution back to 80°C.

The above procedure is followed for the experiment performed in the *in situ* synchrotron experiment. The same procedure is followed to investigate scale evolution (initial 12 hours of immersion only) in preliminary laboratory experiments inside a CO_2 filled glovebox. Details of electrochemical measurements and *in situ*/*ex situ* surface characterisation for both tests are presented below.

Electrochemical measurements and surface characterisation

After transferring the solution, electrochemical impedance spectroscopy (EIS) measurements was carried out using Gamry Instruments Interface 1000 potentiostat. The solution OCP was measured in the time interval between EIS measurements. These measurements were carried out for a total of 28.5 hours of immersion duration.

In situ GIXRD measurements were taken at an incidence angle α = 3° and a photon energy hυ = 14.5 keV (λ = 0.8551 Å). The incident angle of 3° was selected to be above the critical angle of total external reflection reflection of x-rays with the consideration of surface roughing, and background contribution from the kapton polyimide film. These measurements were undertaken using the synchrotron radiation source at beamline 28 (BM28), at the European of Synchrotron Radiation Facility (ESRF) in Grenoble, France. The measurements were recorded on a Dectris 300K-W Pilatus 2D detector with an area of 253.7 mm x 33.5 mm (1475 x 195 pixels). The use of a 2D detector allows to record the whole range of 2θ at a minimum of 7 ms, which offer an advantage over a point detector usually used in laboratory equipment. Measurements were undertaken at a detector position of 20° and 18° from the synchrotron beam source. The measurements were taken every 30 minutes for a total period of 1 minute for each scan. Within this period, part of the solution was

removed using a peristaltic pump to obtain thin film geometry. Thick and thin film geometries for undertaking electrochemical and GIXRD measurements were obtained by controlling the amount of solution above the sample as shown in Figure 6.6. Captured diffraction patterns by the 2D area-detector were processed to produce 1D diffractogram using Esaproject software [230]. Details on data processing is outlined in [208].

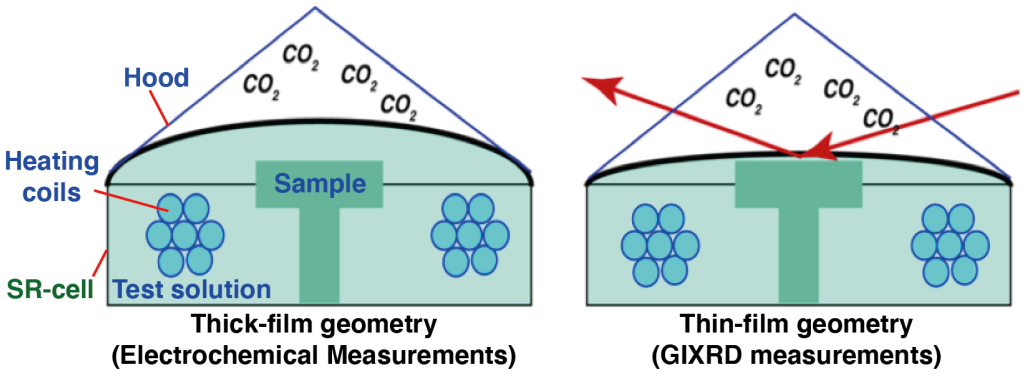

Figure 6.6: Schematic illustration of thick and thin film geometries obtained for electrochemical and GIXRD measurements

As regards the laboratory glovebox experiments, samples were characterised after immersion using *ex situ* GIXRD at a grazing incidence α = 3°using Philips X'Pert MPD diffractometer (CuKα source, λ = 1.54 Å). SEM images were obtained using FEI Quanta650 SEM.

6.3 Results and Discussion

6.3.1 Preliminary laboratory glove box experiments

Figure 6.7 shows the average corrosion rate profile of Fe substrate in CO_2 saturated solution at pH = 6.8, T = 80°C over 12 hours of immersion. The results shown in the figure are repeats of two tests performed in a CO_2-filled glovebox using the SR-cell. Corrosion rates were calculated from EIS data and

assuming a Stern-Geary coefficient of β = 52 mV. The corrosion rate profile shows a trend of decreasing corrosion rates with a sharper drop in the initial $\sim$ 2 hours. Corrosion rates continue to decrease but at a lower rate of until the end of the 12th hour of immersion. The decrease in corrosion rate can be an indication of a formation of *semi-protective* scale.

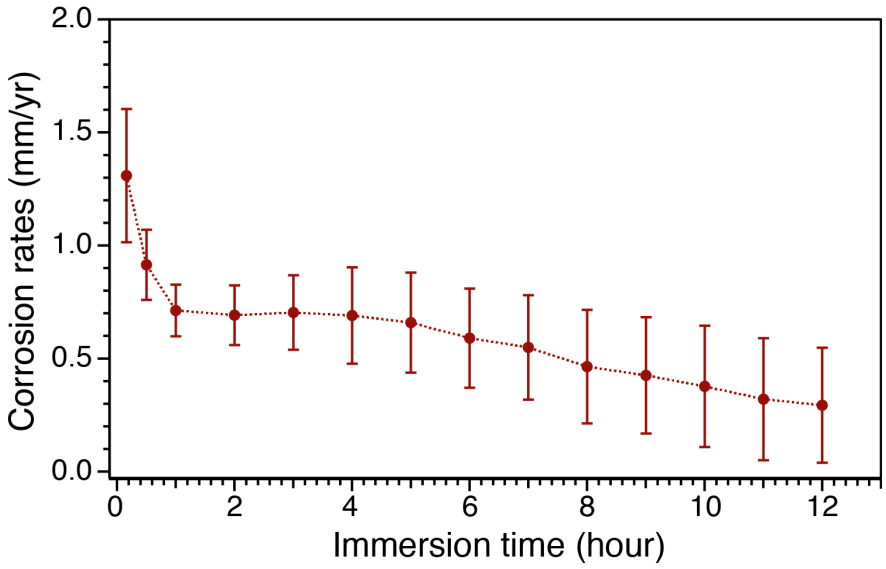

Figure 6.7: Average corrosion rate of Fe substrate immersed in CO_2 saturated water (T = 80°C, pH = 6.8) in SR-cell performed in a glovebox as a function of immersion time of 12 hours

Post immersion *ex situ* GIXRD diffractograms and SEM images from the immersed Fe substrate for the two tests are shown in Figure 6.8. The Figure shows three peaks attributed to α-Fe at 2θ = 44°, 65°and 82° from the substrate. Furthermore, diffractograms shows formation of a mixed layer of siderite ($FeCO_3$) and chukanovite ($Fe_2(OH)_2CO_3$). SEM images in Figure 6.8 shows the scale formed in both runs on Fe substrate. It can be seen that a mixture of chukanovite (platy crystals) and siderite (cylindrical crystals). In addition, surfaces are not fully covered with the scale. These preliminary experiments demonstrate that sweet corrosion scales are likely to be formed within the time-scale of the synchrotron experiment.

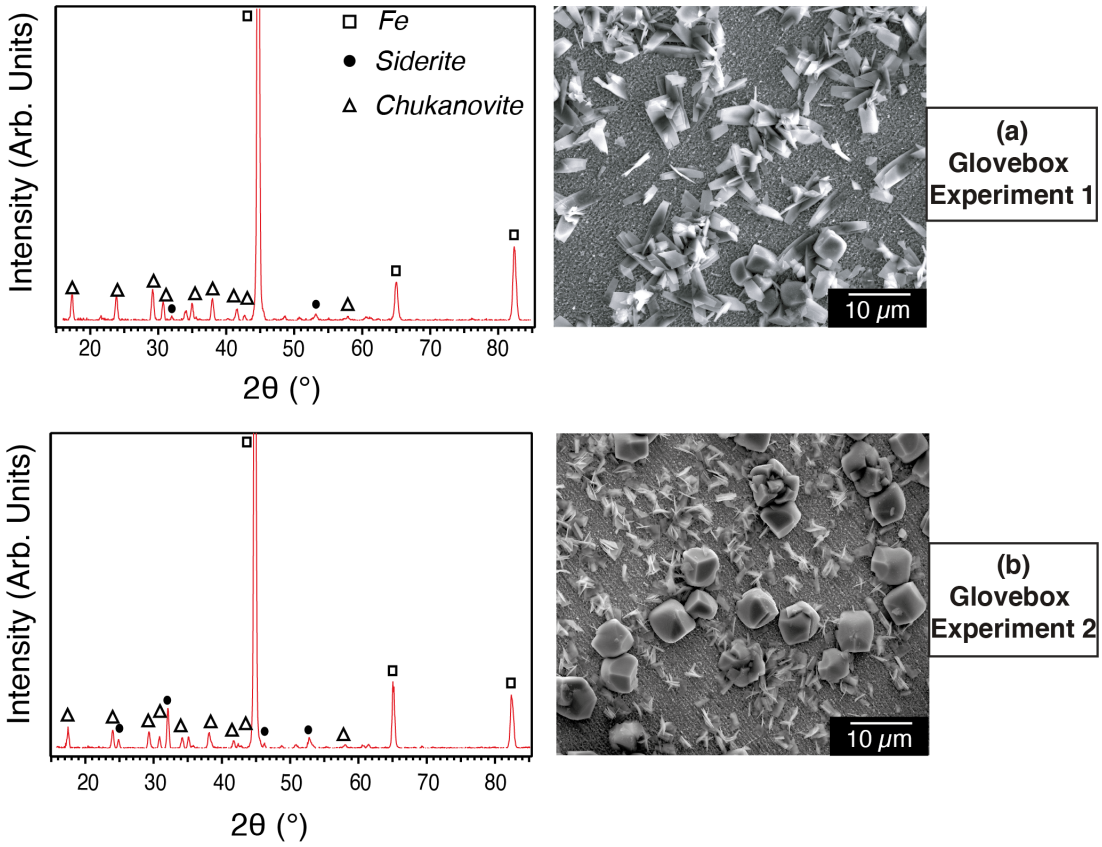

Figure 6.8: GIXRD diffractogram (α_i = 3°, CuKα source, λ = 1.54 Å) of Fe substrates immersed in CO_2 saturated water (T = 80°C, pH = 6.8) as a function of immersion time (12 h). All plots are normalised to the intensity of Fe{110} peak at 2θ = 23.5°.

6.3.2 *In situ* synchrotron experiment

Figure 6.9 shows the corrosion rate profile of Fe substrate in CO_2 saturated solution at pH = 6.8, T = 80°C during the first 12 hours of immersion. The corrosion rates are calculated using EIS data assuming Stern-Geary coefficient of β= 56 mV. The corrosion rates decreased from $\sim$ 1.1 mm/yr at the 1st measurement (0.16 h after immersion) to $\sim$ 0.06 mm/yr at the 12th hour of immersion. In the initial 4 hours of immersion, corrosion rate decreased sharply from 1.1 mm/yr to 0.22 mm/yr (decreased by 80%). This is followed by a slower rate to approximately steady corrosion rate from 5 - 12 hours of immersion. This corrosion rate profile suggest formation of a protective scale.

Figure 6.9 also shows a comparison of corrosion rates between *in situ* synchrotron and glovebox experiments. In both cases, similar significant drop in corrosion rates is observed within the first 2-4 hours of immersion due to the formation of scale. However, the average corrosion rates in the glovebox experiment were higher between the 2nd and 12th hour of immersion than in the *in situ* experiment. This difference decreases with time between the experiments towards the 12th hour of immersion and the final corrosion rate of the synchrotron experiment lies within the error of corrosion rate in the glovebox experiments.

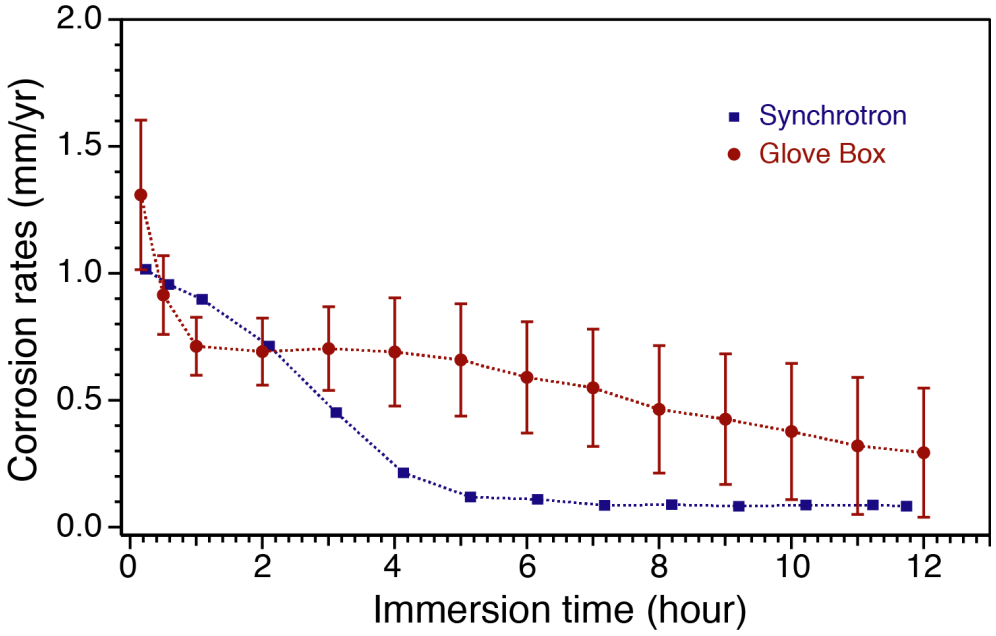

Figure 6.9: Comparison of corrosion rates between *in situ* synchrotron and glovebox experiments of Fe substrate immersed in CO_2 saturated water (T = 80°C, pH = 6.8) in SR-cell as a function of 12 hours of immersion. As only one *in situ* experiment was performed, no error bars are shown.

Regarding the *in situ* GIXRD results, Figure 6.10 shows series of diffractograms as a function of the 12 h immersion period. The polished substrate diffractogram plot at the bottom of Figure 6.10 was acquired prior to solution transfer (at immersion time t = 0 hours) to the cell in a dry CO_2 atmosphere. From this plot, two peaks at 2θ = 23.5° and 32.8° can be assigned to the α-Fe {110} and {002} planes, respectively, arising from the substrate. Broad peaks

at low incidence angle are due to the polyimide kapton film [115, 208]. All diffractograms are normalised to the most intense α-Fe {110} peak.

After immersion, siderite is the only detected phase that formed on Fe substrate as revealed by the series of diffractograms. The most intense siderite {104} peak started to appear after 1 hour of immersion. Siderite peak intensities continued to increase as immersion time increased.

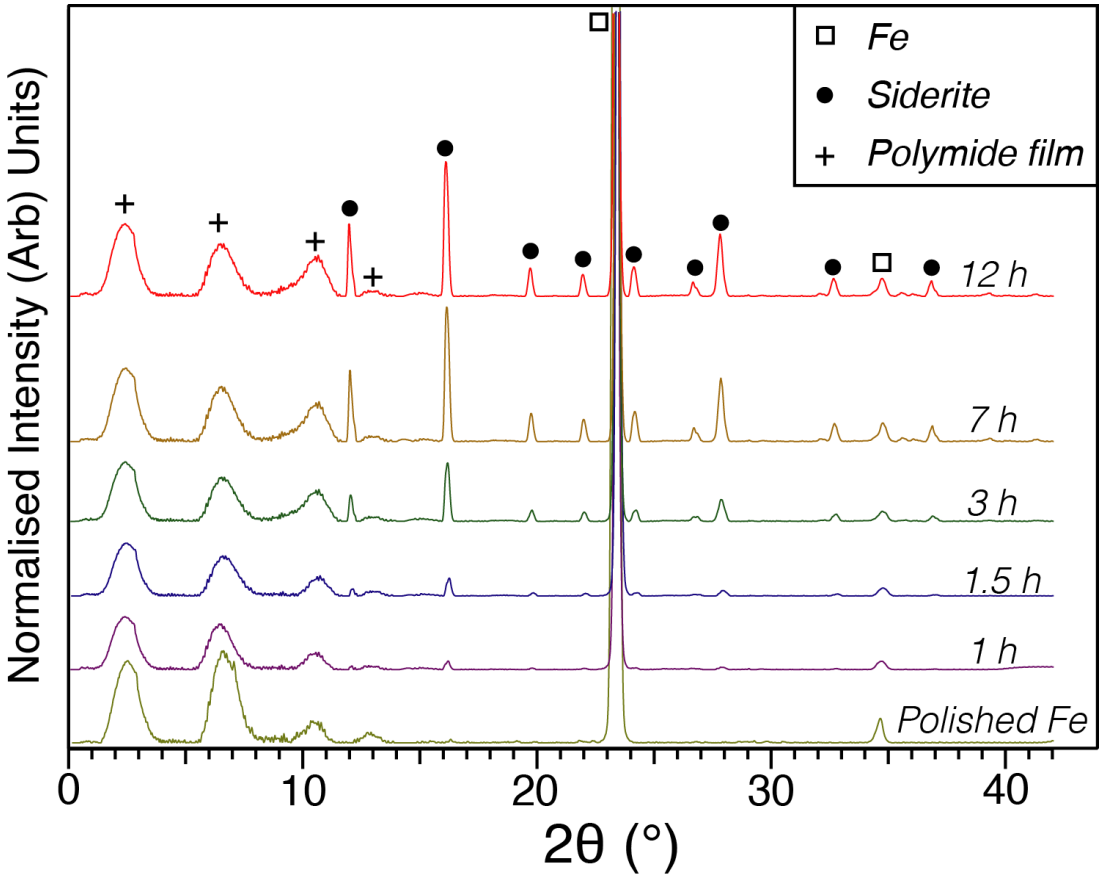

Figure 6.10: Series of synchrotron GIXRD diffractograms of Fe substrate immersed in CO_2 saturated water (T = 80°C, pH = 6.8) as a function of immersion time (12 h). All plots are normalised to the intensity of Fe{110} peak at 2θ = 23.5°.

Comparing the phases formed within the scale after 12 hours of immersion between this *in situ* synchrotron experiment and the the two *ex situ* preliminary glovebox experiments (Figure 6.8 and 6.10, only siderite was formed on the substrate in the *in situ* experiment, whereas a mixture of

siderite and chukanovite scale was formed in the glovebox experiments. From this comparison, one observation is that the scales evolved in these three experiments were not quite reproducible in terms of protectiveness and the phases formed. Such irreproducibility is not unexpected as it was also observed in Joshi et al. work [5]. Their study, where Fe substrate was immersed in the same environment as in this work, showed similar variation in corrosion rates, type and amount of scale formed in the first 72 hours of immersion.

Now focusing on the *in situ* synchrotron experiment, and to further investigate the rate of siderite growth as function of immersion time, Figure 6.11 (a) shows the relative intensity of siderite as a function of immersion time. Each point represents relative intensity of siderite {104} peak with respect to normalised iron {110} peak. As it can be seen from the plot, the siderite peak intensity increase was rapid after its appearance ($\sim$ after 1 hour of immersion) up to the 7^{th} hour before it plateaus at $\sim$ 0.12 relative intensity. Corrosion rates are plotted in the same figure showing how siderite growth influenced the decrease in corrosion rates. The corrosion rate drop observed has in fact followed the same trend as rate of siderite growth. Figure 6.11 (b) illustrates the similarity between the trends by plotting the normalised corrosion rate data and the inverse normalised relative siderite intensity data. This figure shows clearly that the corrosion rate and siderite growth rate are almost overlaid indicating that siderite formation was the reason behind the 18x drop in corrosion rate. The initial high corrosion rate provided high local concentration of Fe^{2+} near the surface of Fe substrate and resulting in $FeCO_3$ precipitation at a higher rate. As the film grows and protects the substrate from further corrosion, the rate at which siderite formation decreases due to lower Fe^{2+} available and this results in the steady region at which no substantial change in both corrosion rates and siderite peak intensities.

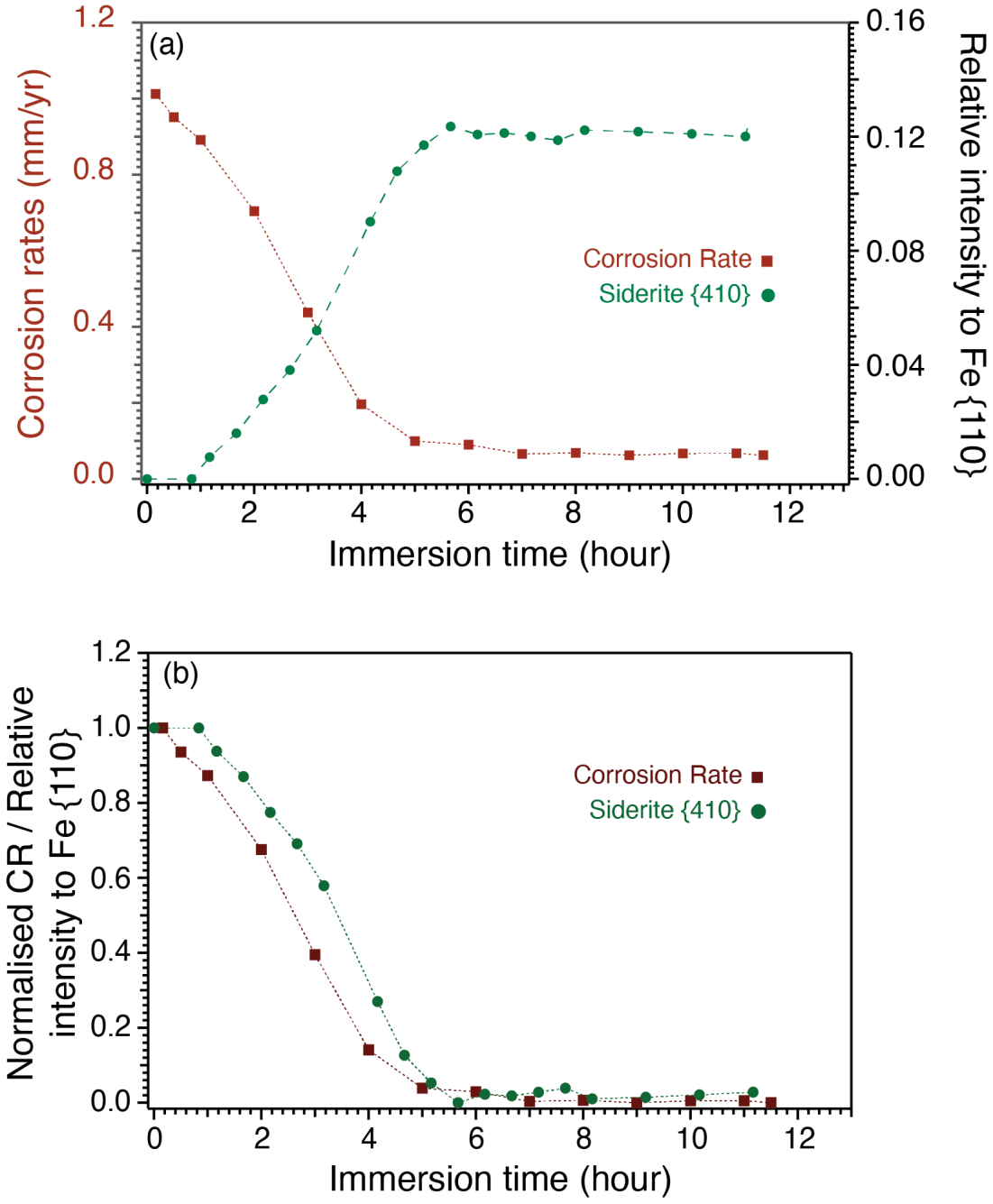

Figure 6.11: (a) Relative siderite {104} peak intensity with respect to normalised Fe {110} (green) and corresponding corrosion rate (red) and (b) Normalised corrosion rate and inverse normalised relative siderite {104} peak intensity, of Fe substrate immersed in CO_2 saturated water (T = 80°C, pH = 6.8) in SR-cell performed for *in situ* synchrotron experiment a function of immersion time of 12 hours.

6.3.3 Effect of temperature excursions on scale growth and dissolution

Figure 6.12 shows a series of diffractograms as function of temperature. The temperature dropped from 80°C to 27°C as the system was allowed to cool down between the 12th hour of immersion and the 15th hour of immersion. This was followed by re-heating to 80°C until the 28th hour of immersion. The diffractograms are normalised to the Fe {110} peak. In this figure, siderite intensity generally decreases as the temperature drops to 27°C. This is followed by an increase in siderite peak intensity as the temperature is increasing again to 80°C.

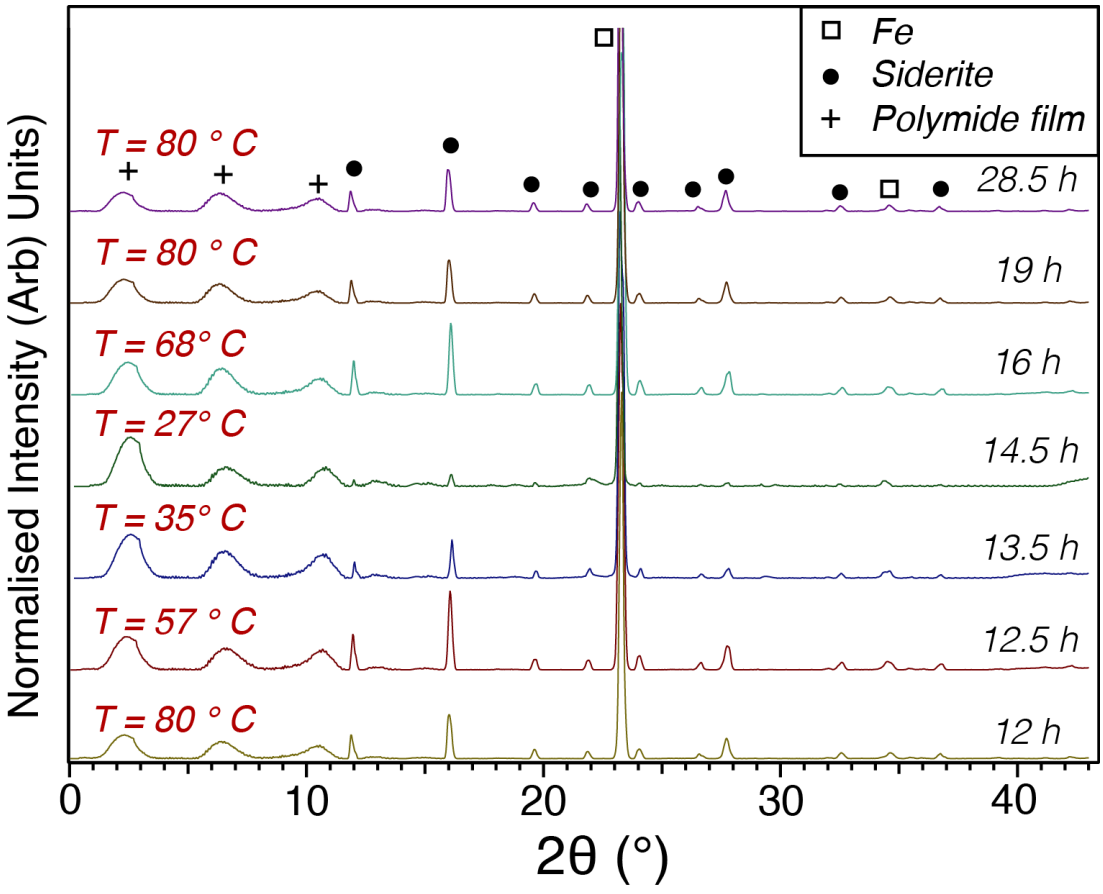

Figure 6.12: Series of synchrotron GIXRD diffractograms of Fe substrate immersed in CO_2 saturated water (T = 80°C, pH = 6.8) during cooling and heating cycle from 12-28 hours of immersion. All plots are normalised to the intensity of Fe{110} peak at 2θ = 23.5°.

Figure 6.13 plots the change in {104} siderite peak intensity relative to the normalised iron {110} from 10 - 28.5 hours of immersion along with the changes in estimated corrosion rates. As demonstrated in the figure, the relative siderite peak intensity decreased from 0.12 to 0.018 (85% decrease) when temperature reaches 27 °C. The intensity increases again as the temperature increase reaching a plateau after 19 hours of immersion. The intensity reaches the same relative value to what it was before cooling. This trend can be attributed to siderite scale dissolution and regrowth. The scale reaches a plateau within two hours, where no substantial change in the amount of scale formed, compared to 7 hours of immersion at the beginning of the immersion. Interestingly, higher relative siderite peak intensities were observed at temperatures of 57°C and 68°C compared to at 80°C. The reason behind this increase is quite unclear and it can possibly be either due to an increase in scale formation at these temperatures or an artefact of the measurement. Further work is required to investigate the reason behind such an increase at these intermediate temperatures.

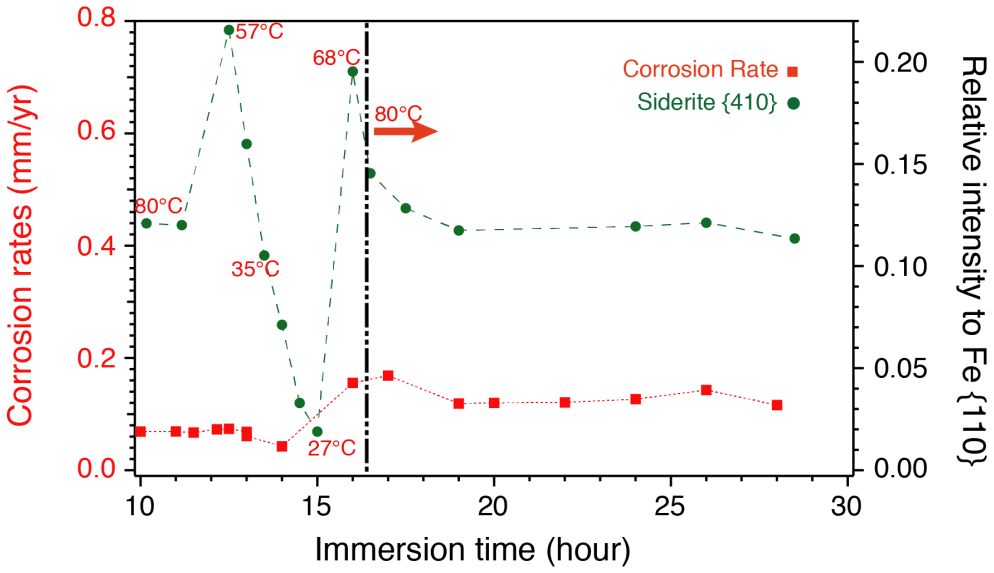

Figure 6.13: Relative siderite {104} peak intensity with respect to normalised Fe {110} (green) and corresponding corrosion rate (red) of Fe substrate immersed in CO_2 saturated water (T = 80°C, pH = 6.8) in SR-cell performed for *in situ* synchrotron experiment during immersion period from 10-28 hours.

Focusing on corrosion rate changes, the estimated corrosion rates remained almost steady during cooling/heating period. It is difficult to draw any conclusions about scale dissolution from corrosion rate data. This is because of the decrease in corrosion kinetics as a result of temperature decrease. As the temperature increases back to 80 °C, a slight increase in corrosion rates from ∼0.066 mm/yr to ∼0.12 mm/yr indicate that the regrown scale is slightly less protective.

The decrease in temperature, as the results above indicate, resulted in 85% of scale dissolution. As the temperature decreases, siderite solubility increases favouring its dissolution. Furthermore, the pH decreases to pH 6.11 (measured experimentally) as a result of the temperature drop, which also increases siderite solubility. To verify if the conditions at 25 °C are non-scaling, high purity Fe was immersed in a CO_2-saturated de-H_2O for an immersion period of 72 hours in a jacketed glass-cell setup in a N_2 filled glovebox. Figure 6.14 shows post immersion GIXRD diffractogram and corresponding SEM image of the surface. The figure shows only three α-Fe peaks and the SEM image shows a scale-free surface.

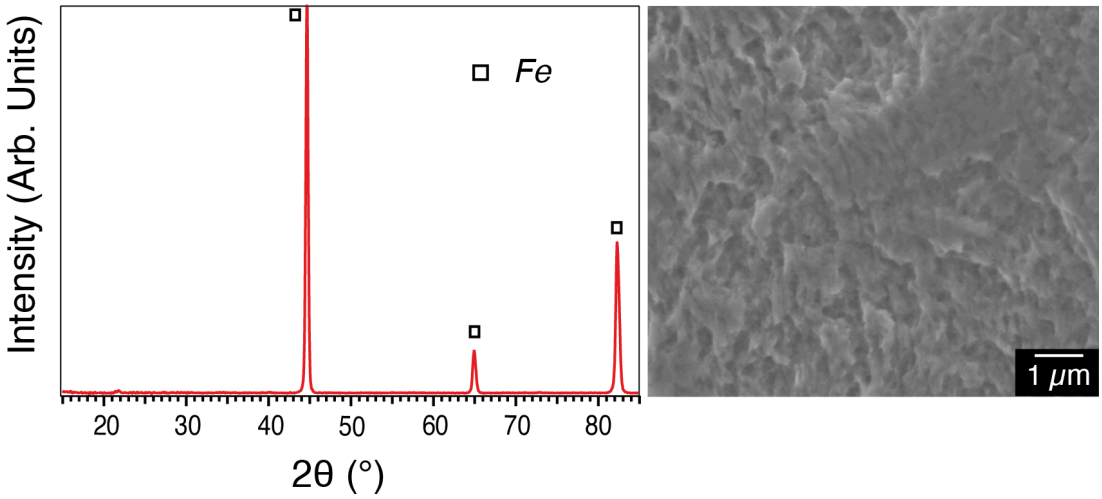

Figure 6.14: SEM image and GIXRD diffractogram (α_i = 3°, CuKα source, λ = 1.54 Å) of Fe substrate immersed in CO_2 saturated water (T = 25°C, pH = 6.11) as a function of immersion time (72 h).

6.3.4 EIS analysis

EIS can provide a useful insight to help understand corrosion behaviour/kinetics [155]. However, physical understanding is crucial before extracting any numerical responses from data fitted to equivalent circuit models [231]. Analysis of EIS data discussed in this section are split here into two parts; the first 12 hours of immersion at 80°C, and the period after cooling/heating cycle (17-28 hours of immersion) at 80 °C. It is challenging to link between EIS and physical data at the period where the temperature is changing. This is simply due to the complexity of the system where both corrosion kinetics and scale dissolution can play a role in substrate corrosion behaviour reflected in EIS measurements. Therefore, the discussion here is only limited to immersion periods at constant temperature. Analysis of EIS data from *in situ* experiment are only presented below. Same analysis and data fitting procedure was done for the initial 12 hours of immersion in glovebox experiments.

Initial 12 hours of immersion

Figure 6.15 shows the impedance spectra measured as a function of the initial 12 hours of immersion presented in Nyquist plot and corresponding Bode plots. Nyquist plot in Figure 6.15 a), shows a single capacitive semi-circle at 1 and 4 hours of immersion. This is followed by a change from the 7^{th} hour of immersion and beyond to an extended loop comprises of two overlapped semi-circles as illustrated by dashed lines in Figure 6.15 a). The diameter of semi-circles presented in the Nyquist plot generally increases with immersion time. However, very small difference can be observed between the Nyquist plot at 7^{th} and 12^{th} hours of immersion. Similar observation can be attained from bode plot in Figure 6.15 b) as the amplitude increases in the same manner with immersion time. The corresponding phase angle Bode plot in Figure 6.15 c) shows a peak increase from -40° to -70° and a shift in peak position towards higher frequencies as immersion time increases. Similar to Nyquist plot, a

small difference is observed here between 7 and 12 hours of immersion.

The response which resulted in a change from one to two semi-circles in the Nyquist plot and the phase shift peak increase in Bode plots suggests an increase in amount of scale developed on the substrate [75, 126]. This is confirmed by the increase seen in siderite peak intensity observed from *in situ* GIXRD shown in Figure 6.11.

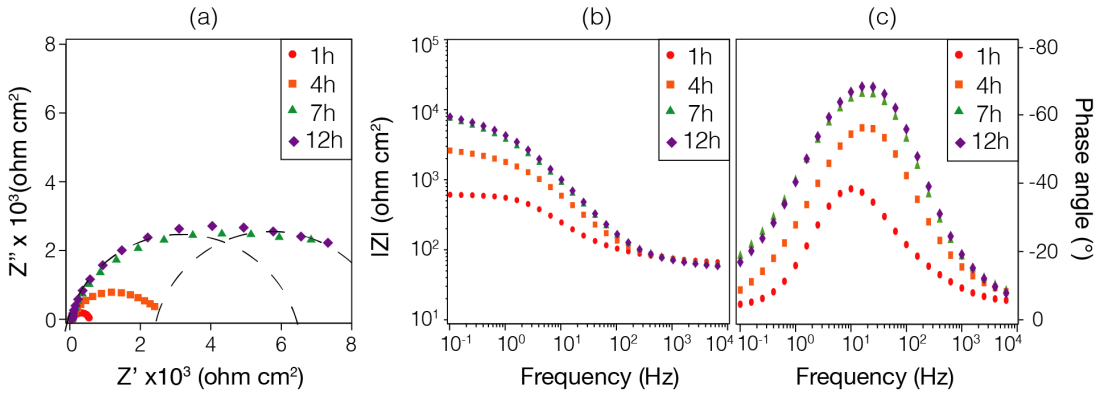

Figure 6.15: EIS data of synchrotron GIXRD diffractograms of Fe substrate immersed in CO_2 saturated water (T = 80°C, pH = 6.8) as a function of immersion time (1, 4 ,7 and 12 hours) represented in (a) Nyquist, (b) Bode and (c) phase angle plots.

Equivalent circuit models were used to fit and quantitatively represent measured EIS data. In order to show fitting quality, an example of original and fitted data are presented in Figure 6.16 along with the equivalent circuit used to fit the data. Measured EIS data in the first 6 hours of immersion were fitted using a simple Randles electrochemical equivalent circuit model for actively corroding metal presented in Figure 6.16 a). From this equivalent circuit, $R_s$is the solution resistance (Ω cm^2), $R_{ct}$is the charge transfer resistance (Ω cm^2) and Q_{dl} is constant phase element (CPE) representing double layer capacitance (C_{dl}). CPE is used to account for the non-ideal behaviour of double layer resulting in a depressed semicircle as it can be seen from the Nyquist plot in Figure 6.16 a) [231]. Although the physical meaning is not yet clear but the non-ideal behaviour can be possibly due to the surface roughness from the corrosion process [232].

In the period from 7-12 hours of immersion, the data were fitted using a nested equivalent circuit model as shown in Figure 6.16 b). Added parameters in this circuit to account for an additional electrochemical process due to the presence of corrosion scale layer are; corrosion scale resistance (R_{scale}) and CPE (Q_{scale}) representing double layer capacitance of the corrosion scale. From this equivalent circuit, features at high frequency data are associated with charge transfer resistance $R_{ct}$and double layer capacitance C_{dl}while low frequency data are associated with scale resistance and scale capacitance C_{scale}[126, 140, 151, 232].

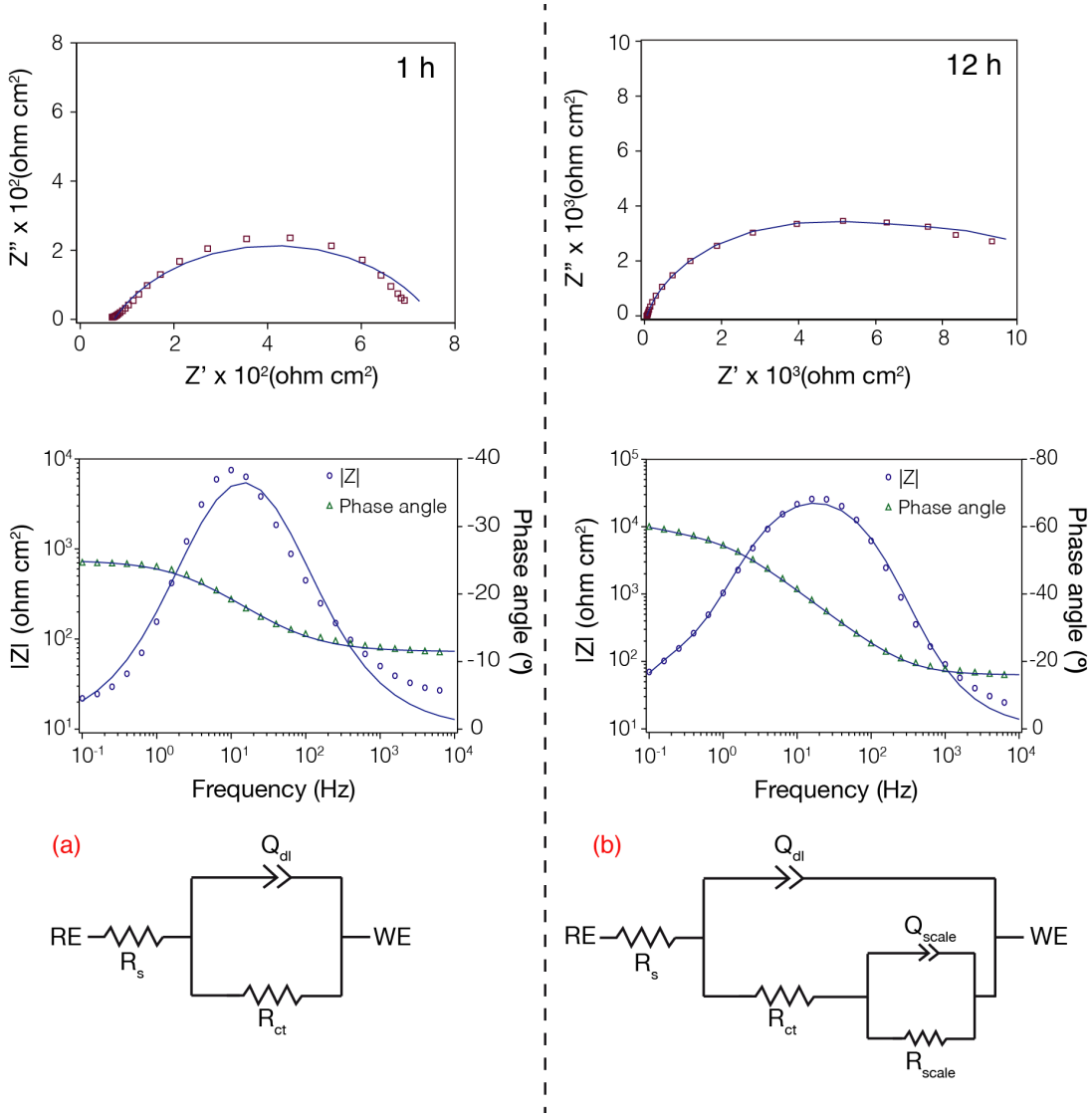

Figure 6.16: Example of EIS data fitting represented in Nyquist and Bode plots. Data fitted using (a) Randles circuit for actively corroding metal or (b) nested circuit for scaled metal.

Table 6.2 lists fitted parameters' values during the initial 12 hours of immersion. Is it seen that R_{ct} increases from 536 Ω cm^2 in the 1st hour before it reaches 5866 Ω cm^2 in the 7th hour of immersion and increases slightly to 6514 Ω cm^2 after 12 hours. This is analogous to the corrosion rate trend (which was obtained using R_{ct}) as shown in Figure 6.9. The C_{dl} value decrease from 41 in the 1st hour to $\sim$ 10 μF/cm^2 towards the 7-12th hour of immersion. This decrease is the reason behind the peak shift presented in phase angle Bode plot in Figure 6.15 c). The range of capacitance values lies in the typical range of double layer capacitance of bare metal/iron (1-100 μF/cm^2) reported in the literature [233–235]. The increase in siderite peak intensity from *in situ* GIXRD data (Figure 6.11) can support the measured electrochemical behaviour represented in the increase in charge transfer resistance (R_{ct}) and the decrease in double layer capacitance (C_{dl}). As the amount of siderite formed on the surface increases, the exposed metal surface area decreases resulting in the decrease seen in double layer capacitance values. Furthermore, the layer offers a resistive barrier (R_{scale}) limiting the access of corrosive medium to metal surface, which in turn results in an increase of charge transfer resistance (R_{ct}).

Table 6.2: EIS fitted paramaters from measured data during of Fe substrate immersed in CO_2 saturated water (T = 80°C, pH = 6.8) as a function of immersion time of initial 12 hours

Time (h)	R_s (Ω cm^2)	R_{ct} (Ω cm^2)	n	Q_{dl} (s^n/Ω cm^2)	C_{dl} (μF/cm^2)	R_{scale} (Ω cm^2)	n	Q_{scale} (s^n/Ω cm^2)	C_{scale} (μF/cm^2)	χ^2
1	56.7	536	0.71	2.43E-04	41	-	-	-	-	0.003
3	53.1	1092	0.72	1.31E-04	19	-	-	-	-	0.002
5	49.7	4189	0.79	5.59E-05	12	-	-	-	-	0.002
7	50.1	5866	0.83	3.56E-05	9.6	2963	0.86	3.68E-04	194	0.002
9	48.9	6423	0.84	3.59E-05	10	2901	0.89	4.10E-04	247	0.002
12	49.4	6514	0.85	3.56E-05	11	2664	0.90	4.27E-04	275	0.002

From the data fitted using nested equivalent circuit model, C_{scale}increases from 194 to 275 μF/cm^2. In comparison, these capacitance values are higher than double layer capacitance. The increase in capacitance values can be associated with the increase in surface area offered by the formed scale layer [236].

Immersion period after temperature excursion 17-28h

Moving to the second period from 17-28th of immersion at 80°C after introducing cooling & heating cycle. Figure 6.17 shows impedance spectra measured as a function immersion time presented in Nyquist plot and corresponding bode plots. EIS data represented by Nyquist plot in Figure 6.17 a) shows a clear change in electrochemical kinetics between the 12th (before cooling) and 17th (after heating) hour of immersion. The diameter of semi-circle at high frequency range decreased. Also, a two-time constant represented by the second semi-circle can be clearly distinguished from 17th hour data. After this drop, the capacitive semi-circles diameter increases again with time to show again an extended loop comprising of two semi-circles. However, the magnitude of loop is still smaller than what it after 12 hours (before cooling). Similar observation can be seen from Bode plot in Figure 6.17 b). No drastic changes can be seen from phase angle Bode plot in Figure 6.17 c) apart from a slight peak shift to lower phase angles and higher frequencies.

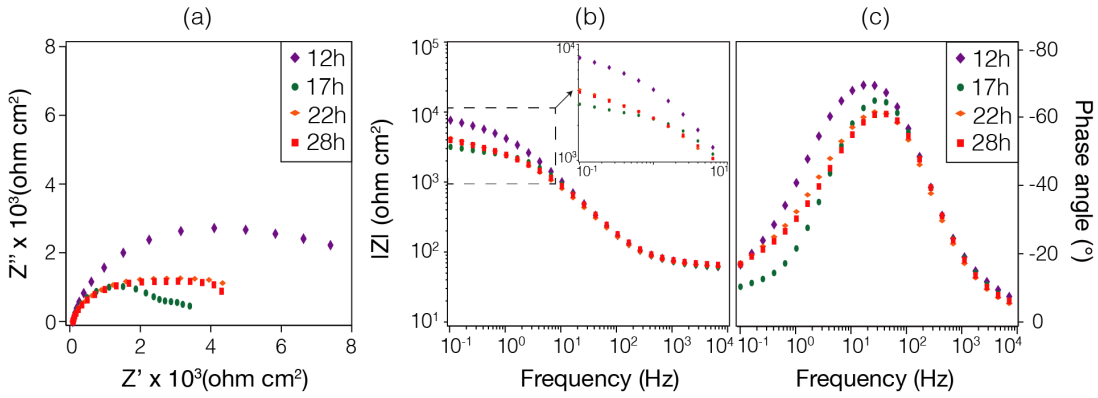

Figure 6.17: EIS data of synchrotron GIXRD diffractograms of Fe substrate immersed in CO_2 saturated water (T = 80°C, pH = 6.8) as a function of immersion time (12, 17 ,22 and 28 hours) represented in (a) Nyquist, (b) Bode and (c) phase angle plots.

The decrease in impedance amplitude as seen in Nyquist and Bode plots indicate a decrease charge transfer resistance (R_{ct}). This can be seen in the listed fitted parameters' values from EIS data in Table 6.3. All the data was fitted using scale equivalent circuit shown in Figure 6.16 b). The decrease in

resistance values (or a small increase in corrosion rates) is quite an interesting observation although the change in siderite peak intensity from *in situ* GIXRD measurements (Figure 6.13) was insignificant. This leaves us with two possible reasons on why the corrosion rates did not reach the previous values before the cooling-heating cycle. One, is that the cooling-heating cycle influenced the properties of the formed scale (e.g. porosity), resulting in such a slight increase in corrosion rates. The other explanation is that the homogeneity of scale regrowth after temperature excursion is different across the whole sample, knowing that 25% of the sample is scanned by GIXRD (which is considerably large percentage of the sample) and corrosion rate measurements are of averaging the entire exposed surface of the substrate.

Table 6.3: EIS fitted paramaters from measured data during of Fe substrate immersed in CO_2 saturated water (T = 80°C, pH = 6.8) during immersion period 12-28 hours

Time (h)	R_s (Ω cm^2)	R_{ct} (Ω cm^2)	n	Q_{dl} (s^n/Ω cm^2)	C_{dl} (μF/cm^2)	R_{scale} (Ω cm^2)	n	Q_{scale} (s^n/Ω cm^2)	C_{scale} (μF/cm^2)	χ^2
12	49.4	6514	0.85	3.56E-05	11	2664	0.90	4.27E-04	275	0.0020
17	48.6	2602	0.86	3.22E-05	8.7	1000	0.86	1.70E-03	885	0.0003
22	49.1	2491	0.83	4.15E-05	9.0	3210	0.63	3.77E-04	27.8	0.0003
28	51.3	2282	0.83	3.62E-05	8.0	3176	0.60	3.82E-04	21.6	0.0004

6.4 Conclusion

SR-cell has been employed in this study to investigate sweet corrosion scale evolution/dissolution in an *in situ* synchrotron experiment of Fe immersed in CO_2 -saturated solution (T= 25°C - 80°C, pH=6.1 - 6.8) for a total duration of 28 hours. At scaling conditions of 80°C and pH = 6.8, *in situ* GIXRD plots showed formation of siderite as a corrosion product in the initial 12 hours of immersion. From the *in situ* GIXRD plots, amount of siderite was found to be increasing rapidly from the 1st until 7th hours of immersion. It was found that substrate corrosion rate decreases and follows the same trend as the increase

in amount of siderite confirming that an increase in siderite amount/coverage is directly related to corrosion behaviour of the sample. When compared with laboratory experiments, corrosion rates followed similar trend as in the *in situ* experiment but slightly higher corrosion rates were observed. Post immersion ex situ GIXRD characterisation of these experiments showed formation of chukanovite and siderite.

A cooling and heating cycle was introduced to the system between 12-28 hours of immersion to study the influence of temperature excursion on the established scale. The scale dissolved after 2 hours from dropping the temperature to 25°C. As the temperature increased back to 80°C, siderite regrows back to a similar amount formed prior to introducing the cooling/heating cycle. However, estimated corrosion rates increased slightly in this case. Figure 6.18 presents a summary of the *in situ* synchrotron experiment.

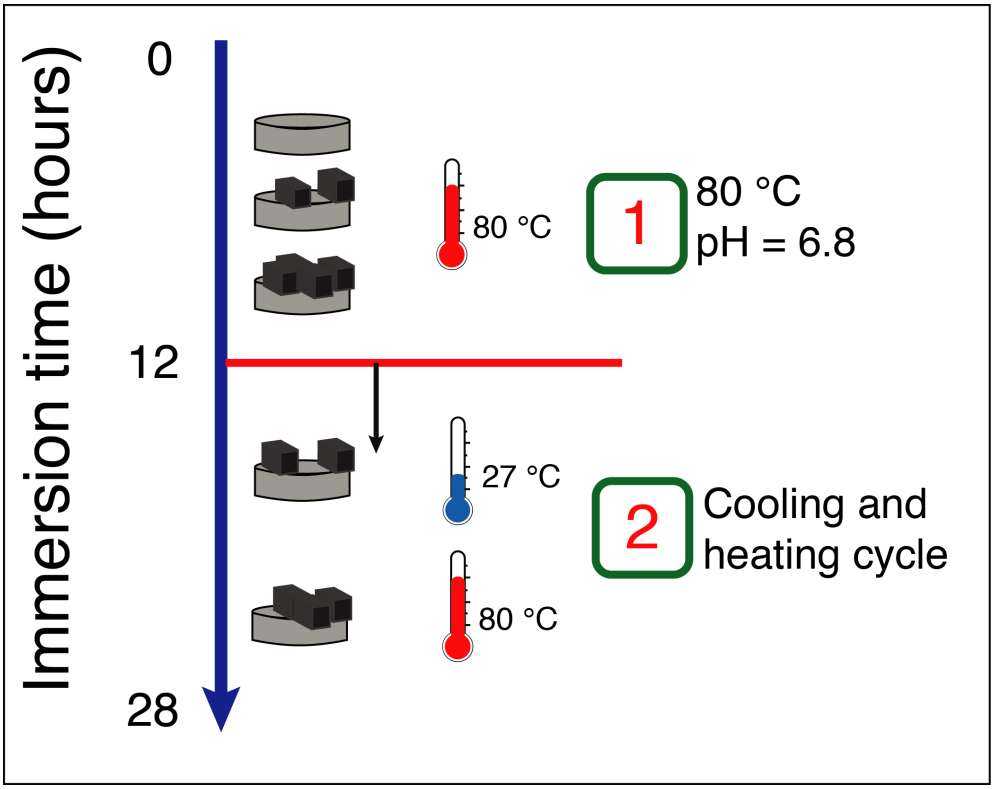

Figure 6.18: Summary Fe substrate immersed in CO_2 saturated water (T = 25°C - 80°C, pH = 6.1 - 6.8) for 28 hours immersion time.

Chapter 7.

Summary and Future Work

This goal of the research in this thesis is to improve understanding of oilfield sweet scale evolution, utilising a number of *ex situ* and *in situ* techniques. The main points of interest from the results chapters (4-6) are summarized below.

Previous work within the research group reported a '*cylindrical*' siderite crystal habit forming on a corroding Fe substrate after immersion in CO_2-saturated water (buffered to pH = 6.8, T = 80°C and P_{CO_2} = 0.54 bar). Similar crystal habits were observed elsewhere in the literature, although not explicitly described; a rhombohedral siderite crystal habit was observed on corroding substrates in another studies conducted under different conditions.

A theoretical model predicting siderite crystal habit showed that an increase in $\Delta\mu$Fe (or $Fe^{2+}_{(aq)}$ concentration) results in a change in the habit from rhombohedral to cylindrical and then to an elongated cylindrical habit by a further increase in $\Delta\mu$Fe. Therefore, in *Chapter 4*, the siderite crystal habit was explored firstly on corroding Fe substrates and non-corroding PTFE substrates after immersion in CO_2 saturated 0.01 M $FeCl_2$ solutions (pH = 6.8, T = 80°C and P_{CO_2} = 0.54 bar). Experimental observation of siderite crystal habit was consistent with the theoretical model and it showed formation of a rhombohedral crystal on PTFE substrate (Fe poor condition), while cylindrical habit formed on Fe substrate (Fe rich condition). These observations were further confirmed by increasing the concentration of $Fe^{2+}_{(aq)}$ from 0.01 M to 0.1 M resulting in a change from rhombohedral to cylindrical habit on PTFE substrates. Under the same conditions, an elongation of the siderite cylindrical habit formed on Fe substrate was observed, which is also consistent with the theoretical modelling. Furthermore, the crystallographic orientation of the {104} siderite crystal facets was proven, employing EBSD technique in conjunction with confocal microscopy, and in order to confirm the assignments of the facets based on the theoretical model.

Exploring the siderite crystal habit on Fe substrates was extended in *Chapter 5* to include the impact of CO_2 partial pressure. For this purpose, an

autoclave facility was developed and exploited with careful considerations of experimental design and procedure, to avoid any experimental artefacts in the observed results. The results showed that an increase in CO_2 partial pressure from 0.5 bar to 4 bar resulted in a change in the siderite crystal habit from cylindrical to rhombohedral habit. Again, this observation is also consistent with the theoretical model of the siderite crystal, which predicts this change with the increase in $\Delta\mu CO_2$ (analogous to CO_2 partial pressure). In addition to the crystal habit change, corrosion rates estimated from electrochemical techniques suggested that an increase in the temperature (from T = 80°C to 150 °C) and pressure (from P_{CO_2} = 0.5 bar to 4 bar) results in a formation of a more protective scale on Fe substrate after immersion for 24 hours. This was supplemented with scale characterisation by SEM and GIXRD, which showed higher coverage, thicker and more densely packed scale formed at higher temperatures and pressures.

Chapter 6 presented an improved design of a custom-built cell implemented to perform both *in situ* synchrotron radiation GIXRD and electrochemical measurements on a Fe substrate immersed in CO_2-saturated solution. This chapter focused initially on the evolution of sweet scale at a constant temperature CO_2-saturated solution (pH = 6.8, T = 80°C). During this immersion period of 12 hours, analysis of electrochemical data and acquired diffractograms demonstrated that siderite was mainly responsible for the reduction in corrosion rate. After this initial period, the influence of temperature excursion on the formed scale was investigated by cooling the solution to ~25°C, then heating back to 80°C. The results showed dissolution of formed siderite scale at lower temperature, followed by scale regrowth to a slightly less protective siderite scale as the temperature increased to 80°C.

Linking the results from all chapters, it is clear that the scale formation is greatly influenced by several factors. This work offered a different view point in studying sweet corrosion scale by showing how several factors can influence the siderite crystal habit that if controlled (e.g. habit engineering) to form less

reactive version of the habit, can provide an alternative approach to corrosion control by improving the degree of scale protection and minimising the risk of breakdown. As the *in situ* synchrotron experiment showed that the sweet scale was prone to dissolution as a function of temperature, a way forward to complement this work is to: (i) compare the dissolution rates of the different siderite crystal habits, and (ii) the dissolution rates of the different facets, {104} and {*hk*0}, in the cylindrical habit. This can potentially be investigated by implementing an *in situ* confocal/optical microscopy technique using a suitable cell, similar to the one developed for *in situ* GIXRD work.

Regarding the factors influencing the siderite crystal habit, it is worth exploring the scale habit evolution as a function of time. In addition, the influence of other factors can be explored, such as: corrosion inhibitors, scale inhibitors and organic acids, which are commonly present in oilfield pipelines.

A similar approach can be employed to investigate chukanovite crystal habits and investigate the influence of various conditions. As it was shown that chukanovite does not seem to offer the same degree of protection provided by siderite, further work is required to understand whether chukanovite can possibly impede protective siderite scale formation at early stages of scale formation.

Finally, as shown in *Chapter 5*, experiments performed at higher pressures and temperatures using an autoclave setup are usually more challenging. Further changes in the experimental setup can potentially provide certain improvements, especially regarding sample removal after immersion. Placing the autoclave setup in a N_2-filled glove box can minimise the risk of scale modification upon exposure of the substrate directly to air post-immersion. This setup can be expanded to further study a wider range of temperatures and pressures. Also, it can be employed with further modifications to study sour systems or mixed sour and sweet systems.

References

[1] L. T. Popoola, A. S. Grema, G. K. Latinwo, B. Gutti, and A. S. Balogun, "Corrosion problems during oil and gas production and its mitigation," *International Journal of Industrial Chemistry*, vol. 4, no. 1, p. 35, 2013.

[2] M. Kermani, D. Harrop, *et al.*, "The impact of corrosion on oil and gas industry," *SPE Production & Facilities*, vol. 11, no. 03, pp. 186–190, 1996.

[3] C. I. Ossai, B. Boswell, and I. J. Davies, "Pipeline failures in corrosive environments–A conceptual analysis of trends and effects," *Engineering Failure Analysis*, vol. 53, pp. 36–58, 2015.

[4] M. Kermani and A. Morshed, "Carbon dioxide corrosion in oil and gas production—a compendium," *Corrosion*, vol. 59, no. 8, pp. 659–683, 2003.

[5] G. R. Joshi, K. Cooper, X. Zhong, A. B. Cook, E. A. Ahmad, N. M. Harrison, D. L. Engelberg, and R. Lindsay, "Temporal evolution of sweet oilfield corrosion scale: Phases, morphologies, habits, and protection," *Corrosion Science*, vol. 142, pp. 110–118, 2018.

[6] J. Han, S. Nešić, Y. Yang, and B. N. Brown, "Spontaneous passivation observations during scale formation on mild steel in CO2 brines," *Electrochimica Acta*, vol. 56, no. 15, pp. 5396–5404, 2011.

[7] E. Gulbrandsen, J. H. Morard, *et al.*, "Study of the possible mechanisms of steel passivation in CO2 corrosion," in *Corrosion*, NACE International, 1999.

[8] R. M. Fernández-Domene, J. Andrews, R. Leiva-García, and R. Akid, "Galvanic Corrosion Following Local Breakdown of a Scale Formed on X-65 in CO2 Saturated Solutions," in *Corrosion*, NACE International, 2015.

[9] F. Pessu, R. Barker, and A. Neville, "Pitting and uniform corrosion of X65 carbon steel in sour corrosion environments: the influence of CO2, H2S, and temperature," *Corrosion*, vol. 73, no. 9, pp. 1168–1183, 2017.

[10] M. G. Fontana, *Corrosion engineering*. Tata McGraw-Hill Education, 2005.

[11] P. R. Roberge, *Corrosion engineering*. Mcgraw-hill New York, NY, USA:, 2008.

[12] D. Landolt, "Introduction to surface reactions: electrochemical basis of corrosion," *Corrosion Technology-New York and Basel*, vol. 17, pp. 1–18, 2002.

[13] P. R. Roberge, *Handbook of corrosion engineering*. McGraw-Hill, 2000.

[14] U. Soytaş and R. Sarı, *Routledge Handbook of Energy Economics*. Routledge, 2019.

[15] R. Heidersbach, *Metallurgy and corrosion control in oil and gas production*. John Wiley & Sons, 2018.

[16] Department of Trade and Industry, "An Overview of Offshore Oil and Gas Exploration and Production Activities," 2001.

[17] S. Papavinasam, *Corrosion control in the oil and gas industry*. Elsevier, 2013.

[18] R. Jarvis and A. Goddard, "An analysis of common causes of major losses in the onshore oil, gas & petrochemical industries.," *Loss Prevention Bulletin*, no. 255, 2017.

[19] C. De Waard and D. Milliams, "Carbonic acid corrosion of steel," *Corrosion*, vol. 31, no. 5, pp. 177–181, 1975.

[20] C. De Waard, U. Lotz, and D. Milliams, "Predictive model for CO2 corrosion engineering in wet natural gas pipelines," *Corrosion*, vol. 47, no. 12, pp. 976–985, 1991.

[21] B. Linter and G. Burstein, "Reactions of pipeline steels in carbon dioxide solutions," *Corrosion science*, vol. 41, no. 1, pp. 117–139, 1999.

[22] L. Moiseeva, "Carbon dioxide corrosion of oil and gas field equipment," *Protection of metals*, vol. 41, no. 1, pp. 76–83, 2005.

[23] S. Nesic, N. Thevenot, J. L. Crolet, D. Drazic, *et al.*, "Electrochemical properties of iron dissolution in the presence of CO2-basics revisited," in *Corrosion*, Nace International, 1996.

[24] T. Tanupabrungsun, B. Brown, S. Nesic, *et al.*, "Effect of pH on CO2 corrosion of mild steel at elevated temperatures," *Corrosion*, no. 48, 2013.

[25] S. Nešić, "Key issues related to modelling of internal corrosion of oil and gas pipelines–A review," *Corrosion science*, vol. 49, no. 12, pp. 4308–4338, 2007.

[26] G. Schmitt, M. Horstemeier, *et al.*, "Fundamental aspects of CO2 metal loss corrosion-Part II: Influence of different parameters on CO2 corrosion mechanisms," in *Corrosion*, NACE International, 2006.

[27] A. Dugstad *et al.*, "Mechanism of protective film formation during CO2 corrosion of carbon steel," in *Corrosion*, Nace International, 1998.

[28] C. Palacios and J. Shadley, "Characteristics of corrosion scales on steels in a CO2-saturated NaCl brine," *Corrosion*, vol. 47, no. 2, pp. 122–127, 1991.

[29] K. Videm and A. Koren, "Corrosion, passivity, and pitting of carbon steel in aqueous solutions of HCO3-, CO2, and Cl-," *Corrosion*, vol. 49, no. 9, pp. 746–754, 1993.

[30] S. N. Smith, M. W. Joosten, *et al.*, "Corrosion of carbon steel by H2S in CO2 containing oilfield environments," in *Corrosion*, NACE International, 2006.

[31] Y. Zheng, J. Ning, B. Brown, D. Young, S. Nesic, *et al.*, "Mechanistic study of the effect of iron sulfide layers on hydrogen sulfide corrosion of carbon steel," *Corrosion*, p. 5933, 2015.

[32] W. Sun and S. Nesic, "A mechanistic model of H2S corrosion of mild steel," *Corrosion*, 2007.

[33] Y.-S. Choi, S. Nesic, and S. Ling, "Effect of H2S on the CO2 corrosion of carbon steel in acidic solutions," *Electrochimica Acta*, vol. 56, no. 4, pp. 1752–1760, 2011.

[34] J. N. Butler, *Carbon dioxide equilibria and their applications*. Routledge, 2019.

[35] W. Stumm and J. J. Morgan, *Aquatic chemistry: chemical equilibria and rates in natural waters*, vol. 126. John Wiley & Sons, 2012.

[36] R. E. Zeebe and D. Wolf-Gladrow, *CO2 in seawater: equilibrium, kinetics, isotopes*. No. 65, Gulf Professional Publishing, 2001.

[37] Z. Duan and R. Sun, "An improved model calculating CO2 solubility in pure water and aqueous NaCl solutions from 273 to 533 K and from 0 to 2000 bar," *Chemical geology*, vol. 193, no. 3-4, pp. 257–271, 2003.

[38] D. Li and Z. Duan, "The speciation equilibrium coupling with phase equilibrium in the H2O–CO2–NaCl system from 0 to 250 C, from 0 to 1000 bar, and from 0 to 5 molality of NaCl," *Chemical Geology*, vol. 244, no. 3-4, pp. 730–751, 2007.

[39] D. A. Palmer and R. Van Eldik, "The chemistry of metal carbonate and carbon dioxide complexes," *Chemical Reviews*, vol. 83, no. 6, pp. 651–731, 1983.

[40] A. Kahyarian, M. Achour, and S. Nesic, "7 - CO2 corrosion of mild steel," in *Trends in Oil and Gas Corrosion Research and Technologies* (A. El-Sherik, ed.), Woodhead Publishing Series in Energy, pp. 149 – 190, Boston: Woodhead Publishing, 2017.

[41] A. Kahyarian, M. Achour, and S. Nesic, "34 - Mathematical modeling of uniform CO2 corrosion," in *Trends in Oil and Gas Corrosion Research and Technologies* (A. El-Sherik, ed.), Woodhead Publishing Series in Energy, pp. 805 – 849, Boston: Woodhead Publishing, 2017.

[42] R. Weiss, "Carbon dioxide in water and seawater: the solubility of a non-ideal gas," *Marine chemistry*, vol. 2, no. 3, pp. 203–215, 1974.

[43] J. E. Oddo, M. B. Tomson, *et al.*, "Simplified calculation of CaCO3 saturation at high temperatures and pressures in brine solutions," *Journal of Petroleum Technology*, vol. 34, no. 07, pp. 1–583, 1982.

[44] M. Nordsveen, S. Nešic, R. Nyborg, and A. Stangeland, "A mechanistic model for carbon dioxide corrosion of mild steel in the presence of protective iron carbonate films—part 1: theory and verification," *Corrosion*, vol. 59, no. 5, pp. 443–456, 2003.

[45] J. J. Carroll, J. D. Slupsky, and A. E. Mather, "The solubility of carbon dioxide in water at low pressure," *Journal of Physical and Chemical Reference Data*, vol. 20, no. 6, pp. 1201–1209, 1991.

[46] Z. Duan and D. Li, "Coupled phase and aqueous species equilibrium of the H2O–CO2–NaCl–CaCO3 system from 0 to 250 C, 1 to 1000 bar with NaCl concentrations up to saturation of halite," *Geochimica et Cosmochimica Acta*, vol. 72, no. 20, pp. 5128–5145, 2008.

[47] L. C. Garg and T. H. Maren, "The rates of hydration of carbon dioxide and dehydration of carbonic acid at 37," *Biochimica et Biophysica Acta (BBA)-General Subjects*, vol. 261, no. 1, pp. 70–76, 1972.

[48] D. M. Kern, "The hydration of carbon dioxide," *Journal of Chemical Education*, vol. 37, no. 1, p. 14, 1960.

[49] A. L. Soli and R. H. Byrne, "CO2 system hydration and dehydration kinetics and the equilibrium CO2/H2CO3 ratio in aqueous NaCl solution," *Marine chemistry*, vol. 78, no. 2-3, pp. 65–73, 2002.

[50] Z. Duan, R. Sun, C. Zhu, and I.-M. Chou, "An improved model for the calculation of CO2 solubility in aqueous solutions containing Na+, K+, Ca2+, Mg2+, Cl-, and SO42-," *Marine Chemistry*, vol. 98, no. 2-4, pp. 131–139, 2006.

[51] S. Nešić and W. Sun, "Shreir's Corrosion: Corrosion in acid gas solutions, Vol. 2," 2010.

[52] A. Kahyarian, M. Achour, and S. Nesic, "CO_2 corrosion of mild steel," in *Trends in Oil and Gas Corrosion Research and Technologies*, pp. 149–190, Elsevier, 2017.

[53] A. Kahyarian and S. Nesic, "A New Narrative for CO2 Corrosion of Mild Steel," *Journal of The Electrochemical Society*, vol. 166, no. 11, pp. C3048–C3063, 2019.

[54] J. K. Nørskov, T. Bligaard, A. Logadottir, J. Kitchin, J. G. Chen, S. Pandelov, and U. Stimming, "Trends in the exchange current for hydrogen evolution," *Journal of The Electrochemical Society*, vol. 152, no. 3, pp. J23–J26, 2005.

[55] J. O. Bockris and D. Koch, "Comparative rates of the electrolytic evolution of hydrogen and deuterium on iron, tungsten and platinum," *The Journal of Physical Chemistry*, vol. 65, no. 11, pp. 1941–1948, 1961.

[56] Y. Xu, "The hydrogen evolution reaction on single crystal gold electrode," *International Journal of Hydrogen Energy*, vol. 34, no. 1, pp. 77–83, 2009.

[57] M. Devanathan and Z. Stachurski, "The mechanism of hydrogen evolution on iron in acid solutions by determination of permeation rates," *Journal of the electrochemical society*, vol. 111, no. 5, pp. 619–623, 1964.

[58] J. Bockris, J. McBreen, and L. Nanis, "The hydrogen evolution kinetics and hydrogen entry into a-iron," *Journal of the electrochemical society*, vol. 112, no. 10, pp. 1025–1031, 1965.

[59] G. Schmitt and B. Rothmann, "Studies on the Corrosion Mechanism of Unalloyed Steel in Oxygen-Free Carbon Dioxide Solutions, Part I. Kinetics of the Liberation of Hydrogen," *Werkstoffe und Korrosion*, vol. 28, pp. 816–822, 1977.

[60] A. Wieckowski, E. Ghali, M. Szklarczyk, and J. Sobkowski, "The behaviour of iron electrode in CO2- saturated neutral electrolyte—I. Electrochemical study," *Electrochimica Acta*, vol. 28, no. 11, pp. 1619–1626, 1983.

[61] A. Wieckowski, E. Ghali, M. Szklarczyk, and J. Sobkowski, "The behaviour of iron electrode in CO2- saturated neutral electrolyte—II. Radiotracer study and corrosion considerations," *Electrochimica acta*, vol. 28, no. 11, pp. 1627–1633, 1983.

[62] T. Hurlen, S. Gunvaldsen, R. Tunold, F. Blaker, and P. Lunde, "Effects of carbon dioxide on reactions at iron electrodes in aqueous salt solutions," *Journal of electroanalytical chemistry and interfacial electrochemistry*, vol. 180, no. 1-2, pp. 511–526, 1984.

[63] T. Tran, B. Brown, S. Nesic, *et al.*, "Corrosion of mild steel in an aqueous CO2 environment—basic electrochemical mechanisms revisited," *Corrosion*, 2015.

[64] E. Remita, B. Tribollet, E. Sutter, V. Vivier, F. Ropital, and J. Kittel, "Hydrogen evolution in aqueous solutions containing dissolved CO2: Quantitative contribution of the buffering effect," *Corrosion Science*, vol. 50, no. 5, pp. 1433–1440, 2008.

[65] J. Han, J. Zhang, and J. W. Carey, "Effect of bicarbonate on corrosion of carbon steel in CO2 saturated brines," *International Journal of Greenhouse Gas Control*, vol. 5, no. 6, pp. 1680–1683, 2011.

[66] G. Ogundele and W. White, "Some observations on corrosion of carbon steel in aqueous environments containing carbon dioxide," *Corrosion*, vol. 42, no. 2, pp. 71–78, 1986.

[67] A. Dugstad, "Fundamental aspects of CO2 metal loss corrosion-part 1: mechanism," *Corrosion*, 2006.

[68] R. Barker, D. Burkle, T. Charpentier, H. Thompson, and A. Neville, "A review of iron carbonate (FeCO3) formation in the oil and gas industry," *Corrosion Science*, vol. 142, pp. 312–341, 2018.

[69] B. JO'M, D. Drazic, and A. Despic, "The electrode kinetics of the deposition and dissolution of iron," *Electrochimica Acta*, vol. 4, no. 2-4, pp. 325–361, 1961.

[70] B. JO'M and D. Drazic, "The kinetics of deposition and dissolution of iron: Effect of alloying impurities," *Electrochimica Acta*, vol. 7, no. 3, pp. 293–313, 1962.

[71] D. M. Dražić, "Iron and its Electrochemistry in an Active State," in *Modern Aspects of Electrochemistry*, pp. 69–192, Springer, 1989.

[72] X. Ming, X.-L. Wang, F. Du, J.-W. Yin, C.-Z. Wang, and G. Chen, "First-principles study of pressure-induced magnetic transition in siderite FeCO3," *Journal of Alloys and Compounds*, vol. 510, no. 1, pp. L1–L4, 2012.

[73] C. M. S. Figueiredo, A. G. B. Junior, E. M. Flaten, R. Beck, and M. Seiersten, "Crystal growth of FeCO3 in mixed monoethylene glycol and water solvent," *Crystal Research and Technology*, vol. 50, no. 5, pp. 354–361, 2015.

[74] D. C. Palmer, "Crystal Maker Software Ltd.." Available online: http://crystalmaker.com/crystalmaker/index.html (Last accessed 15-Dec-2019.

[75] M. Gao, X. Pang, and K. Gao, "The growth mechanism of CO2 corrosion product films," *Corrosion Science*, vol. 53, no. 2, pp. 557–568, 2011.

[76] J. Mullin, "5 - nucleation," in *Crystallization (Fourth Edition)* (J. Mullin, ed.), pp. 181 – 215, Oxford: Butterworth-Heinemann, fourth edition ed., 2001.

[77] W. Sun, S. Nešić, and R. C. Woollam, "The effect of temperature and ionic strength on iron carbonate (FeCO3) solubility limit," *Corrosion Science*, vol. 51, no. 6, pp. 1273–1276, 2009.

[78] C. A. Silva, X. Liu, and F. J. Millero, "Solubility of siderite (FeCO 3) in NaCl solutions," *Journal of solution chemistry*, vol. 31, no. 2, pp. 97–108, 2002.

[79] M. L. Johnson, *Ferrous carbonate precipitation kinetics: A temperature ramped approach*. PhD thesis, 1991.

[80] M. Johnson and M. Tomson, "Ferrous carbonate precipitation kinetics and its impact CO 2 corrosion," *M. L. Johnson, M. B. Tomson, Corrosion 91/268, NACE, Houston, TX. Per Copy 5*, 1991.

[81] R. D. Braun, "Solubility of iron (II) carbonate at temperatures between 30 and 80," *Talanta*, vol. 38, no. 2, pp. 205–211, 1991.

[82] S. Guo, L. Xu, L. Zhang, W. Chang, and M. Lu, "Corrosion of alloy steels containing 2% chromium in CO2 environments," *Corrosion Science*, vol. 63, pp. 246–258, 2012.

[83] R. Davey and J. Garside, *From molecules to crystallizers*. Oxford University Press, 2000.

[84] T. Tanupabrungsun, D. Young, B. Brown, S. Nešic, *et al.*, "Construction and verification of pourbaix diagrams for CO2 corrosion of mild steel valid up to 250 C," in *Corrosion*, NACE International, 2012.

[85] S. Savoye, L. Legrand, G. Sagon, S. Lecomte, A. Chausse, R. Messina, and P. Toulhoat, "Experimental investigations on iron corrosion products formed in bicarbonate/carbonate-containing solutions at 90 C," *Corrosion Science*, vol. 43, no. 11, pp. 2049–2064, 2001.

[86] F. Pessu, R. Barker, and A. Neville, "The influence of pH on localized corrosion behavior of X65 carbon steel in CO2-saturated brines," *Corrosion*, vol. 71, no. 12, pp. 1452–1466, 2015.

[87] I. V. Pekov, N. Perchiazzi, S. Merlino, V. N. Kalachev, M. Merlini, and A. E. Zadov, "Chukanovite, Fe2 (CO3)(OH) 2, a new mineral from the weathered iron meteorite Dronino," *European Journal of Mineralogy*, vol. 19, no. 6, pp. 891–898, 2007.

[88] I. Pignatelli, E. Mugnaioli, R. Mosser-Ruck, O. Barres, U. Kolb, and N. Michau, "A multi-technique, micrometer-to atomic-scale description of a synthetic analogue of chukanovite, Fe2 (CO3)(OH) 2," *European Journal of Mineralogy*, vol. 26, no. 2, pp. 221–229, 2014.

[89] M. Saheb, D. Neff, P. Dillmann, H. Matthiesen, E. Foy, and L. Bellot-Gurlet, "Multisecular corrosion behaviour of low carbon steel in anoxic soils: characterisation of corrosion system on archaeological artefacts," *Materials and corrosion*, vol. 60, no. 2, pp. 99–105, 2009.

[90] M. Saheb, M. Descostes, D. Neff, H. Matthiesen, A. Michelin, and P. Dillmann, "Iron corrosion in an anoxic soil: Comparison between thermodynamic modelling and ferrous archaeological artefacts characterised along with the local in situ geochemical conditions," *Applied geochemistry*, vol. 25, no. 12, pp. 1937–1948, 2010.

[91] M. Saheb, D. Neff, P. Dillmann, H. Matthiesen, and E. Foy, "Long-term corrosion behaviour of low-carbon steel in anoxic environment: characterisation of archaeological artefacts," *Journal of Nuclear Materials*, vol. 379, no. 1-3, pp. 118–123, 2008.

[92] M. L. Schlegel, C. Bataillon, K. Benhamida, C. Blanc, D. Menut, and J.-L. Lacour, "Metal corrosion and argillite transformation at the water-saturated, high-temperature iron–clay interface: a microscopic-scale study," *Applied Geochemistry*, vol. 23, no. 9, pp. 2619–2633, 2008.

[93] M. L. Schlegel, C. Bataillon, C. Blanc, D. Pret, and E. Foy, "Anodic activation of iron corrosion in clay media under water-saturated conditions at 90 C: Characterization of the corrosion interface," *Environmental Science & Technology*, vol. 44, no. 4, pp. 1503–1508, 2010.

[94] T. Tanupabrungsun, *Thermodynamics and kinetics of carbon dioxide corrosion of mild steel at elevated temperatures*. PhD thesis, Ohio University, 2012.

[95] I. Azoulay, C. Rémazeilles, and P. Refait, "Determination of standard Gibbs free energy of formation of chukanovite and Pourbaix diagrams of iron in carbonated media," *Corrosion science*, vol. 58, pp. 229–236, 2012.

[96] B. Ingham, M. Ko, G. Kear, P. Kappen, N. Laycock, J. Kimpton, and D. Williams, "In situ synchrotron X-ray diffraction study of surface scale formation during CO2 corrosion of carbon steel at temperatures up to 90° C," *Corrosion Science*, vol. 52, no. 9, pp. 3052–3061, 2010.

[97] B. Ingham, M. Ko, N. Laycock, J. Burnell, P. Kappen, J. Kimpton, and D. Williams, "In situ synchrotron X-ray diffraction study of scale formation during CO2 corrosion of carbon steel in sodium and magnesium chloride solutions," *Corrosion Science*, vol. 56, pp. 96–104, 2012.

[98] G. Lin, M. Zheng, Z. Bai, and X. Zhao, "Effect of temperature and pressure on the morphology of carbon dioxide corrosion scales," *Corrosion*, vol. 62, no. 6, pp. 501–507, 2006.

[99] W. Sun and S. Nesic, "Basics revisited: kinetics of iron carbonate scale precipitation in CO2 corrosion," *Corrosion*, 2006.

[100] J. Heuer and J. F. Stubbins, "Microstructure analysis of coupons exposed to carbon dioxide corrosion in multiphase flow," *Corrosion*, vol. 54, no. 7, pp. 566–575, 1998.

[101] S. Papavinasam, A. Doiron, J. Li, D.-Y. Park, P. Liu, *et al.*, "Sour and sweet corrosion of carbon steel: general or pitting or localized or all of the above?," in *Corrosion*, NACE International, 2010.

[102] W. Sun, *Kinetics of iron carbonate and iron sulfide scale formation in CO 2/H 2 S corrosion*. PhD thesis, Ohio University, 2006.

[103] Y.-S. Choi, F. Farelas, S. Nešić, A. A. O. Magalhães, and C. de Azevedo Andrade, "Corrosion behavior of deep water oil production tubing material under supercritical CO2 environment: part 1—effect of pressure and temperature," *Corrosion*, vol. 70, no. 1, pp. 38–47, 2013.

[104] Z. F. Yin, Y. Feng, W. Zhao, Z. Bai, and G. Lin, "Effect of temperature on CO2 corrosion of carbon steel," *Surface and Interface Analysis: An International Journal devoted to the development and application of techniques for the analysis of surfaces, interfaces and thin films*, vol. 41, no. 6, pp. 517–523, 2009.

[105] M. H. Nazari, S. Allahkaram, and M. Kermani, "The effects of temperature and pH on the characteristics of corrosion product in CO2 corrosion of grade X70 steel," *Materials & Design*, vol. 31, no. 7, pp. 3559–3563, 2010.

[106] R. Jasinski, "Corrosion of N80-type steel by CO2/water mixtures," *Corrosion*, vol. 43, no. 4, pp. 214–218, 1987.

[107] Y. Zhang, X. Pang, S. Qu, X. Li, and K. Gao, "Discussion of the CO2 corrosion mechanism between low partial pressure and supercritical condition," *Corrosion Science*, vol. 59, pp. 186–197, 2012.

[108] R. De Marco, Z.-T. Jiang, D. John, M. Sercombe, and B. Kinsella, "An in situ electrochemical impedance spectroscopy/synchrotron radiation grazing incidence X-ray diffraction study of the influence of acetate on the carbon dioxide corrosion of mild steel," *Electrochimica acta*, vol. 52, no. 11, pp. 3746–3750, 2007.

[109] P. Refait, J. Bourdoiseau, M. Jeannin, D. Nguyen, A. Romaine, and R. Sabot, "Electrochemical formation of carbonated corrosion products on carbon steel in deaerated solutions," *Electrochimica Acta*, vol. 79, pp. 210–217, 2012.

[110] V. Pandarinathan, K. Lepková, and W. Van Bronswijk, "Chukanovite (Fe2 (OH) 2CO3) identified as a corrosion product at sand-deposited carbon steel in CO2-saturated brine," *Corrosion Science*, vol. 85, pp. 26–32, 2014.

[111] S. Al-Hassan, B. Mishra, D. Olson, and M. Salama, "Effect of microstructure on corrosion of steels in aqueous solutions containing carbon dioxide," *Corrosion*, vol. 54, no. 6, pp. 480–491, 1998.

[112] B. Ingham, M. Ko, N. Laycock, N. M. Kirby, and D. E. Williams, "First stages of siderite crystallisation during CO2 corrosion of steel evaluated using in situ synchrotron small-and wide-angle X-ray scattering," *Faraday discussions*, vol. 180, pp. 171–190, 2015.

[113] M. H. Sk, A. M. Abdullah, M. Ko, B. Ingham, N. Laycock, R. Arul, and D. E. Williams, "Local supersaturation and the growth of protective scales during CO2 corrosion of steel: Effect of pH and solution flow," *Corrosion Science*, vol. 126, pp. 26–36, 2017.

[114] B. Ingham, M. Ko, P. Shaw, M. H. Sk, A. M. Abdullah, N. Laycock, and D. E. Williams, "Effects of Oxygen on Scale Formation in CO2 Corrosion of Steel in Hot Brine: In Situ Synchrotron X-ray Diffraction Study of Anodic Products," *Journal of The Electrochemical Society*, vol. 165, no. 11, pp. C756–C761, 2018.

[115] E. W. L. Chan, *Magnetite and its galvanic effect on the corrosion of carbon steel under carbon dioxide environments*. PhD thesis, Curtin University, 2011.

[116] A. Dunlop, H. Hassell, and P. Rhodes, "Fundamental considerations in sweet gas well corrosion," in *Corrosion*, pp. 461–4624, 1983.

[117] D. W. Shannon, "Corrosion of Iron-base Alloys versus Alternate Materials in Geothermal Brines (Interim Report-Period Ending October 1977)," tech. rep., Pacific Northwest National Lab.(PNNL), Richland, WA (United States), 1977.

[118] M. Ueda, H. Takabe, *et al.*, "Effect of environmental factor and microstructure on morphology of corrosion products in CO2 environments," in *Corrosion*, NACE International, 1999.

[119] E. Van Hunnik, E. Hendriksen, B. F. Pots, *et al.*, "The Formation of Protective Fe3Co2 Corrosion Product Layers in CO Corrosion," in *Corrosion*, Nace International, 1996.

[120] L. G. Gray, B. G. Anderson, M. J. Danysh, and P. R. Tremaine, "Effect of pH and temperature on the mechanism of carbon steel corrosion by aqueous carbon dioxide," *Corrosion*, vol. 40, 1990.

[121] W. Li, B. Brown, D. Young, and S. Nešić, "Investigation of pseudo-passivation of mild steel in CO2 corrosion," *Corrosion*, vol. 70, no. 3, pp. 294–302, 2013.

[122] Y. Yang, B. Brown, S. Nesic, *et al.*, "Study of Protective Iron Carbonate Layer Dissolution in a CO2 Corrosion Environment," in *NACE Corrosion Conference and Expo*, 2012.

[123] S. Nesic, K.-L. J. Lee, V. Ruzic, *et al.*, "A mechanistic model of iron carbonate film growth and the effect on CO2 corrosion of mild steel," *Corrosion*, vol. 2237, 2002.

[124] A. B. Gavanluei, B. Mishra, D. L. Olson, *et al.*, "Corrosion rate measurement of a downhole tubular steel at different CO2 partial pressures and temperatures and calculation of the activation energy of the corrosion process," *Corrosion*, pp. 17–21, 2013.

[125] M. Suhor, M. Mohamed, A. M. Nor, M. Singer, S. Nesic, *et al.*, "Corrosion of mild steel in high CO2 environment: Effect of the FeCO3 layer," in *Corrosion*, NACE International, 2012.

[126] G. Zhang, M. Lu, Y. Qiu, X. Guo, and Z. Chen, "The relationship between the formation process of corrosion scales and the electrochemical mechanism of carbon steel in high pressure CO2-containing formation water," *Journal of The Electrochemical Society*, vol. 159, no. 9, pp. C393–C402, 2012.

[127] L. N. Plummer and E. Busenberg, "The solubilities of calcite, aragonite and vaterite in CO2-H2O solutions between 0 and 90 C, and an evaluation of the aqueous model for the system CaCO3-CO2-H2O," *Geochimica et cosmochimica acta*, vol. 46, no. 6, pp. 1011–1040, 1982.

[128] P. Bénézeth, G. D. Saldi, J.-L. Dandurand, and J. Schott, "Experimental determination of the solubility product of magnesite at 50 to 200 C," *Chemical Geology*, vol. 286, no. 1-2, pp. 21–31, 2011.

[129] H. Mansoori, D. Young, B. Brown, and M. Singer, "Influence of calcium and magnesium ions on CO2 corrosion of carbon steel in oil and gas production systems-A review," *Journal of Natural Gas Science and Engineering*, vol. 59, pp. 287–296, 2018.

[130] C. Ding, K.-w. Gao, and C.-f. Chen, "Effect of Ca2+ on CO2 corrosion properties of X65 pipeline steel," *International Journal of Minerals, Metallurgy and Materials*, vol. 16, no. 6, pp. 661–666, 2009.

[131] K. Gao, F. Yu, X. Pang, G. Zhang, L. Qiao, W. Chu, and M. Lu, "Mechanical properties of CO2 corrosion product scales and their relationship to corrosion rates," *Corrosion Science*, vol. 50, no. 10, pp. 2796–2803, 2008.

[132] L. M. Tavares, E. M. da Costa, J. J. de Oliveira Andrade, R. Hubler, and B. Huet, "Effect of calcium carbonate on low carbon steel corrosion behavior in saline CO2 high pressure environments," *Applied Surface Science*, vol. 359, pp. 143–152, 2015.

[133] E. Eriksrud and T. Sontvedt, "Effect of Flow on CO sub 2 Corrosion Rates in Real and Synthetic Formation Waters.(Retroactive Coverage)," *Advances in CO sub 2 Corrosion.*, vol. 1, pp. 20–38, 1984.

[134] S. Navabzadeh Esmaeely, Y.-S. Choi, D. Young, and S. Nešić, "Effect of calcium on the formation and protectiveness of iron carbonate layer in CO2 corrosion," *Corrosion*, vol. 69, no. 9, pp. 912–920, 2013.

[135] S. N. Esmaeely, D. Young, B. Brown, and S. Nešić, "Effect of incorporation of calcium into iron carbonate protective layers in CO2 corrosion of mild steel," *Corrosion*, vol. 73, no. 3, pp. 238–246, 2016.

[136] D. W. Shannon, "Role of chemical components in geothermal brine on corrosion," *CORROSION/78, paper*, no. 57, 1978.

[137] E. Gulbrandsen and K. Bilkova, "Solution chemistry effects on corrosion of carbon steels in presence of CO2 and acetic acid," *Corrosion*, 2006.

[138] K. George, S. Wang, S. Nesic, and K. De Waard, "Modeling of CO2 corrosion of mild steel at high pressures of CO2 and in the presence of acetic acid," *NACE Corrosion*, 2004.

[139] O. A. Nafday, *Film formation and CO2 corrosion in the presence of acetic acid*. PhD thesis, Ohio University, 2004.

[140] J. Mora-Mendoza and S. Turgoose, "Fe3C influence on the corrosion rate of mild steel in aqueous CO2 systems under turbulent flow conditions," *Corrosion Science*, vol. 44, no. 6, pp. 1223–1246, 2002.

[141] R. Nyborg, E. Gulbrandsen, T. Loeland, K. Nisancioglu, *et al.*, "Effect of steel microstructure and composition on inhibition of CO2 corrosion," in *Corrosion*, NACE International, 2000.

[142] F. Farelas, B. Brown, S. Nesic, *et al.*, "Iron carbide and its influence on the formation of protective iron carbonate in CO2 corrosion of mild steel," *Corrosion*, vol. 2291, 2013.

[143] J. Crolet, N. Thevenot, and S. Nesic, "Role of conductive corrosion products in the protectiveness of corrosion layers," *Corrosion*, vol. 54, no. 3, pp. 194–203, 1998.

[144] M. Ueda and H. Takabe, "Effect of environmental factor and microstructure on morphology of corrosion products in COsub 2 environments,"

[145] S. Ieamsupapong, B. Brown, M. Singer, S. Nesic, *et al.*, "Effect of solution pH on corrosion product layer formation in a controlled water chemistry system," *Corrosion*, vol. 9160, 2017.

[146] A. Dugstad, H. Hemmer, and M. Seiersten, "Effect of steel microstructure on corrosion rate and protective iron carbonate film formation," *Corrosion*, vol. 57, no. 4, pp. 369–378, 2001.

[147] J. S. Andrews, *A Comprehensive Comparison of Experimental Techniques to Investigate CO_2 Corrosion of Iron and Carbon Steels*. PhD thesis, University of Manchester, 2018.

[148] C. Escrivà-Cerdán, S. W. Ooi, G. R. Joshi, R. Morana, H. Bhadeshia, and R. Akid, "Effect of tempering heat treatment on the co2 corrosion resistance of quench-hardened cr-mo low-alloy steels for oil and gas applications," *Corrosion Science*, vol. 154, pp. 36–48, 2019.

[149] K. Cooper, *Oilfield Corrosion Scales: Composition, Structure and Morphology*. PhD thesis, The University of Manchester (United Kingdom), 2018.

[150] G. R. Joshi, *Elucidating sweet corrosion scales*. PhD thesis, University of Manchester, 2015.

[151] G. Zhang and Y. Cheng, "On the fundamentals of electrochemical corrosion of X65 steel in CO2-containing formation water in the presence of acetic acid in petroleum production," *Corrosion Science*, vol. 51, no. 1, pp. 87–94, 2009.

[152] S. Wang, K. George, and S. Nesic, "High pressure CO2 corrosion electrochemistry and the effect of acetic acid," *Corrosion*, vol. 4375, 2004.

[153] F. Farelas, M. Galicia, B. Brown, S. Nesic, and H. Castaneda, "Evolution of dissolution processes at the interface of carbon steel corroding in a CO2 environment studied by EIS," *Corrosion Science*, vol. 52, no. 2, pp. 509–517, 2010.

[154] M. Stern and A. L. Geary, "Electrochemical polarization I. A theoretical analysis of the shape of polarization curves," *Journal of the electrochemical society*, vol. 104, no. 1, pp. 56–63, 1957.

[155] R. G. Kelly, J. R. Scully, D. Shoesmith, and R. G. Buchheit, *Electrochemical techniques in corrosion science and engineering*. CRC Press, 2002.

[156] R. G. Kelly, J. R. Scully, D. Shoesmith, and R. G. Buchheit, "The polarization resistance method for determination of instantaneous corrosion rates," in *Electrochemical Techniques in Corrosion Science and Engineering*, pp. 135–160, CRC Press, 2002.

[157] J. Chamberlain and K. R. Trethewey, *Corrosion for Science and Engineering*. Longman Scientific & Technical, 1995.

[158] R. Cottis, *Shreir's Corrosion (4 Volume Set)*. Elsevier Science & Technology, 2010.

[159] M. Walock, *Nanocomposite coatings based on quaternary metalnitrogen*. PhD thesis, Paris, ENSAM, 2012.

[160] W. Zhou, R. Apkarian, Z. L. Wang, and D. Joy, "Fundamentals of scanning electron microscopy (SEM)," in *Scanning microscopy for nanotechnology*, pp. 1–40, Springer, 2006.

[161] W. D. Callister Jr and D. G. Rethwisch, *Fundamentals of materials science and engineering: an integrated approach*. John Wiley & Sons, 2012.

[162] I. M. Watt, *The principles and practice of electron microscopy*. Cambridge University Press, 1997.

[163] R. Anderhalt, "X-ray microanalysis in nanomaterials," in *Scanning Microscopy for Nanotechnology*, pp. 76–100, Springer, 2006.

[164] J. I. Goldstein, D. E. Newbury, J. R. Michael, N. W. Ritchie, J. H. J. Scott, and D. C. Joy, *Scanning electron microscopy and X-ray microanalysis*. Springer, 2017.

[165] V. Randle and O. Engler, *Introduction to texture analysis: macrotexture, microtexture and orientation mapping*. CRC press, 2014.

[166] M. Sezen, "Focused Ion Beams (FIB)—Novel Methodologies and Recent Applications for Multidisciplinary Sciences," *Modern Electron Microscopy in Physical and Life Sciences*, p. 121, 2016.

[167] L. A. Giannuzzi *et al.*, *Introduction to focused ion beams: instrumentation, theory, techniques and practice*. Springer Science & Business Media, 2004.

[168] E. Zolotoyabko, *Basic concepts of X-ray diffraction*. John Wiley & Sons, 2014.

[169] B. D. Cullity and S. R. Stock, *Elements of X-ray Diffraction*, vol. 3. Prentice hall New Jersey, 2001.

[170] A. Chatterjee, "X-ray diffraction," *Handbook of analytical techniques in concrete science and technology*, pp. 275–332, 2000.

[171] O. Sakata and M. Nakamura, "Grazing incidence x-ray diffraction," in *Surface Science Techniques*, pp. 165–190, Springer, 2013.

[172] (ICDD), "The International Centre for Diffraction Data," 2019.

[173] M. Panalytical, "High score Plus." Available online: https://www.malvernpanalytical.com/en/products/category/software/x-ray-diffraction-software/highscore (Last accessed 15-Dec-2019.

[174] S. Hulbert and G. Williams, "Synchrotron radiation sources," tech. rep., Brookhaven National Lab., Upton, NY (US), 1998.

[175] ESRF, "European Synchrotron Radiation Facility," 2019.

[176] Xmas, "The UK Materials Science Facility at the ESRF," 2019.

[177] O. Schneider, G. Ilevbare, J. Scully, and R. Kelly, "Confocal laser scanning microscopy as a tool for in situ monitoring of corrosion underneath organic coatings," *Electrochemical and Solid-State Letters*, vol. 4, no. 12, pp. B35–B38, 2001.

[178] Keyence, "Multi-file Analysis Application."

[179] Keyence, "3D Laser Scanning Microscope, VK-X100K/X105/X110 VK-X200K/X210," 2019.

[180] B. DeGraff and J. Demas, "Luminescence-based oxygen sensors," in *Reviews in fluorescence 2005*, pp. 125–151, Springer, 2005.

[181] R. Tuttle *et al.*, "Corrosion in oil and gas production," *Journal of petroleum technology*, vol. 39, no. 07, pp. 756–762, 1987.

[182] T. E. Perez, "Corrosion in the oil and gas industry: an increasing challenge for materials," *Jom*, vol. 65, no. 8, pp. 1033–1042, 2013.

[183] H. Bai, Y. Wang, Y. Ma, Q. Zhang, and N. Zhang, "Effect of CO2 partial pressure on the corrosion behavior of J55 carbon steel in 30% crude oil/brine mixture," *Materials*, vol. 11, no. 9, p. 1765, 2018.

[184] J. Han, B. Brown, and S. Nešic, "Investigation of the galvanic mechanism for localized carbon dioxide corrosion propagation using the artificial pit technique," *Corrosion*, vol. 66, no. 9, pp. 095003–095003, 2010.

[185] R. Nyborg, A. Dugstad, *et al.*, "Understanding and prediction of mesa corrosion attack," in *Corrosion*, NACE International, 2003.

[186] R. Nyborg *et al.*, "Initiation and growth of mesa corrosion attack during CO2 corrosion of carbon steel," in *Corrosion*, NACE International, 1998.

[187] J. Han, Y. Yang, S. Nesic, B. N. Brown, *et al.*, "Roles of passivation and galvanic effects in localized CO2 corrosion of mild steel," *Corrosion*, vol. 8332, 2008.

[188] J. Han, D. Young, H. Colijn, A. Tripathi, and S. Nesic, "Chemistry and structure of the passive film on mild steel in CO2 corrosion environments," *Industrial & Engineering Chemistry Research*, vol. 48, no. 13, pp. 6296–6302, 2009.

[189] L. Zheng, J. Landon, N. S. Matin, and K. Liu, "FeCO3 coating process toward the corrosion protection of carbon steel in a postcombustion CO2 capture system," *Industrial & Engineering Chemistry Research*, vol. 55, no. 14, pp. 3939–3948, 2016.

[190] Y. Hua, R. Barker, T. Charpentier, M. Ward, and A. Neville, "Relating iron carbonate morphology to corrosion characteristics for water-saturated supercritical CO2 systems," *The Journal of Supercritical Fluids*, vol. 98, pp. 183–193, 2015.

[191] Y. Hua, R. Barker, and A. Neville, "Effect of temperature on the critical water content for general and localised corrosion of X65 carbon steel in the transport of supercritical CO2," *International Journal of Greenhouse Gas Control*, vol. 31, pp. 48–60, 2014.

[192] K. Chokshi, W. Sun, and S. Nesic, "Iron carbonate scale growth and the effect of inhibition in CO2 corrosion of mild steel," in *NACE International Corrosion Conference & Expo, Paper*, vol. 5285, 2005.

[193] O. A. Nafday and S. Nesic, "Iron carbonate scale formation and CO2 corrosion in the presence of acetic acid," 2005.

[194] A. Oshima, S. Ikeda, T. Seguchi, and Y. Tabata, "Improvement of radiation resistance for polytetrafluoroethylene (PTFE) by radiation crosslinking," *Radiation Physics and Chemistry*, vol. 49, no. 2, pp. 279–284, 1997.

[195] R. Singh, *Oilfield Corrosion Scaling: Sour Environments*. PhD thesis, University of Manchester, 2020.

[196] E. A. Ahmad, H.-Y. Chang, M. Al-Kindi, G. R. Joshi, K. Cooper, R. Lindsay, and N. M. Harrison, "Corrosion protection through naturally occurring films: New insights from iron carbonate," *ACS applied materials & interfaces*, vol. 11, no. 36, pp. 33435–33441, 2019.

[197] E. Merson, A. Kudrya, V. Trachenko, D. Merson, V. Danilov, and A. Vinogradov, "The Use of Confocal Laser Scanning Microscopy for the 3D Quantitative Characterization of Fracture Surfaces and Cleavage Facets.," *Procedia Structural Integrity*, vol. 2, pp. 533–540, 2016.

[198] P. Davies and V. Randle, "Combined application of electron backscatter diffraction and stereo-photogrammetry in fractography studies," *Journal of microscopy*, vol. 204, no. 1, pp. 29–38, 2001.

[199] D. Slavik and R. Gangloff, "Environment and microstructure effects on fatigue crack facet orientation in an Al Li Cu Zr alloy," *Acta materialia*, vol. 44, no. 9, pp. 3515–3534, 1996.

[200] P. Davies, M. Novovic, V. Randle, and P. Bowen, "Application of electron backscatter diffraction (EBSD) to fracture studies of ferritic steels," *Journal of microscopy*, vol. 205, no. 3, pp. 278–284, 2002.

[201] P. Mohseni, J. Solberg, M. Karlsen, O. Akselsen, and E. Østby, "Application of combined EBSD and 3D-SEM technique on crystallographic facet analysis of steel at low temperature," *Journal of microscopy*, vol. 251, no. 1, pp. 45–56, 2013.

[202] G. Themelis, S. Chikwembani, and J. Weertman, "Determination of the orientation of Cu Bi grain boundary facets using a photogrammetric technique," *Materials Characterization*, vol. 24, no. 1, pp. 27–40, 1990.

[203] R. D. Shannon, "Revised effective ionic radii and systematic studies of interatomic distances in halides and chalcogenides," *Acta crystallographica section A: crystal physics, diffraction, theoretical and general crystallography*, vol. 32, no. 5, pp. 751–767, 1976.

[204] D. Burkle, R. De Motte, W. Taleb, A. Kleppe, T. Comyn, S. Vargas, A. Neville, and R. Barker, "In situ SR-XRD study of FeCO3 precipitation kinetics onto carbon steel in CO2-containing environments: The influence of brine pH," *Electrochimica Acta*, vol. 255, pp. 127–144, 2017.

[205] M. Tomson, M. Johnson, *et al.*, "How ferrous carbonate kinetics impacts oilfield corrosion," in *SPE International Symposium on Oilfield Chemistry*, Society of Petroleum Engineers, 1991.

[206] R. De Marco, Z.-T. Jiang, B. Pejcic, and E. Poinen, "An in situ synchrotron radiation grazing incidence X-ray diffraction study of carbon dioxide corrosion," *Journal of The Electrochemical Society*, vol. 152, no. 10, pp. B389–B392, 2005.

[207] Y. Yang, G. Joshi, and R. Akid, "Correction: Electrochemical Investigation of the Corrosion of Different Microstructural Phases of X65 Pipeline Steel under Saturated Carbon Dioxide Conditions. Materials 2015, 8, 2635–2649," *Materials*, vol. 8, no. 12, pp. 8728–8730, 2015.

[208] G. R. Joshi, K. Cooper, J. Lapinski, D. L. Engelberg, O. Bikondoa, M. G. Dowsett, R. Lindsay, *et al.*, "In Situ Grazing Incidence X-ray Diffraction of Sweet Corrosion Scaling on Carbon Steel," *Corrosion*, 2015.

[209] S. J. Dyer and G. M. Graham, "The effect of temperature and pressure on oilfield scale formation," *Journal of Petroleum Science and Engineering*, vol. 35, no. 1-2, pp. 95–107, 2002.

[210] A. S. for Testing and P. Materials (Filadelfia, "ASTM E562-11: standard test method for determining volume fraction by systematic manual point count," ASTM, 2011.

[211] J. Schindelin, I. Arganda-Carreras, E. Frise, V. Kaynig, M. Longair, T. Pietzsch, S. Preibisch, C. Rueden, S. Saalfeld, B. Schmid, *et al.*, "Fiji: an open-source platform for biological-image analysis," *Nature methods*, vol. 9, no. 7, p. 676, 2012.

[212] M. Indig and A. McIlree, "High temperature electrochemical studies of the stress corrosion of Type 304 stainless steel," *Corrosion*, vol. 35, no. 7, pp. 288–295, 1979.

[213] E. Barsoukov and J. R. Macdonald, *Impedance spectroscopy: theory, experiment, and applications*. John Wiley & Sons, 2018.

[214] G. L. Fredrickson, P. K. Tripathy, M. R. Shaltry, S. D. Herrmann, T.-S. Yoo, D. C. Horvath, R. O. Hoover, G. Cao, T. Y. Karlsson, and R. Gakhar, "A Perspective and Guide to Electrochemical Measurements in Molten Salt Systems," *Journal of the Electrochemical Society*, vol. 166, no. INL/JOU-19-54206-Rev000, 2019.

[215] Gamry Instruments, USA, *FAS2 Femtostat Operator's Manual*, 5 ed.

[216] Palm Sens, *PSAN0402- Galvanic Isolation in Applications*, 4 2019.

[217] F. Izquierdo-Ruiz, L. Bonales, V. Muñoz-Iglesias, and O. Prieto-Ballesteros, "Measurements of pH under extreme conditions," in *European Planetary Science Congress*, vol. 8, 2013.

[218] S. Lvov, X. Zhou, S. Ulyanov, and A. Bandura, "Reference systems for assessing viability and accuracy of pH sensors in high temperature subcritical and supercritical aqueous solutions," *Chemical Geology*, vol. 167, no. 1-2, pp. 105–115, 2000.

[219] D. Midgley, "A review of pH measurement at high temperatures," *Talanta*, vol. 37, no. 8, pp. 767–781, 1990.

[220] K. Reineke, A. Mathys, and D. Knorr, "Shift of pH-value during thermal treatments in buffer solutions and selected foods," *International journal of food properties*, vol. 14, no. 4, pp. 870–881, 2011.

[221] David Parkhurst and Richard Webb, "PHREEQC." Available online: https://www.usgs.gov/software/phreeqc-version-3/ (last accessed: 15-Dec-2019.

[222] Bryan Research and Engineering, "ProMax."

[223] B. Meyssami, M. O. Balaban, and A. A. Teixeira, "Prediction of pH in model systems pressurized with carbon dioxide," *Biotechnology progress*, vol. 8, no. 2, pp. 149–154, 1992.

[224] M. Ko, B. Ingham, N. Laycock, and D. Williams, "In situ synchrotron X-ray diffraction study of the effect of microstructure and boundary layer conditions on CO2 corrosion of pipeline steels," *Corrosion Science*, vol. 90, pp. 192–201, 2015.

[225] M. Ko, N. J. Laycock, B. Ingham, and D. Williams, "In situ synchrotron X-ray diffraction studies of CO2 corrosion of carbon steel with scale inhibitors ATMPA and PEI at 80° C," *Corrosion*, vol. 68, no. 12, pp. 1085–1093, 2012.

[226] M. Ko, B. Ingham, N. Laycock, and D. Williams, "In situ synchrotron X-ray diffraction study of the effect of chromium additions to the steel and solution on CO2 corrosion of pipeline steels," *Corrosion Science*, vol. 80, pp. 237–246, 2014.

[227] D. Burkle, R. De Motte, W. Taleb, A. Kleppe, T. Comyn, S. Vargas, A. Neville, and R. Barker, "Development of an electrochemically integrated SR-GIXRD flow cell to study FeCO3 formation kinetics," *Review of Scientific Instruments*, vol. 87, no. 10, p. 105125, 2016.

[228] T. G. Digges, S. J. Rosenberg, and G. W. Geil, "Heat treatment and properties of iron and steel," tech. rep., NATIONAL BUREAU OF STANDARDS GAITHERSBURG MD, 1966.

[229] G. Dicken. Private Communication, 2017.

[230] M. G. Dowsett and A. Adriaens, "esaProject." Available online: https://warwick.ac.uk/fac/cross_fac/xmas/other_projects/esaproject/. (Last accessed 15-Dec-2019).

[231] R. Cottis and S. Turgoose, *Electrochemical Impedance and Noise*. NACE International Publication, 1999.

[232] Y. Chen and W. Jepson, "EIS measurement for corrosion monitoring under multiphase flow conditions," *Electrochimica Acta*, vol. 44, no. 24, pp. 4453–4464, 1999.

[233] D. C. Grahame, "The electrical double layer and the theory of electrocapillarity.," *Chemical reviews*, vol. 41, no. 3, pp. 441–501, 1947.

[234] M. E. Orazem and B. Tribollet, "Electrochemical impedance spectroscopy," 2008.

[235] J. Murray, P. Moran, and E. Gileadi, "Utilization of the specific pseudocapacitance for determination of the area of corroding steel surfaces," *Corrosion*, vol. 44, no. 8, pp. 533–538, 1988.

[236] B. Kinsella, Y. Tan, and S. Bailey, "Electrochemical impedance spectroscopy and surface characterization techniques to study carbon dioxide corrosion product scales," *Corrosion*, vol. 54, no. 10, pp. 835–842, 1998.